

**DOE-ER-0313/30  
Distribution  
Categories  
UC-423, -424**

**FUSION MATERIALS  
SEMIANNUAL PROGRESS REPORT  
FOR THE PERIOD ENDING  
June 30, 2001**

**Prepared for  
DOE Office of Fusion Energy Sciences  
(AT 60 20 10 0)**

**DATE PUBLISHED: OCTOBER 2001**

**Prepared for  
OAK RIDGE NATIONAL LABORATORY  
Oak Ridge, Tennessee 37831  
Managed by  
U.T.-Battelle, LLC  
For the  
U.S. DEPARTMENT OF ENERGY  
Under Contract DE-AC05-00OR22725**

## FOREWORD

This is the thirtieth in a series of semiannual technical progress reports on fusion materials science activities supported by the Fusion Energy Sciences Program of the U.S. Department of Energy. This report focuses on research addressing the effects on materials properties and performance from exposure to the neutronic, thermal, and chemical environments anticipated in the chambers of fusion experiments and energy systems. This research is a major element of the national effort to establish the materials knowledge base of an economically and environmentally attractive fusion energy source. Research activities on issues related to the interaction of materials with plasmas are reported separately.

The results reported are the product of a national effort involving a number of national laboratories and universities. A large fraction of this work, particularly in relation to fission reactor irradiations, is carried out collaboratively with partners in Japan, Russia, and the European Union. The purpose of this series of reports is to provide a working technical record for the use of program participants, and to provide a means of communicating the efforts of fusion materials scientists to the broader fusion community, both nationally and worldwide.

This report has been compiled and edited under the guidance of S. J. Zinkle by Renetta Godfrey, Oak Ridge National Laboratory. Their efforts, and the efforts of the many persons who made technical contributions, are gratefully acknowledged.

S. E. Berk  
Facilities and Enabling Technologies Division  
Office of Fusion Energy Sciences

## CONTENTS

<b>1.0</b>	<b>VANADIUM ALLOYS</b>	1
<b>1.1</b>	<b>DEFORMATION BEHAVIOR OF UNALLOYED VANADIUM AT 400°C and 500°C</b> – D. T. Hoelzer and A. F. Rowcliffe (Oak Ridge National Laboratory)	2
	<p>The tensile deformation behavior of unalloyed vanadium has been determined at 400°C and 500°C for strain rates in the range of <math>10^{-1}</math>/s to <math>10^{-5}</math>/s. The concurrence of serrated flow effects in the Lüders extension and work hardening regimes of tensile stress-strain curves is associated with negative strain rate sensitivity of stress parameters.</p>	
<b>1.2</b>	<b>BIAXIAL THERMAL CREEP OF V-4Cr-4Ti IN A LITHIUM ENVIRONMENT</b> – M. L. Grossbeck (Oak Ridge National Laboratory)	8
	<p>Results have been obtained at 765°C for times up to nearly 2000 hours and for 1100 hours at 665°C. At this early stage, the data are consistent with the biaxial measurements in a vacuum environment performed at PNNL at 765°C. At the lower temperature, the Li results are showing slightly higher creep rates. However, the strains are small and have large relative errors. Better comparisons will be made as the tests progress. The steady-state creep regime is very small with an early onset of tertiary creep at 765°C. No creep failures have occurred. A Larson-Miller analysis has shown that no failures are yet expected based upon the PNNL results and uniaxial creep tests on the same alloy performed at ANL.</p>	
<b>1.3</b>	<b>EVALUATION OF THE DHCE EXPERIMENT</b> – L. R. Greenwood, D. L. Baldwin, G. W. Hollenberg and R. J Kurtz (Pacific Northwest National Laboratory)	15
	<p>The Dynamic Helium Charging Experiment (DHCE) experiment was conducted in the Fast Flux Test Facility (FFTF) during cycle 12, which was completed in 1992. The purpose of the experiment was to enhance helium generation in vanadium alloys to simulate fusion reactor helium-to-dpa ratios with a target goal of 4-5 appm He/dpa. The Fusion Materials Science Program is considering mounting another experiment in hopes of gathering additional data on the effect of helium on the mechanical and physical properties of vanadium structural materials. Pacific Northwest National Laboratory was assigned the task of evaluating the feasibility of conducting another DHCE experiment by carefully evaluating the results obtained of the first DHCE experiment. This report summarizes the results of our evaluation and presents recommendations for consideration by the Materials Science Coordinators Organization.</p>	
<b>1.4</b>	<b>OXIDATION OF V-4Cr-4Ti AT LOW PRESSURES</b> – B. A. Pint and J. R. DiStefano (Oak Ridge National Laboratory)	30
	<p>Specimens of V-4Cr-4Ti have been exposed to He environments from 1 atm down to <math>10^{-4}</math> atm in order to determine oxidation kinetics and effects on mechanical properties. At <math>10^{-4}</math> atm He, the reaction kinetics were nearly linear at 700°C. However, at <math>10^{-3}</math> atm He, the specimen mass gains were lower and followed a sub-parabolic rate, very similar to the behavior observed in 1 atm of</p>	

He. These results suggest that an external oxide layer may be forming at the higher pressures. During exposures in 1 atm He, specimens form an external oxide layer and retain some tensile ductility after exposure. To confirm an earlier result, specimens with various exposure times (and thus oxygen levels) were annealed for 2000h at 700°C. The ductility of those specimens which had an external oxide before annealing was reduced to zero, illustrating that a surface oxide on V-4Cr-4Ti is a source of oxygen for further embrittlement.

**1.5 SEM/TEM STUDY OF V-4Cr-4Ti LASER WELDMENTS** - Y. Yan, R. E. Cook, H. Tsai, and D. L. Smith (Argonne National Laboratory) 34

Mechanical properties and microstructures of laser weldments of Heat NIFS-1 V-4Cr-4Ti alloys were investigated by impact testing, optical microscopy, SEM, and TEM. Optical metallography shows that grain sizes in the weld are greater than those in the base material. The grains are equiaxed near the middle of the weld and elongated (oriented in the direction of freeze progression) near the edge. Element mapping in SEM shows that the Ti and C content of the secondary phase particles ( $\gg 300$  nm) is significantly higher in the banded structure than in the matrix, and the banded structure in the base metal seems to disappear in the weld zone. Impact testing with laser weld specimens in as-machined condition (by electric discharge machining with water as the flushing fluid) indicated that the ductile-to-brittle-transition temperature of Heat NIFS-1 is higher than that of Heat 832665. Small particles (50-100 nm) are observed at the grain boundary of the NIFS-1 laser weld. Energy-dispersive spectroscopy (EDS) analyses show that the chemical composition appears to vary from grain to grain of the laser weld.

**2.0 CERAMIC COMPOSITE MATERIALS** 44

**2.1 RESPONSE OF SiC/SiC TO TRANSIENT THERMAL CONDITIONS: A REVIEW** – R. H. Jones (Pacific Northwest National Laboratory) 45

The database on thermal shock behavior of SiC/SiC composites is very limited. The existing data suggests continuous fiber ceramic matrix composites, such as SiC/SiC, exhibit very good thermal shock characteristics but most data was obtained for  $-T$  conditions as a result of quenching from an elevated temperature. Thermal shock in a fusion energy system will result from plasma discharge and will result in a  $+T$ . One study was reported for SiC/SiC composites given a  $+T$  with no loss in strength following 25 cycles at a heating rate of 1700°C/s. Monolithic SiC failed in 1.5 cycles at a heating rate of 1400°C/s. Thermal fatigue test results also suggest that SiC/SiC composites will exhibit little or no degradation for 100's of cycles. It was estimated that radiation could, in an extreme case, cause a reduction in the thermal shock performance from a calculated  $T_c$  of 957K to about 300K if the fiber strength is reduced by 50%. Newer composites with greater radiation resistance should have a much smaller change in the  $T_c$ .

**2.2 STRUCTURAL RELAXATION IN AMORPHOUS SILICON CARBIDE – 55**  
L. L. Snead and S. J. Zinkle (Oak Ridge National Laboratory)

High purity single crystal and chemically vapor deposited silicon carbide has been amorphized under fast neutron irradiation. The gradual transition in physical properties from the as-amorphized state to a more relaxed amorphous state prior to crystallization is studied. For the three bulk properties studied: density, electrical resistivity, and thermal conductivity, large property changes occur upon annealing between the amorphization temperature and the point of crystallization. These physical property changes occur in the absence of crystallization and are attributed to short, and perhaps medium range ordering during annealing. It is demonstrated that the physical properties of amorphous SiC can vary greatly, and are likely a function of the irradiation state producing the amorphization. The initiation of crystallization as measured using bulk density and in-situ TEM is found to be  $\sim 875^{\circ}\text{C}$ , though the kinetics of crystallization above this point are seen to depend on the technique used. It is speculated that in-situ TEM and other thin-film approaches to studying crystallization of amorphous SiC are faulted due to thin-film effects.

**2.3 AN UPDATE ON THE KFIB EXPERIMENT – G. E. Youngblood and 64**  
R. H. Jones (Pacific Northwest National Laboratory) W. Kowbel (MER Corporation), Paul de Heij (NRG Petten) and Akira Kohyama (Kyoto University).

An updated sample test matrix for the KFIB experiment is presented. The pre-irradiation test results for all fiber and SiC/SiC composite materials included in the test matrix, presented at the 4th IEA Workshop on SiC/SiC for Fusion Structural Applications held in Frascati, Italy, October 12- 13, 2000, are reviewed. The KFIB samples have been delivered for capsule loading. They are scheduled to be irradiated from October-November, 2001 through April-May, 2002 to similar doses (2-4 dpa-SiC) in the ATR (Idaho Falls) at  $300^{\circ}\text{C}$  and the HFR (Petten) at 625 and  $975^{\circ}\text{C}$ . To assess irradiation enhanced creep (IEC) in SiC fibers, a bend stress relaxation module was added to the HFR sample matrix at each irradiation temperature.

**2.4 STRENGTH AND DIMENSIONAL CHANGE OF NEUTRON-IRRADIATED 72**  
**HIGH-QUALITY 3D CARBON FIBER COMPOSITE –** L. L. Snead,  
T. D. Burchell, and A. L. Qualls (Oak Ridge National Laboratory)

The effects of neutron irradiation to  $\sim 7$  dpa at 500 and  $800^{\circ}\text{C}$  on a high quality, three-dimensional balanced weave composite (FMI-222) is presented. Strength and dimensional stability for this system is compared to earlier work on this material, at lower dose, and contrasted with that of a well studied isotropic graphite (POCO AXF-5Q) irradiated at identical conditions. For both irradiation temperatures the composite strength in bending is substantially increased. Interestingly, while both irradiation temperatures cause contraction along the bend bar axis, the amount of contraction is greater for the higher temperature irradiation. Moreover, for the  $500^{\circ}\text{C}$  specimens nearly isotropic contraction leads to a corresponding decrease in volume, though an apparent large increase in volume occurs for the  $800^{\circ}\text{C}$  irradiated composite due to very anisotropic dimensional change. As the FMI-222 is a balanced-weave, isotropic composite, non-isotropic swelling behavior was unexpected, and is explained in

terms of the fiber dimensional stability model previously presented, and the composite nature of this material.

### **3.0 FERRITIC MARTENSITIC STEELS** 79

#### **3.1 EFFECT OF CHROMIUM, TUNGSTEN, TANTALUM, AND BORON ON MECHANICAL PROPERTIES OF 5-9Cr-WVTaB STEELS** - R. L. Klueh and M. A. Sokolov (Oak Ridge National Laboratory) 80

Although the results of studies on reduced-activation ferritic/martensitic steels have demonstrated the excellent properties of 7-10Cr-2WVTa martensitic steels little information is available concerning the effect of chromium over the 5-10% range, where the steels transform to martensite when normalized or quenched. In this work, the effect of chromium, tungsten, and tantalum was investigated for the martensitic 5-9% Cr steels. The effect of boron was also investigated, because it has often been used in these types of steels to improve properties.

#### **3.2 MICROSTRUCTURAL EVOLUTION OF REDUCED-ACTIVATION 9Cr-STEELS IN HFIR-CTR-62/63 EXPERIMENT** - N. Hashimoto and R. L. Klueh (Oak Ridge National Laboratory) 91

The microstructures of reduced-activation ferritic/martensitic steels, 9Cr-1MoVNb and 9Cr-1MoVNb-2Ni, irradiated at 400°C up to 12 dpa in the High Flux Isotope Reactor (HFIR), were investigated by transmission electron microscopy. Irradiation-induced cavities were observed in both steels. The cavity number density of the 9Cr-1MoVNb-2Ni was higher than that of 9Cr-1MoVNb due to the higher concentration of helium. The swelling of the 9Cr-1MoVNb and the 9Cr-1MoVNb-2Ni was 0.002% and 0.004%, respectively. Irradiation-induced  $a_0\langle 100 \rangle$  and  $(a_0/2)\langle 111 \rangle$  type dislocation loops were observed in the all irradiated steels; number density and mean diameter of  $a_0\langle 100 \rangle$  type loops was higher and smaller than that of  $(a_0/2)\langle 111 \rangle$  type loops. There was a tendency for the number density of loops in 9Cr-1MoVNb-2Ni to be higher than in 9Cr-1MoVNb. Irradiation-produced precipitates, identified  $M_2X$  phase, were found in the 9Cr-1MoVNb-2Ni.

### **4.0 COPPER ALLOYS** 98

#### **4.1 TRUE STRESS-STRAIN BEHAVIOR OF AS-IRRADIATED AND POST IRRADIATION ANNEALED PURE COPPER** – D. J. Edwards (Pacific Northwest National Laboratory), B. N. Singh and Palle Toft (Risø National Laboratory) 99

Post-irradiation annealing experiments were conducted on neutron-irradiated pure copper (from 0.01 to 0.3 dpa at 100°C) to explore the possibility of mitigating the effects of radiation hardening on the strength and ductility. The post-irradiation annealing (PIA) condition of 300°C for 50 hours yielded mixed results and did not completely remove the effects of irradiation. However, there were changes brought about in the microstructure that led to the removal of the yield point phenomenon and restored some of the unirradiated ductility and work hardening. The true stress-strain curves have been calculated for both the as-irradiated and the PI annealed Cu and compared to that of the unirradiated

pure copper. The true stresses at which the as-irradiated samples begin to neck (based on the engineering stress-strain curves) are similar for the 0.1 to 0.3 dpa samples and are similar to that of the unirradiated copper. On the other hand, the as-irradiated 0.01 dpa condition and all of the post-annealed conditions begin necking at lower stresses, but at similar strains. The work hardening rate in the as-irradiated copper (0.1 to 0.3 dpa), when compared on Kocks-Mecking plots, shows that after a few percent strain, the macroscopic work hardening behavior mimics that of the unirradiated pure copper in the latter stages of work hardening. The PI annealing does little to restore the elongation compared to the as-irradiated state, yet lowers the yield strength, removes the yield point phenomenon and causes the material to begin necking at a lower stress. Compression testing is offered as a method to extend the mechanical properties testing to minimize the geometrical instabilities inherent in the tensile testing and explore the full range of work hardening up to failure.

## **5.0 BCC REFRACTORY METALS AND ALLOYS** 109

No contributions.

## **6.0 AUSTENITIC STAINLESS STEELS** 110

### **6.1 DETERMINATION OF THE LOWER TEMPERATURE LIMIT OF VOID SWELLING OF STAINLESS STEELS AT RELATIVELY LOW DISPLACEMENT RATES** – S. I. Porollo, (Institute of Physics and Power Engineering, Russia), F. A. Garner (Pacific Northwest National Laboratory) 111

The lower limit for void swelling of austenitic stainless steel was investigated using a flow restrictor component from the low-flux breeder zone of the BN-350 fast reactor in Kazakhstan. This component was constructed of annealed 12X18H10T, an alloy similar to AISI 321 which is used in Russian reactors for applications where AISI 304L would be used in comparable Western and Japanese reactors. Extensive sectioning to produce 114 separate specimens, followed by examination of the radiation-induced microstructure showed that void swelling in the range of temperatures and dpa rates of PWR interest occurs down to ~305°C. At 330°C the swelling reached ~1% at 20 dpa. Comparison of these data with other published results from Russian LWR reactors at <10 dpa confirms that the lowest temperature that stainless steels can begin swelling appears to be ~300°C. Since fusion and PWR spectra generate similar levels of hydrogen and helium, it is expected that these conclusions are also applicable to fusion devices operating at comparable dpa rates.

### **6.2 GENERATION AND RETENTION OF HELIUM AND HYDROGEN IN AUSTENITIC STEELS IRRADIATED IN A VARIETY OF LWR AND TEST REACTOR SPECTRAL ENVIRONMENTS** - F. A. Garner, B. M. Oliver, L. R. Greenwood, D. J. Edwards and S.M. Bruemmer (Pacific Northwest National Laboratory), M. L. Grossbeck, (Oak Ridge National Laboratory) 127

In fission and fusion reactor environments stainless steels generate significant amounts of helium and hydrogen by transmutation. The primary sources of helium are boron and nickel, interacting with both fast and especially thermal neutrons. Hydrogen arises primarily from fast neutron reactions, but is also introduced into steels at often much higher levels by other environmental

processes. Although essentially all of the helium is retained in the steel, it is commonly assumed that most of the hydrogen is not retained. It now appears that under some circumstances, significant levels of hydrogen can be retained, especially when helium-nucleated cavities become a significant part of the microstructure. A variety of stainless steel specimens have been examined from various test reactors, PWRs and BWRs. These specimens were exposed to a wide range of neutron spectra with different thermal/fast neutron ratios. Pure nickel and pure iron have also been examined. It is shown that all major features of the retention of helium and hydrogen can be explained in terms of the composition, thermal/fast neutron ratio and the presence or absence of helium-nucleated cavities. In some cases, the hydrogen retention is very large and can exceed that generated by transmutation, with the additional hydrogen arising from either environmental sources and/or previously unidentified radioisotope sources that may come into operation at high neutron exposures.

**6.3 NEUTRON-INDUCED MICROSTRUCTURAL EVOLUTION OF Fe-15Cr-16Ni ALLOYS AT ~ 400°C DURING NEUTRON IRRADIATION IN THE FFTF FAST REACTOR** – T. Okita, T. Sato and N. Sekimura (University of Tokyo), F. A. Garner and L. R. Greenwood (Pacific Northwest National Laboratory), W. G. Wolfer (Lawrence Livermore National Laboratory), and Y. Isobe (Nuclear Fuel Industries Ltd., Japan) 148

An experiment conducted at ~400°C on simple model austenitic alloys (Fe-15Cr-16Ni and Fe-15Cr-16Ni-0.25Ti, both with and without 500 appm boron) irradiated in the FFTF fast reactor at seven different dpa rates clearly shows that lowering of the atomic displacement rate leads to a pronounced reduction in the transient regime of void swelling. While the steady state swelling rate (~1%/dpa) of these alloys is unaffected by changes in the dpa rate, the transient regime of swelling can vary from <1 to ~60 dpa when the dpa rate varies over more than two orders of magnitude. This range of dpa rates covers the full span of fusion, PWR and fast reactor rates. The origin of the flux sensitivity of swelling arises first in the evolution of the Frank dislocation loop population, its unfauling, and the subsequent evolution of the dislocation network. There also appears to be some flux sensitivity to the void nucleation process. Most interestingly, the addition of titanium suppresses the void nucleation process somewhat, but does not alter the duration of the transient regime of swelling or its sensitivity to dpa rate. Side-by-side irradiation of boron-modified model alloys in this same experiment shows that higher helium generation rates homogenize the swelling somewhat, but do not significantly change its magnitude or flux sensitivity. The results of this study support the prediction that austenitic alloys irradiated at PWR-relevant displacement rates will most likely swell more than when irradiated at higher rates characteristic of fast reactors. Thus, the use of swelling data accumulated in fast reactors may possibly lead to an under-prediction of swelling in lower-flux PWRs and fusion devices.

- 6.4 INVESTIGATION OF THE SYNERGISTIC INFLUENCE OF IRRADIATION TEMPERATURE AND ATOMIC DISPLACEMENT RATE ON THE MICROSTRUCTURAL EVOLUTION OF ION-IRRADIATED MODEL AUSTENITIC ALLOY Fe-15Cr-16Ni** – T. Okita, T. Iwai and N. Sekimura (Tokyo University), F. A. Garner (Pacific Northwest National Laboratory) 165

A comprehensive experimental investigation of microstructural evolution has been conducted on Fe-15Cr-16Ni irradiated with 4.0 MeV nickel ions in the High Fluence Irradiation Facility of the University of Tokyo. Irradiations proceeded to dose levels ranging from ~0.2 to ~26 dpa at temperatures of 300, 400 and 500°C at displacement rates of  $1 \times 10^{-4}$ ,  $4 \times 10^{-4}$  and  $1 \times 10^{-3}$  dpa/sec. This experiment is one of two companion experiments directed toward the study of the dependence of void swelling on displacement rate. The other experiment proceeded at seven different but lower dpa rates in FFTF-MOTA at ~400°C. In both experiments the swelling was found at every irradiation condition studied to monotonically increase with decreases in dpa rate. The microstructural evolution under ion irradiation was found to be very sensitive to the displacement rate at all three temperatures. The earliest and most sensitive component of microstructure to both temperature and especially displacement rate was found to be the Frank loops. The second most sensitive component was found to be the void microstructure, which co-evolves with the loop and dislocation microstructure. These data support the prediction that void swelling will probably be higher in lower-flux fusion devices and PWRs at a given irradiation temperature when compared to irradiations conducted at higher dpa rates in fast reactors.

- 7.0 MHD INSULATORS, INSULATING CERAMICS AND OPTICAL MATERIALS** 173
- 7.1 STUDY OF THE LONG-TERM STABILITY OF MHD COATINGS FOR FUSION REACTOR APPLICATIONS** – B. A. Pint and J. R. DiStefano (Oak Ridge National Laboratory) 174

Bulk specimens of two candidate compositions, CaO and AlN+0.04wt.%Y, for insulating coatings in a lithium-cooled fusion reactor have been exposed to lithium in 1000 h isothermal tests at 500°-800°C to determine the maximum temperature at which acceptable compatibility is likely. Because high mass losses for AlN were observed at 700°C, additional testing has focused on this temperature in order to examine what changes may slow the rate of dissolution. Changing from a vanadium alloy test capsule to a Mo capsule appears to have the largest effect at 700°C. For single crystal specimens of CaO, high mass losses have been observed after exposure at 600°C. In this case, changing to a Mo capsule or adding Ca or O to the lithium have not consistently showed a beneficial effect. For testing at 700°C, neither doping the Li with Ca or O altered the high mass losses. These results suggest that CaO may be limited to exposure temperatures of less than 600°C but that AlN may be able to operate above 600°C.

**7.2 IN-SITU FORMATION OF CaO INSULATOR COATINGS ON VANADIUM ALLOYS** - D. L. Smith, J-H. Park, and K. Natesan (Argonne National Laboratory) 178

A key issue for the self-cooled lithium blanket concept with a vanadium alloy structure is the development of an electrically insulating coating on the coolant channel walls to mitigate the magneto-hydrodynamic pressure drop in a high magnetic field. A systematic investigation of the thermodynamics and kinetics of oxygen and calcium interactions in the vanadium alloy/lithium system is being conducted to define the system parameters required for in-situ formation of a CaO coating on vanadium alloys. This paper presents results of theory and modeling as well as experimental results on the formation of CaO coatings on vanadium alloys after exposure at temperatures of 600 – 700°C to lithium with a small fraction of Ca added. Coatings of 10 - 30  $\mu\text{m}$  with high electrical resistivity have been formed.

**7.3 DEVELOPMENT, CHARACTERIZATION, AND Li COMPATIBILITY OF AN ELECTRICALLY INSULATING CaO COATING ON V-4Cr-4Ti ALLOY** - K. Natesan, M. Uz, D. L. Rink, and D. L. Smith (Argonne National Laboratory) 186

As part of the U.S. Department of Energy's Fusion Program, research is being conducted to develop an electrically insulating and liquid-Li-compatible CaO coating on V-4Cr-4Ti alloy. CaO has been identified as the primary coating candidate for this application, based on its high electrical resistivity and thermodynamic stability in Li at the temperatures of interest (400-700°C). This report deals with the development and characterization of a CaO coating deposited on V-4Cr-4Ti alloy specimens by a vapor transport process that uses double Ca-deposition/oxidation steps. The specimen surfaces were analyzed after each step during the process, and the surfaces, along with their cross-sections, were analyzed after exposure to liquid Li. The analysis and characterization were done by one or more techniques, including scanning electron microscopy, energy-dispersive X-ray analysis, X-ray diffraction, and measurement of electrical resistivity external to Li. Here, we present the new developments and results obtained since the last reporting period that ended on December 31, 2000.

**7.4 DEVELOPMENT OF ELECTRICALLY INSULATING COATINGS BY MOCVD TECHNIQUE** - Z. Zeng and K. Natesan (Argonne National Laboratory) 196

This report addresses the development and characterization of CaO and  $\text{Y}_2\text{O}_3$  coatings that were applied on V-4Cr-4Ti alloy by an MOCVD process. Several coupon specimens were coated with CaO or  $\text{Y}_2\text{O}_3$  by the process developed at ANL. The specimens were analyzed and the coatings were characterized before exposure to a liquid Li environment. The analysis and characterization used one or more of scanning electron microscopy (SEM), energy-dispersive X-ray analysis (EDX), and X-ray diffraction (XRD) techniques. Results are presented, with emphasis on microstructural analysis and electrical resistivity of the coatings. We plan to expose the coated specimens in liquid Li of varying chemistry at temperatures of 500-700°C.

<b>8.0</b>	<b>BREEDING MATERIALS</b>	204
	No contributions.	
<b>9.0</b>	<b>RADIATION EFFECTS, MECHANISTIC STUDIES, AND EXPERIMENTAL METHOD</b>	205
<b>9.1</b>	<b>ATOMISTIC SIMULATION OF DISLOCATION-DEFECT INTERACTIONS IN CU</b> – B. D. Wirth, V. V. Bulatov and T. Diaz de la Rubia (Lawrence Livermore National Laboratory)	206
	The mechanisms of dislocation-defect interactions are of practical importance for developing quantitative structure-property relationships, mechanistic understanding of plastic flow localization and predictive models of mechanical behavior in metals under irradiation. In copper and other face centered cubic metals, high-energy particle irradiation produces hardening and shear localization. Post-irradiation microstructural examination in Cu reveals that irradiation has produced a high number density of nanometer sized stacking fault tetrahedra. Thus, the resultant irradiation hardening and shear localization is commonly attributed to the interaction between stacking fault tetrahedra and mobile dislocations, although the mechanism of this interaction is unknown. In this work, we present a comprehensive molecular dynamics simulation study that characterizes the interaction and fate of moving dislocations with stacking fault tetrahedra in Cu using an EAM interatomic potential. This work is intended to produce atomistic input into dislocation dynamics simulations of plastic flow localization in irradiated materials.	
<b>10.</b>	<b>DOSIMETRY, DAMAGE PARAMETERS, AND ACTIVATION CALCULATIONS</b>	213
<b>10.1</b>	<b>NEUTRON DOSIMETRY AND DAMAGE CALCULATIONS FOR THE HFIR-RB-11J,12J IRRADIATIONS</b> – L. R. Greenwood (Pacific Northwest National Laboratory) and C. A. Baldwin (Oak Ridge National Laboratory)	214
	Neutron fluence measurements and radiation damage calculations are reported for the joint U.S. Japanese experiments RB-11J and RB-12J which were conducted in the removable beryllium (RB) position of the High Flux Isotope Reactor (HFIR) at Oak Ridge National Laboratory (ORNL). These experiments employed a $\text{Eu}_2\text{O}_3$ thermal shield for the first time to reduce the thermal neutron fluence. The maximum total neutron fluence at midplane was $1.85 \times 10^{22}$ n/cm <sup>2</sup> ( $9.5 \times 10^{21}$ n/cm <sup>2</sup> above 0.1 MeV), resulting in about 5.5 dpa and 3.6 appm helium in type 316 stainless steel.	
<b>11.</b>	<b>MATERIALS ENGINEERING AND DESIGN REQUIREMENTS</b>	220
	No contributions.	
<b>12.</b>	<b>IRRADIATION FACILITIES AND TEST MATRICES</b>	221
	No contributions.	

## **1.0 VANADIUM ALLOYS**

## **DEFORMATION BEHAVIOR OF UNALLOYED VANADIUM At 400°C and 500°C - D. T. Hoelzer and A. F. Rowcliffe (Oak Ridge National Laboratory)\***

### **OBJECTIVE**

The broad objective of this work is to investigate the influence of the interstitial elements on the deformation behavior of BCC alloys.

### **SUMMARY**

The tensile deformation behavior of unalloyed vanadium has been determined at 400°C and 500°C for strain rates in the range  $10^{-1}$ /s to  $10^{-5}$ /s. The occurrence of serrated flow effects in the Lüders extension and work hardening regimes of tensile stress-strain curves is associated with negative strain rate sensitivity of stress parameters.

### **PROGRESS AND STATUS**

#### **Introduction**

The deformation behavior of unalloyed vanadium was shown to exhibit dynamic strain aging (DSA) at 200°C and 300°C for strain rates ranging from  $10^{-1}$ /s to  $10^{-5}$ /s [1]. The appearance of serrated yielding (continuous) and jerky flow (discontinuous) in the Lüders strain and work hardening regimes of stress-strain curves and a concomitant negative value in strain rate sensitivity (SRS) for flow stresses was found to be associated with the DSA phenomenon. In addition, the shape, frequency, and magnitude of the serrations and jerky flow depended on temperature, strain, and strain rate. The measured time between load drops for serrations as a function of temperature and strain rate indicated that the DSA effect was due to the migration of interstitial C and O atoms to dislocations below ~300°C. The purpose of this study is to investigate the DSA effect in vanadium at temperatures above 300°C in order to develop a better understanding of the interaction between Ti and interstitial atoms by comparing it with the V-4Cr-4Ti alloy [2-4].

#### **Experimental Procedure**

Sheet tensile specimens of the type SS-3 (nominal gage dimensions  $0.76 \times 1.52 \times 7.6$  mm) were prepared from unalloyed vanadium (Teledyne Wah-Chang heat no. 820642). A 6.4mm thick plate was cut from the vanadium ingot, hot rolled at ~1050°C to a thickness of 2.5mm (60% reduction) and then cold rolled to 1.5mm (40% reduction). Specimens were electro-discharge machined from the 1.5mm thick plate and annealed at 1000°C for 1 hour in a vacuum of  $< \sim 3 \times 10^{-7}$  torr followed by furnace cooling. This procedure resulted in a uniform microstructure consisting of recrystallized grains with an average grain size of  $89 \pm 5 \mu\text{m}$ . Tensile testing was carried out under a vacuum of  $\sim 2 \times 10^{-7}$  torr using a screw-driven machine. Specimens were held at the test temperature for 20-30 minutes before starting the test. Data were acquired digitally at rates of 20 points per second (pps) for tests conducted at  $10^{-1}$ /s and  $10^{-3}$ /s strain rates and 0.2pps at  $10^{-5}$ /s strain rate.

#### **Results**

Data obtained from testing the specimens at 400°C and 500°C with strain rates of  $10^{-1}$ ,  $10^{-3}$ , and  $10^{-5}$  are summarized in Table 1. In addition, data from the tests at 200°C and 300°C are also included for comparison. The engineering stress-strain curves for 400°C and 500°C are shown in

---

\*Oak Ridge National Laboratory (ORNL) is operated for the U.S. Department of Energy by UT-Battelle, LLC under contract DE-AC05-00OR22725.

Table 1. Temperature and Strain Rate Dependence of Unalloyed Vanadium Tensile Properties.

Specimen	Test Temp.	Strain Rate	Lower Yield Stress $\sigma_y$	Ultimate Tensile Strength $\sigma_u$	Stress for 8% Strain $\sigma_s$	Luders Strain $\epsilon_L$	Uniform Strain $\epsilon_u$	Total Strain $\epsilon_t$
ID	$^{\circ}\text{C}$	$\text{s}^{-1}$	MPa			%		
PV46	200	$10^{-1}$	124	193	172	1.4	29.0	42.8
PV44	200	$10^{-3}$	105	188	161	0.8	24.1	36.2
PV45	200	$10^{-5}$	100	194	187	0.8	11.1	17.6
PV41	300	$10^{-1}$	116	183	174	0.4	14.2	20.6
PV42	300	$10^{-3}$	115	240	213	0.8	15.2	21.1
PV43	300	$10^{-5}$	118	297	238	1.4	19.4	27.8
PV47	400	$10^{-1}$	108	228	194	0.5	19.9	27.5
PV48	400	$10^{-3}$	111	294	236	0.8	17.1	23.5
PV49	400	$10^{-5}$	112	318	240	1.0	22.0	29.2
PV50	500	$10^{-1}$	103	264	211	0	22.2	28.0
PV51	500	$10^{-3}$	90	280	214	0	21.2	36.9
PV52	500	$10^{-5}$	95	222	210	0.7	11.7	35.0

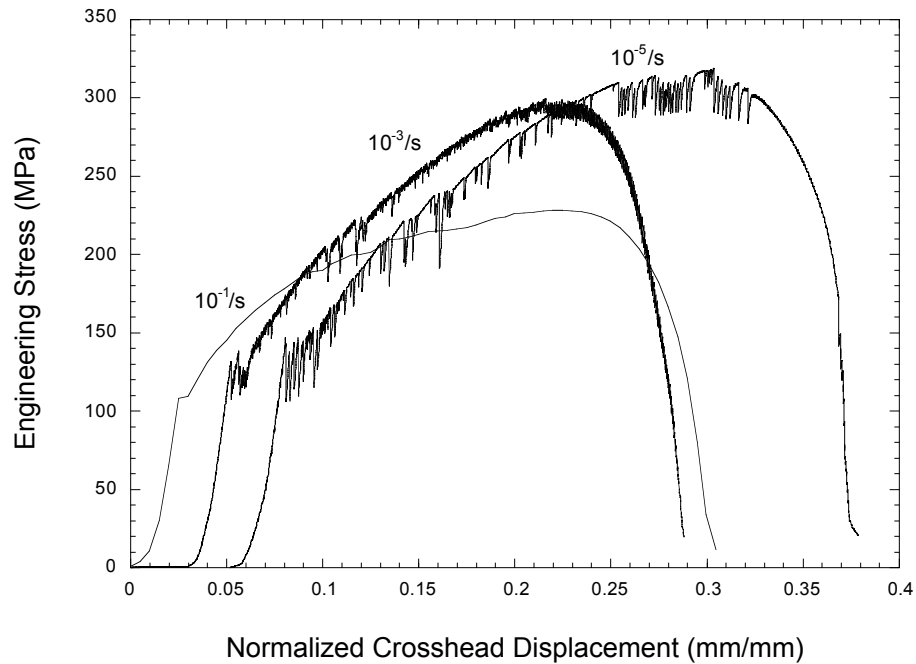


Figure 1. The stress-strain curves for vanadium at 400°C.

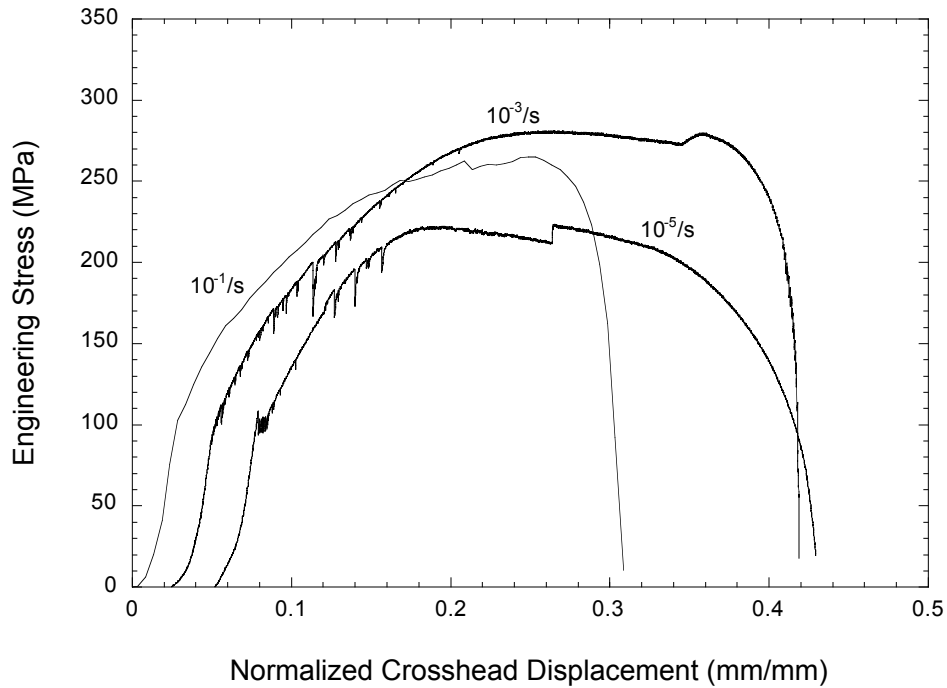


Figure 2. The stress-strain curves for vanadium at 500°C.

Figures 1 and 2, respectively. The curves have been offset along the normalized crosshead displacement axis for comparison of the elastic and Lüders extension regimes. Most of the specimens exhibited Lüders extensions ranging from 0.5 to 1.0%; only specimens tested at 500°C with strain rates of  $10^{-1}/s$  and  $10^{-3}/s$  showed no Lüders extensions. Serrations associated with the Lüders extension are propagated by an average stress which is defined as the lower yield stress,  $\sigma_y$ . Upon completion of the Lüders extension, the deformation proceeds with initially an increase in the work hardening rate on the stress-strain curve that eventually decreases until the ultimate stress,  $\sigma_u$ , is achieved. All of the stress-strain curves exhibited both continuous oscillations (serrated yielding) and discontinuous (jerky flow) behavior in the plastic flow regimes of stress strain curves. The results indicated that both the frequency and magnitude of the serrations changed with temperature, strain, and strain rate. For tests carried out at a rate of  $10^{-1}/s$ , the data acquisition system was not sufficiently rapid to detect load drops associated with the serrations. Therefore, the presence of jerky flow could not be directly ascertained at this strain rate.

The strain-rate dependence was determined for the lower yield stress,  $\sigma_y$ , and for a parameter,  $\sigma_s$ , which is the stress required to produce a strain of 8% after the completion of the Lüders extension. The 8% strain is an arbitrary value selected to represent material in the strain-hardening regime. The strain-rate dependence of these stress parameters for temperatures ranging from 200°C to 500°C are presented in Figures 3 and 4 along with logarithmic curve fits to the data.

The strain rate sensitivity,  $m$ , was calculated for  $\sigma_y$ ,  $\sigma_s$ , and  $\sigma_u$  at each temperature and are compiled in Table 2. The  $m$  values were calculated from:

$$m = \frac{1}{\sigma} \frac{\partial \sigma}{\partial \ln \dot{\epsilon}} \Big|_{\epsilon, T}$$

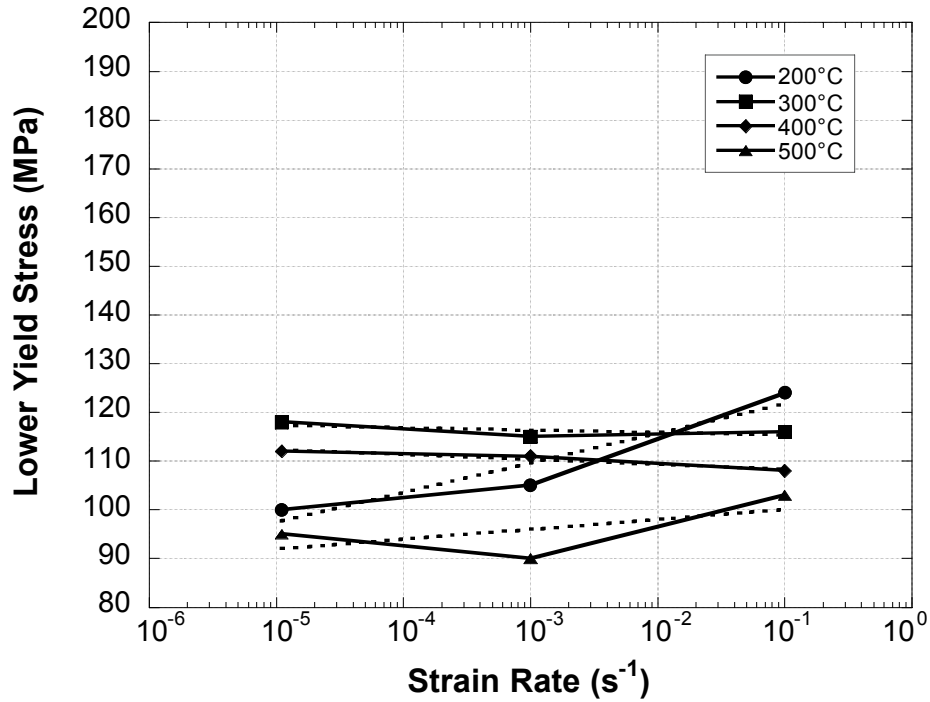


Figure 3. Effect of strain rate on the lower yield strength of vanadium tested at temperatures of 200°C to 500°C.

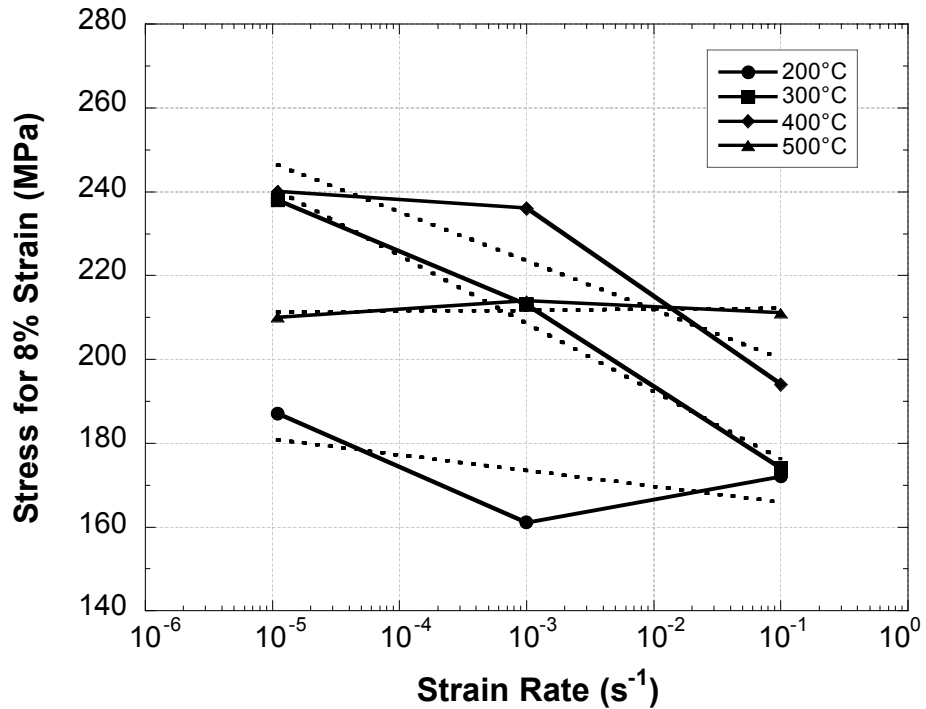


Figure 4. Effect of strain rate on the tensile strength (measured at 8% strain in the strain-hardening regime) of vanadium tested at temperatures of 200°C to 500°C.

where  $\sigma$  is the stress and  $\dot{\epsilon}$  is the strain rate, and are represented by the slope of the logarithmic curve fits shown in Figures 3 and 4. The results indicate that the SRS of  $\sigma_y$  is positive at 200°C, virtually independent of strain rate at 300°C and 400°C, and is slightly positive again at 500°C. The data for  $\sigma_y$  at 500°C actually shows a U-shape dependence with strain rate (Fig. 3). A different behavior in SRS was observed for  $\sigma_s$  and  $\sigma_u$ ; both are negative between 200°C and 400°C and slightly positive at 500°C. The maximum magnitude in negative SRS for  $\sigma_s$  and  $\sigma_u$  was found to occur at 300°C.

The appearance of serrations and jerky flow in stress-strain curves at 400°C (Fig. 1) coincided with the negative  $m$  values of  $\sigma_s$  and  $\sigma_u$ . At 500°C, serrations and jerky flow are also observed in stress-strain curves but typically occur below 8% strain. This observation correlates with the SRS values measured at 500°C, which is slightly positive at  $\sigma_s$  ( $m=0.001$ ) and becomes more positive at  $\sigma_u$  ( $m=0.019$ ). In addition, the frequency and magnitude of the serrations and jerky flow are significantly greater for stress-strain curves at 400°C compared to those at 500°C. It should be mentioned that due to the data acquisition problem described above, serrations and jerky flow were not observed in any stress-strain curves using the  $10^{-1}/s$  strain rate. However, the negative SRS values measured at 300°C [1] and 400°C suggest that serrated yielding is occurring during these tests but detection is limited by the sensitivity of the data acquisition system.

Table 2. Strain rate sensitivity,  $m$ , values calculated for several stress parameters of vanadium.

Temperature	Strain Rate Sensitivity ( $m$ )		
	Lower Yield Stress ( $\sigma_y$ )	Stress at 8% Strain ( $\sigma_s$ )	Ultimate Stress ( $\sigma_u$ )
200°C	0.024	-0.009	-0.001
300°C	-0.002	-0.034	-0.053
400°C	-0.004	-0.023	-0.037
500°C	0.009	0.001	0.019

## Discussion

The results of this study, combined with those previously reported [1] indicate that the phenomenon of dynamic strain aging occurs between 200°C and 500°C. The magnitude of SRS has a maximum negative value at 300°C and remains negative up to 400°C and then diminishes rapidly at higher temperatures. As discussed earlier, the magnitude of the DSA phenomenon decreases in the temperature-strain rate regime where the mobility of the interstitial solutes is sufficiently high for Cottrell atmospheres to migrate along with rapidly moving dislocations.

Examination of the details of the stress-strain curves for vanadium show the existence of two types of discontinuities. The first type consists of high frequency periodic oscillations (serrated yielding) with an approximate saw-tooth pattern; the amplitude varies with temperature and with strain rate in the range 3-8 Mpa. The second type consists of an irregularly spaced series of load drops with magnitudes in the range 8-20Mpa (discontinuous yielding). Further work is in progress to understand the spatio-temporal behavior of these oscillations and to relate their magnitude and frequency to the mobilities of the interstitial solutes.

The results of the testing at 400°C and 500°C lead us to a re-evaluation of our earlier conclusion that alloying with Cr and Ti leads to an increase in the temperature range for DSA of approximately

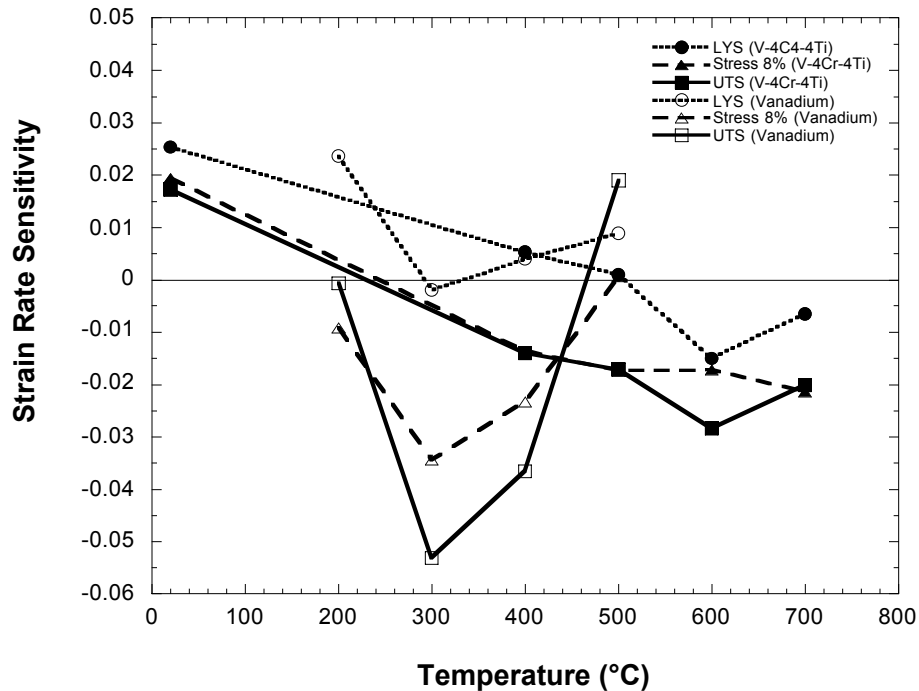


Figure 5. The strain rate sensitivity parameter,  $m$ , as a function of temperature for vanadium and V-4Cr-4Ti.

100°C [1]. In Figure 5 the strain rate sensitivity parameter,  $m$ , for the three stress parameters is plotted as a function of temperature. These data indicate that the maximum negative value of SRS for vanadium occurs at about 300°C and that as a result of alloying the temperature at which SRS achieves a maximum negative value is increased to around 600°C. In other words, alloying with Ti and Cr increases the temperature range for DSA by about 300°C. This is most probably related to the strong interaction between Ti and the interstitial population and the consequent decrease in interstitial mobility.

## REFERENCES

1. D.T. Hoelzer and A.F. Rowcliffe, "Deformation Behavior of Unalloyed Vanadium," Fusion Materials Semiannual Progress Report, DOE/ER-0313/28, June 2000, p. 56.
2. A.N. Gubbi, A.F. Rowcliffe, W.S. Eatherly, and L.T. Gibson, "Effects of Strain Rate, Test Temperature, and Environment on the Tensile Properties of Vanadium Alloys," Fusion Materials Semiannual Progress Report, DOE/ER-0313/20, June 1996, p. 38.
3. A.F. Rowcliffe, D.T. Hoelzer, and S.J. Zinkle, "High Temperature Tensile Properties and Deformation Behavior of V-4Cr-4Ti," Fusion Materials Semiannual Progress Report, DOE/ER-0313/26, June 1999, p. 25.
4. A.F. Rowcliffe, S.J. Zinkle, and D.T. Hoelzer, "Effect of Strain Rate on the Tensile Properties of Unirradiated and Irradiated V-4Cr-4Ti," Journal of Nuclear Materials, **283-287**, 2000, p. 508.
5. F.A. Schmidt and J.C. Warner, J. Less-Common Metals, **26**, 1972, p. 325.

## **BIAXIAL THERMAL CREEP OF V-4Cr-4Ti IN A LITHIUM ENVIRONMENT–** M. L. Grossbeck (Oak Ridge National Laboratory)\*

### **OBJECTIVE**

The goal of this research is to evaluate the creep behavior of vanadium alloys under conditions where oxygen is not increased during the creep testing. This will permit thermal creep to be separated from irradiation creep and helium effects in DHCE experiments and will aid in interpretation of the vacuum thermal creep experiments now being performed.

### **SUMMARY**

Results have been obtained at 765°C for times up to nearly 2000 hours and for 1100 hours at 665°C. At this early stage, the data are consistent with the biaxial measurements in a vacuum environment performed at PNNL at 765°C. At the lower temperature, the Li results are showing slightly higher creep rates. However, the strains are small and have large relative errors. Better comparisons will be made as the tests progress. The steady-state creep regime is very small with an early onset of tertiary creep at 765°C. No creep failures have occurred. A Larson-Miller analysis has shown that no failures are yet expected based upon the PNNL results and uniaxial creep tests on the same alloy performed at ANL.

### **INTRODUCTION**

This investigation is conducted to determine the creep behavior of V-4Cr-4Ti in a lithium environment to prevent absorption of oxygen which is inevitable even in an ultra-high vacuum. This investigation complements a similar study of the same alloy, and same heat, using an ultra-high vacuum environment conducted at PNNL.<sup>1</sup>

It is of primary importance to control interstitial impurities since they have a profound hardening and embrittling effect on vanadium and its alloys.<sup>2,3</sup> Since oxygen is absorbed readily under all attainable pressures and diffuses more rapidly than nitrogen, it is expected to increase during high temperature testing, and this has been observed.<sup>1,4</sup>

The present experiments use an environment of liquid Li at temperatures in the range of 665-800°C. Under these conditions, oxygen is removed from vanadium and ultimately forms Li<sub>2</sub>O. The effect of oxygen has been confirmed in pure vanadium by Shirra who observed a decrease in creep rate of five orders of magnitude at 650°C by increasing oxygen concentration from 220 to 750 ppm.<sup>5</sup> A smaller but still large extension of creep rupture life due to increased oxygen was observed in V-Ti alloys. A Li environment not only serves to prevent oxygen contamination but is also relevant to fusion devices using vanadium first wall and blanket structures cooled by Li.<sup>6,7</sup>

### **EXPERIMENTAL**

Pressurized tubes were chosen as the specimens since they permit testing a large number of specimens covering a wide range of stresses. All specimens at a given temperature can be tested in a single container and furnace. Specimens were fabricated from drawn tubing of V-4Cr-4Ti from

---

\*Oak Ridge National Laboratory (ORNL) is operated for the U.S. Department of Energy by UT-Battelle, LLC under contract DE-AC05-00OR22725.

Teledyne Wah Chang Heat 832665.<sup>8,9</sup> End caps of the same alloy were electron-beam welded in place and the internal pressure attained by sealing a small hole in one end cap with a laser welder while the specimen was in a pressure chamber at the desired pressure of He. The tubes were 25.4

mm in length by 4.57 mm in diameter and 4.57 mm wall thickness. The tubes received a heat treatment of 1000°C/1 hour wrapped in Ta foil in a vacuum below  $10^{-4}$  Pa.

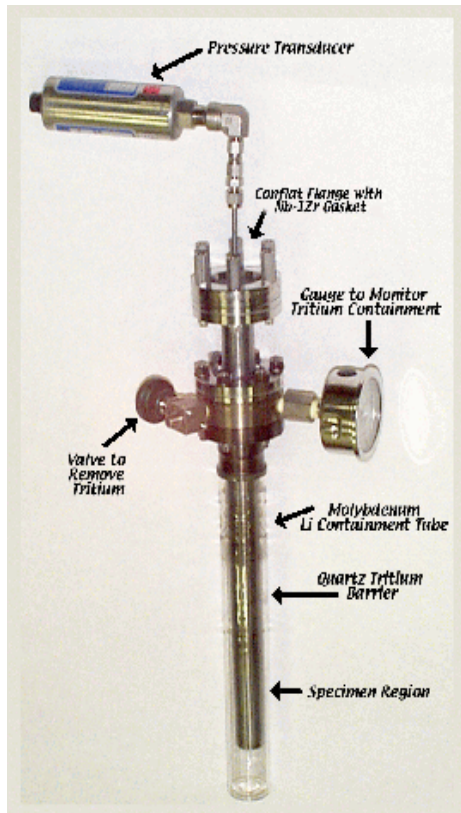


**Fig. 1 –  
Refractory metal retort for Li tests**

The specimens were held at test temperature in a retort of Mo, TZM alloy, and Nb-1Zr in order to contain the high-temperature liquid Li. The retort, shown in Fig. 1, has a 25.4 mm diameter Mo tube with caps and flanges of Mo welded in place. The mating flange on the top uses a knife edge seal of the Conflat\* design with a mating flange of Nb-1Zr. A gasket of Nb-1Zr was used for the flange seal. This design differs from the one reported earlier which used a c-ring gasket.<sup>3</sup> It was found that the c-ring design often allowed small leaks. At a distance of about 120 mm from the top flange, where the temperature is below 100°C, stainless steel tubing is used to attach to the pressure transducer which has a stainless steel diaphragm. No significant amount of lithium vapor is expected to reach the stainless steel. The retort serves an additional purpose as a prototype containment for a similar test with the addition of tritium to simulate the generation of helium by (n, ) reactions. For this purpose, a quartz tube was added to serve as a barrier to diffusion of tritium. A thermocouple was fastened to the quartz tube in the region of the specimens and the retort placed in a tube furnace. A calibration of the thermocouple was achieved by placing a shielded thermocouple directly into the molten Li through a hole in the cap for a short-term test.

The entire furnace was situated inside a glove box in a high-purity argon atmosphere. Oxygen and moisture were maintained at 1 ppm or below, and a nitrogen purification system was used to reduce nitrogen to similar levels, although nitrogen was not monitored. This atmosphere enabled the specimens to be removed from the Li at a reduced temperature but still molten.

Pressure in the chamber was recorded at 120 s intervals to monitor rupture of the tube specimens. Since the retort was sealed, the increase in pressure from a leaking tube remained, producing a step change in internal pressure.

Following removal of the specimens from the Li and subsequently from the Ar atmosphere, the residual Li was removed with liquid anhydrous ammonia, followed by ethanol, followed by water. This sequence was used to prevent contamination by hydrogen.<sup>10</sup> The tubes were then measured by a non-contacting laser micrometer. A helical pattern of 500 measurements was made in the central 12.7 mm of the tubes to a precision of  $\pm 250$  nm.

## RESULTS

At the present time, results are available for 765°C at 200, 1064, and 1927 hours and for 665°C at 242 and 1105 hours. The results are reported in Table 1 where effective uniaxial stress and strain are given.<sup>11</sup> For tubes that have leaked, no data are used since the time of failure is unknown, and negative values are to be considered possible measurement errors due to the very small strains observed.

**Table 1 - Creep data in terms of effective stress and strain**

Specimen	Eff. stress (MPa)	Effective Strain, %		
		200 Hrs	1064 Hrs	1927 Hrs
V5	25	-.0037	-.017	-.016
V8	42	.017	.016	.078
V3	59	.027	.039	.38
V10	59	.0007	-.016	.36
V7	75	.033	.13	2.5
V4	84	.031	.30	5.9
		242 Hrs	1105 Hrs	
V12	59	.023	.034	
V2	75	.025	.031	
V11	75	.0074	.0022	
V9	83	.027	.040	
V6	100	.022	leaked	
V1	117	-.010	.0044	
V13	133	.014	leaked	

Figure 2 shows data from the vacuum tests conducted at PNNL and the uniaxial tests conducted at ANL.<sup>12</sup> Specimens from all three investigations at stress levels in the range of 84-90 MPa are compared. The ANL data show large primary creep as opposed to almost no primary creep in pressurized tubes, a phenomenon observed with irradiation creep in pressurized tubes.<sup>13</sup> The pressurized tube data are similar in that, for the three temperatures investigated, 700, 765, and 800°C, the results for the Li tubes at 765°C are in the middle.

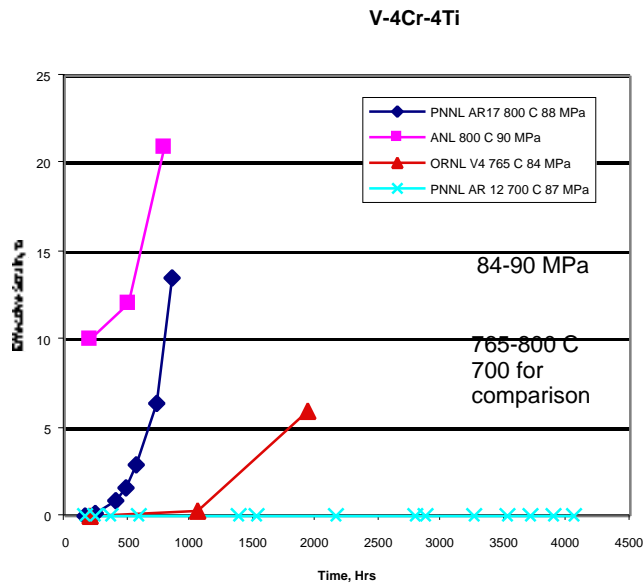


**Fig. 2 - Creep strain in V-4Cr-4Ti comparing temperature and stress state**

A similar comparison for a stress range of 67-75 MPa shows similar behavior. Results for 665°C, shown in Fig. 3 show larger creep strains than observed at 700°C in the vacuum environment. However, experimental scatter is rather large, especially for the 700°C data. A more valid comparison awaits longer term tests now in progress. All specimens in the present study show little secondary creep.

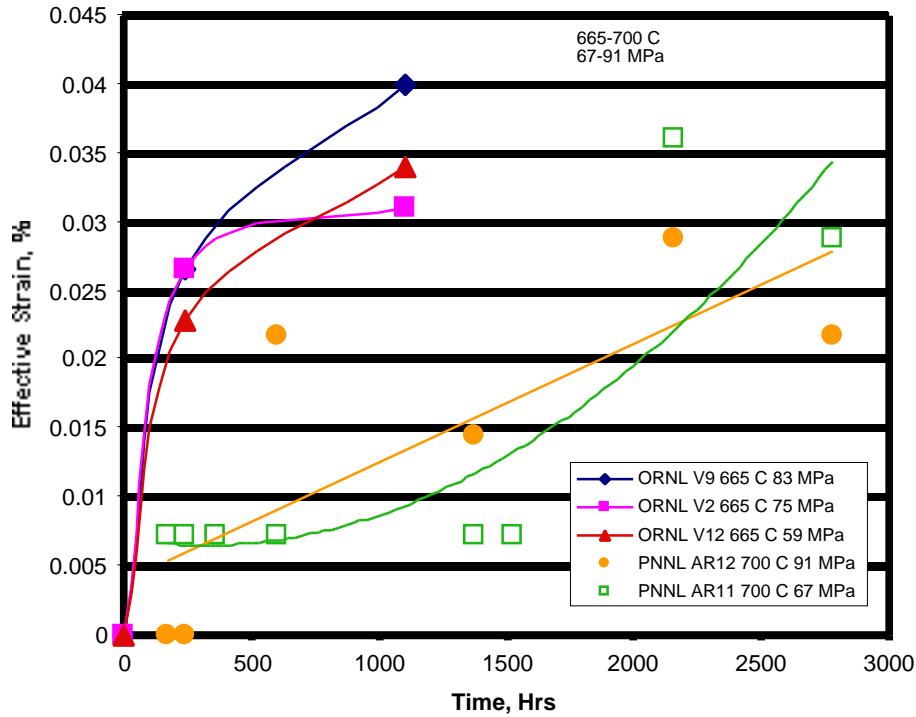


Fig. 3 – Creep strain showing higher strains in the Li test than in the vacuum test despite lower temperature

The dependence upon stress is illustrated in Fig. 4 for 765°C, where non-linear behavior is observed. Fitting the curves to a power law equation,  $\dot{\epsilon} = A\sigma^n$ , where  $\dot{\epsilon}$  is strain rate,  $\sigma$  is the stress, and A and n are constants, yields values of n, the stress exponent, in the range of 1 to 5. The temperature dependence may be analyzed using an equation similar to the Dorn equation:<sup>14</sup>

$$\dot{\epsilon} = \frac{A}{T} \sigma^n e^{-Q/k} \quad (1)$$

where T is the kelvin temperature, Q is the activation energy, k is Boltzmann's constant, A and n are constants, and  $\dot{\epsilon}$  and  $\sigma$  are defined above. Using data for 765°C and neglecting the weak 1/T dependence, an activation energy of 2.8 eV was obtained.

## DISCUSSION

Since oxygen increases slowly, the oxygen concentrations in the lithium environment tests are not yet very different from those of the vacuum tests. An increase of 30% in oxygen was observed after 2812 hours in a vacuum at 800°C.<sup>1</sup> In light of the difference in temperature, and the few specimens

that have shown significant creep, no conclusions were drawn from the comparison. However, after longer exposure times, more data will be available to make a valid comparison. More temperatures will also be explored to match the vacuum data more closely.

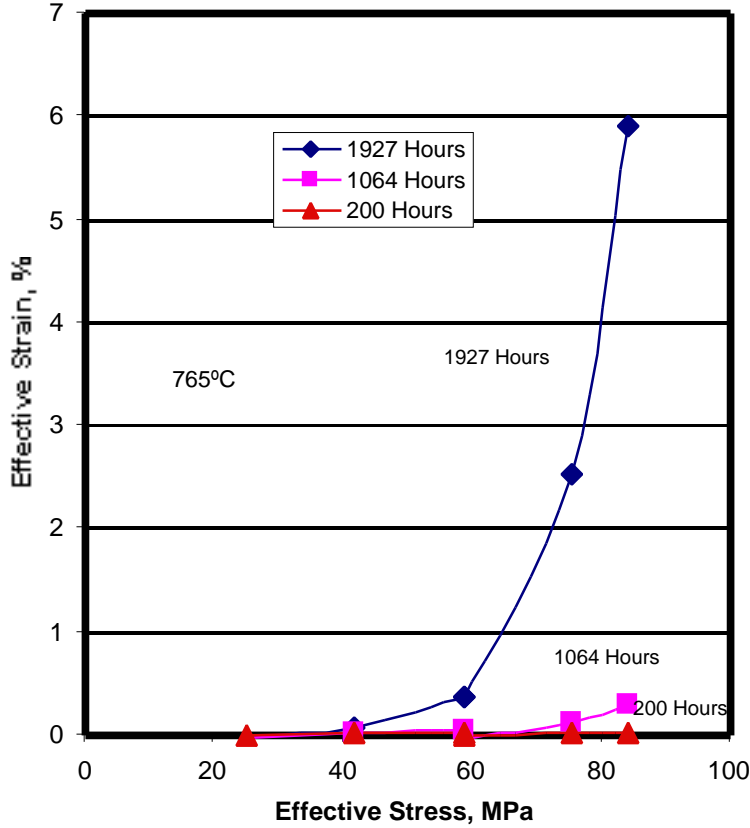


Fig. 4 – Creep strain as a function of stress for the Li-exposed tests

The leaking tubes indicated in Table 1 resulted from weld failures, not creep failures. No creep ruptures were observed at either of the two temperatures. To confirm consistency of this with existing data, an analysis was made using the concept of the Larson-Miller parameter (Fig. 5),

$$P = T(\log t_r + 20) / 100 \quad (2)$$

where T is the absolute temperature and  $t_r$  is the rupture time in hours.<sup>15</sup> Data from the vacuum tests conducted at PNNL and the uniaxial tests at ANL have been plotted by Kurtz and appear in Fig. 4.<sup>1</sup> The data from the present study are also plotted in Fig. 5 as if the measurement time were the rupture time. This pseudo-Larson-Miller parameter plot shows that the specimens in the present experiment lie below the trend line of the actual creep rupture data, and that the tubes were not expected to rupture.

The range of the stress exponent of 1-5 is expected to be narrowed as more data are obtained, but values greater than one are indicative of diffusion-controlled dislocation climb creep. For solid-solution alloys, a value of 3 is often observed.<sup>14</sup>

The activation energy is compared with other studies in Table 2. The observed value of 2.8 eV is in close agreement with the value measured in the vacuum experiment of 3.1 eV. It is also close to the

value of 2.3 eV observed by Bohm and Schirra in a V-5%Ti alloy.<sup>16</sup> Values slightly lower than the activation energy for self diffusion of 3.2 eV are expected since dislocation glide processes are also operating, and this appears to be supported by the very short intervals of steady-state creep.

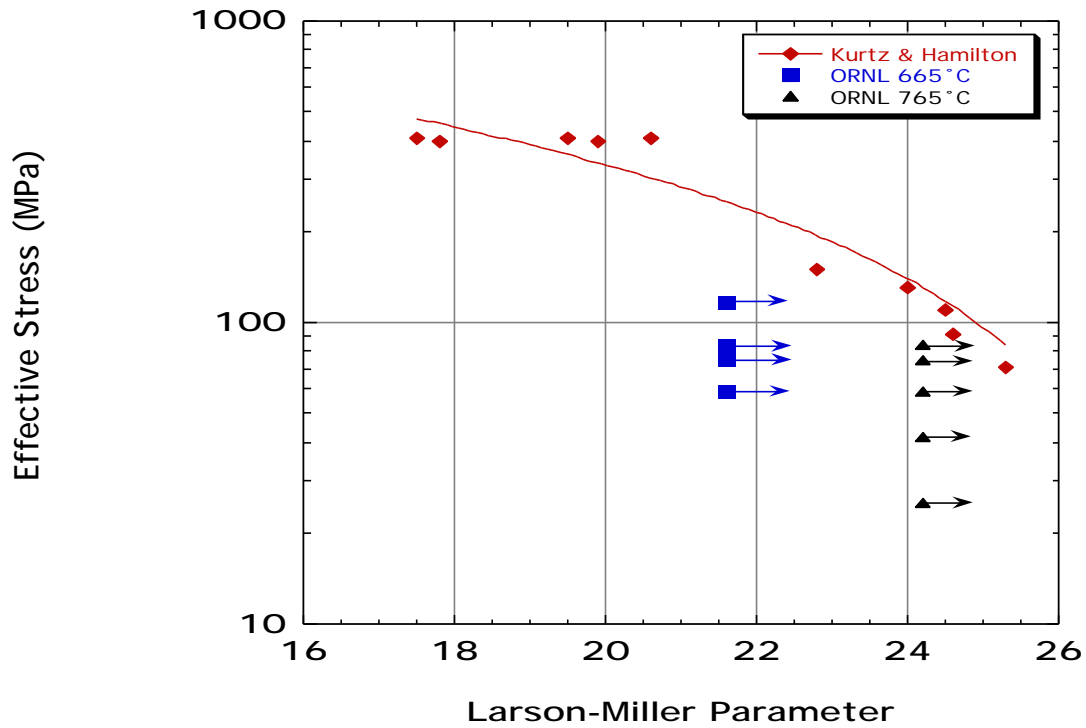


Fig. 5. – Pseudo-Larson-Miller parameter plot showing that the Li samples are not expected to fail

Table 2. Activation energy for creep and self-diffusion

Stress State	Laboratory	Act. Energy, eV
Biaxial	ORNL	2.8
Biaxial	PNNL	3.1
Uniaxial	ANL	5.7
Uniaxial	Bohm and Schirra	2.3
Self-diffusion <sup>17</sup>		3.2

## CONCLUSIONS

1. An experimental apparatus has been developed for handling liquid lithium for creep testing of pressurized tubes. All metals in contact with Li are refractory metal, including gaskets. It was concluded that a thermocouple well protruding into the liquid lithium is necessary and will be incorporated. Operating experience was also obtained for using a retort with a tritium barrier in anticipation of the next series of experiments.
2. The creep rates observed are consistent with those obtained from specimens in a vacuum environment, with the exception of 665°C where creep rates are higher for the lithium environment. Longer exposures will have to be achieved before confidence can be gained in this observation.
3. At 765°C, no creep failures were observed after an exposure of 1927 hours at effective stress levels up to 87 MPa.
4. Tertiary creep initiates early, with a short region of steady-state creep.
5. The observed activation energy of 2.8 eV is consistent with other measurements and with the activation energy for self-diffusion within experimental error.

## FUTURE WORK

The creep tests will continue to generate more data for longer exposure times. In addition, the retorts will be modified to accommodate thermocouple wells directly in the lithium. When the modifications are made, other temperatures will be investigated.

## REFERENCES

1. R.J. Kurtz and M.L. Hamilton, *J. Nucl. Mater.* 283-287 (2000) 628.
2. T. Kainuma, N. Iwao, T. Suzuki, R. Watanabe, *J. Nucl. Mater.* 80 (1979) 339.
3. M.L. Grossbeck, Evaluation of Thermal Creep of V-4Cr-4Ti in a Lithium Environment, *Fusion Materials Semiannual Progress Report for Period Ending June 30, 2000*, DOE/ER-0313/28 p. 48.
4. E. Fromm and E. Gebhardt, *Gase und Kohlenstoff in Metallen*, Springer-Verlag, Berlin, (1976).
5. M. Schirra, KfK 2440, 2<sup>nd</sup> ed, Kernforschungszentrum Karlsruhe (1989).
6. R.W. Conn, *J. Nucl. Mater.* 85&86 (1979) 9.
7. D.L. Smith, *J. Nucl. Mater.* 103&104 (1981) 19.
8. D.L. Smith, H.M. Chung, B.A. Loomis, H.-C. Tsai, *J. Nucl. Mater.* 233-237 (1996) 356.
9. M.L. Grossbeck, R.L. Klueh, E.T. Cheng, J.R. Peterson, M.R. Woolery, E.E. Bloom, *J. Nucl. Mater.* 258-263 (1998) 1778.
10. D.L. Crandall, D.J. Marts, T.R. Reed, G.R. Smolik, *Space Nuclear Power Systems 1987*, Ed. M.S. El-Genk, M.D. Hoover, Orbit Book, Malabar, FL (1988) 457.
11. E.R. Gilbert and L.D. Blackburn, *Trans ASME, J. Eng. Mater Tech.* 99 Series H, No. 2 (1977) 168.
12. K. Natesan, W.K. Soppet, and D.L. Rink, DOE/ER-0313/28, U.S Department of Energy, Oak Ridge, TN (2001) 39.
13. J.P. Foster, K. Bunde, and E.R. Gilbert, *J. Nucl. Mater.* 257 (1998) 118.
14. H.E. Boyer, *Atlas of Creep and Stress-Rupture Curves*, ASM, Metals Park, OH, (1988).
15. F.R. Larson and J. Miller, *Trans. ASME* 74 (1952) 765.
16. H. Bohm and M. Schirra, *J. Less Comm. Metals* 12 (1967) 280.
17. R.F. Peart, *Diffusion in Body-Centered*

**EVALUATION OF THE DHCE EXPERIMENT** - L. R. Greenwood, D. L. Baldwin, G. W. Hollenberg and R. J. Kurtz (Pacific Northwest National Laboratory)\***OBJECTIVE**

To evaluate the results of the DHCE experiment to enhance helium production in vanadium alloys in order to assess the readiness to conduct a future DHCE experiment.

**SUMMARY**

The Dynamic Helium Charging Experiment (DHCE) experiment was conducted in the Fast Flux Test Facility (FFTF) during cycle 12, which was completed in 1992. The purpose of the experiment was to enhance helium generation in vanadium alloys to simulate fusion reactor helium-to-dpa ratios with a target goal of 4-5 appm He/dpa. The Fusion Materials Science Program is considering mounting another experiment in hopes of gathering additional data on the effect of helium on the mechanical and physical properties of vanadium structural materials. Pacific Northwest National Laboratory was assigned the task of evaluating the feasibility of conducting another DHCE experiment by carefully evaluating the results obtained of the first DHCE experiment. This report summarizes the results of our evaluation and presents recommendations for consideration by the Materials Science Coordinators Organization.

Background

A very brief description of the experiment is that vanadium alloys are encapsulated in TZM capsules along with lithium and a "mother" alloy that is pre-charged with tritium. When the reactor comes up to power and the capsule temperature rises, the tritium diffuses out of the mother alloy and reaches an equilibrium distribution between the liquid lithium and vanadium alloys. As the tritium decays,  $^3\text{He}$  is produced in the vanadium alloys. When the irradiation is stopped and the temperature falls, the tritium returns mostly to the lithium. The  $^6\text{Li}$  content was varied along with the tritium charging in an attempt to provide a nearly constant generation of  $^3\text{He}$  from the decay of tritium and replacement from the  $^6\text{Li}(n,\alpha)t$  reaction. Tritium leakage from the capsules and the distribution of tritium between the lithium and the vanadium alloys are the most important temperature-dependent parameters. Ideally, if all the parameters are well understood and chosen appropriately, then the DHCE concept is capable of producing nearly constant helium to dpa ratios in the vanadium alloys during the irradiation.

At the time the experiment was designed, there was considerable uncertainty concerning the distribution of tritium between the liquid and the vanadium alloy specimens. It should further be noted that the limited data available at the time on the tritium distribution for vanadium alloys predicted about a factor of 10 increase over pure vanadium.[1] In view of these uncertainties, the experiment was designed assuming a range of possible distribution ratios ( $K_A = 0.073$  to  $0.73$ ) for the capsules at temperatures between 430 and 600°C, where  $K_A$  is the atomic ratio of tritium in V to that in liquid Li. This design uncertainty is important to remember in any evaluation of the DHCE results in that the plan was to hopefully span the range of tritium distribution values so that at least some of the vanadium specimens would have fusion relevant helium-to-dpa values.

---

\*Pacific Northwest National Laboratory (PNNL) is operated for the U.S. Department of Energy by Battelle Memorial Institute under contract DE-AC06-76RLO-1830.

### *Post-Test Prediction of Helium Levels*

In view of the DHCE results, it is now clear that the tritium distribution coefficients for vanadium alloys and Li are generally similar to those for pure vanadium (except in a few cases, as noted above) rather than about a factor of 10 higher than vanadium, as was assumed when the DHCE experiment was designed [1,2]. Improved models of tritium leakage from the TZM capsules are also now available [2]. Hence, the obvious question is to determine how well the DHCE data can be described and explained using these new tritium distribution coefficients and tritium leakage parameters.

The DHCE calculations are somewhat complicated in that they depend on the FFTF power history, nuclear reaction rates, tritium decay, tritium distributions, and tritium diffusion. Calculations are performed separately for each capsule condition considering the initial tritium in the mother alloy,  $^6\text{Li}$  enrichment, irradiation position in the reactor, and capsule temperature. Revised calculations were performed using the new tritium distribution coefficients and tritium leakage parameters. The new calculations show  $^3\text{He}$  values at the end of irradiation time, March 19, 1992. The assumption was made that the tritium all went into the lithium rather than remaining in the alloys at the end of irradiation. The capsules remained in FFTF for about 9 months at 220°C and then were at room temperature for 6-9 months before opening at ANL. Hence, it is possible that some of the  $^3\text{He}$  generated during this 15-18 month interval wound up in the vanadium alloys; however, tritium distribution calculations at these lower temperatures predict that virtually all of the tritium will reside in the lithium. Tritium measurements were conducted for one sample of V-4Cr-4Ti at each level of the DHCE experiment. [3] These measurements were performed by measuring the  $^3\text{He}$  increase in the samples over a period of about 50 days. Two of the samples in positions 4D1 and 4D2 showed tritium values that were statistically above the background, although with significant uncertainties. If these data are extrapolated back to the end of irradiation and the decay of tritium is calculated, then it is possible that up to about 35% of the  $^3\text{He}$  in the samples at these positions may have been generated from tritium decay after the irradiation. However, most of the samples were degassed sometime in 1994 prior to the  $^3\text{He}$  measurements in 1995, so the exact tritium decay period is not precisely known. In any case, it is possible that some of the  $^3\text{He}$  values from the 430°C capsules are biased due to the retention of tritium in these samples. Tritium trapping is also a possibility, as is discussed below.

### *Comparison of Data and Calculations*

All of the  $^3\text{He}$  data and the new calculations are shown in Table 1. This table was taken from Reference 2, except that we have added the  $^6\text{Li}$  enrichments, the calculated post-test tritium levels given the initial tritium charge, the measured post-test tritium levels, the desired concentration of tritium in Li, the solubility limit of tritium in Li, the new  $K_A$  and tritium leakage values. The calculated post-test tritium levels attempted to account for the tritium inventory at about the time the capsules were opened, taking into account the reactor history, decay, generation from  $^6\text{Li}$  and  $^3\text{He}$  reactions, and tritium leakage from the capsules. The measured post-test tritium levels may not include all of the tritium, as discussed in reference [15].

It is obvious comparing the calculated  $^3\text{He}$  values with the experimentally measured levels that three of the alloys (V-1Si, V-5Fe, and V-5Cr-5Ti (Si, Al, Y)) exhibited much higher  $^3\text{He}$  than the other specimens, as discussed below. If one ignores the results for these three alloys, then the rest of the data is in acceptable agreement with the new calculations (within a factor of two), as shown in Figures 1 – 4. Figure 1 shows the dependence of the  $^3\text{He}$

produced on initial tritium charge for specimens irradiated at all three temperatures. Figures 1 – 3 show separate plots for each of the three irradiation temperatures. There are three significant deviations from this trend (agreement within a factor of two). One measured value of 34.7 appm for V-3Ti-1Si at 430°C, one value of 26.3 appm for V-5Cr at 600°C, and one value of 74 appm for V-4Cr-4Ti (ANL) irradiated at 600°C.

The fact that three of the alloys (V-1Si, V-5Fe, and V-5Cr-5Ti (Si, Al, Y)) consistently show much higher  $^3\text{He}$  levels than the other seven alloys would seem to imply that the composition or microstructure of these materials results in much higher tritium solubility and/or trapping. Information cited in Reference 1 suggests that alloys with Y have much higher solubilities for tritium, which could explain the very high values for the V-5Cr-5Ti (Si, Al, Y). Calculations carried out by Natesan [4] show that Y is a very strong H getter; V, Ti and Nb are intermediate H getters, and Cr, Mo are non-getters. For example, Natesan's

Table 1.  $^3\text{He}$  Concentration in V-Alloys from DHCE Experiment Compared to Revised Calculations

Parameter	Capsule						
	4D1	4D2	5E2	5D1	5E1	5C1	5C2
DPA	25	27	13	14	18	18	14
Temperature, °C	430	430	430	500	500	600	600
$^6\text{Li}$ fraction	0.05	0.045	0.01	0.065	0.01	0.08	0.08
Initial Tritium, Ci	99	70	26	74	57	16	18
Final Tritium, Ci	90	66	22	55	37	8.7	10.4
Post-test Tritium, Ci*	46.3	38.4	3.4	ND	~24.1	4.5	12.3
$^3\text{H}$ / Li, appm (desired)	31,000	22,000	9,300	19,000	14,300	4,900	4,500
$^3\text{H}$ / Li, appm (limit)**	17,400	17,400	17,400	34,450	34,450	75,700	75,700
$K_A^{***}$	0.0136	0.0136	0.0136	0.0197	0.0197	0.0294	0.0294
$^3\text{H}$ , leakage	$4.9 \times 10^{-9}$	$4.9 \times 10^{-9}$	$4.9 \times 10^{-9}$	$2.0 \times 10^{-8}$	$2.0 \times 10^{-8}$	$8.9 \times 10^{-8}$	$8.9 \times 10^{-8}$
<b>Calculated <math>^3\text{He}</math></b>	<b>10.1</b>	<b>10.1</b>	5.38	14.2	10.0	4.55	4.34
V	8.83	15.2	2.54	31.6	12.3		10.4
V-5Ti	18.0	12.2	3.05	19.2	7.19		8.10
V-5Ti (BL46)		15.5					8.59
V-5Cr	6.45				3.35		26.3
V-5Nb	7.65				6.78		5.70
V-5Mo	9.81				3.56		8.22
V-5Mo							5.02
V-3Ti-1Si	34.7				5.02		6.25
V-4Cr-4Ti (BL47)	11.6	9.04	2.46	14.0	5.51	8.02	6.80
V-4Cr-4Ti (ANL)	9.86	20.9	2.48	14.1	5.58	7.90	74.0
<b>High <math>^3\text{He}</math> Alloys</b>							
V-1Si	105				59.9		48.8
V-5Fe	80.6				34.9		93.4
V-5Cr-5Ti(Si,Al,Y)	177				108		260

\*Data may not include all of the tritium, as discussed in reference 13.

\*\*Solubility limit of H in Li.

\*\*\* $K_A$  is the tritium distribution coefficient between the liquid lithium and the vanadium alloys.

calculations show that at a H pressure of  $10^{-6}$  torr the concentration of H in Y at  $600^{\circ}\text{C}$  is roughly two to four orders of magnitude larger than in V, Ti and Nb. Further, at the same temperature and H pressure the H concentration in Cr and Mo is between three and four orders of magnitude below that in V. We were not able to estimate the getter strength of these elements when alloyed with V or, perhaps more importantly, when these elements form second phases, but work performed by Matsui, et al. [5] provides some insight into the relative tritium trapping efficiency for some of the binary alloys. Matsui, et al. charged pure V and five binaries with tritium at  $400^{\circ}\text{C}$  to study the effect of He on tensile properties. All specimens were charged in the same container at the same temperature and tritium gas pressure. The specimens were held under these conditions for a predetermined time for tritium to decay to  $^3\text{He}$ . The measured  $^3\text{He}$  levels following this exposure were V-5Fe (154 ppm), V-5Mo (267 ppm), V-5Cr (269 ppm), V (363 ppm), V-5Nb (405 ppm), and V-5Ti (688 ppm). The trend of the measured  $^3\text{He}$  levels generally follows the trend of H solubility in the various alloying elements. This same trend is not observed in the DHCE binary alloys. Based on solubility data alone one would predict that the V-5Fe should have one of the lowest  $^3\text{He}$  levels rather than one of the highest.

The other two high  $^3\text{He}$  alloys, V-1Si and V-5Fe, are known to have high swelling with the formation of a large number of voids following irradiation in FFTF [6-10]. Recent experiments with irradiated stainless steel have shown that H can be trapped in these voids along with He [11-14]. Hence, it is possible that the high  $^3\text{He}$  content of these alloys is due to tritium trapping which could significantly increase the total tritium in these materials above the solubility limit. If tritium were trapped, it would stay trapped after the irradiation, causing some additional  $^3\text{He}$  generation after the samples were removed from the reactor, as

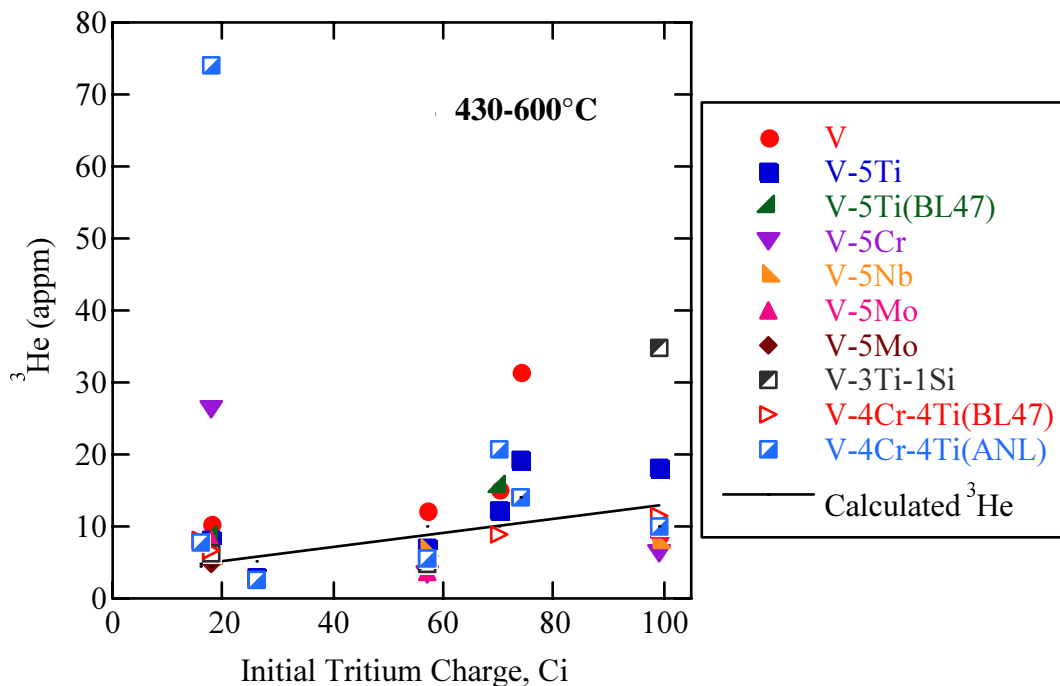


Figure 1. Dependence of measured and predicted  $^3\text{He}$  levels for several vanadium alloys irradiated in FFTF between  $430$  and  $600^{\circ}\text{C}$  as a function of the initial tritium charge.

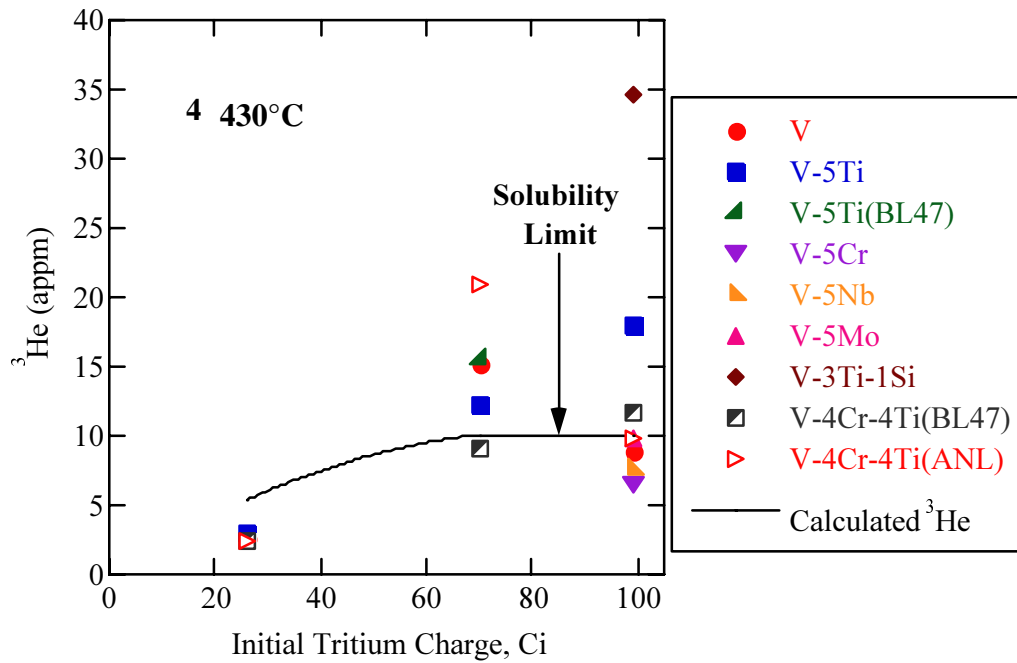


Figure 2. Dependence of measured and predicted  $^3\text{He}$  levels for several vanadium alloys irradiated in FFTF at 430 °C as a function of the initial tritium charge.

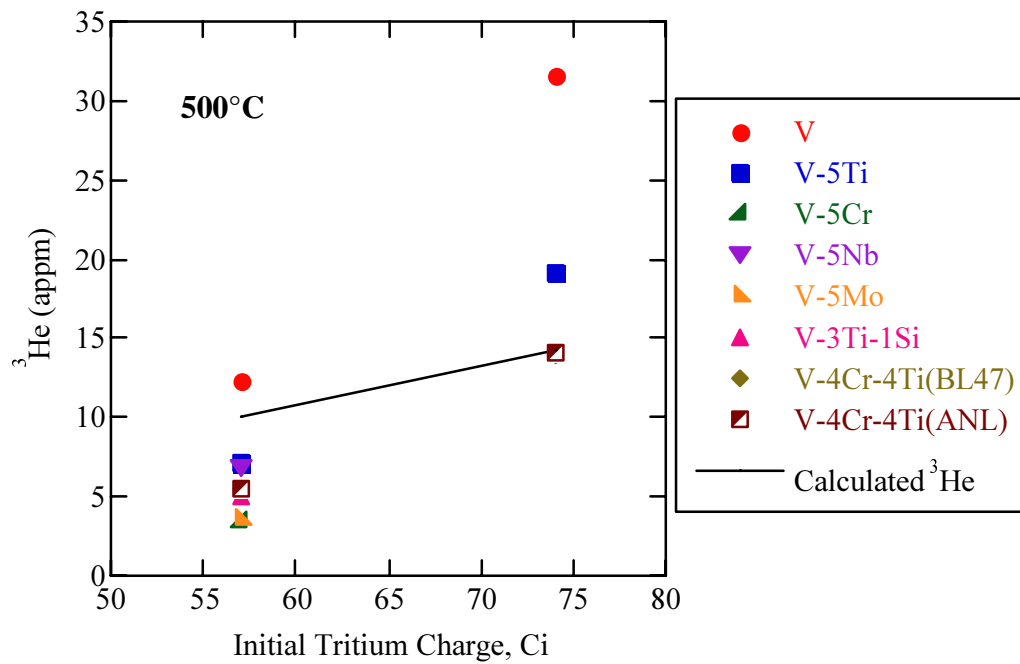


Figure 3. Dependence of measured and predicted  $^3\text{He}$  levels for several vanadium alloys irradiated in FFTF at 500 °C as a function of the initial tritium charge.

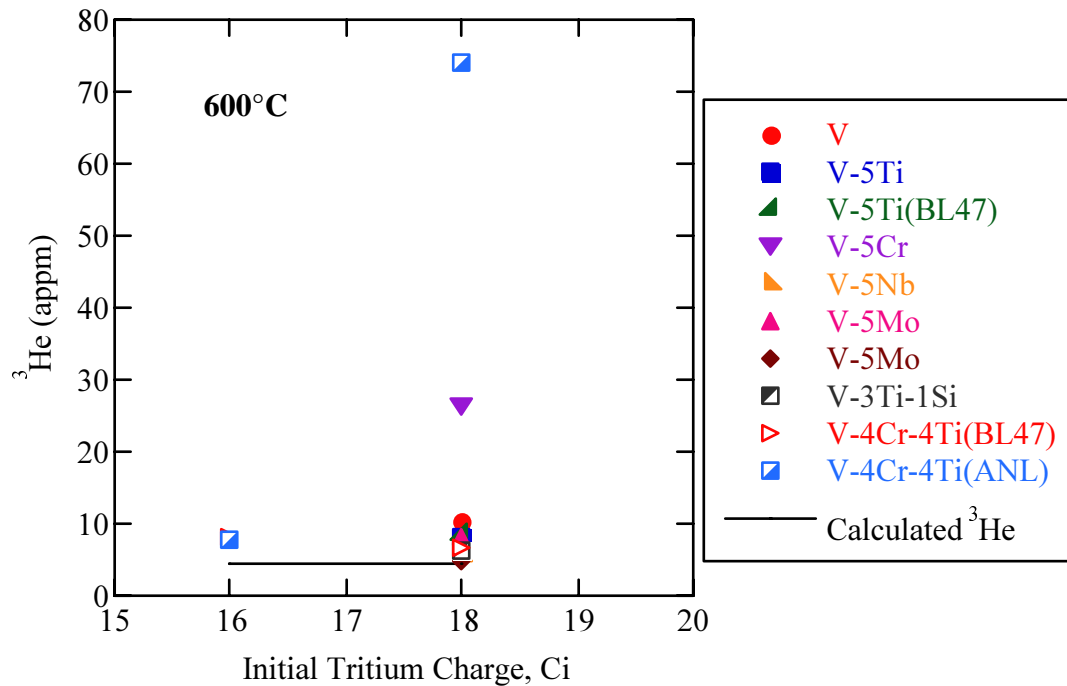


Figure 4. Dependence of measured and predicted  $^3\text{He}$  levels for several vanadium alloys irradiated in FFTF at 600 °C as a function of the initial tritium charge.

discussed previously. In reference 1 it was noted that helium bubbles were observed in some of the alloys, although the three alloys with higher  $^3\text{He}$  levels were not examined in this reference. Such helium bubbles might well allow the trapping of tritium. The data generated by Nakajima, et al. on V-5Cr also showed the formation of voids and high swelling at 600°C and relatively modest swelling at lower temperatures. This trend is in rough agreement with the DHCE results in that only the 600°C  $^3\text{He}$  measurement was elevated for V-5Cr. Nakajima, et al, did not see any significant swelling for V-5Mo, V-5Ti and V-20Ti. It has been well documented that Ti effectively suppresses swelling in V alloys even when elements that promote high swelling, such as Fe, are present [8]. Thus, a swelling argument cannot be invoked to explain the high  $^3\text{He}$  readings in the V-3Ti-1Si specimen at 430°C or the V-4Cr-4Ti (ANL) specimen at 600°C. It is apparent from the foregoing that understanding the cause of the systematically higher levels of  $^3\text{He}$  in these materials is essential before another DHCE experiment can be conducted with these materials.

Comparison of the data and calculations at 430 and 500°C show reasonable agreement (with the two exceptions noted). However, at 600°C, the data appear to generally exceed the calculations. This would suggest that either the tritium leakage rate at 600°C is lower than the new recommended value and/or the tritium distribution coefficient is higher than the new recommended value. Changing either of these parameters could easily improve the fit to the data except for the one very high value of 74 appm for V-4Cr-4Ti.

#### *Solubility of H in Lithium*

When the original DHCE calculations were performed, the solubility limits for H in lithium were not considered. Figure 5 shows the H solubility in Li from C. C. Addison [16], as

described by the equation  $\ln(H)=8.112 - 5314/T$ , at%. However, there is some scatter on solubility data in the literature, as shown later in Figure 7. In the original DHCE experiment, two of the capsules contained tritium levels that exceed this limit. The impact of this is that the LiH that formed in the capsule was limited by the LiH solubility limit, such that the soluble tritium did not exceed the limit shown in Figure 5. Consequently, the tritium levels were correspondingly reduced in the vanadium, thereby reducing the production of  $^3\text{He}$ . These revised calculations are shown in Table 1 as well as the curved line on the plot at 430°C in Figure 2.

The presence of precipitated LiH in contact with the V samples should not increase the level of  $^3\text{He}$  production. If the system is in the two-phase region, then the partial pressure of precipitated LiH is exactly what is shown on the dissociation pressure diagram at the selected temperature (see Figure 6). If excess LiH or H is added and the system is in equilibrium, then the excess LiH drops out of solution and the partial pressure does not change. In the two-phase region, at equilibrium, the pressure depends only on temperature and not on concentration. This pressure is the same at the surface of the LiH as it is above the Li since they are expected to be in equilibrium. Therefore, neither the solubility nor dissociation pressure are dependent upon the excess quantity of H or LiH added to the lithium. To drive more H into V (in the two-phase region), the addition of excess LiH will NOT do it, only higher temperatures will accomplish that. Although it does not seem reasonable that non-equilibrium conditions could exist for these temperatures and lengths of exposure, such non-equilibrium conditions might increase the tritium in the samples temporarily. It should also be noted that the scatter in the data shown in Figure 6 (or the solubility data shown later in Figure 7) results in about a factor of 2 uncertainty in our ability to predict or explain data from the DHCE experiment or to design a future experiment.

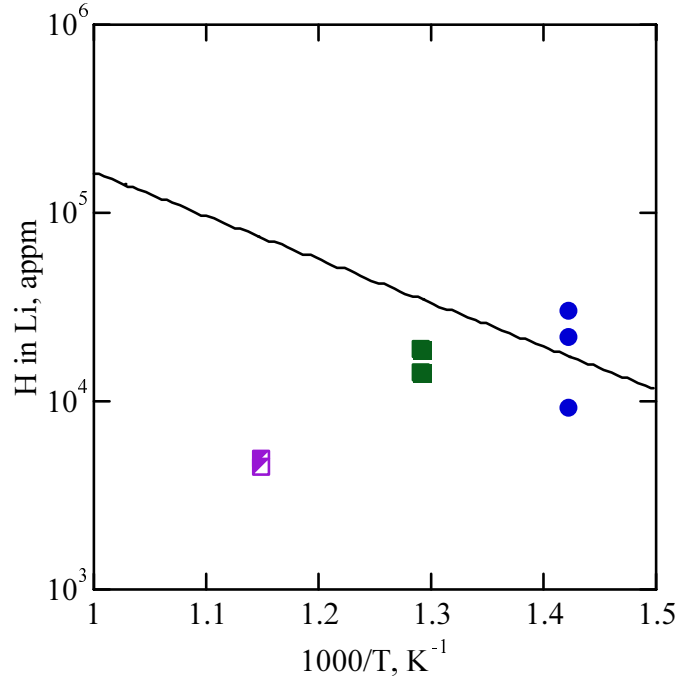


Figure 5. Solubility of H in Li (line) compared to the desired levels of tritium (points) for the DHCE capsules listed in Table 1.

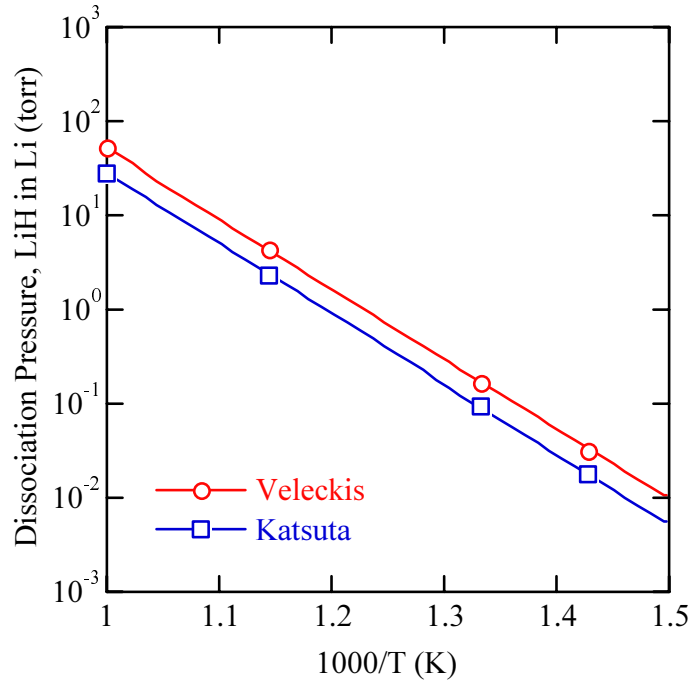


Figure 6. Dissociation pressure of LiH in Li [15,16].

#### *Scoping Calculations for a New DHCE Experiment*

The original Dynamic Helium Charging Experiment (DHCE) was conducted in the fast reactor FFTF. It is now proposed that a new DHCE experiment be conducted in some other suitable reactor and we have taken ATR as a base case, although the experiment might also be conducted in HFIR. Therefore, calculations were performed to determine whether a future DHCE experiment in ATR is feasible, given the results of the first DHCE experiment, as well as revised estimates of the tritium distribution coefficients between Li and V, the tritium solubility in lithium, and the tritium leakage rates from the capsules.

The main objective of a DHCE type experiment is to achieve fusion-like ratios of helium generation to displacement damage. A fusion reactor first wall spectrum has a He(appm)/dpa ratio of about 5 in vanadium. The original DHCE experiment generally reached He/dpa ratios of only 0.3 to 1.0 mainly due to overestimation of the tritium distribution coefficients for V and Li. The most obvious way to correct this problem is to simply add more tritium to the mother alloy at the start of the experiment. The  ${}^6\text{Li}$  content is then similarly elevated to maintain a constant level of tritium. However, this solution may not work at lower temperatures due to tritium solubility limits in lithium. The addition of more tritium simply forms precipitated LiT and the soluble tritium will not exceed the solubility limit, correspondingly reducing the tritium (and  ${}^3\text{He}$  formation) in the vanadium alloys. The solubility of hydrogen in lithium is shown in Figure 7. Note that there is some scatter in the experimental data, as will be discussed later.

#### *Calculations for ATR*

Table 2 summarizes the results of calculations performed for a proposed DHCE irradiation in

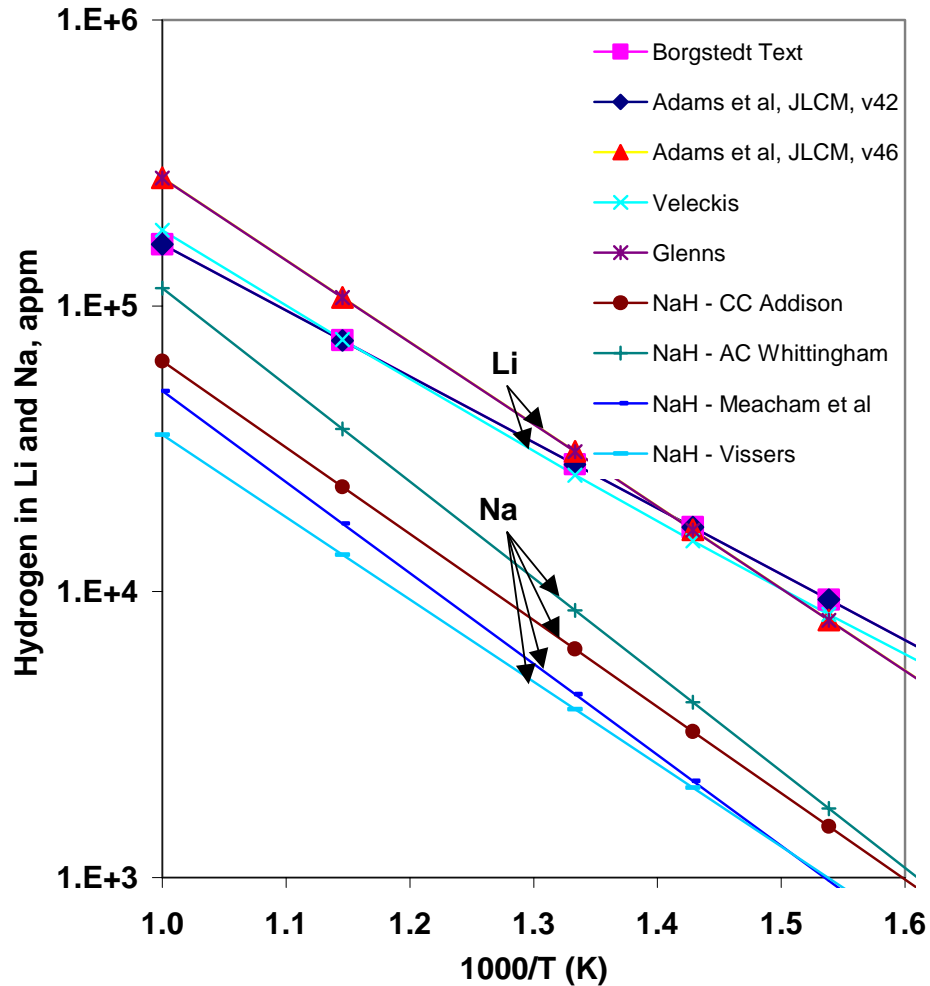


Figure 7. Solubility of H in Li, Na and NaK [14, 17-24].

ATR at temperatures between 430 and 700°C, using the same tritium distribution coefficients and leakage rates as were used to reevaluate the first DHCE experiment. The second and third columns show the Curies of tritium and corresponding tritium appm levels in lithium that would be required to achieve fusion-like He/dpa ratios at 1 and 2 FPY (full power year). The first row for each temperature ignores the tritium solubility in lithium whereas the second row (with the “Solubility Limit” label) gives both the solubility limits and reduced He/dpa ratios. As can be seen, the tritium solubilities limit the achievable He/dpa ratios at lower temperatures. At 430°C, the solubilities limit the achievable He/dpa ratio to just under 1. Adding more tritium doesn’t help since it forms LiT and is thereby prevented from diffusing into the vanadium alloys. At 500°C, the achievable He/dpa ratio increases to about 3, which is about half of the desired value.

At higher temperatures, tritium solubility in lithium is no longer an issue. However, at the highest temperature of 700°C, the helium generation in vanadium is limited by the high tritium leak rate. (The tritium leak rates are given in Table I except for the value at 700 °C, which was calculated to be 2.9E-7 atoms/s.) As discussed above, the new tritium leak rates appear to be too high at 600°C, suggesting that the tritium leakage may be overestimated at higher temperatures by the new equations presented in Reference 2. However, even allowing for this possibility, it may be difficult to achieve the desired He/dpa ratios, especially at longer irradiation times such as 2 FPY where the ratio may decrease to half the desired value.

The He/dpa calculations shown in Table 2 are for the midplane position of ATR. It should be pointed out that the ratio would of course be higher away from midplane since the dpa rate is lower while the helium production would stay the same. Consequently, the He/dpa ratio could be up to a factor of 2 higher at other locations, although this does come at the cost of a corresponding lower net dpa in the alloys at the end of the irradiation.

#### *Additional Problems in Experimental Design*

The results of the original DHCE experiment showed considerable variability in the He levels achieved for alloys irradiated under identical conditions. As discussed above, three of the alloys (V-1Si, V-5Fe, and V-5Cr-5Ti (Si, Al, Y)) appear to have consistently higher  $K_A$  values than do the rest of the alloys. The other two or three high results are very inconsistent and no satisfactory explanation for their behavior has been developed. If these assumptions are correct, then the design of a future DHCE experiment is more complicated since separate capsules would be required for the main grouping of alloys and the three higher alloys. Otherwise, all of the materials in a capsule cannot achieve the same He/dpa ratios given the identical irradiation conditions.

#### Conclusions

If we accept the assumption that the tritium solubilities are higher than anticipated in the three alloys V-1Si, V-5Fe, and V-5Cr-5Ti (Si, Al, Y) (data supports this for Y additions, at least), then the revised calculations using the new parameters in Reference 2 produce acceptable agreement with the measured  $^3\text{He}$  data. "Acceptable" in this case would mean

Table 2.  $^3\text{He}$ /dpa Ratios for a DHCE Experiment in ATR at Midplane

Temperature, °C	$^3\text{H}$ , Ci	$^3\text{H}$ , appm	$^6\text{Li}$ , at%	He/dpa	
				1 FPY	2 FPY
430	320	96,000	5	5.0	4.1
$^3\text{H}$ Solubility Limit		17,400		0.9	0.7
500	225	67,500	25	5.2	4.3
$^3\text{H}$ Solubility Limit		34,450		2.7	2.2
600	160	48,000	80	5.5	4.4
$^3\text{H}$ Solubility Limit		75,700			
700	320	96,000	100	4.1	2.6
$^3\text{H}$ Solubility Limit		141,500			

within a factor of two in most cases. As noted above, the only exception to this conclusion would be that the new recommended values for tritium distribution and leakage appear to either underestimate the tritium solubility or overestimate the tritium leakage at 600°C. Of course, this could be viewed as a positive conclusion if we want to extend the DHCE concept to higher temperatures.

It should also be pointed out that there are several other important factors that could help to explain the differences between the  $^3\text{He}$  data and the calculations, as has been mentioned in previous correspondence on this subject. For example, there are significant uncertainties in the initial tritium loading values as well as possible losses on welding. (Better measurements and controls during loading might reduce this uncertainty.) Note the discrepancies between the calculated final tritium levels listed in Table 1 and the measured values. We recognize the difficulties associated with experimental measurement of the post-test tritium levels, but the data in Table 1 suggest that the initial tritium charge may not have been what was planned or that tritium leakage was higher than calculated (using the newly revised parameters from Reference 2). The most notable capsule is 5E2 in which the measured post-test tritium level was only about 15% of the predicted value. The measured  $^3\text{He}$  levels for specimens from 5E2 are also uniformly only about 50% of the predicted value. Reference 1 mentioned a number of problems associated with charging of the mother alloys and capsule fabrication that might have contributed to differences in the initial tritium charge. Another possibility is that imperfections in individual capsules might strongly influence the tritium leakage rates. An additional possibility is that individual samples might have had less exposure to the lithium, due to protrusion above the Li, which would tend to lower the  $^3\text{He}$  due to the much lower concentration of tritium in the gas phase. Such specimen protrusion was observed by Tsai, et al. [15] during capsule disassembly. Due to the high packing density of the specimens some were observed to protrude above the level of the Li bond. A recommendation from that report, which we fully support, is to review capsule design and specimen packing density to ensure proper Li bonding of all specimens. Finally, as mentioned previously, tritium measurements performed on some of the specimens indicate that some of the  $^3\text{He}$  in the 430 °C samples may have been produced by tritium remaining in the samples after the irradiation.

Since the new calculations produce reasonable agreement with most of the DHCE data, we would expect that we can confidently predict, within a factor of two or better, the performance of additional experiments, assuming that we take into account the solubility limits for H in Li and other possible effects such as H trapping by Y or at voids. One obvious conclusion from the data is that DHCE-1 did not achieve the desired fusion reactor helium to dpa ratios of 4-5 (except for the three alloys that had unusually high  $^3\text{He}$  values). The reason for this is that the best data available at the time significantly over predicted the tritium solubility in most of the vanadium alloys. (The design assumed  $K_A$  values from 0.073 to 0.73 for the vanadium alloys whereas the true values appear to be in the range of 0.01 to 0.03, similar to pure vanadium). Of course, this means that if the same experiment were to be repeated today, one would have to increase the initial tritium loading (and increase the  $^6\text{Li}$  enrichment) significantly in order to hit the desired helium to dpa ratio. Such increased loading is certainly possible, although the design would have to carefully consider safety questions involving potential increases in the pressure that might be reached in some capsules due to higher tritium and especially  $^4\text{He}$  from  $^6\text{Li}$  reactions. Of course, since FFTF is no longer operational, the entire experiment needs to be redesigned around another reactor such as ATR or HFIR, taking into account the increased thermal neutron flux and need for thermal shielding.

### Possible Solutions and Recommended Work

As suggested in Reference 2, the tritium solubility limit problem with pure Li in ATR might be avoided by switching to Na, NaK, a mixture of Na and Li, or any similar mixture that has a lower solubility of tritium than does lithium. Preliminary calculations for ATR using pure Na confirm that we could achieve tritium distributions resulting in the desired He/dpa ratios. However, it is essential that the Sievert's constant for tritium solubility in this mixture of liquid metals exceed that of vanadium. Consequently, pure Na and NaK would not be good choices since they have lower tritium solubilities, as shown in Figure 8.

Mixtures with Li might give the desired characteristics, although Li and Na separate into two phases at lower temperatures. If the tritium solubility is not higher in the liquid metal, we cannot introduce the tritium into the capsule using a mother alloy at reactor startup, since most of the tritium will stay in the mother alloy, and the tritium will remain in the samples at the end of the irradiation. Both of these effects lead to helium production in the vanadium alloys before and after the irradiation rather than having helium and dpa produced at the same time. Furthermore, it is highly desirable that the mixture of liquid metals includes  $^6\text{Li}$  so that we can replace the tritium lost to decay and diffusion. Calculations using pure Na show that the He/dpa ratio steadily declines during the course of the irradiation, thereby complicating our interpretation of the dependence of material property changes on the He/dpa ratio.

Figure 7 shows the available hydrogen solubility data in the literature for Li and Na (there is a similar scatter in the Sievert's constant data in figure 8). Looking at this scatter in the data, it is not clear that tritium solubility data is sufficiently accurate for these other possible mixtures of liquid metals to allow for the confident design of a DHCE experiment. Consequently, more work may be needed to determine these tritium solubilities, especially if we want to use a mixture of Na or NaK and Li in order to use the  $^6\text{Li}$  reaction to replace tritium lost to decay and diffusion.

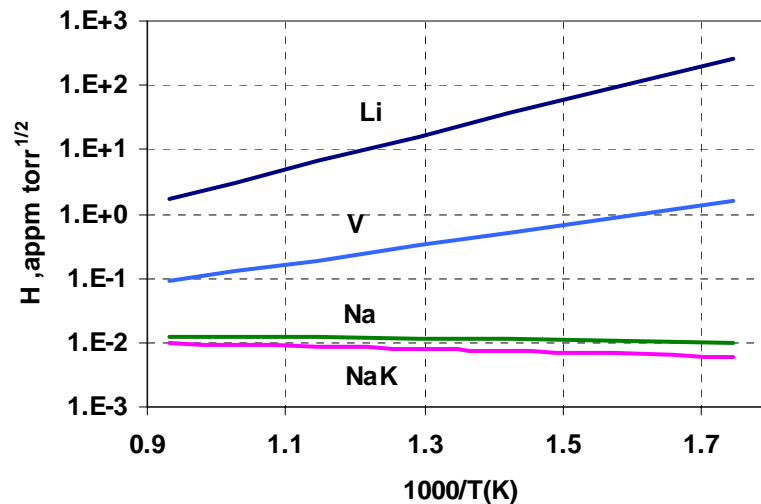


Figure 8. Temperature dependence of Sievert's constants are shown for H in Li, V, Na, and NaK [27].

Secondly, work is clearly needed to determine the distribution coefficients for tritium in the three alloys that showed much higher He levels than most of the other materials. These effects need to be better understood before an experiment can be designed to confidently predict He/dpa ratios in all of these materials. An experiment could be designed excluding these materials; however, these alloys may be of particular interest to fusion applications, especially V-5Cr-5Ti.

It is recommended that additional gas measurements be performed on the samples from the DHCE experiment, if these specimens are still available. Additional He measurements might help to resolve some of the discrepancies in the He data, especially the random high flyers for a few of the samples. Additional hydrogen or tritium measurements of the three alloys showing very high helium levels might resolve the question of whether these effects are due to tritium trapping. Examination of the samples by H. Chung et al noted the presence of bubbles in many of the samples. It has been suggested that such helium bubbles may also trap hydrogen or tritium. Tritium trapping would, of course, produce additional  $^3\text{He}$  in the samples after the end of irradiation until the tritium was degassed.

As discussed previously, the tritium leakage rates appear to be over predicted at the higher temperatures. Understanding these differences would be critical to a future design at 700°C, where the current leak rates may prevent us from achieving the desired He/dpa ratio. It may be possible to use capsule materials with better leakage characteristics or a double encapsulation approach, but this remains to be demonstrated.

In summary, a future DHCE experiment in ATR can be performed with our current knowledge for a restricted range of parameters, namely for the main grouping of alloys in the previous DHCE experiment (excluding the three with higher He levels), and at medium temperatures between about 550 to 650°C. This in itself might be a very useful experiment to conduct. However, if we want to expand the range of alloys and temperatures, then more work is clearly needed prior to such an expanded DHCE experiment.

## **FUTURE WORK**

Although this evaluation shows that a future DHCE experiment is feasible in ATR, HFIR, or some other reactor, obviously, a great deal more effort is required to design such an experiment. Thermal neutron shielding is required for any mixed spectrum reactor to reduce the transmutation of vanadium to chromium and to control the burnup of  $^6\text{Li}$  and  $^3\text{He}$ . It is especially important to evaluate the burnout of the thermal neutron shielding since the shields will most likely need to be replaced during the course of a DHCE experiment.

## **REFERENCES**

- [1] D. L. Smith, H. Matsui, L. Greenwood, and B. Loomis, "Experimental Method for Investigating Helium Effects in Irradiated Vanadium," *J. Nucl. Mater.*, 155-157 (1988) 1359-1363.
- [2] D. L. Smith, "Helium Analysis from the DHCE – 1 Simulation Experiment," *Fusion Reactor Materials Semiannual Progress Report, DOE/ER-0313/29* (2001) 26-33.
- [3] H. M. Chung, B. A. Loomis, L. Nowicki, and D. L. Smith, "Effect of Dynamically Charged Helium on Tensile Properties of V-5Ti, V-4Cr-4Ti, and V-3Ti-1Si," *Fusion Reactor Materials Semiannual Progress Report, DOE/ER-0313/19* (1995) 77-82.

- [4] K. Natesan, "Influence of Nonmetallic Elements on the Compatibility of Structural Materials with Liquid Alkali Metals," *J. Nucl. Mater.*, 115 (1983) 251-262.
- [5] H. Matsui, M. Tanaka, M. Yamamoto, A. Hasegawa and K. Abe, "Mechanical Properties of Vanadium Alloys Doped with Helium Using Various Techniques," *ASTM STP 1175* (1993) 1215-1227.
- [6] H. Nakajima, S. Yoshida, Y. Kohno, and H. Matsui, "Effect of Solute Addition on Swelling of Vanadium After FFTF Irradiation," *J. Nucl. Mater.*, 191-194 (1992) 952-955.
- [7] F. A. Garner, and M. B. Toloczko, "Persistence of Microstructural Evolution in Irradiated Metals and its Consequences at High Radiation Exposure," *Rad. Effects & Defects in Solids*, 148, (1999) 479-514.
- [8] K. Fukumoto, A. Kimura. and H. Matsui, "Swelling Behavior of V-Fe Binary and V-Fe-Ti ternary Alloys," *J. Nucl. Mater.*, 258-263 (1998) 1431-1436.
- [9] T. Iwai, N. Sekimura and F. A. Garner, "Effects of Helium on Void Swelling in Boron Doped V-5Fe Alloys," *J. Nucl. Mater.*, 258-263 (1998) 1512-1516.
- [10] F. A. Garner, D. S. Gelles, H. Takahashi, S. Ohnuki, H. Kinoshita, and B. A Loomis, "High Swelling Rates Observed in Neutron-Irradiated V-Cr and V-Si Binary Alloys," *J. Nucl. Mater.*, 191-194 (1992) 948-951.
- [11] F. A Garner, and L. R. Greenwood, "Neutron Irradiation Effects in Fusion or Spallation Structural Materials: Some Recent Insights Related to Neutron Spectra," *Rad. Effects & Defects in Solids*, 144, (1998) 251-286.
- [12] F. A. Garner, B. M. Oliver, L. R. Greenwood, D. J. Edwards, and M. L. Grossbeck, "Surprising Results Concerning the Generation and Retention of Hydrogen in Neutron-Irradiated Metals and Alloys," Unpublished Research.
- [13] F. A. Garner, B. M. Oliver, L. R. Greenwood, D. J. Edwards and S. M. Bruemmer, "Generation and Retention of Helium and Hydrogen in Austentic Steels Irradiated in a Variety of LWR Spectral Environments," Unpublished Research.
- [14] W. G. Wolfer, F. A. Garner and E. P. Simonen, "A Model to Explain the Unexpectedly large Retention of Hydrogen in Metals Irradiated at High Temperatures That Produces High Densities of Bubbles or Voids," Unpublished Research.
- [15] H. Tsai, R. V. Strain, H. M. Chung and D. L. Smith, "Status of the Dynamic Helium Charging Experiment," *Fusion Reactor Materials Semiannual Progress Report*, DOE/ER-0313/16 (1994) 220-224.
- [16] C. C. Addison, "The Chemistry of the Liquid Alkali Metals," John Wiley & Sons, 1984.
- [17] E. Veleckis, E. H. Van Deventer, and M. Blander, "The Lithium-Lithium Hydride System," *Jou. Physical Chemistry*, 78, No. 19 (1974) 1933-1940.

- [18] H. Katsura, R. Ishigai, and K. Furukawa, "Equilibrium Pressure and Solubility of Hydrogen in Liquid Lithium," *Nucl. Technology*, 32 (1977) 297-303.
- [19] H. U. Borgstedt, "Liquid Metal Systems," Plenum Press (1982) 477.
- [20] P. F. Adams, M. G. Down, P. Hubberstey, and R. J. Pulham, "Solubilities and Solution and Solvation Enthalpies for Nitrogen and Hydrogen in Liquid Lithium," *J. of the Less-Common Metals*, 42 (1975) 325-334.
- [21] P. F. Adams, P. Hubberstey, R. J. Pulham, and A. E. Thunder, "Depression of the Freezing Point of Lithium by Deuterium, and the Solubility of Deuterium in Liquid Lithium: A Comparison with Hydrogen," *J. of the Less-Common Metals*, 46 (1976) 285-289.
- [22] E. Veleckis, R. M. Yonco, and V. A. Maroni, "Solubility of Lithium Deuteride in Liquid Lithium," *J. of the Less-Common Metals*, 55 (1977) 85-92.
- [23] G. W. Hollenberg, private communication, 2001.
- [24] A. C. Whittingham, "An Equilibrium and Kinetic Study of the Liquid Sodium-Hydrogen Reaction and Its Relevance to Sodium-Water Leak Detection in LMFBR Systems," *J. Nucl. Mater.*, 60 (1976) 119-131.
- [25] S. A. Meacham, E. F. Hill, and A. A. Gordon, "The Solubility of Hydrogen in Sodium," *Atomic Power Development Associates*, 241 (1970).
- [26] D. R. Vissers, J. T. Holmes, and L. G. Bartholme, "A Hydrogen-Activity Meter for Liquid Sodium and Its Application to Hydrogen Solubility Measurements," *Nuclear Technology*, 21 (1974) 235-244.
- [27] K. Natesan, and D. L. Smith, "Effectiveness of Tritium Removal for a CTR Lithium Blanket by Cold Trapping Secondary Liquid Metals Na, K, and NaK," *Nuclear Technology*, 22 (1974) 138-145.

**OXIDATION OF V-4Cr-4Ti AT LOW PRESSURES** -- B. A. Pint and J. R. DiStefano (Oak Ridge National Laboratory)**OBJECTIVE**

The objective of this task is to assess the high temperature oxidation behavior of V-4Cr-4Ti in low oxygen pressure environments and any related effect on mechanical properties. Many reactor designs involve vanadium alloys in high temperature environments such as vacuum or helium which will contain some level of oxygen and hydrogen impurities. Testing is being conducted in vacuum with low oxygen pressures,  $10^{-3}$ - $10^{-6}$ Pa ( $10^{-5}$ - $10^{-8}$ Torr), and in high-purity helium and argon at 400-700°C. Recent emphasis has been on determining kinetics of oxidation at 600-700°C.

**SUMMARY**

Specimens of V-4Cr-4Ti have been exposed to He environments from 1atm down to  $10^{-4}$  atm in order to determine oxidation kinetics and effects on mechanical properties. At  $10^{-4}$  atm He, the reaction kinetics were nearly linear at 700°C. However, at  $10^{-3}$  atm He, the specimen mass gains were lower and followed a sub-parabolic rate, very similar to the behavior observed in 1atm of He. These results suggest that an external oxide layer may be forming at the higher pressures. During exposures in 1 atm He, specimens form an external oxide layer and retain some tensile ductility after exposure. To confirm an earlier result, specimens with various exposure times (and thus oxygen levels) were annealed for 2000h at 700°C. The ductility of those specimens which had an external oxide before annealing was reduced to zero, illustrating that a surface oxide on V-4Cr-4Ti is a source of oxygen for further embrittlement.

**PROGRESS AND STATUS****Experimental Procedure**

All of the experiments were conducted on V-4Cr-4Ti (Heat#832665). Prior to exposure, the specimens were annealed at 1050°C to produce a uniform grain size. Specimens were 0.76mm thick tensile specimens. Low pressure exposures were conducted in an ultra high vacuum system in which a base vacuum of  $10^{-7}$ Pa ( $10^{-9}$ Torr) could be achieved. For testing in He at 76,000Pa (1 atm), the high vacuum valve was closed after pumpdown followed by the introduction of He. Excess gas pressure was removed through an oil bubbler. A micrometering valve was used to achieve He partial pressures of  $10^{-3}$  or  $10^{-4}$ atm. Oxygen content was determined by weighing the samples before and after exposure. A power law was then used to fit the data at each pressure and temperature:

$$M = k \cdot t^{1/n}$$

where M is mass, k and n are constants and t is time. For linear reaction kinetics,  $n=1$  and for parabolic,  $n=2$ .

## Results and Discussion

### Reaction Kinetics in He at 700°C

The reaction kinetics of V-4Cr-4Ti at 600° and 700°C were previously determined at oxygen partial pressures from  $10^{-3}$ - $10^{-6}$ Pa ( $10^{-5}$ - $10^{-8}$ Torr) and at 1atm of high purity He<sup>1-2</sup>. In general, the results in oxygen showed a linear relationship between pressure and reaction rate and a nearly linear relationship with time at  $10^{-4}$ - $10^{-6}$ Pa ( $10^{-6}$ - $10^{-8}$ Torr), but deviations were observed at  $10^{-3}$ Pa. The linear-parabolic behavior ( $n=1.4$ ) at  $10^{-3}$ Pa ( $10^{-5}$ Torr) was attributed to the formation of a surface oxide which then inhibited oxygen uptake into the substrate. Under these conditions, specimen surfaces became discolored as mass increases exceeded 0.5–2% and room temperature tensile ductility was reduced to zero. In 1atm He, a similar phenomenon was observed with very high mass gains combined with the formation of a surface oxide which resulted in an  $n$  value of 3.0. These results are plotted for reference in Figure 1 (dashed lines).

The high mass gains in 1atm He are not surprising because, even with high purity ( $<1$ ppm  $O_2$ ) He, the oxygen pressure would be  $10^{-1}$ Pa. In a He-cooled fusion reactor, the He pressure would be even higher but, with purification, the  $O_2$  pressure could be lower. In order to simulate that environment, the He pressure was dropped to levels of  $10^{-3}$  and  $10^{-4}$ atm in an attempt to achieve

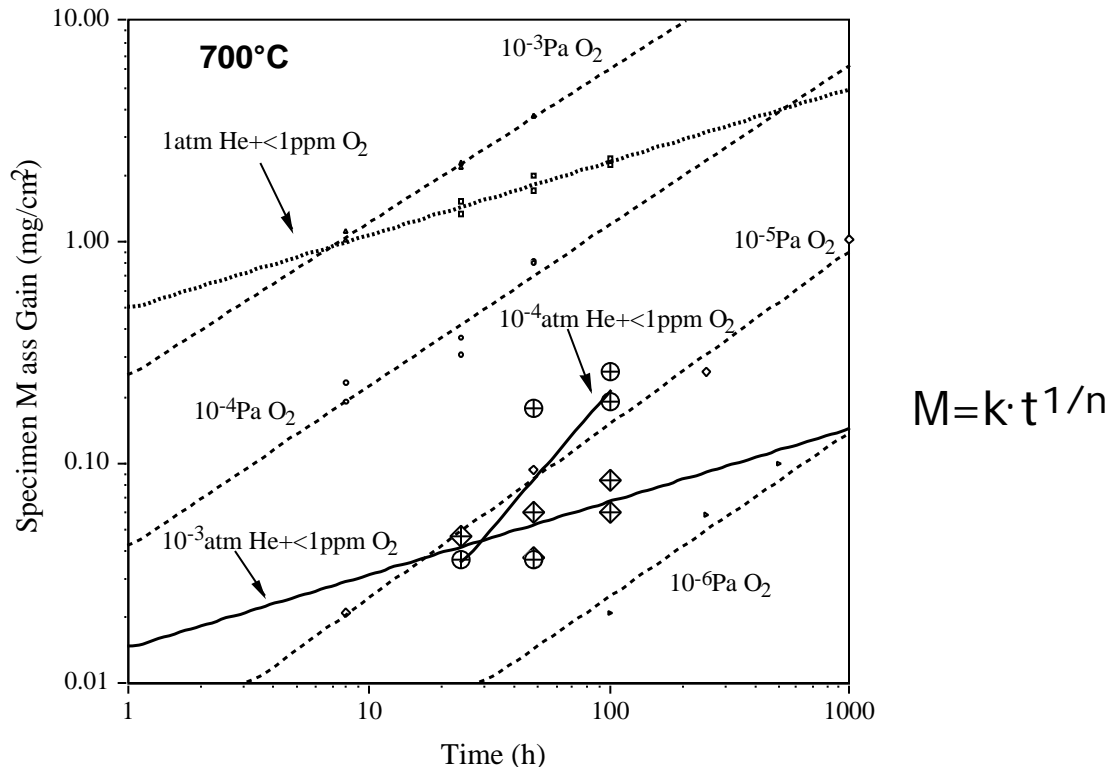


Figure 1. Log-log plot of the mass gains observed in this work at 700°C in low pressures of high purity ( $<1$ ppm O) He (solid lines). At  $10^{-4}$ atm He, the mass gains were similar to that observed in  $10^{-5}$ Pa  $O_2$ . At  $10^{-3}$ atm He, the mass gains were lower and the reaction kinetics were similar to that observed in 1 atm He.

oxygen pressures of  $10^{-4}$  and  $10^{-5}$ Pa, respectively. The mass gain results for 5 tests at each pressure are shown in Figure 1 with the a power law fit of the data (solid lines). At  $10^{-4}$ atm He, the data fell near the previous results for  $10^{-5}$ Pa  $O_2$  which corresponds very well to the predicted oxygen level in the gas. The n value was 0.8. At  $10^{-3}$ atm He, the mass gain values were lower and n was 3.0, identical to the value at 1 atm He. This suggests that at the higher pressure there may have been oxide film formation which inhibited oxygen uptake or that there was a change in the rate of oxygen adsorption due to the higher He pressure. Characterization of the specimens is being conducted along with additional experiments at longer times and different He pressures.

### **Mechanical Properties**

As previously reported,<sup>3</sup> sub-size sheet tensile specimens (SS-3) of unoxidized, annealed V-4 Cr-4 Ti have a room temperature elongation of ~30%, but exposure to oxygen can significantly lower this value. As observed above, the formation of an external oxide layer can significantly change the reaction kinetics. For Fe- or Ni-base alloys, an external oxide is termed protective if it limits further reaction. However, in the case of refractory metals like vanadium, the oxide needs to prevent embrittlement of the alloy in order to be considered protective. Previous work<sup>2</sup> indicated that annealing for 2000h at 700°C reduced the ductility of specimens with a surface oxide from 10% total elongation at 25°C to 0%. To confirm this observation, a series of specimens were oxidized to create a range of added oxygen levels up to 10,000ppm. The higher oxygen levels were achieved by exposure at 600°C in 1 atm He where a surface oxide was formed. Half of the specimens were fractured after exposure and the other half were annealed for 2000h at 700°C. Figure 2 shows the room temperature ductility results for this set of specimens. For control, a specimen with no added oxygen and one with a low level of added oxygen (136ppm) also were annealed for 2000h at 700°C. Compared to the unannealed results, the specimens with little or no added oxygen showed only a small loss in ductility after annealing. However, the specimens which formed surface oxides all showed severe embrittlement after annealing, Figure 2. Because of the high solubility of oxygen in vanadium, it is likely that during the 700°C anneal the surface oxide dissolved, providing a source for additional oxygen to embrittle the specimen. In fact, the specimens were lighter in color after the anneal, indicating a change in the surface oxide thickness. These results indicate that the surface oxide on vanadium is not protective and that a change in oxidation kinetics as a result of surface oxide formation should not be interpreted as an improvement in performance. During prolonged high temperature exposure, even in the absence of further oxygen uptake, the presence of a surface oxide provides a source for oxygen which can embrittle the underlying substrate. Further experimental work in this area may include varying the surface area to volume ratio to test model predictions for the critical oxygen levels needed to embrittle specimens with different geometries.

### **REFERENCES**

1. B. A. Pint, J. R. DiStefano, J. Bentley and L.D. Chitwood, DOE/ER-0313/27 (1999) 40.
2. B. A. Pint, J. R. DiStefano and L. D. Chitwood, DOE-ER-0313/28 (2000) 3.
3. J. R. DiStefano and J. H. DeVan, J. Nucl. Mater. 249 (1997) 150.

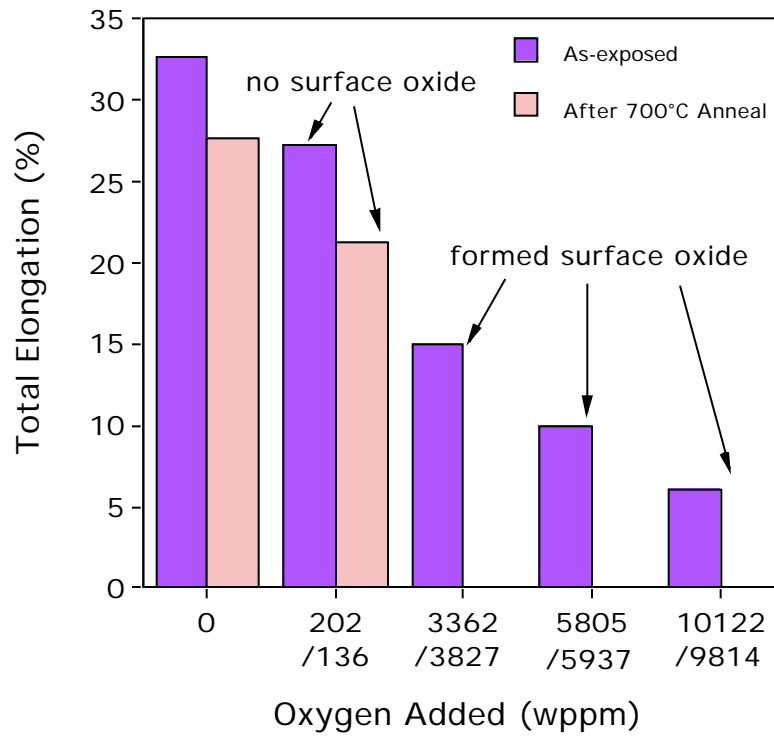


Figure 2. Total elongation at room temperature as a function of added oxygen with and without annealing for 2000h at 700°C. Specimens which formed a surface oxide and were annealed were severely embrittled.

## **SEM/TEM STUDY OF V-4Cr-4Ti LASER WELDMENTS**

Y. Yan, R. E. Cook, H. Tsai, and D. L. Smith (Argonne National Laboratory)

### **OBJECTIVE**

The objective of this task is to perform a scanning electron microscopy (SEM) and transmission electron microscopy (TEM) study of laser welds on V-4Cr-4Ti alloys and to evaluate the effects of weld parameters on the properties of weldments.

### **SUMMARY**

Mechanical properties and microstructures of laser weldments of Heat NIFS-1 V-4Cr-4Ti alloys were investigated by impact testing, optical microscopy, SEM, and TEM. Optical metallography shows that grain sizes in the weld are greater than those in the base material. The grains are equiaxed near the middle of the weld and elongated (oriented in the direction of freeze progression) near the edge. Element mapping in SEM shows that the Ti and C content of the secondary phase particles (300 nm) is significantly higher in the banded structure than in the matrix, and the banded structure in the base metal seems to disappear in the weld zone. Impact testing with laser weld specimens in as-machined condition (by electric discharge machining with water as the flushing fluid) indicated that the ductile-to-brittle-transition temperature of Heat NIFS-1 is higher than that of Heat 832665. Small particles (50-100 nm) are observed at the grain boundary of the NIFS-1 laser weld. Energy-dispersive spectroscopy (EDS) analyses show that the chemical composition appears to vary from grain to grain of the laser weld.

### **BACKGROUND**

Laser welding offers potential advantages for welding vanadium alloys, including increased flexibility for field and large-component welding with acceptable atmospheric control. A pulsed Nd:YAG laser with a fiber optic delivery system is used to conduct a systematic investigation of the weld parameters and environmental control requirements for obtaining high-integrity laser welds of vanadium alloys. The current effort is focused on evaluating laser welds on an 4-mm-thick plate of V-4Cr-4Ti alloy. The postwelding characterization includes Charpy-impact testing and microstructural characterization of the welds.

Impact testing laser weld specimens in as-machined condition (by electric discharge machining with water as the flushing fluid) indicated that the ductile-to-brittle-transition temperature (DBTT) of Heat NIFS-1 is lower than that of heat 832665 [1]. The objective of this paper is to determine whether there is a notable difference between the microstructures of the laser welds of these two heats, because such a difference could affect the results of the Charpy tests.

### **EXPERIMENTAL PROCEDURE**

The starting material for this study was obtained from Heat NIFS-1 of V-4Cr-4Ti alloy. Laser welding was performed at a Nd:YAG laser welding facility [2]. The laser weldment was produced by butt welding of two 3.8 mm thickness annealed plates. Direction of the weld travel was perpendicular to the rolling direction of the plate, as shown in Fig. 1. Details of the welding procedure are given in Ref. 2.

After mechanical polishing and electropolishing [3], microscopy examinations were conducted. Transmission electron microscopy (TEM) studies were carried out using a Philips-CM30

microscope, and scanning electron microscopy (SEM) observations were performed using a Hitachi S-4700-II field emission gun microscope at Argonne National Laboratory.

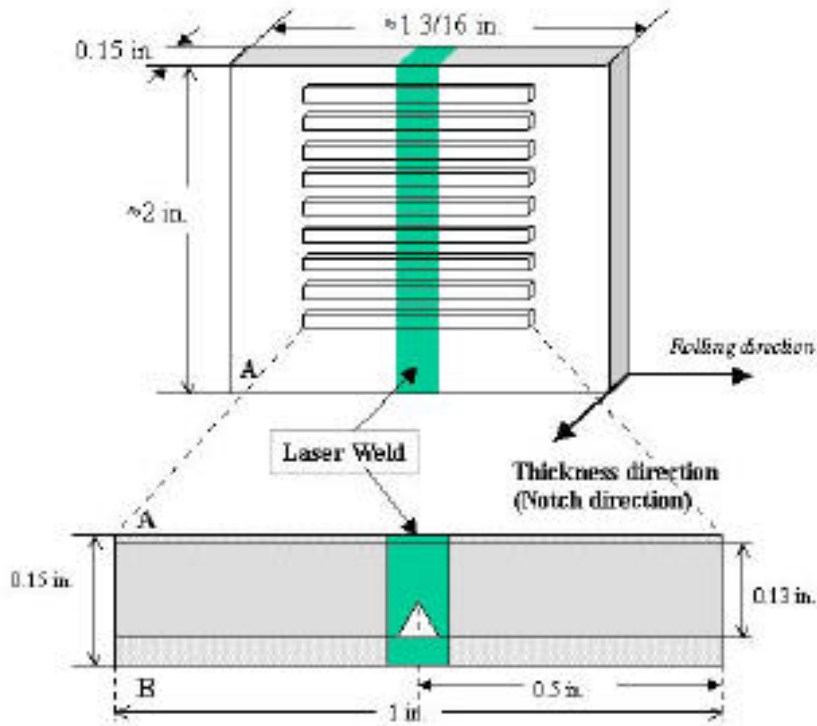


Fig. 1 Schematic illustration of the fabrication of Charpy specimens.

## RESULTS

Impact tests on as-machined laser welds indicated that the DBTT of the weld specimens from Heat NIFS-1 is  $<187^{\circ}\text{C}$ , which is much lower than that of the weld specimens from the heat 832665. Details of the impact testing were given in a previous report [4].

To elucidate the microstructure of the weld zone, specimens were cut in an orientation perpendicular to the direction of the weld and perpendicular to the rolling direction. After polishing and etching, optical microscopy was conducted first, to investigate grain morphology and possible microstructural inhomogeneities. An area that contained the base metal, the heat-affected zone (HAZ), and the weldments from Heat NIFS-1 is shown in Fig. 2. A characteristic banded structure, aligned in the direction of rolling, was observed in the base metal [5]. The weld appears to be sound, with good depth of penetration. The interface between the weld zone and the HAZ can be

clearly identified, and the grains in the weld are elongated in the direction perpendicular to the interface.

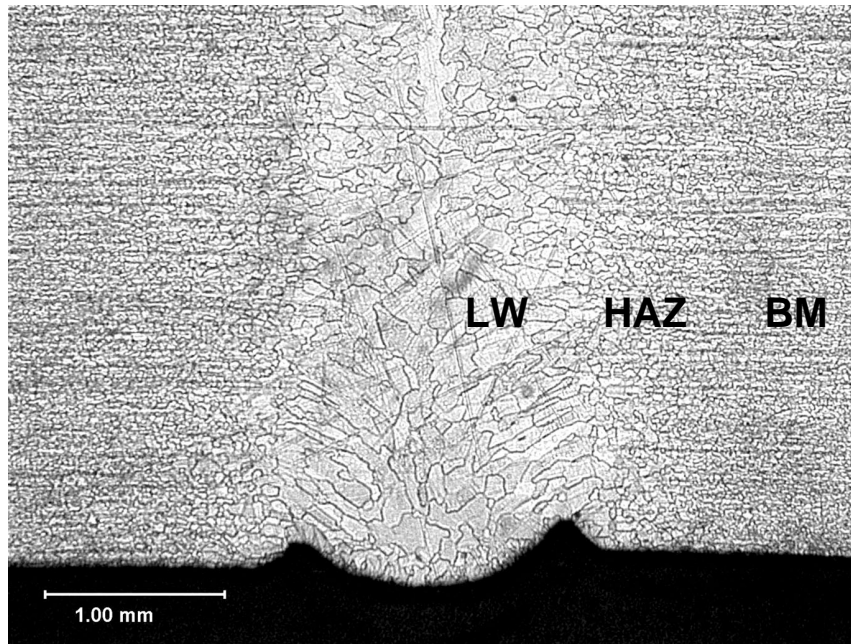


Fig. 2. Photograph showing the laser weld (LW), heat affected zone (HAZ), and base metal (BM) of V-4Cr-4Ti laser weldment from Heat NIFS-1.

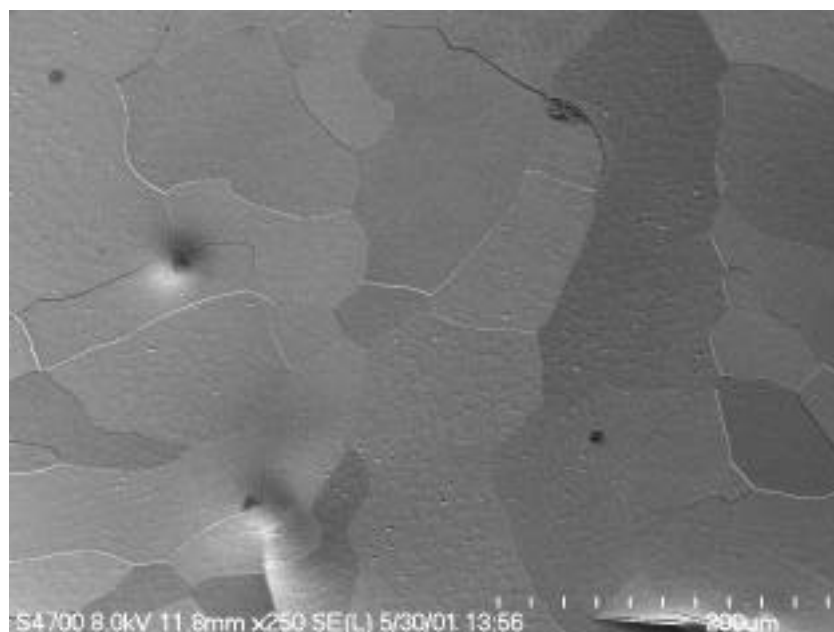
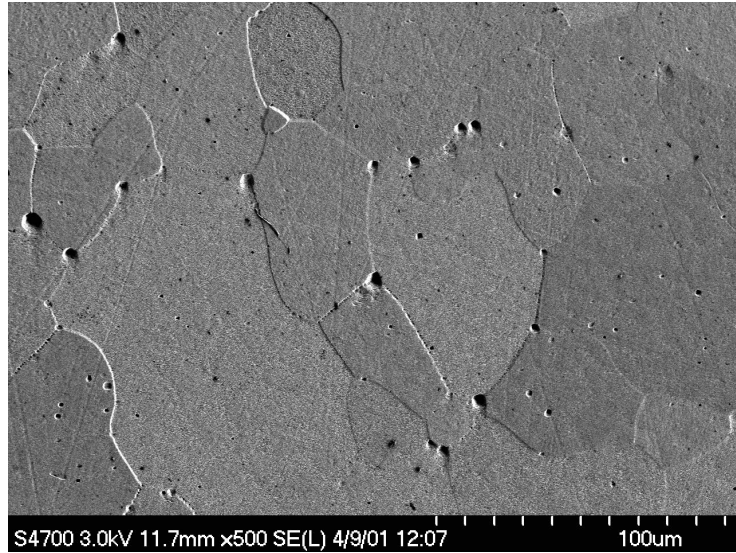
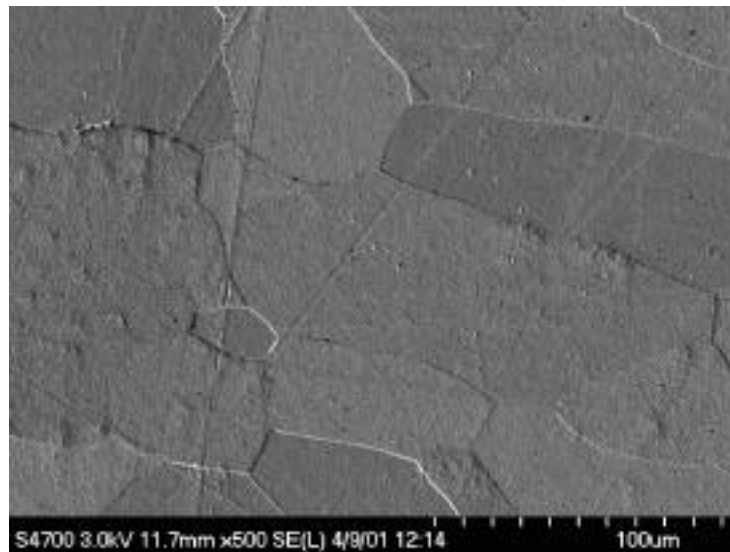


Fig. 3. SEM image of laser weld area denoted LW in Fig. 2, showing absence of band structure.

Figure 3 is a SEM micrograph of the laser weld area, denoted as LW in Fig. 2. The grain size in the weld is increased to  $100\ \mu\text{m}$  from  $20\text{-}30\ \mu\text{m}$  in the base metal, and the banded structure in the base metal disappears in the weld zone. Higher-magnification SEM micrographs of the laser weld from Heat NIFS-1 are shown in Figs. 4a and b. "Macro defects" were observed in the area close to the edge (see Fig. 4a), and the density of these defects is relatively low in the area away from the edge (Fig. 4b). It has been found that the size of the macro defect is  $5\ \mu\text{m}$ , which is nearly 10-20 times larger than that of the secondary particles in the banded structure. Most of the larger macro defects are at the triple points or grain boundaries of the laser weld.



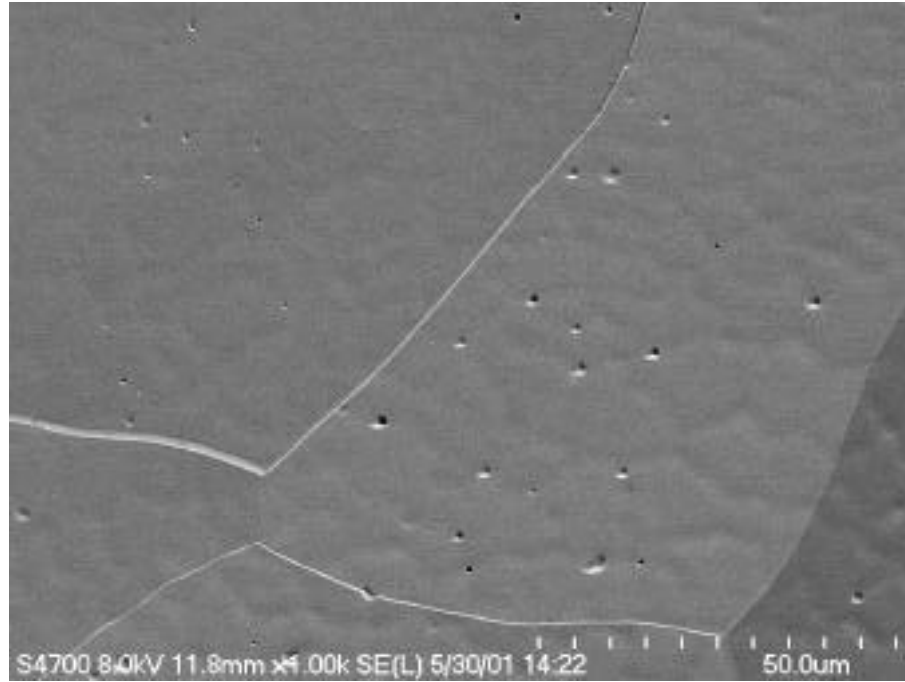
(a)



(b)

Fig. 4 SEM images of laser weld: (a) high density of macro defects (voids) in area close to edge ( $500\ \text{nm}$ ); (b) low density of voids in area away from edge ( $>500\ \text{nm}$ ).

The SEM image in Fig. 5a shows that some defects are also inside the grains in the laser weld from Heat NIFS-1. The size of the defects is 0.5-1.0  $\mu\text{m}$  in the etched sample, much smaller than those shown in Fig. 4a. Many of the defects in Fig. 5a exhibit a typical morphology of etched dislocations, as shown in Fig. 5b. Globular-shaped defects were also observed (Fig. 5c). The density of the defects inside the grain is  $5.2 \times 10^9/\text{cm}^2$  in the examined area (Fig. 5a).



(a)

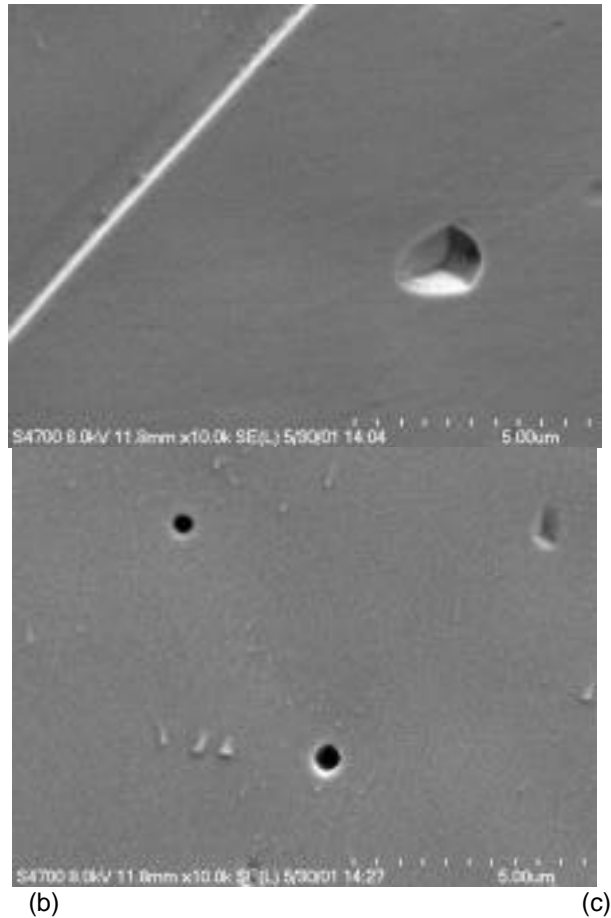


Fig. 5 SEM images showing (a) defects inside of grains after the etching, (b) high-magnification image of etched dislocation, and (c) void or secondary phases.

Figure 6 is an intermediate-magnification micrograph that shows the grain boundary in Heat NIFS-1. At the triple points (Fig. 6), it is that the grain boundaries likely join together at some special angles, such as  $90^\circ$ ,  $120^\circ$ , or  $135^\circ$ . Also there is a tendency for grain boundary interfaces to be faceted at the triple points. The faceted planes are presumably some low-index crystallographic planes, which are usually in favor of formation energy for grain boundaries. High-resolution SEM study indicates that there are some small particles at the grain boundary of the laser weld of Heat NIFS-1 (Figs. 7a and b). The grain size is 50-100 nm, which is much smaller than that of the secondary particles (200-300 nm) observed in the band structure of the base metal. Some larger particles (100-200 nm) were also observed, as shown in Fig. 7a.

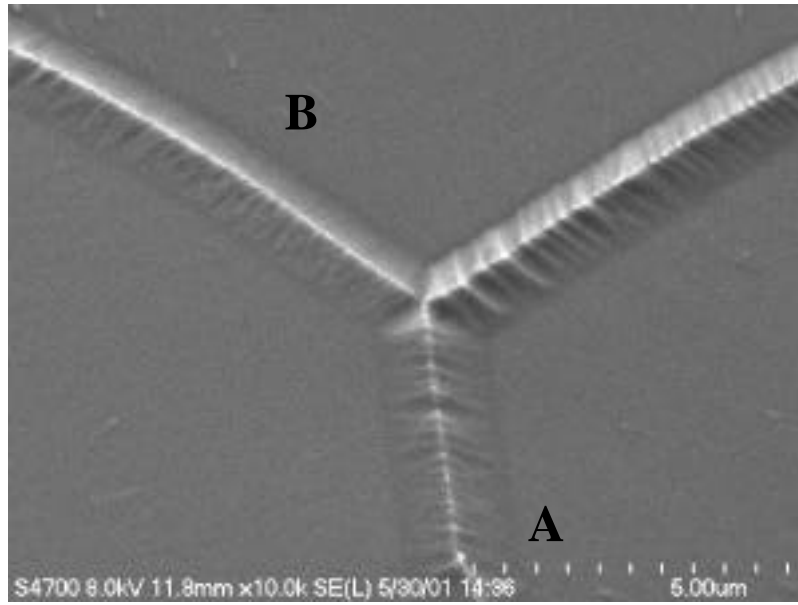
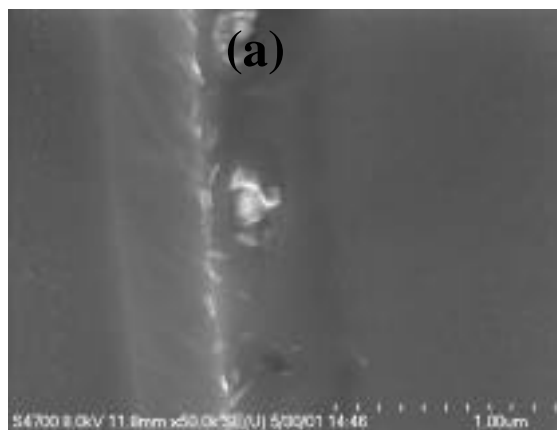


Fig. 6. SEM image showing grain boundary morphology of Heat NIFS-1.



(b)



Fig. 7. High-resolution SEM images showing small particles (50-100 nm) at (a) grain boundary A and (b) grain boundary B in Fig. 6.

Figure 8 is a high-resolution SEM image showing small particles on a grain boundary. The boundary plane was inclined to the sample surface because of differing etching processes to adjacent grains with various orientations. The small particles are uniformly distributed on the grain boundary planes, and the density of the particles is  $8.1 \times 10^9/\text{cm}^2$ . TEM study confirmed the existence of the small particles at the grain boundary of the laser weld from Heat NIFS-1. Figure 9 is a TEM micrograph showing the small particles at a grain boundary of the laser weld. The bright-field image was taken at the kinematical condition to reduce the stain contrast, and the specimen was tilted as the boundary projection could be seen in the beam direction.

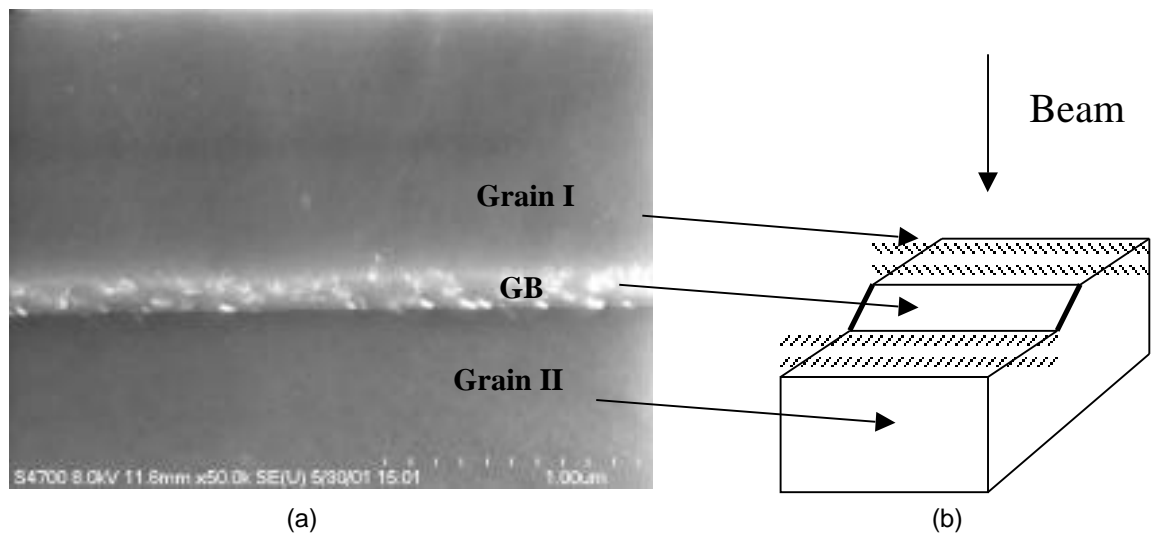


Fig. 8. (a) High-resolution SEM image showing small particles ( $<100$  nm) on a grain boundary. (b) boundary plane was inclined to sample surface because of differing etching processes to adjacent grains with various crystallographic orientations.

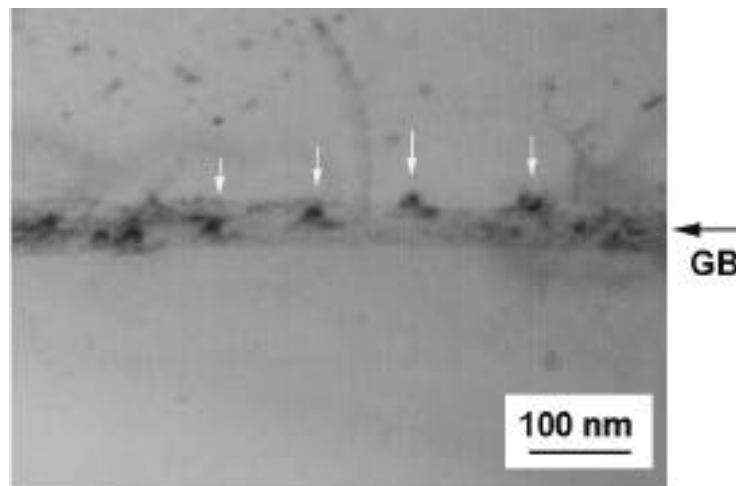


Fig. 9. TEM micrograph showing small particles at grain boundary of laser weld. Bright-field image was taken at kinematical condition, and specimen was tilted to see boundary projection in the beam direction.

Figures 10a and b show secondary electron (SE) and back scattering electron (BSE) images of the laser weld, respectively. The different contrast in the BSE image suggests that the composition of the grains could vary from grain to grain or from place to place. Preliminary energy-dispersive spectroscopy analyses indicate that the composition change from grain to grain in the laser weld could be 2%. A quantitative EDX study is underway and the results will be reported in the future.

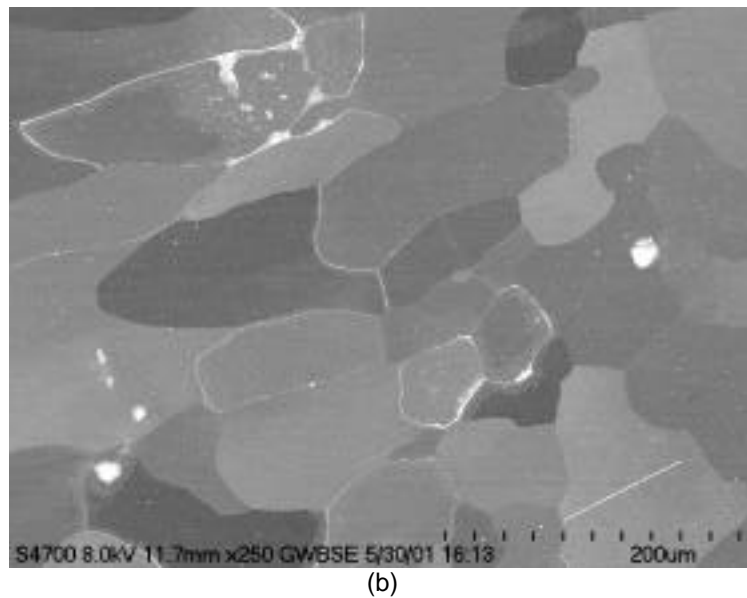
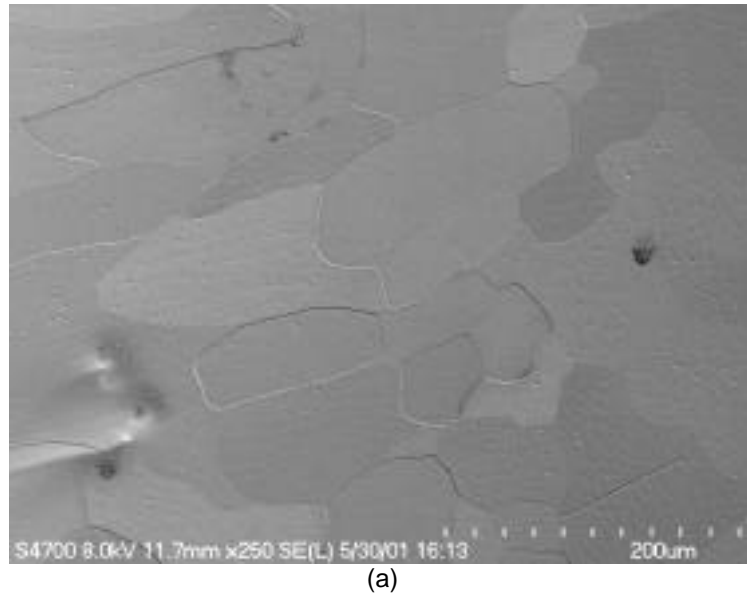


Fig. 10. (a) Secondary electron image and (b) back-scattering electron image of laser weld.

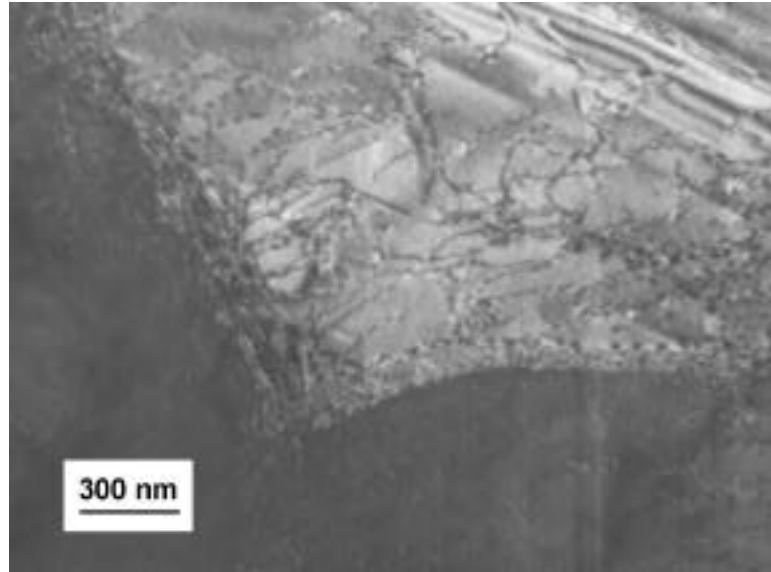


Fig. 11. TEM image showing high density of dislocations in electron polished thin foil of laser weld.

Figure 11 is a TEM micrograph showing a low-angle boundary in the electron polished thin foil of the laser weld. A high density of dislocations was observed around the grain boundary. A detailed TEM study on the chemical composition at the grain boundary is underway; and the results will be reported in the next report.

#### **FUTURE ACTIONS**

SEM and TEM studies will be performed on the laser weld of Heat 832665 to evaluate the effect of microstructure on impact properties.

#### **REFERENCES**

- [1] Z. Yu, D. L. Smith, Y. Yan, H. Tsai, T. Nagasaka, and T. Murgoa, Characterization and Impact Properties of V-4Cr-4Ti Laser Weldments, ICFRM, to be published in 2001.
- [2] Z. Xu, D. L. Smith, Y. Yan, and C. B. Reed, Laser welding of V-4Cr-4Ti alloy, in Fusion Materials Semiannual Progress Report, DOE/ER-0313/29, Dec. 2000.
- [3] Y. Yan, H. Tsai, W. C. Kettman, and D. L. Smith, Effect of heat treatment on microstructure of V-4Cr-4Ti materials, in Fusion Materials Semiannual Progress Report, DOE/ER-0313/28, June 2000, pp. 72-76.
- [4] Y. Yan, H. Tsai, A. D. Storey, D. L. Smith, and Z. Xu, Impact properties of V-4Cr-4Ti Laser Weldments from the General Atomics heat, in Fusion Materials Semiannual Progress Report, DOE/ER-0313/29, Dec. 2000, pp. 50-53.
- [5] Y. Yan, H. Tsai, and D. L. Smith, Microstructural examination on V-4Cr-4Ti rods and creep tubes, in Fusion Materials Semiannual Progress Report, DOE/ER-0313/297, Dec. 1999, pp. 23-31

## **2.0 CERAMIC COMPOSITE MATERIALS**

## **RESPONSE OF SiC/SiC TO TRANSIENT THERMAL CONDITIONS: A REVIEW - R. H. Jones (Pacific Northwest National Laboratory)\***

### **OBJECTIVE**

The objective of this review is to evaluate the database on thermal shock and thermal fatigue effects in SiC/SiC composites, to determine if there is sufficient data to predict the impact of thermal transients on their properties and if so to predict this behavior.

### **SUMMARY**

The database on thermal shock behavior of SiC/SiC composites is very limited. The existing data suggests continuous fiber ceramic matrix composites, such as SiC/SiC, exhibit very good thermal shock characteristics but most data was obtained for  $-\Delta T$  conditions as a result of quenching from an elevated temperature. Thermal shock in a fusion energy system will result from plasma discharge and will result in a  $+\Delta T$ . One study was reported for SiC/SiC composites given a  $+\Delta T$  with no loss in strength following 25 cycles at a heating rate of  $1700^{\circ}\text{C/s}$ . Monolithic SiC failed in 1.5 cycles at a heating rate of  $1400^{\circ}\text{C/s}$ . Thermal fatigue test results also suggest that SiC/SiC composites will exhibit little or no degradation for 100's of cycles. It was estimated that radiation could, in an extreme case, cause a reduction in the thermal shock performance from a calculated  $\Delta T_c$  of 957K to about 300K if the fiber strength is reduced by 50%. Newer composites with greater radiation resistance should have a much smaller change in the  $\Delta T_c$ .

### **PROGRESS AND STATUS**

#### Background

Transient thermal conditions will occur in a fusion energy system from both the system duty cycle and plasma discharge processes. Shutdown of the system for either scheduled or unscheduled maintenance will result in a temperature decrease of the blanket that inevitably will cause some stress build-up in the material. The stress magnitude will be dependent on the cooling rate and thermal gradients. This type of cycle is usually referred to as thermal-fatigue, involves the entire blanket and is measured in the laboratory in simulated thermal cycling tests or low-cycle fatigue (mechanical) tests. Start-up will also induce stress of the opposite sign to that produced by shutdown and may relax the cool-down stresses. Plasma discharge will induce a rapid heating of a small volume of plasma-facing material and some larger volume of blanket material. Transmission of the thermal energy through the blanket and therefore the temperature change and stress response will be very design and material dependent.

Cooling the surface of a material faster than the interior results in a surface tensile stress while heating the surface of a material faster than the interior results in a surface compressive stress. The heating or cooling rate and  $\Delta T$  determine the magnitude of the stress. The maximum temperature can also affect the material microstructure and properties. The magnitude of the stress is determined by the heating rate through the resulting thermal gradient. For thermal shock conditions, the thermal diffusivity may be sufficiently slow that a thermal gradient is not established in the short-term such that the surface stress is determined by the energy deposition and resulting surface temperature and not by a thermal gradient. Assuming that the residual stresses have relaxed to zero at the operating temperature, cooling during a shutdown will result in a surface tensile stress and a plasma discharge in a surface compressive stress. In composite materials, internal stresses are also determined by the differential thermal expansion between the

---

\*Pacific Northwest National Laboratory (PNNL) is operated for the U.S. Department of Energy by Battelle Memorial Institute under contract DE-AC06-76RLO-1830.

fiber and matrix so that the analysis of thermal stress is more complex than for a monolithic material. It is conceivable that the internal stresses could reverse the thermal gradient stress.

### Thermal Shock Behavior of Ceramic Composites

Thermal shock behavior is an important aspect of monolithic ceramic materials because their low fracture toughness, low thermal conductivity and high elastic modulus renders them susceptible to failure under transient thermal conditions. Thermal shock studies of monolithic ceramics cover a range of testing methods, failure analysis methods and models that have been reviewed by Wang and Singh [1].

Models of thermal shock fall into two categories: 1) those based on fracture resistance (initiation of cracks on the surface) and 2) crack propagation resistance. Fracture resistance models predict a thermal shock resistance parameter  $R$  that is equal to the  $\Delta T_c$  the maximum allowable temperature difference to which a body can be subjected without the initiation of fracture under both steady state heat flow or severe transient thermal conditions. This parameter is defined by Equation 1:

$$\Delta T_c = R = \sigma_t (1-\nu)/\alpha E \quad (1)$$

where  $\sigma_t$  is the material's tensile strength,  $E$  is the Young's modulus,  $\alpha$  is the coefficient of thermal expansion and  $\nu$  the Poisson's ratio. The fracture strength can be considered equal to the tensile strength in brittle materials. For this analysis, the fracture strength is equal to the thermal stress on the surface at  $\Delta T_c$ . There are several variants of this parameter for different heating conditions. The maximum allowable black body radiation to which opaque materials can be subjected is given by  $R_{rad}$ , the maximum allowable black body temperature to which semitransparent materials can be subjected by  $R_{trans}$ , and the case where a material is undergoing creep by  $R_{cr}$ .

The crack propagation resistance models rely on the available amount of elastic energy stored in the material that is available for crack propagation. This is similar to the Griffith fracture criterion that balances the elastic energy available for crack propagation with the surface energy required to advance the crack. An equation for  $R'''$  that defines the minimum elastic energy at fracture available for crack propagation as:

$$R''' = E/\sigma_t^2 (1-\nu) \quad (2)$$

where the parameters have the same meaning as in Equation 1. It is important to note that these two failure criteria give different responses to fracture strength and elastic modulus. Material with a high fracture strength and low Young's modulus is desired to optimize  $R$ , but a material with a low fracture strength and high Young's modulus is needed to optimize  $R'''$ .

Quenching into liquid media is the most common method for introducing a negative  $\Delta T$  with common quenching media being water, silicone oil, liquid metal, methyl alcohol and glycerine. Methods for producing a positive  $\Delta T$  include heating a sample with a plasma jet, laser, tungsten halogen lamp, electron beam, hot gas jet, arc discharge and hydrogen-oxygen flame from a rocket engine. A number of methods are used to assess the thermal shock damage including: 1) measuring the dynamic moduli of elasticity using ultrasonic waves, 2) measuring the Young's modulus by the mechanical resonance method, 3) measuring the change in specific damping capacity, 4) monitoring the change in the spectra of ultrasonic pulses passed through a specimen, 5) recording acoustic emission signals during quenching and 6) measuring the thermal diffusivity change. Each technique has advantages and disadvantages especially in regard to detection of surface versus interior cracks.

Comparisons (1) between calculated and measured values of  $R$  (or  $\Delta T_c$ ) for monolithic  $Al_2O_3$  give a calculated value of  $84^\circ C$  and measured value of  $200^\circ C$ . Similar differences were noted for monolithic SiC with the calculated values always less than the measured values. Differences between the ideal and actual quenching conditions is the cause of this discrepancy and a correction term is added to the calculated values to compensate for this difference. This correction is  $f(\beta)$  where  $\beta = r_o h/k$ ,  $r_o$  is the relevant semidimension of the sample,  $h$  the heat transfer coefficient of the environment and  $k$  is the thermal conductivity of the material. The function  $f(\beta) = 1.5 + 4.67/(\beta - 0.5 \exp(-51/\beta))$ . For rapid quenching conditions  $\beta$  is large and  $f(\beta)$  is approximately 1.5. A similar value can be assumed for the rapid heating resulting from a plasma discharge. Wang and Singh [1] reported ratios between the calculated and experimental values of  $R$  for  $Al_2O_3$  and SiC as 2.4 and between 1.9 and 3.8, respectively. Clearly, a  $f(\beta)$  of 1.5 is too small to correct the difference between the calculated and measured values.

#### *Thermal Shock of Monolithic Ceramics*

There have been extensive studies of the thermal shock behavior of monolithic ceramics because this is a critical property for many applications. Wang and Singh [1] have reviewed this literature for SiC and  $Al_2O_3$  and their conclusion is that their thermal shock behavior has been found to be in good agreement with theory especially with the Hasselman unified theory [2]. Wang and Singh [1] compared the thermal shock behavior of SiC produced by CVD, hot pressing and pressureless sintering. Monolithic SiC produced by chemical vapor deposition (CVD) comes closest to being representative of the matrix of a SiC/SiC composite made by chemical vapor infiltration. The thermal shock was measured by residual flexure strength following quenching. The CVD SiC exhibited a strength increase following the thermal quench, the hot-pressed material exhibited a distinct  $T_c$  of about  $500^\circ C$ , and the sintered material showed a gradual strength decrease. The lack of a strength decrease for the CVD SiC quenched from temperatures up to  $1000^\circ C$  was suggested as being a result of surface flaw healing during the heating step and the sample being too small to give the needed thermal stresses for a  $\Delta T_c$  higher than  $1000^\circ C$ . The CVD SiC had a room temperature thermal conductivity of  $250 \text{ W/m-K}$  while the hot-pressed material had a room-temperature thermal conductivity of  $87 \text{ W/m-K}$ . The thermal conductivity affects the value of  $\beta$ , as described above, but for severe quench conditions where  $\beta \gg 1$ , the  $f(\beta)$  approaches 1.5 independent of the thermal conductivity. For  $\beta < 1$  the value  $R'$  is a function of thermal conductivity as given by equation three below:

$$R' = \sigma_t (1-\nu)k / \alpha E \quad (3)$$

where  $k$  is the thermal conductivity.

Takeda and Maeda [3] evaluated the effect of thermal conductivity on the thermal shock behavior of SiC by adding BeO and AlN to hot-pressed SiC material. The thermal conductivities with these additives were  $100 \text{ W/m-K}$  and  $65 \text{ W/m-K}$ , respectively while the  $\Delta T_c$ 's were  $680$  and  $450^\circ C$ , respectively. This is in comparison to a  $\Delta T_c$  of about  $500^\circ C$  for hot-pressed material tested by Wang and Singh [1] with a thermal conductivity of  $87 \text{ W/m-K}$ . These results are qualitatively consistent with Equation 3 with increasing thermal conductivity resulting in an increasing  $R'$ . Since the materials were not made from the same starting powder or with the same hot-pressing conditions a quantitative correlation is not possible but a linear relationship between  $R'$  and  $\kappa$  is suggested.

#### *Thermal Shock of Ceramic Composites*

Thermal shock studies have been conducted on particle, whisker, and fiber reinforced ceramic matrix composites. Lee and Case [4] studied the thermal shock behavior of SiC whisker reinforced  $Al_2O_3$  and showed that there was a gradual increase in the internal friction and decrease in the elastic modulus with increasing number of thermal cycles. These changes are

presumably the result of thermal shock induced microcracks. Tiegs and Becher [5] found that the addition of 20 % SiC whiskers to  $\text{Al}_2\text{O}_3$  produced a material that exhibited no loss in strength following a single  $\Delta T$  of  $900^\circ\text{C}$  while there was minor strength loss after 10 cycles at a  $\Delta T$  of  $300^\circ\text{C}$ . The composite material had a fracture strength of 620 MPa while the monolithic material had a flexure strength of 310 MPa.

Wang and Singh [1] concluded that fiber reinforced ceramic composites possess superior thermal shock resistance in comparison with monolithic ceramics. Catastrophic failure is averted with these materials. These conclusions are supported by several studies of composites with continuous fiber reinforcement of SiC, glass and  $\text{Si}_3\text{N}_4$ . Only the SiC/SiC composite results will be summarized since the thermal shock behavior of composites is dependent on the difference in thermal expansion between the fiber and matrix in addition to the thermal stress from the thermal gradient.

Wang and Singh [6,7] measured the retained flexural strength of SiC/SiC composites quenched from temperatures up to  $1000^\circ\text{C}$ , Figure 1. The composites were reinforced with Nicalon (presumably CG given the date of the reference) and CVI and polymer derived matrices with the fibers woven in a two-dimensional fabric. The composite with the CVI matrix had a  $\Delta T_c$  of about  $750^\circ\text{C}$  while the composite with a polymer derived matrix had a  $\Delta T_c$  of  $400^\circ\text{C}$ . These  $\Delta T_c$  were defined by a decrease in the residual strength but the decrease was gradual and not discontinuous, as observed for monolithic material. Even with a  $\Delta T$  of  $1000^\circ\text{C}$  the residual strengths were 85% and 75%, respectively for the CVI and polymer derived matrix material. These results suggest that the polymer derived SiC matrix has a lower matrix fracture strength than does the CVI matrix material. However, this is not the case since the matrix cracking stress is 150 MPa for the CVI material and 250 MPa for the polymer derived matrix material. Wang and Singh [7] explain the difference in the thermal shock response of these two composites as resulting from different damage processes. They suggest that debonding between the fiber and matrix controls the thermal shock behavior of the CVI material while fiber damage is suggested for the polymer derived matrix composite.

Lamicq et al. [8] also evaluated the thermal shock behavior of two-dimensional SiC/SiC composites with a CVI SiC matrix. These materials exhibited a residual strength of 85% following a quench with a  $\Delta T$  of  $300^\circ\text{C}$  with no further decrease up to  $1200^\circ\text{C}$ . Fitzer and Gadov [9] also showed that a composite with unidirectional SiC fibers produced by CVD and a matrix produced by CVI resulted in a thermal shock resistance parameter  $2\frac{1}{2}$  times greater than that of hot-pressed SiC.

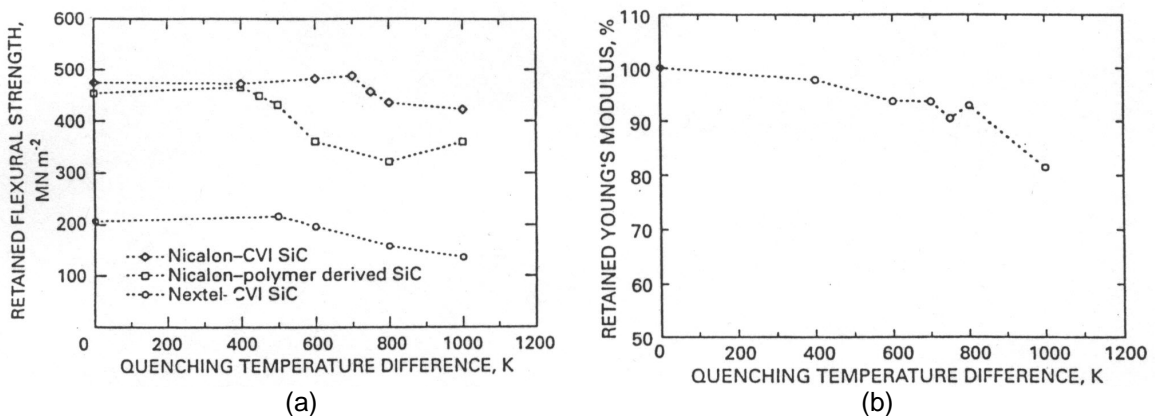


Figure 1. (a) Retained flexural strength v. quenching temperature difference for various continuous fibre reinforced ceramic composites, (b) Effect of quenching temperature difference on retained Young's modulus of Nicalon<sup>TM</sup> fibre-CVI SiC composite.

Quenching from an elevated temperature into water or ice water is the standard method for evaluating the thermal shock of ceramics and ceramic composites; however, this is not prototypical for the heating cycle resulting from a plasma discharge that will result in a  $+\Delta T$  rather than a  $-\Delta T$ . Eckel et al. [10] evaluated the thermal shock behavior of SiC/SiC as a result of a  $+\Delta T$ . They used a  $H_2-O_2$  burner rig with  $\Delta T$  ranging from 1300 to 2300°C. The thermal shock was created by rapid heating in contrast to other reported thermal shock tests where thermal shock was created by rapid cooling. Monolithic SiC failed in 1.5 cycles at a heating rate of 1400°C/s while SiC/SiC composite withstood 25 cycles with a 1700°C/s heating rate with little or no decrease in the tensile strength. A 35% strength loss was noted after 25 cycles with a 1900°C/s heating rate, but this effect was related to erosion and not composite cracking, Figure 2.

In summary, continuous fiber reinforced SiC/SiC composites exhibit excellent thermal shock resistance in both the standard thermal shock test with a  $-\Delta T$  and in a non-standard test conducted by Eckel et al. (8) with a  $+\Delta T$ . The composite material does not exhibit a drastic drop in strength as do monolithic ceramics while they do retain 75% or more of their original strength following  $\Delta T$ 's of up to 1200°C.

#### Models for Thermal Shock Behavior of Ceramic Composites

Thermal stresses in ceramic composites are the result of both the thermal gradient, as with monolithic ceramics, plus the mismatch in thermal expansion between the matrix and fiber. Boccaccini [11] has given the following relationship for a ceramic composite that considers the matrix stress resulting from the thermal gradient and thermal expansion mismatch inducing matrix cracking. There may be some conditions where fiber failure may occur prior to matrix failure although the fibers are stronger than the matrix in most ceramic composites. Also, fiber/matrix interface failure would decrease the strength of the composite but the relationship by Boccaccini [11], Equation 4, does not address this failure possibility.

$$\Delta T_c = (1-\nu) \{ (K_{Ic,m}/2[(r+s)/\pi]^{1/2}) - E_m \Delta \alpha \Delta T_F / [1 + E_m(1-V_f)/E_f V_f] \} / C E_e \alpha_e \quad (4)$$

Where the subscripts m, f and e refer to the matrix, fiber and effective values, V is volume fraction, and C is a non-dimensional constant that is a function of the Biot modulus  $\beta$ , r is the fiber radius, s is the average fiber spacing and  $\Delta T_F$  is the temperature difference between room and the fabrication temperature. The variable  $K_{Ic,m}$  is the matrix fracture toughness.

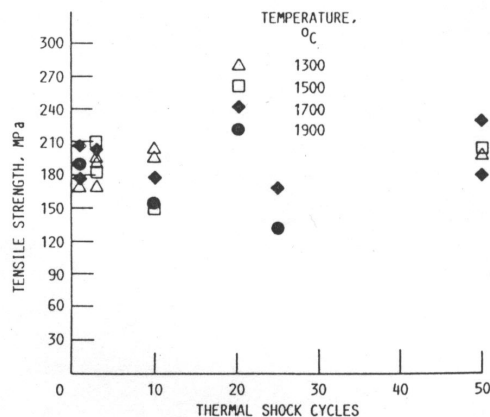


Figure 2. Retained room temperature tensile strength of Nicalon<sup>®</sup>/SiC ceramic composites after thermal shock.

Assuming the values listed in Table 1, Equation 4 predicts a  $\Delta T_c$  of 957K. This value is 200K greater than the 750K reported by Wang and Singh [6,7]. There are several possible factors for this difference: 1) temperature dependence of  $\alpha$ , 2) uncertainty in the  $K_{Ic,m}$  and 3) the  $f(\beta)$  correction as described above. Senor [12] has reported a value for  $\alpha$  of  $3.0 \times 10^{-6} K^{-1}$  for Morton CVD SiC at 25°C and  $4.65 \times 10^{-6} K^{-1}$  at 1100°C. Factoring in the temperature dependence of  $\alpha$  decreases the  $\Delta T_c$  from 957K to 766K a value much closer to that reported by Wang and Singh [6,7]. A fracture toughness value of  $5 \text{ MPa m}^{1/2}$  was used for this calculation but Morton lists a value of  $3.3 \text{ MPa m}^{1/2}$  for CVD-SiC as measured by micro indentation while Carborundum lists a value of  $4.6 \text{ MPa m}^{1/2}$  for Hexaloy SiC using a single edge notch bend specimen. Using the lower value, Equation 4 predicts a  $\Delta T_c$  of 504K. With a fracture toughness of  $5.0 \text{ MPa m}^{1/2}$ , temperature dependence of  $\alpha$  and  $f(\beta)$  considered the calculated  $\Delta T_c$  is 1077K while with a fracture toughness of  $3.3 \text{ MPa m}^{1/2}$ , temperature dependence of  $\alpha$  and  $f(\beta)$  factors considered, the calculated  $\Delta T_c$  is 567K. These values bound the experimental values reported by Wang and Singh [6,7] and show that lower values of  $K_{Ic,m}$  and larger values of  $\alpha$  result in significant decreases in  $\Delta T_c$ .

#### *Radiation Effects on Thermal Shock of SiC/SiC Composites*

There is no experimental data to assess the effects of radiation on thermal shock of SiC/SiC but there is data on the effects of radiation on their physical and mechanical properties. Radiation has been shown to reduce  $E$  and  $\sigma_r$  (13) but to have no effect on  $\alpha$  (14). Recent radiation results for SiC/SiC composites, reinforced with radiation resistant Nicalon Type S fibers, have shown little loss in strength up to 10 dpa but prior work (13), with composites reinforced with Nicalon CG, showed a strength decrease of 50%. This loss in strength was due to two factors: 1) fiber shrinkage induced debonding from the matrix and 2) matrix microcracking during radiation. The value of  $E$  was also noted to decrease with radiation (13) but this decrease was due primarily to matrix microcracking and it is unclear how this will impact the value of  $\Delta T_c$ . One approach to evaluating the effect of the microcracked matrix on thermal shock is to utilize the relationship for crack propagation in the matrix response to thermal shock as described by  $R''$  in Equation 2. This equation shows that  $\Delta T_c$  is inversely proportional to  $\sigma_r^2$  unlike  $R'$  which is directly proportion to  $\sigma_r$ . Use of Equation 2 for  $\sigma_{TS,c}$  in the relationship  $\sigma_m = \sigma_{TS,c} + \sigma_r$  where  $\sigma_m$  is the stress induced in the matrix,  $\sigma_{TS,c}$  is the composite thermal stress and  $\sigma_r$  is the residual stress in the matrix after fabrication. Using the approach by Boccaccini [11] to solve for  $\Delta T_c$  does not result in a valid solution.

Assuming that radiation does not affect  $\alpha$ , reduces  $\sigma_r$  by 50% that translates into a similar decrease in  $K_{Ic,m}$ , that the effect of radiation on  $E$  is through matrix microcracking and fiber

Table 1. Values Assumed for  $\Delta T_c$  Calculation

Parameter	Value
C	0.5
$\nu$	0.3
$E_e$	300 GPa
$\alpha_e$	$3 \times 10^{-6} K^{-1}$
r	$5 \times 10^{-6} \text{ m}$
s	$10 \times 10^{-6} \text{ m}$
$K_{Ic,m}$	$5 \text{ MPa } \sqrt{\text{m}}$

debonding and that thermal shock does not cause further matrix microcracking and fiber debonding, the  $\Delta T_c$ , from Equation 4, of irradiated material will decrease from 957K for unirradiated material to about 300K. This is a three-fold decrease with only a two-fold decrease in the fracture strength. Radiation was shown to decrease the thermal conductivity of SiC by a factor of three (13) but for rapid heating conditions as expected for a plasma discharge where the  $\beta \gg 1$  there will be little effect of thermal conductivity on thermal shock performance.

### Thermal Fatigue Behavior of Ceramic Composites

Thermal fatigue results from stresses induced during thermal cycling. These may be internal stresses or whole body stresses caused by material constraint. Thermal fatigue of materials in a fusion energy system will result from the shut-down/start-up cycles and the temperature change during the cycles. The frequency of these cycles will be determined by the duty cycle of the system and may be low frequency. There have been relatively few studies of the fatigue behavior of CMCs, and most of these have been conducted at high frequencies. Several factors affect the performance of composite materials in cyclic stress applications, for example: (1) compressive stress can cause delamination and microbuckling (15), and (2) tension-tension tests conducted at stresses below the matrix-cracking stress cause little fatigue damage (16). A regime where fiber interface sliding occurs has also been identified by Rouby and Reynaud [17] as causing fatigue damage in tests on 1D SiC/SiC tested at a frequency of 1 Hz and room temperature. Rouby and Reynaud [17] observed an endurance limit at which failure did not occur after 250,000 cycles and a regime where fatigue damage and failure occurred after 5 to 12,000 cycles. The endurance limit observed by Rouby and Reynaud [17] exceeded the matrix-cracking stress by about 30% in contrast to the results of Holmes [16] who observed an endurance limit equal to the matrix-cracking stress.

Kostopoulos et al. [18] measured the high cycle fatigue behavior of a 3D SiC/SiC composite and developed a power-law equation describing the dependence of the number of cycles to failure,  $N_f$ , on the applied stress. The tests were conducted at room temperature in air so there should not be an environmental degradation issue. The tests were conducted at a frequency of 10 Hz and a ratio of minimum to maximum stress, R, of 0.1. A value of  $N_f$  of  $10^9$  cycles corresponds to an applied stress of 85% of the ultimate strength. So clearly, there is little fatigue damage in these materials at room temperature. The following power-law relationship was derived from these results:

$$\sigma_{\text{applied}} / \sigma_{\text{ult}} = a N_f^{-k} \quad (5)$$

where  $\sigma_{\text{applied}}$  is the maximum applied stress during the fatigue test,  $\sigma_{\text{ult}}$  is the ultimate tensile strength of the composite, a is a constant and k is the fatigue strength exponent. Values of a = 2.21 and k = 0.04481 were reported by Kostopoulos et al. [18].

The fatigue behavior at an intermediate loading frequency of 0.25 Hz and at elevated temperature was evaluated by Forio and Lamon [19]. These tests were conducted in air so there is some possibility that there is an environmental effect on Forio and Lamon's [19] results but the material has a B addition to promote the formation of a borosilicate glass to seal the microcracks and protect the fibers and fiber/matrix interface. The tests were conducted at 0.25 Hz, an R value of 0.1 and at 600 and 1100°C. Tests at 1100°C and a maximum stress of 150 MPa resulted in a lifetime of  $4.6 \times 10^4$  cycles while a stress of 220 MPa in a lifetime of  $1.7 \times 10^3$  cycles. The authors report the matrix cracking in the transverse tows occurs at a stress of 150 MPa and matrix cracking in the longitudinal tows at 220 MPa. This change in matrix cracking pattern is likely the cause of the substantial decrease in lifetime with the increase in stress. The elastic modulus decreased by only 12% during the course of the test at 1100°C and a stress of 150 MPa. The composite lifetimes were shorter for tests and the drop in the elastic modulus greater at 600°C relative to 1100°C. For instance, for a maximum stress of 150°C the lifetime at 600°C was only

$1.3 \times 10^4$ . This decrease in lifetime at 600°C is likely the result of the greater viscosity of the borosilicate glass at the lower temperature and therefore, it is less effective in filling in the cracks and protecting the fibers and fiber/matrix interfaces.

Results of low cycle fatigue tests conducted on SiC/SiC at 1100°C in a high-purity Ar environment [20] are shown in Figure 3. This test was conducted at a R value of 0.1 and with 1000 s hold time at load  $f = 10^{-3}$  Hz and 25 cycles at each stress intensity value. Crack velocity decreased with increasing number of load cycles at low stress intensity, as demonstrated by the crack velocities after the first and 25<sup>th</sup> load cycle. This effect was diminished at high stress intensities. The decrease in crack velocity at low stress intensities is understood from observations of decreasing crack velocity as a function of hold time at constant load. This effect results from creep relaxation of the bridging fibers and the resulting increase in the number of fibers bridging the crack. The convergence of the two curves in Figure 3 at high stress intensity results either from fatigue damage with increasing number of cycles or from the fracture of bridging fibers that occurs for either constant or cyclic loads with increasing stress intensities. The crack velocity for the cyclically-loaded specimen is less than that for a statically-loaded specimen over the entire Stage II region. Therefore, it would appear that there was no fatigue damage for this test. Rouby and Reynaud [17] noted that fatigue failure was commensurate with a decrease in the tangential Young's modulus during high-cycle fatigue in 2D SiC/SiC composites. In the results given in Figure 3, the elastic modulus decreased by 20% between the first and last cycle. However, some decrease in modulus is expected as the stress intensity approaches Stage III because of fracture of the bridging fibers. More testing, conducted under constant  $K$  conditions, is required to determine the conditions that induce low-cycle fatigue damage of SiC/SiC at elevated temperatures.

Holmes et. al. [21], measured the cyclic creep or low cycle fatigue behavior of SiC fiber reinforced  $\text{Si}_3\text{N}_4$  at 1200°C for several cycles of creep and recovery times. They found that there were fewer fiber failures when there was a recovery cycle (i.e., the load reduced to  $0.01 P_{\max}$ ) as compared to either static load or cycling without any hold time during the unloaded period. For instance, there were 10% fiber failures for samples loaded 300 s and unloaded 300 s, 30% fiber failures for samples loaded 50 h and unloaded 50 h and 40% fiber failures for sustained loads. They attributed the reduced number of fiber failures to the reduction of fiber stress that occurs during

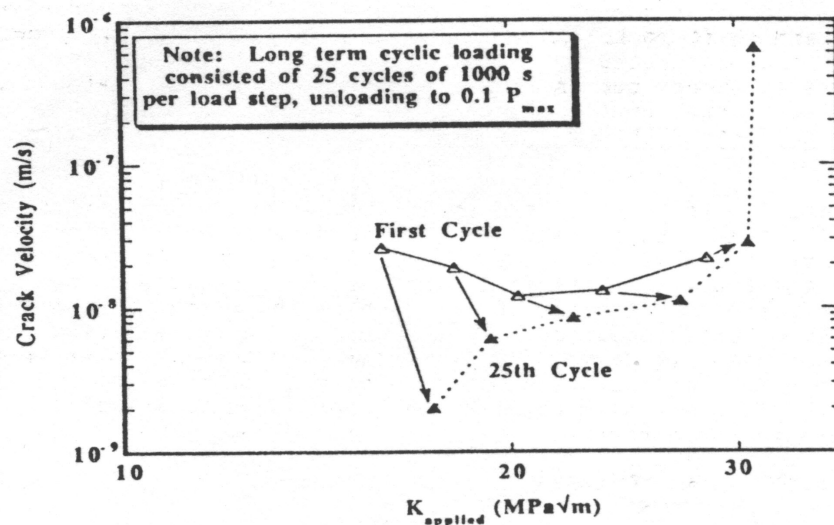


Figure 3. Low cycle fatigue behavior for a SiC/SiC Composite at 1100°C.

the recovery period. The results of Holmes et al. are similar to those of Jones and Henager [20] where the crack growth rates decreased with increasing number of cycles at a given stress intensity. The creep relaxation of the fibers with time and the greater amount of time associated with increasing number of cycles contributed to this decrease.

Wortherm [22] conducted a thermal fatigue test of enhanced SiC/SiC composite material with a temperature change between 600 and 1100°C. A load was also applied to simulate the constraint factor with a stress ratio (minimum to maximum stress) of zero. Both the load and temperature wave forms were triangular with a period of five minutes (frequency of  $3 \times 10^{-3}$  Hz). The stress was applied both in phase with the temperature cycle and 180 out of phase with the temperature cycle. All tests were conducted in laboratory air and in most high-temperature tests of SiC/SiC material, oxidation embrittlement or other environment induced degradation processes dominate the mechanical properties. These degradation processes are not representative of the conditions in a fusion energy system with a high-purity He coolant. However, the results of Wortherm were conducted on enhanced SiC/SiC that contained glass-forming elements that promotes glass formation to protect the fibers from damage by flowing into the matrix microcracks. Coated materials were also evaluated and these samples can also help isolate material behavior from environmental effects. The results of this study showed that the number of cycles to failure,  $N_f$ , decreased with increasing applied stress. Specifically for uncoated material and the stress applied out of phase, the  $N_f$  was 100 at a stress of 150 MPa and 1000 at a stress of 90 MPa. Coated samples had an  $N_f$  about three times higher than the uncoated samples suggesting that environmental effects were a factor in the properties of the uncoated samples. Fitting equation five to this data gives values of  $a = 5.917$  and  $k = 0.2840$ . The larger value of  $k$  for the thermal fatigue results compared to high cycle fatigue results given by Kostopoulos et al. [18] illustrates the larger dependence of the applied stress on the cycles to failure. The room temperature, high cycle fatigue results reported by Kostopoulos et al. [18] exhibited a nearly flat curve of applied stress vs. cycles to failure above about  $6 \times 10^5$  cycles.

The temperature cycle studied by Wortherm [21] is probably not the same as expected in a fusion energy system but the  $\Delta T$  of 500°C may not be too different. Therefore, these results are fairly relevant for a fusion energy system. The proportional limit reported for this material was 60-80 MPa and many designs consider this the limiting stress for these materials. With a maximum stress of 80 MPa the thermal fatigue  $N_f$  is at least 3000 cycles based on the uncoated results and could be 10,000 cycles based on the coated results. Also, a few tests were conducted with a  $\Delta T$  of 600°C with only a small decrease in the  $N_f$ . Therefore, the results of Wortherm [22] and Jones and Henager [20] suggest that thermal fatigue or low-cycle fatigue is not a serious issue for SiC/SiC composites for fusion applications.

## REFERENCES

- [1] H. Wang and R. N. Singh, "Thermal Shock Behavior of Ceramics and Ceramic Composites," Intl. Materials Reviews, Vol 39, No. 6 (1994), p. 228-244.
- [2] D. P. .H. Hasselman, J. Am. Ceram. Soc., 52 (1969) p. 600-604.
- [3] Y. Takeda and K. Maeda, J. Ceram. Soc., Jpn, Intl. 99 (1991) p. 1113-1116.
- [4] W. J. Lee, E. D. Case, Mater. Sci. Eng., A119, (1989), 113.
- [5] T. N. Tiegs, and P. F. Becher: J. Am. Ceram. Soc., (1987), 70, C109-C111.
- [6] H. Y. Wang and R. N. Singh, Ceram. Eng. Sci. Proc., 15 (1994) p. 292-302.
- [7] H. Y. Wang and R. N. Singh, J. Am. Ceram. Soc., 79 (1996) p. 1783-92.

- [8] P. J. Lamicq, G. A. Bernhart, M. M. Dauchier and J. G. Mace, Am. Ceram. Soc., Bull., 65 (1986) p. 336-338.
- [9] E. Fitzer and R. Gadow, Am. Ceram. Soc., Bull., 65 (1986) p. 326-35.
- [10] A. E. Eckel, T. P. Herbell, E. R. Generazio, and J. Z. Gyenkeyesi, Ceram. Eng. Sci. Proc., (1991), 12, p. 1500-1508.
- [11] A. R. Boccaccini, Scripta Mater., Vol. 38 (1998) p. 1211-1217.
- [12] D. Senior, Pacific Northwest National Laboratory, private communication.
- [13] R. H. Jones, D. Steiner, H. L. Heinisch, G. A. Newsome and H. M. Kerch, J. of Nucl. Mater., 245 (1997) p. 87-107.
- [14] G. Youngblood, Pacific Northwest National Laboratory, private communication.
- [15] E. Bakis and W. W. Stinchcomb, in Composite Materials: Fatigue, Fracture, ASTM STP 907, ed. H. T. Hahn, American Society for Testing and Materials, Philadelphia, PA. 1986, p. 314.
- [16] J. W. Holmes, J. Am. Ceram. Soc., 74, (1991) p. 1639.
- [17] D. Rouby and P. Reynaud, in Proc. Conf. On High Temperature Ceramic Matrix Composites held at the 6<sup>th</sup> Eur. Confer. On Composite Materials, Bordeaux, Sept. 20-24, 1993, p. 499.
- [18] V. Kostopoulos, L. Vellios and Y. Z. Pappas, "Fatigue Behavior of 3-d SiC/SiC Composites," J. of Materials Science, 32 (1997) p. 215-220.
- [19] P. Forio and J. Lamon, "Fatigue Behavior at High Temperatures in Air of a 2D SiC/SiC-B-C Composite with Self-Healing Multi-layered Matrix," J. Am. Cer. Soc., in press.
- [20] R. H. Jones and C. H. Henager, Jr., Fusion Reactor Materials Semiannual Progress Report for period ending March 31, DOE/ER-0313/14, 1993, p. 451.
- [21] J. W. Holmes, Y. H. Park, J. W. Jones, J. Am. Ceram. Soc., 76 (1993) p. 1281.
- [22] D. W. Worthem, "Thermomechanical Fatigue Behavior of Coated and Uncoated Enhanced SiC/SiC," presented at 7<sup>th</sup> annual HITEMP Review, 1994, NASA Lewis Research Center, p. 66-1.

## **STRUCTURAL RELAXATION IN AMORPHOUS SILICON CARBIDE**

L. L. Snead and S. J. Zinkle, Metals and Ceramics Division, Oak Ridge National Laboratory, Oak Ridge TN 37830-6138

### **OBJECTIVE**

The objective of this work is to explore the structural relaxation and corresponding physical property changes which occur in amorphous SiC prior to crystallization.

### **SUMMARY**

High purity single crystal and chemically vapor deposited silicon carbide has been amorphized under fast neutron irradiation. The gradual transition in physical properties from the as-amorphized state to a more relaxed amorphous state prior to crystallization is studied. For the three bulk properties studied: density, electrical resistivity, and thermal conductivity, large property changes occur upon annealing between the amorphization temperature and the point of crystallization. These physical property changes occur in the absence of crystallization and are attributed to short, and perhaps medium range ordering during annealing. It is demonstrated that the physical properties of amorphous SiC can vary greatly, and are likely a function of the irradiation state producing the amorphization. The initiation of crystallization as measured using bulk density and in-situ TEM is found to be ~ 875°C, though the kinetics of crystallization above this point are seen to depend on the technique used. It is speculated that in-situ TEM and other thin-film approaches to studying crystallization of amorphous SiC are faulted due to thin-film effects.

### **PROGRESS AND STATUS**

#### **Introduction**

Numerous studies [1-10] have shown that SiC becomes amorphous during ion-beam irradiation at 80-350 K for damage levels of approximately 0.1 to 0.5 dpa (displacements per atom.) The majority of studies relating to SiC amorphization have utilized low-energy (<1 MeV) ion-beams [2-7], with a few researchers studying the amorphization threshold using high energy electrons.[11-14] The effect of irradiation temperature on the critical dose required for amorphization has been studied over the temperature range of 77 to 470 K. It has been shown that the critical dose required for amorphization is a function of the irradiation species, irradiation temperature, and irradiation dose rate. Furthermore, the critical dose for amorphization has been shown to consist of at least three sub-stages (dose jumps),[15] attributed to close-pair recombination of three different point defect configurations. Long-range point-defect migration occurs at temperatures above ~350 K in 2 MeV ion irradiated SiC, and amorphization is not possible, even for high dose (>10 dpa) irradiation at temperature above ~ 425 K. [16]

Mechanical properties such as density, elastic modulus and hardness of amorphized single crystal SiC have been previously estimated from measurements of the surface or buried amorphous layers on the ion beam irradiated material. Specifically, the density has been inferred from surface step height measurements [17-19] or by observing the increase in total range with

---

\*Oak Ridge National Laboratory (ORNL) is operated for the U.S. Department of Energy by UT-Battelle, LLC under contract DE-AC-05-00OR22725.

TEM, [9,10,16,20] or by x-ray techniques [21,22], yielding a density decrease ranging from about -22% to -15%. The residual hardness ( $H_r/H_u$ ) [10,18,19,23] and residual modulus ( $E_r/E_u$ ) [10,23] have likewise ranged in the literature from 45%-70% (relative hardness) and 70-76% (relative modulus.)

In previous work by the authors [24], the ability to amorphize silicon carbide using fast neutrons was demonstrated and this material was used for bulk physical property measurements. Physical property measurement using neutron-amorphized SiC offered the advantage of a bulk sample as compared to making measurements on buried or surface amorphous layer inherent in ion-implantation studies. In this way precise crystalline-to-amorphous property change measurements were possible. Specifically, density was seen to decrease by 10.8%, with residual hardness and modulus ratios of 54% and 55%, respectively.

This paper extends this previous work by studying the relaxation of the amorphous SiC (a-SiC) structure occurring prior to the point of crystallization. Such a structural relaxation process has been observed in thin-film amorphous silicon [25] and recently studied in thin film SiC by Wendler [26].

### **Experimental**

Materials for this study were Cree single-crystal 6-H SiC and Rohm Haas chemically vapor deposited (CVD) SiC, which consists of a very high purity, large grain, highly faulted beta (fcc)

structure. Major impurity concentrations for the CVD SiC, as supplied by the manufacturer for their standard grade of material in weight parts per billion, are: 70-700 N, 30 Na, <34 Mg, 88 S, <40 Fe, <100 Se, 9 Al, <29 Ga, <22 In, Tl<21, 290 B, 28 P and <27 Sb. The Al, Ga, In, Tl and B act as p-type dopants while the P and Sb act as n-type dopants. These materials were irradiated to fluences of 2.6 and 4.0 x 10<sup>25</sup>n/m<sup>2</sup> (E>0.1 MeV) in the target region of the High Flux Isotope Reactor at ORNL. These fluence levels are equivalent to 2.6 and 4 dpa, respectively, using a sublattice-average displacement energy of 40 eV. However, it is noted that there will be greater displacements on the carbon sub-lattice as compared to the silicon sub-lattice. The irradiation temperature was ~70°C. A second set of CVD SiC samples, irradiated to the same fluence in the temperature range of 300-400°C, remained crystalline. Amorphization was determined by bright and dark field imaging and the presence of spot-free, diffuse diffraction patterns. Previous work on the 2.6 dpa material using x-ray diffraction and high resolution TEM (HRTEM) was conducted to determine full amorphization. For the case of the HRTEM, there was a complete absence of structure during attempted lattice imaging.

Annealing of each sample was performed in an air furnace for a 30-minute period followed by a 15-minute cleaning in hydrofluoric acid to remove any surface silica formation. Density was measured at room temperature using a density-gradient-column technique [27] using mixtures of tetrabromomethane and methylene iodide. The accuracy of the measurement was better than 0.001 g/cc and was found to be reproducible in repeated measurements and consistent for duplicate samples. Microscopy was carried out with a Philips CM-12 microscope and a Gatan *in-situ* annealing stage. TEM samples were prepared by conventional thinning and ion milling at 6 keV, 15°, using a liquid-nitrogen-cooled stage. After foil perforation, the specimens were milled at 3 keV, 9° for 10 m at room temperature to reduce surface amorphization associated with the argon implantation. Thermal conductivity was calculated from a flash thermal diffusivity measurement on 6 mm diameter, 10 mm thick specimens. The specific heat of crystalline SiC was assumed. Electrical resistivity was carried out on 1 x 1 x 25 mm bars of CVD SiC using a four-point probe

technique. [28] A Keithley model 238 source measure unit was used to supply the current and a Keithley model 183 sensitive digital micrometer was used to sense the voltage drop. Due to the large change in resistivity of the sample the applied current was varied to ensure Ohmic heating was not affecting the measurement. The applied current range (and accuracy) was 1  $\mu$ A (0.05%) and 1 nA (0.3%.) The accuracy for the potential measurement was < 0.1%. Both irradiated and non-irradiated samples behaved in an Ohmic fashion for all applied current levels.

## **Results and Discussion**

As has been pointed in recent reviews on ion-implantation effects in SiC, [17,22,26] the reported temperature for onset of crystallization in amorphous SiC covers a wide range, from 600°C to 1700°C. Various techniques have been employed to study crystallization including Raman spectroscopy, cross-sectional TEM, and RBS. At first glance, there does not appear to be a material, or technique, dependence responsible for this disparity in crystallization temperature. Figure 1 shows previously published work by the authors [24] on the same single crystal material used in the present study. Dark-field images taken during the in-situ TEM foil annealing of the neutron-amorphized single crystal SiC are shown. At an annealing temperature of 700°C contrast points begin to appear (indicated by white arrows in the left image of the figure.) Using through-focus observation and by using comparative analysis these points were associated with surface contamination and grew slowly, and did not appear to expand through the thickness of the TEM foil. Above ~ 800°C crystallite growth occurred at widely spaced intervals between which large, completely amorphous, areas remained. The middle image of Figure 1 shows an example of the growing “stars “ in the bulk SiC. It was observed that the crystallites grew slowly in the ~800-1100°C temperature range, and that the crystallite growth rate was approximately linear with annealing temperature. However, in the annealing step between 1125 and 1150°C, the crystallization kinetics became very rapid, with both faster growth of the existing crystallites and rapid nucleation of new crystallites throughout the amorphous material. The microstructure taken during the rapid crystal growth is indicated in the right-most image of Figure 1. Following a 30 minute annealing at 1150°C, no evidence of amorphous material was found anywhere in the sample. The diffraction rings of this polycrystalline material were indexed to be beta SiC (fcc).

The crystallization of amorphous SiC shown in Figure 1 does not correspond to crystallization inferred from bulk density measurements given in Figure 2. It is seen (figure 2) that the density of a-SiC increased linearly with annealing above the irradiation temperature (~70°C), and at ~ 885°C a dramatic increase in densification occurs restoring the materials to its original crystalline density of ~ 3.2 g/cc. Full density is achieved by ~ 950°C. Furthermore, high resolution TEM for bulk a-SiC annealed below 800°C finds no evidence of crystallite formation. It can be concluded from this result that the temperature of onset of crystallization during bulk-annealing and in-situ TEM are similar (800-875 K,) but due to thin-film or other effects, a higher temperature is required during in-situ TEM examination for complete crystallization to occur.

The density of the 2.6 and 4.0 dpa neutron-amorphized material was 2.857 and 2.845 g/cc, respectively. In relative terms, the higher dose sample underwent a greater density change, -11.2%, compared to the -10.8% change for the lower dose sample. The room temperature density of the amorphous specimens annealed at temperatures just below the onset of crystallization (~885°C) is ~ 3 g/cc (i.e. ~ 6.3% lower than crystalline SiC.)



The effect of annealing on the electrical resistivity of crystalline and amorphous SiC are given in Figures 3 and 4. The left plot in figure 3 shows the temperature dependence of electrical resistivity for non-irradiated CVD SiC and the electrical resistivity below the amorphization temperature for the a-SiC. For both the non-irradiated and amorphized conditions, the resistivity is seen to follow  $1/T^{1/4}$  dependence, indicative of hopping conduction[39]. Following the analysis performed on a-Si, the defects associated with structural vacancies (dangling bonds) in the random network increases the density of mid-gap states, thus increasing the electrical conductivity, which will be greatly affected by annealing. This is clearly shown in annealing plot of figure 3 which shows the electrical resistivity of a-SiC increasing by  $\sim 3$  orders of magnitude prior to crystallization. It should be noted that upon reaching 885°C, the energy release associated with the crystallization is rapid and sufficient to cause the bulk samples to energetically fracture within the annealing furnace.

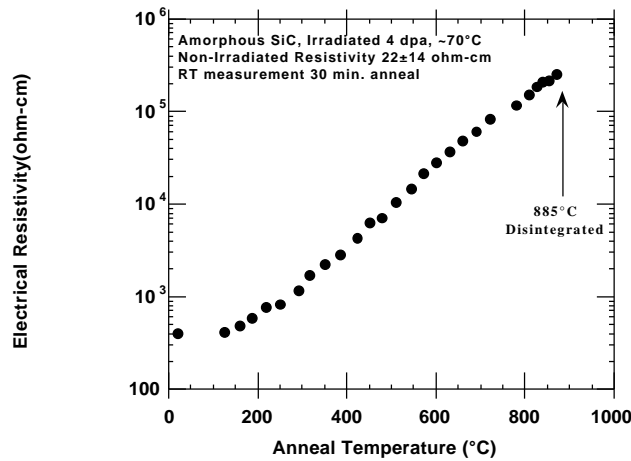
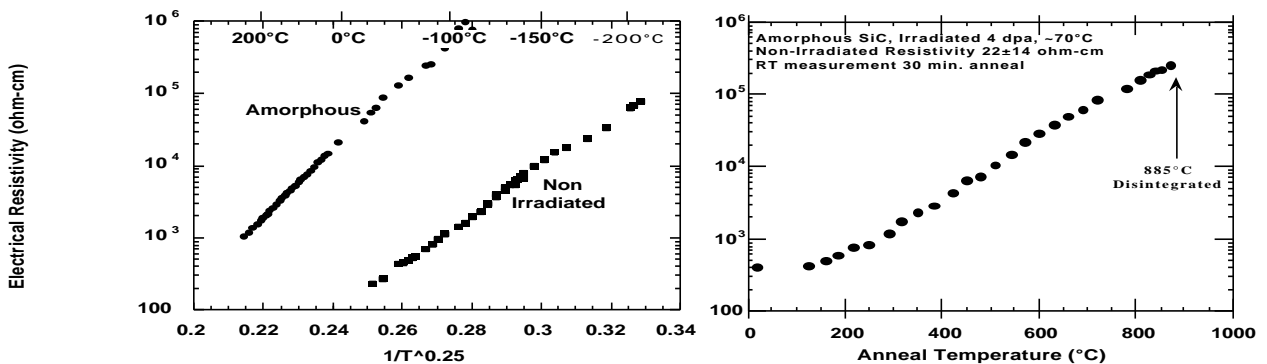
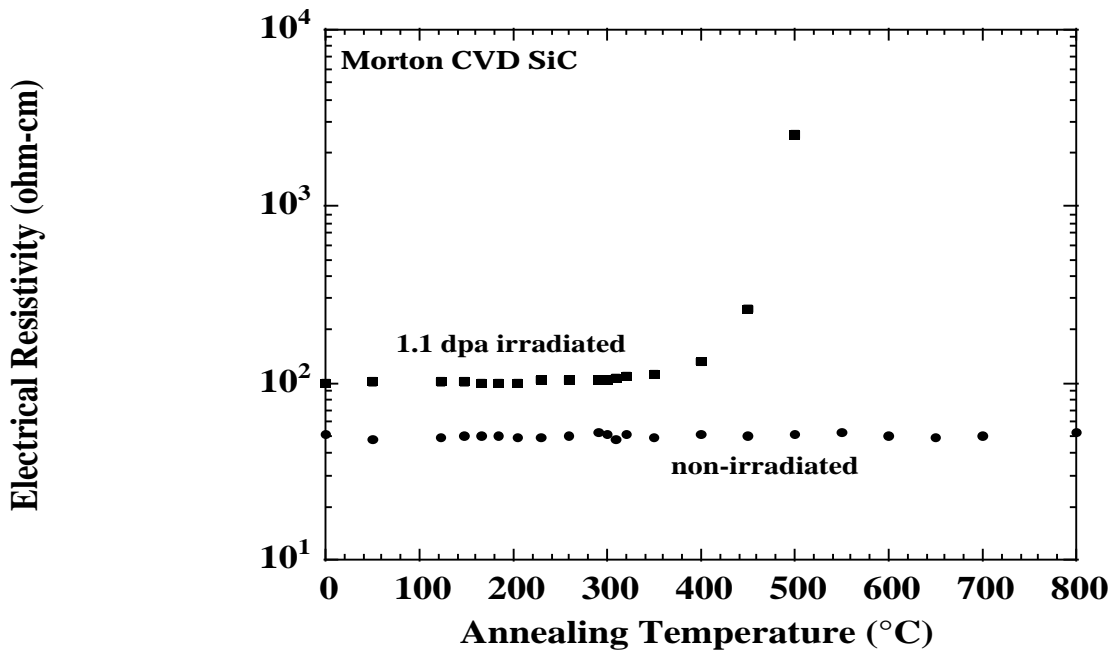


Figure 3. Temperature dependence and the effect of annealing on the electrical resistivity of amorphous SiC.





**Figure 4. Effect of annealing on the room temperature electrical resistivity of 1.1 dpa damaged crystalline CVD SiC.**

The effect of annealing on electrical conductivity of a-SiC can be compared with that of neutron damaged crystalline SiC. Figure 5 shows the electrical resistivity as a function of annealing temperature for CVD SiC, both in the non-irradiated and 1.1 dpa, ~350°C, irradiated condition. The non-irradiated, crystalline material shows constant electrical resistivity of ~50  $\Omega$ -cm following annealing up to 800°C. No change was expected as the processing temperature for CVD SiC is in excess of 1000°C. A small resistivity increase is seen for the 1.1 dpa as-irradiated condition. Several competing factors contribute to the change in the as-irradiated resistivity of crystalline SiC. For example, nuclear transmutation doping will occur, increasing the donor concentration through the  $^{30}\text{Si}(n, \gamma)^{31}\text{Si}$ , and subsequent beta decay to (n-type donor)  $^{31}\text{P}$ . Additionally, 20% of the 290 wppm intrinsic (p-type acceptor) boron would have been removed due to the  $^{10}\text{B}(n, \gamma)^7\text{Li}$  reaction. The elastic collisions between high-energy neutrons and the lattice will also produce simple point defects, increasing the dangling bond density, hence decreasing the material resistivity. Upon annealing of the damaged crystalline SiC, simple point defect migration will remove these dangling bonds increasing the resistivity. From figure 4, the resistivity is seen to asymptotically increase as the annealing temperature exceeds the irradiation temperature, releasing shallowly trapped interstitials or possibly small point defect clusters.

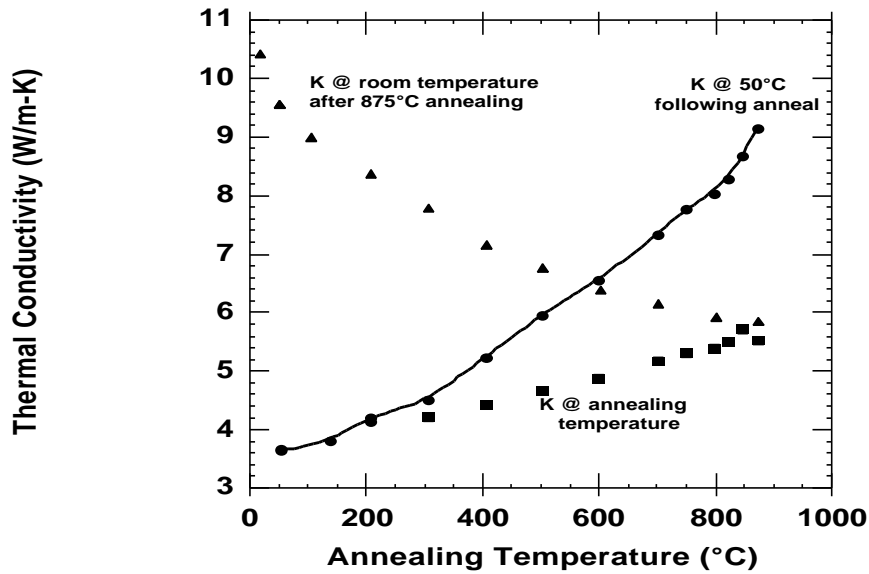


**Figure 5.** Effect of annealing on the thermal conductivity of amorphous SiC. Solid curve represents thermal conductivity at 50°C. Solid squares are thermal conductivity at measurement temperature. Solid triangles are room temperature thermal conductivity following 875°C anneal.

The thermal conductivity of a-SiC measured at 50°C is also seen to dramatically increase with annealing temperature. Figure 5 shows an increase from an as-amorphized value of 3.6 W/m-K to 9.1 W/m-K following annealing up to 875°C. Following each annealing step, the thermal conductivity was measured during cool down and is plotted at the annealing temperature (solid squares in Figure 5.) The room temperature thermal conductivity at the most relaxed state (following the 875°C anneal) is also shown. At 885°C the sample energetically fractured into small pieces. It is interesting to note that the room temperature thermal conductivity in the most relaxed state for a-SiC (~10 W/m-K following the 875°C anneal) is nearly identical to the saturation value for CVD SiC irradiated above the critical temperature for amorphization (i.e. still crystalline.) The non-irradiated room temperature thermal conductivity for the CVD SiC in this study is 333 W/m-K. Irradiation at 300°C appears to reach saturation thermal conductivity by 0.1 dpa at a value of 11 W/m-K. However, the density of the most relaxed a-SiC (~3.0 g/cc after annealing at ~865°C) is substantially less than the highly damaged crystalline material (3.16 g/cc.) In both materials, the temperature dependence of thermal conductivity indicates that phonons are the primary thermal transport mechanism (also obvious from the electrical resistivity data shown in figure 3.) For crystalline materials, vacancies and their associated strain fields substantially reduce thermal conductivity. Upon annealing of the damaged crystalline material, thermal conductivity is increased substantially. The mechanism behind the recovery process of thermal transport for both the amorphous and damaged-crystalline SiC is similar. For the crystalline material, vacancies and their associated strain fields are reduced as interstitials become mobile. In the case of the amorphous material, the local perturbation in the strain field associated with distorted, or non-existent, bonds act as phonon scattering centers. Clearly, increasing the short-range order in the a-SiC during annealing will reduce phonon-defect interaction and increase thermal conductivity as seen in Figure 5.

## CONCLUSIONS

The as-amorphized density of silicon carbide is seen to depend on applied dose and to be function of post-irradiation annealing temperature. This suggests an irradiation-temperature dependence of density (as well as electrical and thermal properties.) Annealing of the amorphous SiC above the amorphization temperature leads to an increase in the bulk amorphous density of ~5%, reaching a value of ~ 3 g/cc at ~ 885 °C, at which point the structure explosively crystallizes. The densification of the amorphous SiC is attributed to annealing out local strain in the amorphous network similar to that seen in amorphous Si. Results on the increase in electrical resistivity and decrease in thermal conductivity of the amorphous SiC during annealing further reinforce this point. Specifically, annealing strained local bonds, or completing the local bonding will reduce the density of mid-gap states increasing electrical resistivity while a reduction in phonon-scattering vacancies (or a reduction in the local strain in the amorphous network) act to enhance thermal conductivity.

## REFERENCES

- [1] D.P. White, J. Appl. Phys 73 (1993) 2254.
- [2] R.R. Hart, H.L. Dunlap, O.J. Marsh, Radiat. Eff. 9 (1971) 261.
- [3] J.M. Williams, C.J. McHargue, B.R. Appleton, Nucl. Instrum and Meth. 209/210 (1983) 317.
- [4] J.A. Spitznagel, S. Wood, W.J. Choyke, N.J. Doyle, J. Bradshaw, S.G. Fishman, Nucl. Instrum. Meth. in Phys. Res. B16 (1986) 237.
- [5] J.A. Edmond, R.F. Davis, S.P. Withrow, K.L. More, J. Mater. Res. 3 (1988) 321.
- [6] N.G. Chechenin, K.K. Bourdelle, A.V. Suvorov, A.V. Suvorov, A.X. Kastilio-Vitloch, Nucl. Instrum. and Meth. in Phys. Res. B65 (1992) 341.
- [7] L.L. Horton, J. Bentley, L. Romana, A. Perez, C.J. McHargue, J.C. McCallum, Nucl. Instrum. Meth. in Phys. Res. B65 (1992) 345.
- [8] W.J. Weber, L.M. Wang, N. Yu, H.J. Hess, Mat. Sci. Eng. A253 (1998) 62.
- [9] L.L. Snead, S.J. Zinkle, in: MRS Symposium on Microstructure of Irradiated Materials eds. I.M. Robertson et al., vol. 373 (MRS, Pittsburgh, 1995) p. 377.
- [10] W.J. Weber, N. Yu, L.M. Wang, N.J. Hess, J. Nucl. Mat. 244 (1997) 258.
- [11] H. Inui, Phil. Mag. B 65 (1992) 1.
- [12] H. Inui, H. Mori, T. Sakata, Phil. Mag. B 66 (1992) 737.
- [13] H. Inui, H. Mori, H. Fujita, Phil. Mag. B 61 (1990) 107.
- [14] A. Matsunaga, C. Kinoshita, K. Nakai, Y. Tomokiyo, J. Nucl. Mater. 179-181 (1991) 457.
- [15] L.L. Snead, To be published (2001).
- [16] L.L. Snead, S.J. Zinkle, in: Microstructure Evolution During Irradiation eds. I.M. Robertson et al., MRS Symposium Proceedings vol. 439 (Materials Research Society, Pittsburgh, 1997) p. 595.
- [17] C.J. McHargue, J.M. Williams, Nucl. Instrum. Meth. in Phys. B80/81 (1993) 889.
- [18] C.J. McHargue, G.C. Farlow, C.W. White, J.M. Williams, B.R. Appleton, H. Naramoto, Mat. Sci. Eng. 69 (1985) 123.
- [19] C.J. McHargue, C.S. Yust, J. Amer. Ceram. Soc. 67 (1984) 117.
- [20] J. Bentley, L.J. Romana, L.L. Horton, C.J. McHargue, in: eds. G.S. Was, L.E. Rehn, D.M. Follstaedt, in: Phase Formation and Modification by Beam-Solid Interactions, Materials Research Soc., 1992 p. 363.
- [21] W. Bolse, J. Conrad, T. Rodle, T. Weber, Surf. Coat. Techn. 74-75 (1995) 927.
- [22] V. Heera, J. Stoemenos, R. Kogler, W. Skorupa, J. Appl. Phys. 77 (1995) 2999.
- [23] C.J. McHargue, D.L. Joslin, J.M. Williams, Nucl. Instrum. Meth. B 46 (1990) 185.

- [24] L.L. Snead, S.J. Zinkle, J.C. Hay, M.C. Osborne, Nucl. Instrum. Meth. in Phys. Res. B 141 (1997) 123.
- [25] U. Zammit, K.N. Madjusoodanan, F. Scudieri, F. Mercuri, Phys. Rev. B 49 (1994) 2163.
- [26] E. Wendler, A. Heft, W. Wesch, Nucl. Instr. Meth. B 141 (1998) 105.
- [27] ASTM., D1505-85. Standard Test Method for Density of Plastics by Density Gradient Technique. 1985.
- [28] ASTM., B 193-87 Standard Test Method for Resistivity of Electrical Conductor Materials.
- [29] W. Jiang, W.J. Weber, S. Thevuthasan, D.E. McCready, Surface and Interface Analysis 27 (1999) 179.
- [30] G.N. VanDenHoven, Z.N. Lang, L. Neisen, Phys. Rev. Lett. 68 (1992) 3714.
- [31] W.C. Sinke, T. Warabisaco, M. Miyao, T. Tokuyama, S. Roorda, F. Saris, J. Noncrys. Sol. 99 (1988) 308.
- [32] S. Roorda et al., Phys. Rev. B 44 (1991) 3702.
- [33] C.N. Waddell, W.G. Spitzer, J.E. Friedrichson, G.K. Hubler, T.A. Kennedy, J Appl. Phys. 44 (1984) 4361.
- [34] S. Roorda, S. Doorn, W.C. Sinke, O.M.L.O. Scholte, E.v. Loenen, Phys. Rev. Lett 62 (1989) 1880.
- [35] E.P. Donovan, F. Spaepen, J.M. Poate, D.C. Jacobson, Appl. Phys. Lett. 55 (1989) 1516.
- [36] G. Muller, S. Kalbitzer, Phil. Mag. B38 (1978) 241.
- [37] S. Coffa, F. Priolo, J.M. Poate, S.H. Glarum, Nucl. Instrum. Meth. Res. B80/81 (1993) 603.
- [38] S. Coffa, J.M. Poate, D.C. Jacobson, W. Frank, W. Gustin, Phys. Rev. B45 (1992) 8355.
- [39] N.F. Mott, E.A. Davis, Electronic Processes in Non-crystalline Materials, Oxford Univ. Press, Oxford, 1979.

**AN UPDATE ON THE KFIB EXPERIMENT** – G. E. Youngblood and R. H. Jones (Pacific Northwest National Laboratory)\*, W. Kowbel (MER Corporation), Paul de Heij (NRG Petten) and Akira Kohyama (Kyoto University).

## **OBJECTIVE**

The primary objective of the experiment called “KFIB” is to assess the thermal conduction (**K**) properties of several advanced SiC **FIB**ers before and after irradiation. The thermal conductivity of SiC/SiC composites made from these fibers (with various SiC-type matrices and architectures) will also be measured before and after irradiation. Models used to predict the transverse and in-plane thermal conductivity of these composites as a function of temperature and dose also will be assessed.

## **SUMMARY**

An updated sample test matrix for the KFIB experiment is presented. The pre-irradiation test results for all fiber and SiC/SiC composite materials included in the test matrix, presented at the 4<sup>th</sup> IEA Workshop on SiC/SiC for Fusion Structural Applications held in Frascati, Italy, October 12-13, 2000, are reviewed. The KFIB samples have been delivered for capsule loading. They are scheduled to be irradiated from October-November, 2001 through April-May, 2002 to similar doses (2-4 dpa-SiC) in the ATR (Idaho Falls) at 300°C and the HFR (Petten) at 625 and 975°C. To assess irradiation enhanced creep (IEC) in SiC fibers, a bend stress relaxation module was added to the HFR sample matrix at each irradiation temperature.

## **PROGRESS AND STATUS**

The KFIB experiment is coordinated at the Pacific Northwest National Laboratory (PNNL), but involves several other organizations who have furnished materials, materials analysis or irradiation facilities for the experiment [1].

### *Irradiation Tests and Schedule*

Two irradiation tests are planned. A low temperature irradiation test will take place in the ATR reactor at 300°C to a dose of 3.6 dpa-SiC. A moderate and a high temperature irradiation test will take place in the HFR Petten reactor at 625°C and 975°C to a dose of about 2.5 dpa-SiC. Both irradiations will commence in October-November, 2001 and will be completed by April-May, 2002. Post-irradiation examinations (PIE) will be carried out in late 2002.

### *Sample Test Matrix*

Preliminary KFIB sample test matrices have been reported [1-2]. However, two types of SiC/SiC composite bend bars and two fiber bend stress relaxation modules recently were added to the HFR Petten sample test matrix. An updated KFIB sample test matrix is given in Table 1.

---

\*Pacific Northwest National Laboratory (PNNL) is operated for the U.S. Department of Energy by Battelle Memorial Institute under contract DE-AC06-76RLO-1830.

**Table 1. Updated KFIB sample test matrix (7/31/01)**

<b>Uniaxial Fiber + Ceraset™ Discs</b> (6.2 mm dia x 2.0 mm thk)	<b>HFR Petten</b> <b>(625°C and 975°C)</b>	<b>ATR</b> <b>(300°C)</b>
Hi-Nicalon <sup>1</sup> (parallel)	4	2
Hi-Nicalon <sup>1</sup> (perpendicular)	2	2
Tyranno SA-3 <sup>2</sup> (parallel)	4	2
Hi-Nicalon Type S <sup>1</sup> (parallel)	4	2
Amoco K1100 graphite <sup>3</sup> (parallel)	0	2
<b>SiC/SiC Composite Discs</b> (6.2 mm dia x 2.0 mm)		
2D-Nicalon S/4xC-SiC multilayers/CVI-SiC <sup>4</sup>	6	4
3D-Nicalon S/PIP - Ceraset™ 1400C <sup>5</sup>	4	4
2D-8HS SA-Tyrannohex HP (100% transverse) <sup>2</sup>	4	3
2D-8HS SA-Tyrannohex HP (50% transverse) <sup>2</sup>	0	2
2D-5HS Nicalon S/150 nm PyC/CVR-PIP SiC <sup>6</sup>	6	0
<b>SiC/SiC Bend Bars</b> (30 mm x 6 mm x 2 mm)		
2D-PW Dupont Hi Nic/150 nm PyC/CVI-SiC <sup>7</sup>	8	0
2D-5HS Nicalon S/150 nm PyC/CVR-PIP SiC <sup>6</sup>	3	0
<b>High-Purity CVD-SiC - Reference</b>		
CVD-SiC (6.0 mm dia x 2.5 mm discs) <sup>8</sup>	5	3
CVD-SiC (25.5 mm long x 1.85 mm sq. bars) <sup>8</sup>	4	0
<b>Fiber Bend Stress Relaxation Modules</b>		
Tyranno SA-3 (10 μm dia) <sup>2</sup>	3	0
Hi-Nicalon S (13 μm dia) <sup>1</sup>	3	0
Textron 2-mill (50 μm dia) <sup>9</sup>	2	0

<sup>1</sup>Nippon Carbon Co., Yokohama, Japan

<sup>2</sup>Ube Industries Ltd., Ube City, Japan

<sup>3</sup>Amoco Corp., USA

<sup>4</sup>Hypertherm High Temperature Composites, Inc., Huntington Beach, CA

<sup>5</sup>JAERI, Tokai-mura, Japan

<sup>6</sup>MER Corp., Tucson, AZ

<sup>7</sup>Dupont Lanxide Composites, Newark, DE

<sup>8</sup>Rohm and Haas (formerly Morton Advanced Materials), Woburn, MA

<sup>9</sup>Textron Specialty Materials, Lowell, MA

The Hi-Nicalon™ and Hi-Nicalon™ Type S SiC fibers were fabricated by the Nippon Carbon Co. using an electron-beam radiation curing process [3]. The Hi-Nicalon™ fiber has excess C (C/Si = 1.39), while the Type S fiber is nearly stoichiometric SiC (C/Si = 1.05). The Tyranno™ SA-3 fiber, also nearly stoichiometric SiC, was fabricated by Ube Industries Ltd. using an oxidative curing process and high temperature (1800°C) sintering. It is noted that the tested Tyranno™ SA-3 fiber, a new smaller diameter version of Tyranno™ SA, has improved thermal creep and high temperature strength compared to the Tyranno™ SA fiber [4]. The Amoco K1100™ graphite fiber is pitch-derived and given a high temperature treatment so that highly graphitic platelets preferentially align parallel to the fiber axis to optimize the axial thermal conductivity [5]. MER currently is developing a composite design that uses stitched bundles of K1100™ graphite fiber in the z-direction to improve the transverse thermal conductivity of a 2D-SiC/SiC composite [6].

To determine the thermal conductivity of advanced SiC or graphite fibers, a composite rod (7-mm dia. x 20 mm) was constructed with uniaxially aligned fibers in an amorphous Ceraset™ matrix. As discussed previously, several discs were sliced from each rod for

thermal diffusivity measurements [1-2]. Irradiation enhanced creep (IEC) will be assessed for two small diameter polymer-derived SiC fibers (Hi-Nicalon™ type S and Tyranno™ SA-3) and a SiC fiber made by chemical vapor deposition (Textron™ 2-mill) by a bend stress relaxation (BSR) test [7].

The unirradiated properties and the rationale for examining the thermal conductivity of the various SiC/SiC composite types listed in Table 1 were presented previously [1-2]. Several bars and thermal diffusivity discs made from monolithic CVD-SiC were included in the KFIB sample matrix as reference materials [8]. Two types of SiC/SiC composite bend bars were added to the HFR sample matrix: (1) 2D-5HS Nicalon S/150 nm PyC/CVR-PIP SiC, a material made by MER using a satin weave (5HS) Hi-Nicalon type S fabric with a hybrid matrix that combines a chemical vapor reaction (CVR) and a polymer infiltration and pyrolysis (PIP) process, and (2) Hi-Nicalon PW/150 nm PyC/CVI-SiC, a material made by Dupont Lanxide with a plain weave (PW) Hi-Nicalon fabric, a thin 150 nm PyC fiber coating and a chemical vapor infiltration (CVI) matrix (the so-called SiC/SiC composite reference material). The latter material has already been examined extensively in helium swelling experiments [9], and is included in the ongoing JUPITER 14J irradiation experiment [10].

#### *Thermal Conductivity Analysis*

The effective thermal conductivity of a composite fiber disc,  $K_{\text{eff}}$ , is determined from:

$$K_{\text{eff}} = \alpha_{\text{eff}} \cdot \rho_{\text{bulk}} \cdot C_p \quad (\text{W/mK}) \quad [1]$$

where  $C_p$  is the calculated heat capacity and  $\alpha_{\text{eff}}$  and  $\rho_{\text{bulk}}$  are the measured thermal diffusivity and bulk density values, respectively. In cases where the sample consisted of two phases, the heat capacity was calculated by a rule of mixtures. For those cases, the following analytic expressions were derived to fit heat capacity data from the literature for SiC and graphite [11] and the Hi-Nicalon™ fiber composition [12]:

$$C_p(\text{SiC}) = 1.0337 + 0.0001949(T) - 36,582/T^2 \quad (\text{J/gK}) \quad [2a]$$

$$C_p(\text{graphite}) = 1.8256 + 0.0002943(T) - 356.3/T \quad (\text{J/gK}) \quad [2b]$$

$$C_p(\text{Hi-Nic}) = 1.0549 + 0.0002367(T) - 39,361/T^2 \quad (\text{J/gK}) \quad [2c]$$

A parallel conduction model was assumed for the fiber disc with uniaxially aligned fibers in an amorphous Ceraset matrix:

$$K_{\text{eff}} = f_f K_f + f_m K_m \quad [3]$$

where  $f_f$  and  $K_f$  are the volume fraction and the thermal conductivity values for the fiber (f) and matrix (m) constituents, respectively. The uniaxial composite discs were purposely made with a high fiber packing fraction so that  $f_m < f_f$ ; and the Ceraset matrix was cured at only 1100°C to preserve its amorphous microstructure so that  $K_m < K_f$ . Therefore, the  $f_m K_m$  term in Eq. [3] is only a small correction term.

From Eq. [3],  $K_f$ -values were estimated up to 1000°C, and the fiber thermal diffusivity ( $\alpha_f$ ) was calculated from:

$$K_f = \alpha_f \cdot \rho_f \cdot C_f \quad [4]$$

where  $\rho_f$  and  $C_f$  are the fiber density and heat capacity values as a function of temperature, respectively.

The laser flash technique for measuring the thermal diffusivity and calculating the thermal conductivity via Eq. [1] assumes that the disc sample is homogeneous among other things [13]. The technique has also been demonstrated to be appropriate for randomly dispersed and continuous fiber-reinforced composites under certain conditions [14]. The relative dimensional and thermal conductivity values of the composite constituents set these conditions. They require that local perturbations from a uniform one-dimensional temperature gradient through the disc sample are not too severe. This will occur if the time constant for lateral heat conduction between the constituents is much smaller than the time constant for axial conduction through the sample. As demonstrated by Lee [14], the largest error expected when using the composite technique for determining the thermal conductivity of fine diameter fibers is due to the difficulty in accurately determining the fiber volume fraction term in Eq. [3].

### Results

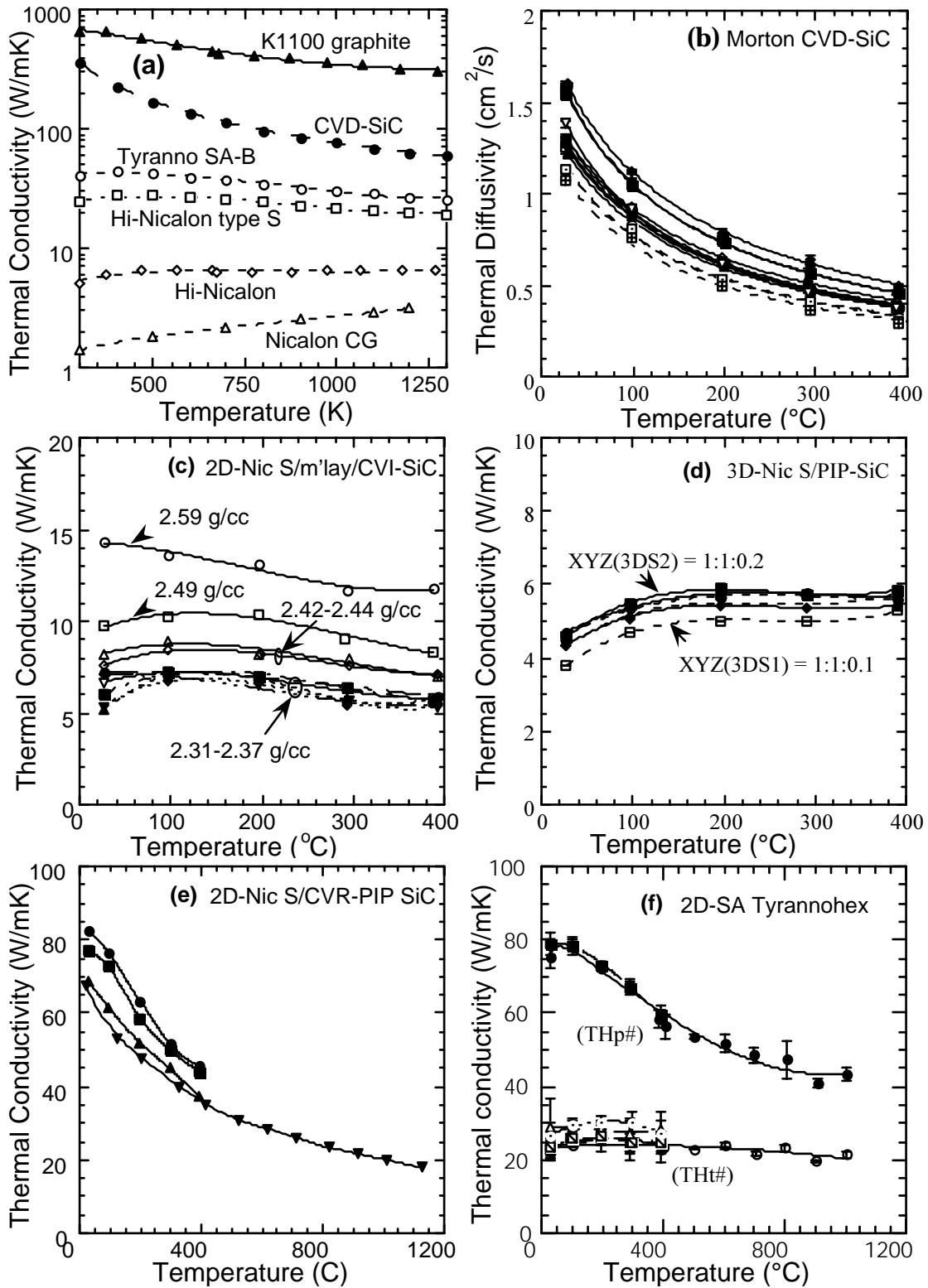
Example base-line thermal diffusivity and conductivity values for unirradiated fiber disc and composite samples are presented in Figures 1(a-f)<sup>1</sup>.

In Figure 1a, the calculated  $K_f$ -values for all the fibers included in the KFIB test matrix are compared to the  $K$ -values for CVD-SiC. For completeness, the  $K_f$ -values for the Nicalon™ CG fiber taken from the literature were added to the figure. The  $K_f$ -values cover three orders of magnitude, with the  $K_f$ -values for the Tyranno™ SA-3 and Hi-Nicalon™ type S being the highest for the SiC fibers; and the  $K_f$ -values for the K1100™ graphite fiber being considerably higher than CVD-SiC  $K$ -values. It is expected that  $K_{eff}$  for SiC/SiC composites made with the Tyranno™ SA-3 or Hi-Nicalon™ type S fibers would exhibit higher thermal conductivity values compared to often tested SiC/SiC made with Nicalon™ CG or even Hi-Nicalon™ fibers. The data also suggest that the anisotropic, but highly conductive K1100™ graphite fiber might be used to boost the thermal conductivity of SiC/SiC composites in special applications, as MER is attempting to do.

In Figure 1b, the thermal diffusivity of the 13 different CVD-SiC samples are shown for the RT-400°C range. The different curves exhibit characteristic  $1/T$  temperature dependence, but also a scatter ( $\pm 20\%$ ) between each other. Even though many of the discs were cut from the same plate, the  $\pm 20\%$  spread in  $\alpha$ -values illustrates the importance of monitoring changes in diffusivity for the same sample before and after irradiation to properly assess degradation due to radiation effects.

In Figure 1c, the transverse thermal conductivity values for ten different samples of the 2D-Nicalon™ S/C-SiC multilayer/CVI-SiC are presented. The  $K$ -values are distributed over a wide range between 5-14W/mK. The samples with higher bulk density values, ranging from

<sup>1</sup> Figure 1(a-f) – next page: (a) Comparison of the axial thermal conductivity for several fiber types with the thermal conductivity of CVD-SiC, (b) The measured thermal diffusivity of 13 unirradiated CVD-SiC samples, (c) The thermal conductivity of unirradiated 2D-Nicalon S/multilayer/CVI-SiC KFIB samples, (d) The thermal conductivity of unirradiated 3D-Nicalon S/PIP-SiC KFIB samples, (e) The thermal conductivity of 2D-Nicalon S/CVR-PIP SiC KFIB samples, and (f) The thermal conductivity of 2D-SA Tyrannohex KFIB samples for two orientations – in plane (upper curves) and transverse (lower curves).



2.31 up to 2.59 g/cc as labeled on the curves, exhibited higher K-values. All samples with densities less than 2.5 g/cc exhibited K-values less than 10 W/mK at ambient. These limited results suggest that achieving high quality composite by the CVI-method might be more difficult when multilayer coatings are used.

In Figure 1d, the thermal conductivity values for six samples of the 3D-Nicalon™ S/PIP-SiC composite are presented. The K-values all fall within a narrow range of about 5-6 W/mK and are similar for the composites made with either 0.1 or 0.2 relative fiber volume fraction in the z-direction. The PIP-SiC matrix for these composites was cured at 1400°C, a temperature too low to enhance the composite thermal conductivity by crystallizing the matrix.

In Figure 1e, the thermal conductivity values for four samples of the 2D-Nicalon™ S/CVR-PIP composite are presented. The K-values averaged about 75 W/mK at ambient, and slightly exceeded 20 W/mK at 1000°C. The high K-values were obtained after giving the composite a HTT of 1800°C, which was sufficiently high to crystallize the matrix. However, to retain composite mechanical properties the SiC fiber must be thermally stable at such a high HTT.

In Figure 1f, the measured K-values are presented for samples of hot-pressed 2D-SA Tyranno™ composite cut so that the fibers were aligned with two different orientations. The two THp# samples had 50% of the fibers parallel and the other 50% transverse to the heat flow direction; and the K-values ranged from about 80 W/mK at ambient down to 42 W/mK at 1000°C. However, the seven THt# samples had 100% of the fibers transverse to the heat flow direction; and the K-values ranged from only 25 W/mK at ambient down to 21 W/mK at 1000°C for this group. Two reasons account for the large differences in K-values for these two groups with different fiber orientations. The thermal conductivity of the Tyranno™ SA fibers is quite high (64 W/mK at ambient [4]), so contributes significantly to  $K_{\text{eff}}$  for the THp# samples with conduction along 50% of the fibers. On the other hand, the THt# samples contain no fibers parallel to the heat flow direction and approximately twice as many transverse interfacial layers as the THp# samples. Apparently, the numerous 50-100 nm thick carbon interlayers that formed between the SA Tyranno fibers during the hot-pressing effectively act as thermal barriers and significantly contribute to lowering the transverse K-values for the THt# samples [15].

## **FUTURE WORK**

The thermal conductivity for several types of advanced SiC fibers and for a highly oriented graphite fiber will be analyzed before and after irradiation. Similar analyses will be performed for composites made with these fibers by using appropriate thermal conductivity models. The results should be available by late-2002.

## **ACKNOWLEDGMENTS**

This work is a joint effort funded by the U.S. DOE Office of Fusion Energy Sciences and the Japan Monbusho fusion materials program. Also, part of this work is being supported by a DOE-SBIR, Phase I (Contract DE-FG03-99ER82823) with the MER Corporation, Tucson, AZ. George Newsome, at the Knolls Atomic Power Laboratory (Schenectady, NY), is managing the capsule loading and irradiation in the ATR reactor. Paul de Heij, at NRG Petten (the Netherlands), is managing the capsule loading and irradiation in the HFR reactor.

**REFERENCES**

- [1] G. E. Youngblood, D. J. Senor, R. H. Jones, W. Kowbel, and Akira Kohyama, "The KFIB Experiment," p. 102 in Fusion Materials Semiannual Progress Report (FMSPR) for period ending June 30, 2000 (DOE/ER-0313/28).
- [2] G. E. Youngblood, R. H. Jones, W. Kowbel, Reiji Yamada, Paul de Heij, Toshihiro Ishikawa and Akira Kohyama, "The KFIB Fiber Thermal Conductivity Experiment," presented at the 4<sup>th</sup> IEA Workshop on SiC/SiC Ceramic Matrix Composites for Fusion Structural Applications, Frascati, Italy, October 12-13, 2000.
- [3] M. Takeda, J. Sakamoto, Y. Imai, H. Ichikawa and T. Ishikawa, "Properties of Stoichiometric Silicon Carbide Fiber Derived from Polycarbosilane," *Ceram. Eng. Sci. Proc.* 15(4), 133-41 (1994).
- [4] K. Kumagawa, H. Yamaoka, M. Shibuya and T. Yamamura, "Fabrication and Mechanical Properties of Improved Si-M-C-(O) Tyranno Fibers," *Ceram. Eng. Sci. Proc.* 19(3), 65-72 (1998).
- [5] Jean-Baptiste Donnet, Serge Rebouillat, Tong Kuan Wang and Jimmy C. M. Peng, p. 149 in *Carbon Fibers*, 3<sup>rd</sup> Ed., Marcel Dekker, Inc., New York, NY, 1998.
- [6] W. Kowbel, "Hybrid 3D SiC/C High Thermal Conductivity Composites," U.S. DOE Phase II SBIR for FY 2000, issued to MER Corp., Tucson, AZ.
- [7] G. E. Youngblood, R. H. Jones, G. N. Morscher and Akira Kohyama, "Creep Behavior for Advanced Polycrystalline SiC Fibers-II, p. 81 in FMSPR for period ending June 30, 1997 (DOE/ER-0313/22).
- [8] D. J. Senor, G. E. Youngblood, D. V. Archer and C. E. Chamberlin, "Recent Progress in Thermal Conductivity Testing of SiC-based Materials for Fusion Reactor Applications," p. 102 in the Proceedings of the Third IEA Workshop on SiC/SiC Ceramic Composites for Fusion Structural Applications, January 29-30, 1999, Cocoa Beach, FL.
- [9] A. Hasegawa, S. Nogami, S. Ohtsuka, K. Abe, R. H. Jones, B. M. Oliver and G. E. Youngblood, "Helium Effects in SiC and SiC/SiC," p. 152, *ibid.*
- [10] G. E. Youngblood, R. H. Jones, Akira Kohyama, Yutoi Katoh, Akira Hasegawa, Reinhard Scholz and Lance Snead, "The HFIR 14J SiC/SiC Composite and SiC Fiber Collaboration," p. 115 in FMSPR for period ending December 31, 1998 (DOE/ER-0313/24).
- [11] Y. S. Touloukian and T. Makita, "Specific Heat," vol. 6 in *Thermophysical Properties of Matter- The TPRC Data Series*, Plenum Publishing Co., New York, NY (1970).
- [12] G. E. Youngblood, R. H. Jones, D. J. Senor, W. Kowbel, J. Webb and Akira Kohyama, "The Thermal Conductivity of SiC and C Fibers," p. 113 in FMSPR for period ending December 31, 1999 (DOE/ER-0313/27).
- [13] J. F. Kerrisk, "Thermal Diffusivity of Heterogeneous Materials – Limits of the Steady-State Approximation," *J. Appl. Phys.*, 43(1), 112-117 (1972).

[14] Hung Joo Lee, "Thermal Diffusivity in Layered and Dispersed Composites," PhD Thesis, Purdue University, May 1975.

[15] G. E. Youngblood, D. J. Senior, R. H. Jones and Samuel Graham, "The Transverse Thermal Conductivity of 2D-SiC/SiC Composites," p. 109 in FMSPR for the period June 30, 2000 (DOE/ER-0313/28).

## **STRENGTH AND DIMENSIONAL CHANGE OF NEUTRON-IRRADIATED HIGH-QUALITY 3D CARBON FIBER COMPOSITE** - L. L. Snead, T. D. Burchell, and A. L. Qualls, Oak Ridge National Laboratory\*

### **OBJECTIVE**

The objective of this work is to gain understanding of the dimensional and strength change in high quality carbon fiber composite under high temperature neutron irradiation.

### **SUMMARY**

The effects of neutron irradiation to ~7 dpa at 500 and 800°C on a high quality, three-dimensional balanced weave composite (FMI-222) is presented. Strength and dimensional stability for this system is compared to earlier work on this material, at lower dose, and contrasted with that of a well studied isotropic graphite (POCO AXF-5Q) irradiated at identical conditions. For both irradiation temperatures the composite strength in bending is substantially increased. Interestingly, while both irradiation temperatures cause contraction along the bend bar axis, the amount of contraction is greater for the higher temperature irradiation. Moreover, for the 500°C specimens nearly isotropic contraction leads to a corresponding decrease in volume, though an apparent large increase in volume occurs for the 800°C irradiated composite due to very anisotropic dimensional change. As the FMI-222 is a balanced-weave, isotropic composite, non-isotropic swelling behavior was unexpected, and is explained in terms of the fiber dimensional stability model previously presented, and the composite nature of this material.

### **PROGRESS AND STATUS**

#### **Introduction**

The effect of neutron irradiation on the strength and dimensional stability of graphites has been well studied and are strongly related. [1-4] For isotropic graphite, irradiation causes an initial densification with increased strength and Young's modulus. Densification is attributed to strain relief and closing of internal porosity by the migration of irradiation-induced carbon interstitials. The irradiation-induced increase in strength for graphite can be quite substantial. For example, nuclear graphites such as Graphnol N3N [5], Grade TSX, H451, and others[6] exhibit a peak increase in brittle-ring strength of approximately 100%. The effect of irradiation on composites has received less attention, though similar trends with graphite have been observed,[7-9]. As example, Burchell demonstrated a 64% increase in brittle-ring strength following an intermediate irradiation dose at 600°C for the high quality, balanced weave FMI-222 composite.

In polycrystalline graphites, neutron irradiation initially causes volumetric shrinkage. On the crystallite scale, the irradiation behavior is quite anisotropic with vacancies forming voids, or microcracks at the crystallite boundaries, and new basal planes by interstitial agglomeration. This causes shrinkage in the  $\langle a \rangle$  direction and strain perpendicular to the basal planes ( $\langle c \rangle$  direction.) Initially, the  $\langle c \rangle$  axis strain is absorbed by intrinsic misalignment of the basal planes and porosity. However, at some (irradiation temperature dependent) dose, the ability to accommodate the  $\langle c \rangle$

---

\*Oak Ridge National Laboratory (ORNL) is operated for the U.S. Department of Energy by UT-Battelle, LLC under contract DE-AC05-00OR22725.

axis strain saturates. The newly forming basal planes then cause  $\langle c \rangle$  swelling and the “turnaround” from macroscopic densification to swelling occurs, leading to multiplication of the strain-induced cracks and severe degradation in the material strength. The point at which the swelling returns to zero is typically taken as the useful lifetime.

It has been speculated that carbon fiber composites, by virtue of their ability to balance the anisotropic swelling on a macroscopic scale, may possess superior mechanical and dimensional properties at high doses and temperatures as compared to graphites. The purpose of this work is to study the dimensional and mechanical performance of a high-quality balanced-weave composite at doses sufficient highly to cause anisotropic swelling in the fiber.

### **Experimental and Results**

Manufacturer supplied thermophysical properties for the two materials of this study are given in Table 1. Bend bars were machined in the as-received condition into 2.3 x 6 x 30 mm and baked at 200°C in air prior to loading into graphite holders. Due to the effect of the relatively large unit cell volume for the composite materials, and the volume constraints associated with irradiation capsules, it was decided not to use the brittle ring geometry typical of previous graphite studies and the previous work with FMI-222. The statistical variability was found to be less with bend bars. The 14J irradiation capsule was irradiated for 8 cycles in the removable beryllium (RB) position of the High Flux Isotope Reactor (HFIR.) The capsule included thermocouples and active sweep gas control for 500 and 800°C temperature regulated zones. Bend testing was carried out at room temperature with cross-head displacement of 0.0085 mm/s. Load and support spans were 6.45 and 19.05 mm, respectively.

**Table 1. Thermophysical properties of materials studied**

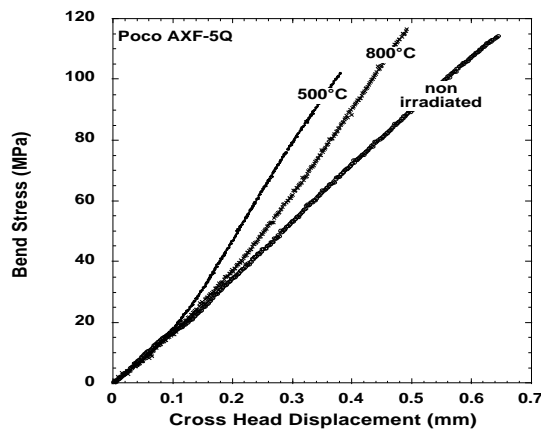
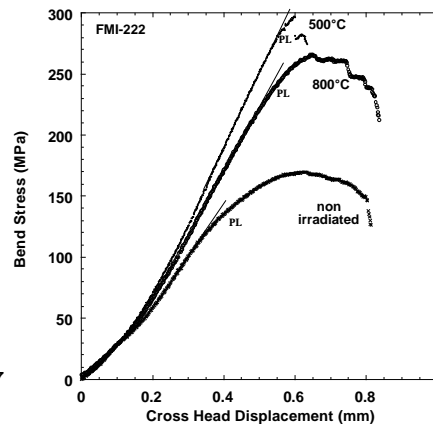
Property	Poco AXF-5Q	FMI-222
Manufacturer	Poco	Fiber Materials Inc.
Architecture	Isotropic Graphite	Balanced 3d weave
Precursor	Pitch based	P-120 Pitch fibers, Pitch Matrix
Grain size/Unit Cell Size ( $\mu\text{m}$ )	5	~900
Thermal Conductivity (W/m-K)	95	200
Apparent Density (g/cc)	1.78	1.96
Flexure Strength MPa	110	175

Table 2 gives the dimensional and flexural strength results as well as the fast neutron fluences. While it is commonly understood that graphite strength is best represented using Weibull statistics, the six samples available for the irradiated condition are less than the 15-30 considered adequate for such analysis. For this reason the normal statistical mean  $\pm 1$  standard deviation is given. It is seen that there is a slight decrease in flexural strength and density (implied from the length change) for Poco irradiated at 500°C. However, this decrease is within the standard

**Table 2. Physical property changes due to irradiation**

	Non-Irradiated	500°C $6 \times 10^{25} \text{ n/m}^2$ ( $E > 0.1 \text{ MeV}$ )	800°C $7.7 \times 10^{25} \text{ n/m}^2$ ( $E > 0.1 \text{ MeV}$ )
Poco AXF-5Q (#tests)	6	6	5
Ultimate Bend Strength, MPa (% change)	113±9	107±7 (-5%)	98±11 (-13%)
Length Change (%)	-	0.06±0.09	1.11±0.17
FMI-222	6	3	3
Proportional Limit, MPa (% change)	135±16	266±23 (+97%)	205±14 (+52%)
Ultimate Bend Strength, MPa (% change)	176±20	286±25 (+63%)	241±22 (+37%)
Macroscopic Length Change (%)	-	- 1.5	-3.6
Macroscopic Width Change (%)	-	- 1.4	1.4
Macroscopic Thickness Change (%)	-	- 1.4	5.9
Apparent Volume Change (%)	-	- 4.3	3.0

deviation. For the 800°C irradiation, a statistically significant decrease in strength (-13%) and density (-3.3%) occurs in Poco. In table 2, the flexural data for the FMI material is presented both with a proportional limit and ultimate bend strength. As the FMI material is a composite architecture, the flexural curve exhibits a departure from linearity, exhibiting “pseudo-ductility,” as crack propagation is mitigated by the fiber tows. This difference in flexural behavior, and the changes in stiffness and strength for the Poco and FMI materials, is illustrated in Figure 1. The point where the flexure curve departs from linearity is defined as the proportional limit.

**Figure 1. Flexural behavior of:**  
**a) Poco AXF-5Q and****b) FMI-222. (PL is proportional limit)**

The as-irradiated behavior of the FMI material contrasts with the Poco. At both irradiation temperatures a large increase proportional limit, flexural strength, and length change occurs in FMI. The increase in the proportional limit for FMI at 500°C (97%) exceeds that of the 800°C (52%), which also holds true for the ultimate bend strength. However, the length change at 500°C is less than half the 3.6% densification observed for the FMI material irradiated at 800°C.

## **Discussion**

As mentioned in the introduction, increased strength with neutron irradiation prior to “turnaround” is well known for graphites and is attributable to: (1) pinning of basal plane dislocations by irradiation-induced defects in the graphite crystallites, and (2) the reduction of internal porosity due to irradiation-induced volume shrinkage (densification.) The transition from strengthening to ultimate disintegration and total loss of load carrying capability is driven by the strains induced by anisotropic dimensional change. The commonly accepted irradiation-induced dimensional change model is for initial densification of isotropic graphite followed by “turnaround” to swelling. This turnaround occurs because of pore generation resulting from the mismatch of irradiation-induced crystal strains. Obviously, the removal of carbon atoms from existing basal planes to form new planes leaves behind vacancies causing shrinkage in the <a> direction. Typically, the amount of densification is less, and the point of “turnaround” to swelling behavior occurs at a lower dose, as the irradiation temperature is increased.[4] The contrasting dimensional change behavior for the FMI-222 composite irradiated at 500 and 800°C can be explained using the previously proposed “core-sheath” microstructural model [8] in which the graphite planes are oriented circumferentially on the fiber, and radially in the fiber core. Following this model, there will be continuous axial shrinkage under irradiation with the fiber diameter moving from shrinkage to swelling behavior.

In the previous work on the FMI-222 composite [8], an apparently linear densification of 1.3% occurred per  $1 \times 10^{25} \text{ n/m}^2$  ( $E > 0.1 \text{ MeV}$ ) neutron dose. The maximum fluence of that study was  $\sim 4.7 \times 10^{25} \text{ n/m}^2$  ( $E > 0.1 \text{ MeV}$ .) A similar densification occurred for a PAN fiber composite, FMI-223, possessing identical matrix and processing as the pitch based fiber composite FMI-222 of this study. The transition to “turnaround” swelling behavior was observed for the FMI-223 material, though not observed in FMI-222. This difference was attributed to the superior radiation stability of the pitch-based fibers. The neutron fluence in this study ( $7.7 \times 10^{25} \text{ n/m}^2$ ) was chosen to achieve turnaround behavior. Based on the dimensional change results (Table 2,) turnaround was achieved. However, the current results are not easily comparable with the earlier work because of the new finding of non-isotropic swelling for the bend bar. Using the shrinkage in length from table 2, apparent densification of 0.6 and 1.4 % per  $1 \times 10^{25} \text{ n/m}^2$  occurs at the 500 and 800°C irradiation temperatures, respectively. This qualitatively agrees with the 1.3% per  $1 \times 10^{25} \text{ n/m}^2$  value of the previous 600°C irradiation. The transition to swelling behavior is evident, however, when taking into account the swelling in the width and thickness of the bend specimens. This gives  $\sim 4\%$  swelling at 500°C and  $\sim 5\text{-}10\%$  at 800°C.

This anisotropic macroscopic dimensional changes can be explained using the core-sheath model for fiber dimensional changes. Assuming that the macroscopic composite behavior is dominated by the fiber changes, one would expect the fibers to initially shrink in the diametral and axial direction, then begin diametral swelling with continued axial shrinkage. For higher temperatures, turnaround occurs more rapidly due to thermal closure of porosity, yielding greater dimensional changes for equivalent neutron dose. Even though this composite is a balanced weave, and would be expected to have isotropic dimensional change, the fact that the length direction of the bend bar has continuous fiber tows parallel to its axis, the length change is dominated by the behavior of the fibers. However, the macroscopic width and thickness dimensions of the bend bar are dominated by the radial swelling of fiber bundles.

This anisotropic behavior is evident by inspection of SEM micrographs of the top surface of the bend bars (Figure 2.) By comparing the 500 and 800°C images it is clear that at 800°C the fiber bundles have undergone significantly higher shrinkage causing gaps as the bundles have shrunk away from the surface. For the 500°C irradiation, the fiber tows and pitch matrix appear to remain coherent with the tow shrinkage equal to the macroscopic dimensional changes of the

composite. Tables 3 and 4 give the dimensional analysis of the fiber bundles within the composite (eg measurement from Figure 2 micrographs.) It is clearly seen from Table 3 that the fiber tow lengths following irradiation decrease, with the least change in the longer, and thereby more constrained, dimensions. Table 4 gives the corresponding increase in width of the fiber bundles caused by the radial swelling of the individual fibers.

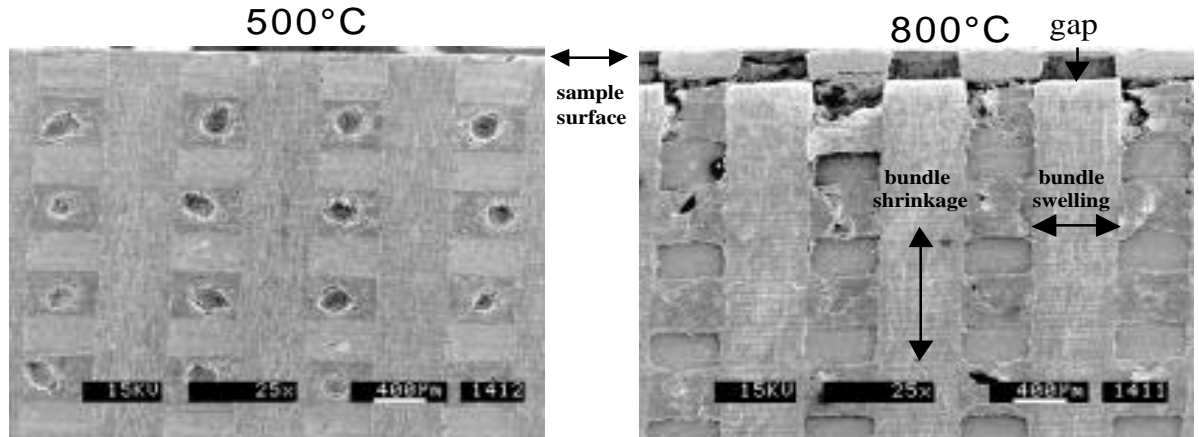


Figure 2. SEM image of surface of 500°C and 800°C irradiated FMI-222 composition.

Table 3. Dimensional change occurring in the fiber bundle lengths upon irradiation.

	Non-Irradiated Dimension (mm)	Change in Length (%)	
		500°C	800°C
Bundle Length Parallel to Bar Length Axis	30	-1.5	-4.25
Bundle Length Parallel to Bar Width Axis	6	-1.4	-5.5
Bundle Length Parallel to Bar Thickness Axis	2.3	-1.4	-7.2

**Table 4. Dimension change occurring in the fiber bundle diameter upon irradiation.**

	Bundle Width ( $\mu\text{m}$ )	Change in Width (%)
Non-Irradiated	320	-
500°C, Irradiated	331	3.4
800°C, Irradiated	363	13.4

It is important to note that, while this balanced weave, isotropic composite has undergone anisotropic dimensional changes, this behavior is being affected by the geometry, and associated constraints, of the sample. It is likely that larger samples would behave in a manner consistent with the fiber-axis-dominated shrinkage seen along the axis of the bend bars. Referring to Table 2, the positive volume changes given are dominated by the bend bar width and thickness swelling, where it is speculated that were the sample cubic, and large enough for many unit cells, the volume change would be better represented by the cube of the length change. However, as the fluence is increased, the strains associated with the anisotropic swelling must eventually lead to destruction of the composite as the fiber diameter becomes increasingly large and resultant strains cause internal fractures.

Previous brittle-ring strength measurements made on FMI-222 irradiated to a dose of  $\sim 2.2 \times 10^{25} \text{ n/m}^2$  ( $E > 0.1 \text{ MeV}$ ) at 600°C exhibited a strengthening of about 64% and a corresponding densification change of  $\sim 3\%$ . In this study, where the fibers are in a regime of gross anisotropic dimensional change (especially at 800°C,) the composite has maintained the radiation enhanced strength.

Specifically, in bending, the fracture strength is 63% higher at 500°C, and 37% higher at 800°C irradiation. This behavior is in contrast to the Poco materials which at identical irradiation and testing conditions underwent a decrease in strength and had entered the isotropic swelling regime.

## CONCLUSIONS

This study has shown that, for a very high quality, balanced weave carbon fiber composite, radiation enhanced fracture strength is retained in the anisotropic swelling regime generally associated with severe loss in strength. This has been demonstrated by comparison of the standard isotropic graphite Poco AXF-5Q and the balanced weave pitch-based fiber composite FMI-222. At the highest dose and temperature,  $7.7 \times 10^{25} \text{ n/m}^2$  and 800°C, the graphite material was seen to undergo swelling with an associated 13% decrease in strength, while the composite material exhibited a 37% higher strength.

## REFERENCES

1. Simmons, J.W.H., *Radiation Damage in Graphite*. International Series of Monographs in Nuclear Energy. Vol. 102. 1965: Pergamon Press.
2. Kelly, B.T., *Physics of Graphite*. 1981, London: Applied Science Publishers.
3. Nightingale, R.E., *Nuclear Graphite*. 1962: Academic Press.
4. Burchell, T.D., *Carbon Materials for Advanced Technologies*, ed. T.D. Burchell. 1999, Kidlington, Oxford, England: Elsevier Science Ltd.

5. Burchell, T.D. and W.P. Eatherly, *The effects of radiation damage on the properties of GraphNOL N3M*. J. Nucl. Mat., 1991. 179-181: p. 205-208.
6. Kennedy, C.R. and E.M. Woodruff, *Irradiation Effects on the Physical Properties of Grade TSX Graphite*. 1989, Westinghouse Hanford Company: Richland Washington.
7. Sato, S., et al., Fusion Engineering and Design, 1990: p. 159-176.
8. Burchell, T.D., W.P. Eatherly, and J.P. Strizak. *The effect of neutron irradiation on the structure and properties of carbon-carbon composite materials*. in *Effects of Radiation on Materials:16th International Symposium, ASTM STP 1175*. 1994: ASTM, Philadelphia.
9. Eto, M., et al., *Mechanical porperties of neutron-irradiated carbon-carbon composites for plasma facing components*. Journal of Nuclear Materials, 1994. 212-215: p. 1223-1227.

### **3.0 FERRITIC/MARTENSITIC STEELS**

## **EFFECT OF CHROMIUM, TUNGSTEN, TANTALUM, AND BORON ON MECHANICAL PROPERTIES OF 5-9Cr-WVTaB STEELS—R. L. Klueh and M. A. Sokolov (Oak Ridge National Laboratory)**

### **OBJECTIVE**

The objective of this work is to develop an understanding of the effect of composition on the ferritic/martensitic steels that are of interest for fusion applications and to use that knowledge to develop steels with improved properties.

### **SUMMARY**

Although the results of studies on reduced-activation ferritic/martensitic steels have demonstrated the excellent properties of 7-10Cr-2WVTa martensitic steels [1-5], little information is available concerning the effect of chromium over the 5-10% range, where the steels transform to martensite when normalized or quenched. In this work, the effect of chromium, tungsten, and tantalum was investigated for the martensitic 5-9% Cr steels. The effect of boron was also investigated, because it has often been used in these types of steels to improve properties.

### **PROGRESS AND STATUS**

#### **Introduction**

Although the results of irradiation experiments on reduced-activation ferritic/martensitic steels show the general superiority of 7-10Cr-2WVTa martensitic steels over the 2.25% Cr (all compositions are in wt. %) bainitic steels and 12% Cr duplex steels [1-10], little information has been generated concerning the effect of chromium over the 5-10% range where the steels transform to martensite when normalized or quenched. In this work, the effect of chromium, tungsten, and tantalum was investigated for the martensitic 5-9% Cr steels. The effect of boron was also investigated, because it has often been used in these types of steels to improve properties.

#### **Experimental Procedure**

Compositions of the steels used in this experiment and their designation are given in Table 1. Nominally the steels are Fe-5Cr-2W-0.25V-0.1C (designated 5Cr-2WV), the 5Cr-2WV with 0.5% Ta (5Cr-2WVTa1), the 5Cr-2WV with 0.1% Ta (5Cr-2WVTa2), an Fe-5Cr-3W-0.25V-0.1C (5Cr-3WV), the 5Cr-3WV with 0.05% Ta (5Cr-3WVTa1), the 5Cr-3WVTa1 with 0.005% B (5Cr-3WVTa1B1), the 5Cr-3WVTa1 with 0.013% B (5Cr-3WVTa1B2), an Fe-7Cr-2W-0.25V-0.05Ta-0.1C (7Cr-2WVTa), an Fe-7Cr-3W-0.25V-0.05Ta-0.1C (7Cr-3WVTa), the 7Cr-2WVTa with 0.005% B (7Cr-2WVTaB), Fe-9Cr-2W-0.25V-0.1C (9Cr-2WV), the 9Cr-2WV with 0.05% Ta (9Cr-2WVTa), and the 9Cr-2WVTa with 0.005% B (9Cr-2WVTaB).

In the Oak Ridge National Laboratory alloy development program for reduced-activation steels [10], eight 18-kg electroslag-remelted heats of 2.25, 5, 9, and 12% Cr heats containing various amounts of W, V, and Ta were prepared by Combustion Engineering Inc, Chattanooga, TN. In addition to Cr, W, V, C, and Ta, elements normally found in such steels (e.g., Mn, Si, etc.) were adjusted to levels typical of commercial practice [10]. Material from the original 18-kg heats of the 5Cr-2WV steel and the 9Cr-2WVTa was used as the master alloy to prepare 450-g vacuum arc-melted button heats for all but the 5Cr-3WV, for which an Fe-2.25Cr-2W-0.25V-0.1C steel was the master alloy.

Table 1 Chemical composition of steels investigated (wt. %)<sup>a</sup>

Steels	C	Mn	Si	Cr	V	W	Ta	B
5Cr-2WV	0.12	0.49	0.23	5.04	0.24	2.01		
5Cr-2WVTa1	0.11	0.46	0.20	4.67	0.25	2.11	0.05	
5Cr-2WVTa2	0.12	0.45	0.19	4.65	0.25	2.14	0.10	
5Cr-3WV	0.096	0.40	0.12	4.97	0.23	3.00		
5Cr-3WVTa1	0.11	0.44	0.22	4.63	0.25	3.01	0.05	
5Cr-3WVTa1B1	0.11	0.43	0.21	4.61	0.25	2.87	0.05	0.005
5Cr-3WVTa1B2	0.11	0.42	0.21	4.61	0.24	2.99	0.05	0.013
7Cr-2WVTa	0.12	0.42	0.19	7.01	0.24	2.01	0.05	
7Cr-3WVTa	0.12	0.42	0.19	6.98	0.24	2.97	0.05	
7Cr-2WVTaB	0.12	0.42	0.19	7.02	0.24	1.98	0.05	0.004
9Cr-2WV	0.12	0.51	0.23	8.95	0.24	2.01		
9Cr-2WVTa	0.11	0.44	0.21	8.90	0.23	2.01	0.06	
9Cr-2WVTaB	0.094	0.40	0.21	8.38	0.23	2.02	0.06	

<sup>a</sup>Other elements analyzed (highest value of eleven heats is shown): P 0.16, S 0.009, Mo 0.02, Nb<0.01, Cu 0.04 Al 0.021, As 0.004, Sn 0.004

The 450-g heats were cast as a 12.7 x 25.4 x 127 mm ingot; half of each ingot was hot rolled to a thickness of 6.4 mm and half to a thickness of 0.76 mm. Mechanical properties tests were made on normalized-and-tempered steel. The steels were austenitized for 0.5 h at 1050°C in a helium atmosphere, after which they were quickly cooled in flowing helium. Specimens were tested in two tempered conditions: 1 h at 700°C and 1 h at 750°C.

Tensile specimens 44.5-mm long with a reduced gage section of 20.3 x 1.52 x 0.76 mm were machined from 0.76-mm sheet with gage lengths parallel to the rolling direction. Specimens were heat treated after machining. Tests were conducted at room temperature, 200, 300, 400, 500, and 600°C in vacuum on a 44-kN Instron universal testing machine at a nominal strain rate of 0.0004 s<sup>-1</sup>.

One-third-size Charpy specimens 3.3 x 3.3 x 25.4 mm with a 0.51-mm-deep 30° V-notch and a 0.05- to 0.08-mm-root radius were machined from the normalized 6.4-mm plate along the rolling direction with the notch transverse to the rolling direction. Specimens were tempered after machining. Details on the test procedure have been published [11-14].

## Results

### Microstructure

The microstructures of the steels were examined by optical microcopy, and all were found to be 100% martensite. Prior-austenite grain sizes were estimated (Table 2), and for the 5Cr steels, it is clear that tantalum causes a decrease in prior-austenite grain size. A similar effect of tantalum was

observed previously for the 9Cr-2WVTa steel when compared with a 9Cr-2WV steel [1]. For a 5Cr steel, it appears that increasing the tungsten had the effect of increasing the grain size, and that boron may have an effect of reducing the grain size (Table 2). For the 7 Cr steel, this effect of tungsten and boron on the grain size was not as obvious, as is the case for boron in the 9Cr steels, where little change was noted.

Table 2 Estimated grain sizes of normalized-and-tempered steels

Steels	Estimated Grain Size	
	ASTM No.	Size ( $\mu\text{m}$ )
5Cr-2WV	6	45
5Cr-2WVTa1	9	16
5Cr-2WVTa2	10	11
5Cr-3WV	6.5	39
5Cr-3WVTa1	8	22
5Cr-3WVTa1B1	8.5	19
5Cr-3WVTa1B2	10	11
7Cr-2WVTa	10	11
7Cr-3WVTa	9.5	14
7Cr-2WVTaB	9.5	14
9Cr-2WVTa	9.5	14

## Tensile Behavior

### 5Cr-W-V-Ta-B Steels

Figure 1 shows the room-temperature yield stress for the seven 5Cr steels for the two normalized-and-tempered conditions (normalized and then tempered either at 700 or 750°C). When no tantalum was present, there was no effect of increasing tungsten from 2% (5Cr-2WV) to 3% (5Cr-3WV). Tantalum additions caused a slight increase in strength for the 5Cr-2WV steel, especially for the 700°C temper. However, there was no difference between 0.05 and 0.10% Ta. There was no difference in the strength of the 5Cr-2WVTa1 and 5Cr-3WVTa1 steels after the 700°C temper, but the 5Cr-3WVTa1 was strongest after the 750°C temper. The addition of B to the 5Cr-3WVTa1 steel produced little difference in the strength of this steel relative to the 5Cr-3WVTa1 for the 700°C temper, but there was a reduction in strength for the boron-containing steels when tempered at 750°C.

Tensile tests were conducted at room temperature to 600°C for steels tempered at 700 and 750°C; only data for the 750°C temper (a typical tempering temperature for these steels) will be presented in detail. After tempering at 750°C (Fig. 2), the yield stress of the 5Cr-3WVTa1 steel was considerably higher than that of the other steels up to 500°C, with all of the tantalum-containing steels being considerably stronger than those without tantalum—the 5Cr-2WV and 5Cr-3WV steels—which had similar strengths. There was only a small difference in the yield stress and ultimate tensile strength for the 5Cr-3WVTa1, indicating that the steel had little work-hardening capacity. Because of this small difference in yield and ultimate of the 5Cr-3WVTa, the ultimate tensile strengths of the

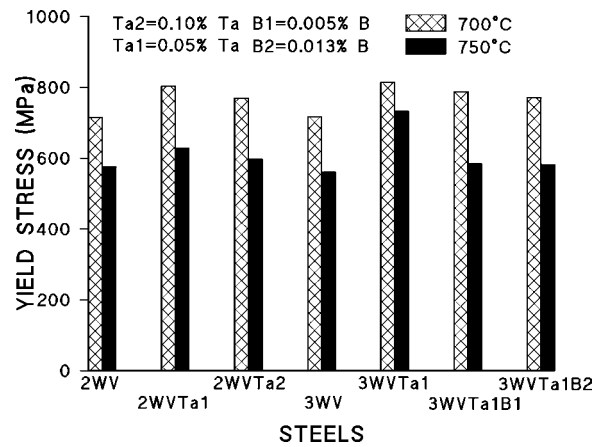


Fig. 1. Yield stress at room temperature of 5Cr steels of different composition.

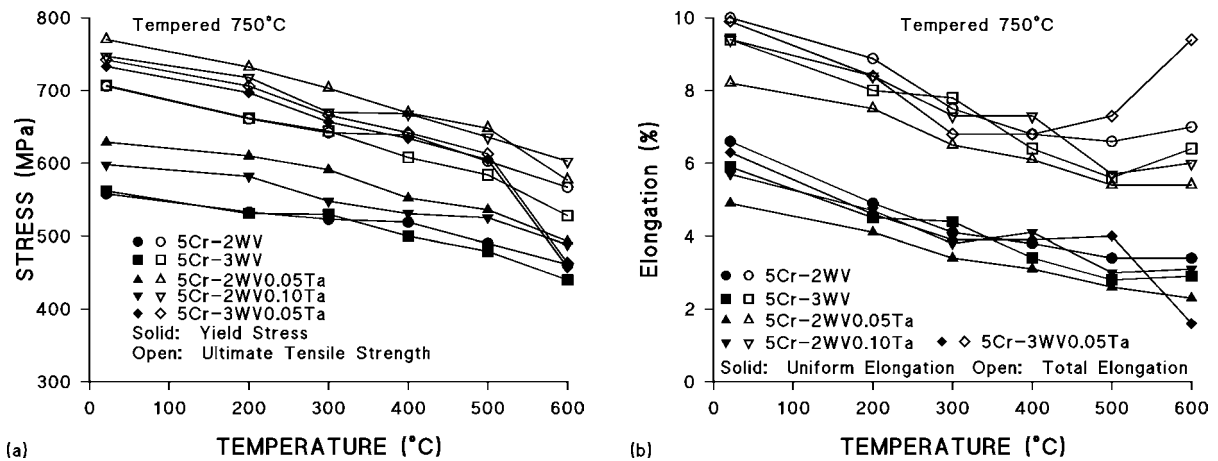


Fig. 2. (a) Yield stress and ultimate tensile strength and (b) uniform and total elongation of 5Cr steels of different composition tempered at 750°C

5Cr-2WVTa1 and 5Cr-2WVTa2 steels were higher than that of the 5Cr-3WVTa1, even though the latter steel had a much higher yield stress from room temperature to 500°C. There was a large decrease in yield stress and ultimate strength of the 5Cr-3WVTa in going from the 500 to 600°C test temperature relative to the change for the 5Cr-2WVTa1 and 5Cr-2WVTa2 steels [Fig. 2(a)]. In fact, the yield stress of the 5Cr-3WVTa1 at 600°C fell below that of the 5Cr-2WVTa1 and 5Cr-2WVTa2 steels, even though the latter were much weaker at the lower temperatures. The 5Cr-2WVTa1 was stronger than the 5Cr-2WVTa2 at all temperatures but 600°C, where they had similar strengths.

The 5Cr-2WVTa1 had the lowest ductility over the entire range, with considerable variability among the other steels [Fig. 2(b)]. The 5Cr-3WVTa1 showed a relatively large increase in total elongation at the highest test temperatures (400-600°C). Contrary to this increase in total elongation at 600°C for the 5Cr-3WVTa1, the uniform elongation showed a relatively large decrease, again emphasizing the lack of strain-hardening capacity for this steel.

When the properties of the tantalum-containing steels with boron were compared to the tantalum-containing steels without boron, the boron-containing steels were the weakest after both the 700 and 750°C [Fig. 3(a)] tempers. The uniform and total elongations generally reflected the strength behavior in that the ductility was relatively high [Fig. 3(b)]. At the highest test temperatures, the total elongation increased, similar to the increase observed for 5Cr-3WVTa1. At 600°C, the uniform elongation decreased, which is also similar to the behavior of the 5Cr-3WVTa1.

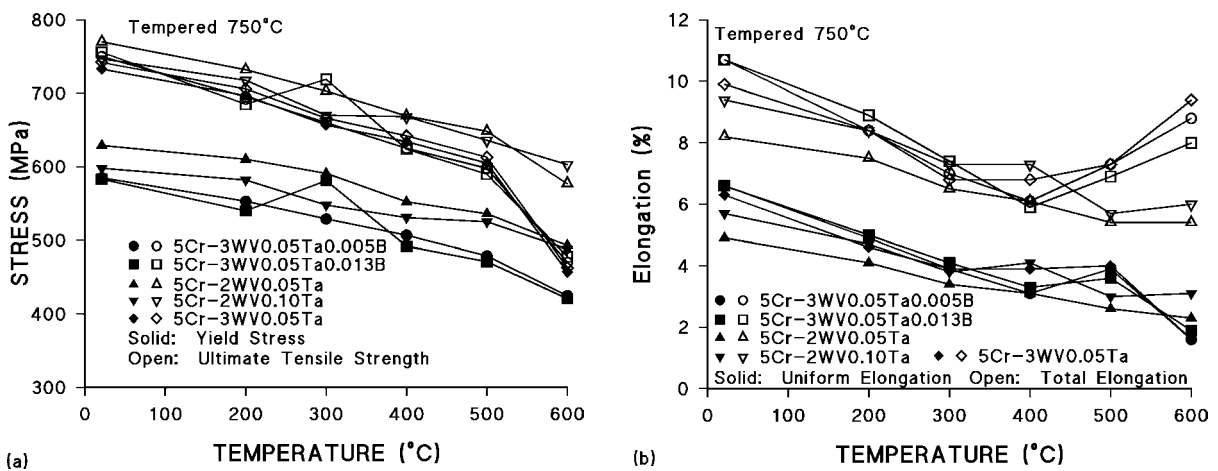


Fig. 3. Comparison of the (a) Yield stress and ultimate tensile strength and (b) uniform and total elongation of boron-containing 5Cr steels with other 5Cr compositions after tempering at 700°C.

### 7Cr-W-V-Ta-B Steels

For the 7Cr composition, the effect of a 1 % W or 0.005% B addition to the 7Cr-2WVTa steel composition was examined. (Note that all of the steels with tantalum and boron except the 5Cr-2WVTa2 and 5Cr-2WVTa1B2 contained 0.05% Ta and 0.005% B. Therefore, these elements will not be designated by a number for the 7 and 9Cr steels, and when comparisons are made with 5Cr-2WVTa1, the latter steel will be designated 5Cr-2WVTa.) Although the 7Cr-3WVTa steel was generally slightly stronger than the other two steels over the range room temperature to 600°C, the difference was relatively small after either the 700 or 750°C [Fig. 4(a)] temper. Similarly, there was relatively little difference in the uniform and total elongation of the three steels [Fig. 4(b)]. Despite being the strongest, the 7Cr-3WVTa steel generally had the highest uniform and total elongation.

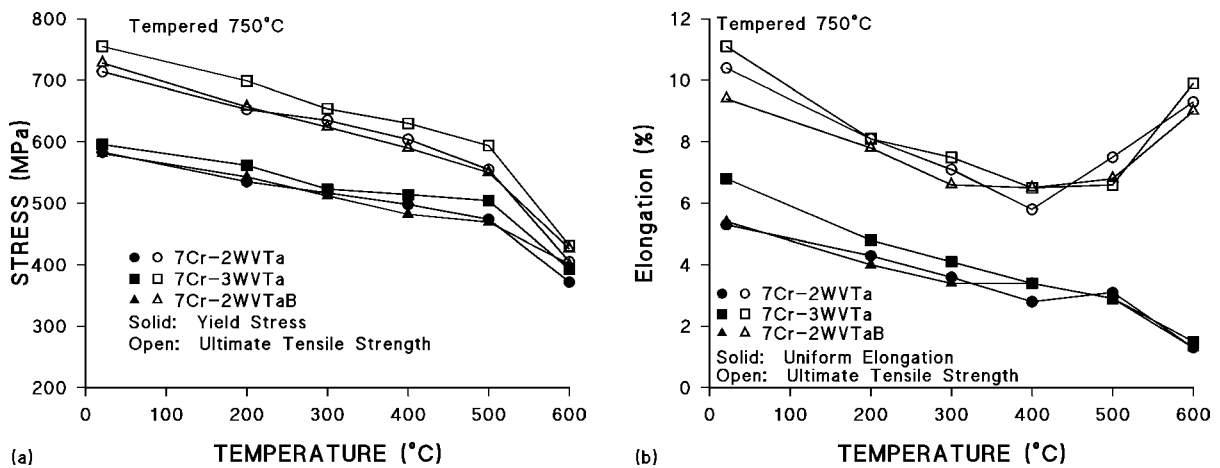


Fig. 4. (a) Yield stress and ultimate tensile strength and (b) uniform and total elongation of 7Cr steels of different composition tempered at 750°C.

#### 9Cr-W-V-Ta-B Steels

The addition of the tantalum to 9Cr-2WV composition to produce 9Cr-2WVTa caused an increase in strength after both the 700 and 750°C [Fig. 5(a)] temper. When tempered at 750°C, the strength of the 9Cr-2WVTaB is similar to that of the 9Cr-2WVTa, except at 600°C, where there was a large reduction in the strength of the 9Cr-2WVTaB relative to the other steels, and it becomes the weakest. The 9Cr-2WV is weakest below 600°C.

The ductilities did not show large differences between the different steels [Fig. 5(b)]. All the steels showed an increase in total elongation in going from 500 to 600°C, with the greatest increase occurring for the 9Cr-2WVTaB, which also showed an increase in going from 400 to 500°C.

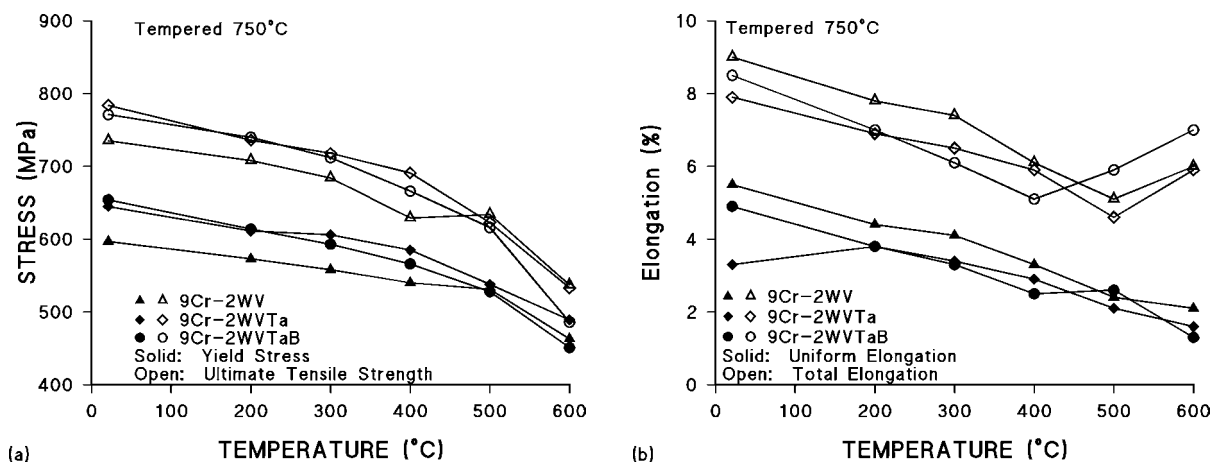


Fig. 5. (a) Yield stress and ultimate tensile strength and (b) uniform and total elongation of 9Cr steels of different composition tempered at 750°C.

### Comparison of 5Cr, 7Cr, and 9Cr Steels

A comparison of the tensile properties of the 5Cr-2WVTa (0.5Ta —Ta1), 7Cr-2WVTa, and 9Cr-2WVTa steels indicated that after the 750°C temper the 5Cr-2WVTa and 9Cr-2WVTa had similar yield stresses and ultimate tensile strengths over the entire temperature range, with the strengths of these two steels well above those for the 7Cr-2WVTa [Fig. 6(a)]. The uniform elongations for the steels [Fig. 6(b)] were quite similar at all test temperatures. Total elongations were also quite similar for the 5 and 9Cr steels at all test temperatures, but the 7Cr-2WVTa steel showed a large increase relative to the other two steels at 500 and 600°C.

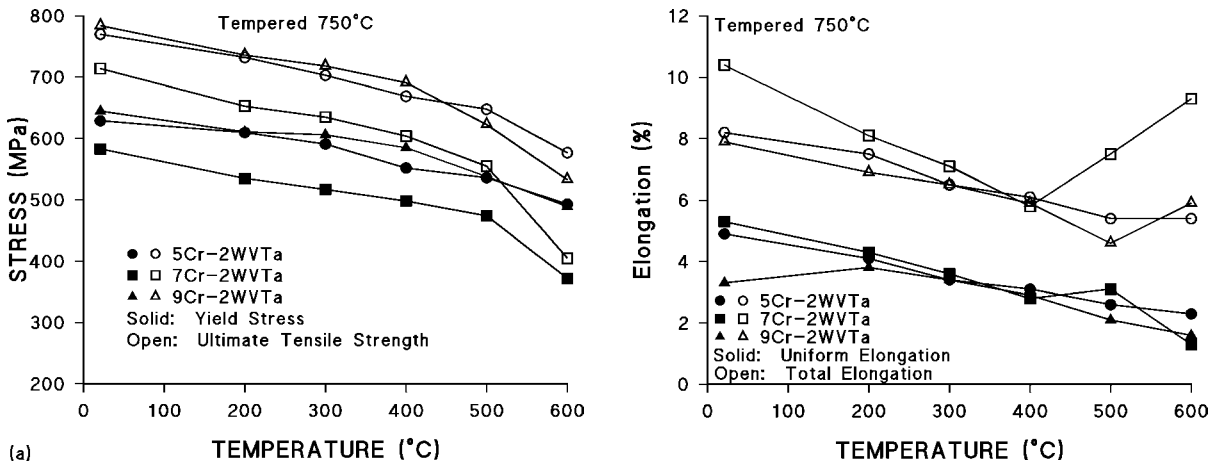


Fig. 6. Comparison of (a) Yield stress and ultimate tensile strength and (b) uniform and total elongation of 5Cr-2WVTa, 7Cr-2WVTa, and 9Cr-2WVTa steels tempered at 750°C.

### Charpy Impact Behavior

#### 5Cr-W-V-Ta-B Steels

By comparing ductile-brittle transition temperatures (DBTT) of the 5Cr-2WV steel with the steels with 0.05 (5Cr-2WVTa) and 0.1% Ta (5Cr-2WVTa2) [Fig. 7(a)], it appears that 0.05% Ta has no effect when tempered at 700°C, but there is an effect after tempering at 750°C. A similar effect was observed by comparing 5Cr-3WV and 5Cr-3WVTa1. No effect of tungsten was observed when the 5Cr-2WV and 5Cr-3WV were compared for the 700°C temper, but the 3% W steel had the lowest DBTT when tempered at 750°C. This same effect was observed by comparing 5Cr-2WVTa1 and 5Cr-3WVTa1 (i.e., the 5Cr-3WVTa1 has the lowest DBTT). On the other hand, a tantalum effect, determined by comparing the 5Cr-2WVTa1 and 5Cr-2WVTa2 steels, was only observed for the 700°C temper. The addition of boron caused a deterioration in the DBTT.

Neither tungsten, tantalum, nor boron favorably affected the upper-shelf energy (USE) (compare the 5Cr-2WV with the other six steels) after either the 700 or 750°C temper [Fig. 7(b)]. After the 750°C temper, the presence of tantalum (either 0.05 or 0.1%) resulted in USE values approaching those of

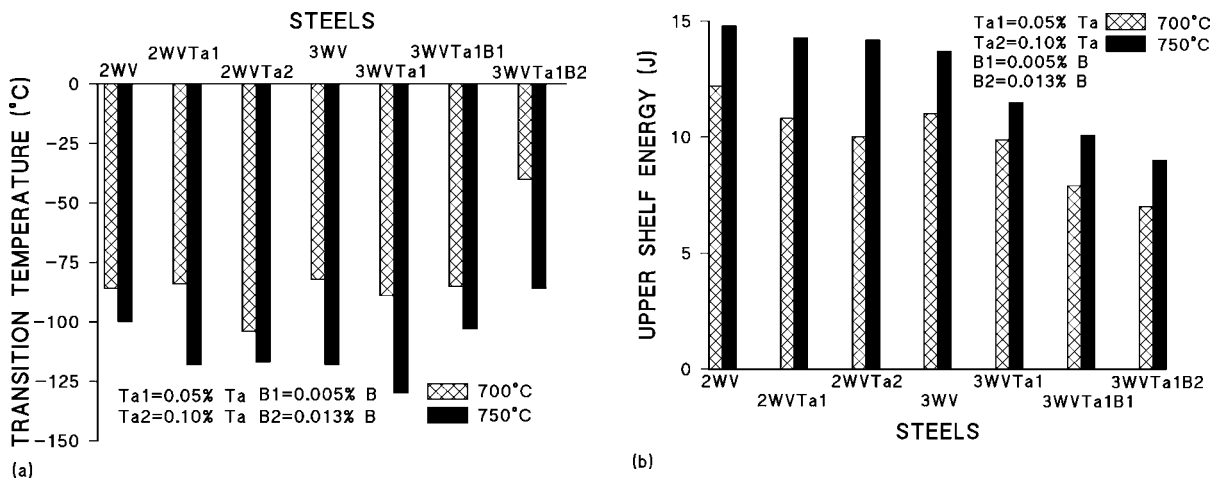


Fig. 7. (a) Ductile-brittle transition temperature and (b) upper-shelf energy of 5Cr steels tempered at 700 and 750°C.

the 5Cr-2WV steel. As was true for the DBTT, the boron additions caused a marked deterioration in the USE.

#### 7Cr-W-V-Ta-B Steels

For the 7Cr steels, the effect of tungsten and boron were studied. The results indicated that boron caused a deterioration of the DBTT [Fig. 8(a)]. An increase in tungsten from 2 to 3% favorably affected the DBTT for specimens tempered at 700°C, but it had no effect after tempering at 750°C. The USE of the 7Cr-3WVTa steel was a little larger than that of the 7Cr-2WVTa steel after both tempers, and the USE of the 7Cr-2WVTaB was little changed from the 7Cr-2WVTa [Fig. 8(b)].

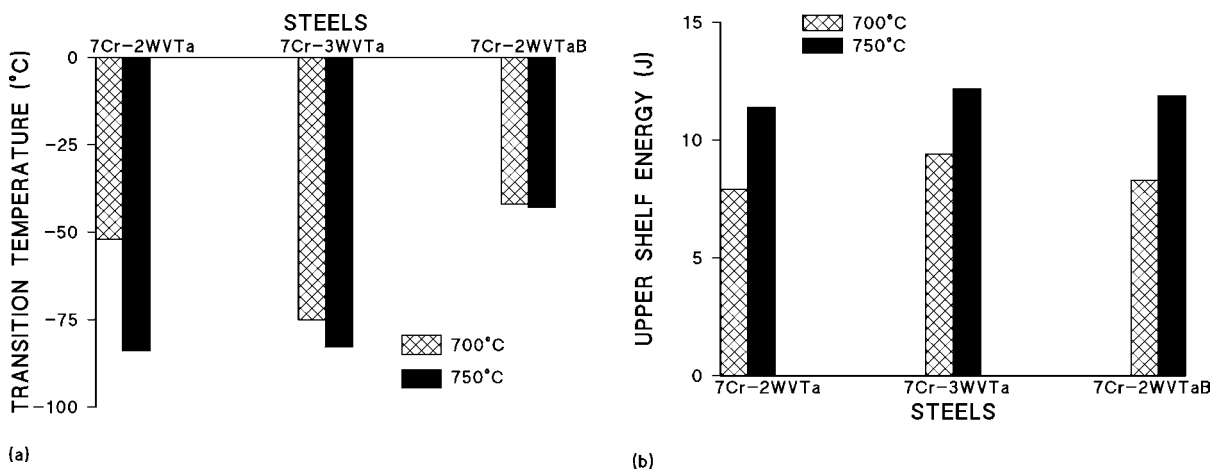


Fig. 8. (a) Ductile-brittle transition temperature and (b) upper-shelf energy of 7Cr steels tempered at 700 and 750°C.

### 9Cr-W-V-Ta-B Steels

The effect of tantalum on the Charpy properties of the 9Cr-2WV steel has been documented [15]. Fig. 9(a) shows this effect, and it also shows the effect of 0.005% B on the 9Cr-2WV Ta steel. In this case, boron favorably affected the transition temperature after both the 700 and 750°C tempers. The USE values of the 9Cr-2WV, 9Cr-2WV Ta, and 9Cr-2WV TaB steels were similar with perhaps a slight advantage for the 9Cr-2WV TaB [Fig. 9(b)].

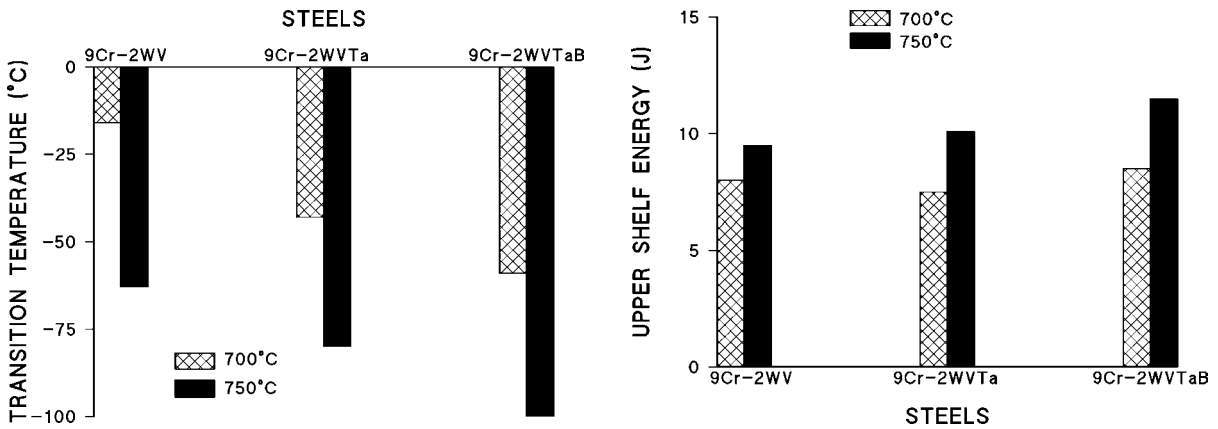


Fig. 9. (a) Ductile-brittle transition temperature and (b) upper-shelf energy of 7Cr steels tempered at 700 and 750°C.

### Comparison of 5Cr, 7Cr, and 9Cr Steels

When the 5Cr-2WV Ta (0.5Ta—Ta1), 7Cr-2WV Ta, and 9Cr-2WV Ta steels were compared [Fig. 10(a)], the 5Cr-2WV Ta had the lowest DBTT after both tempering treatments. There was little

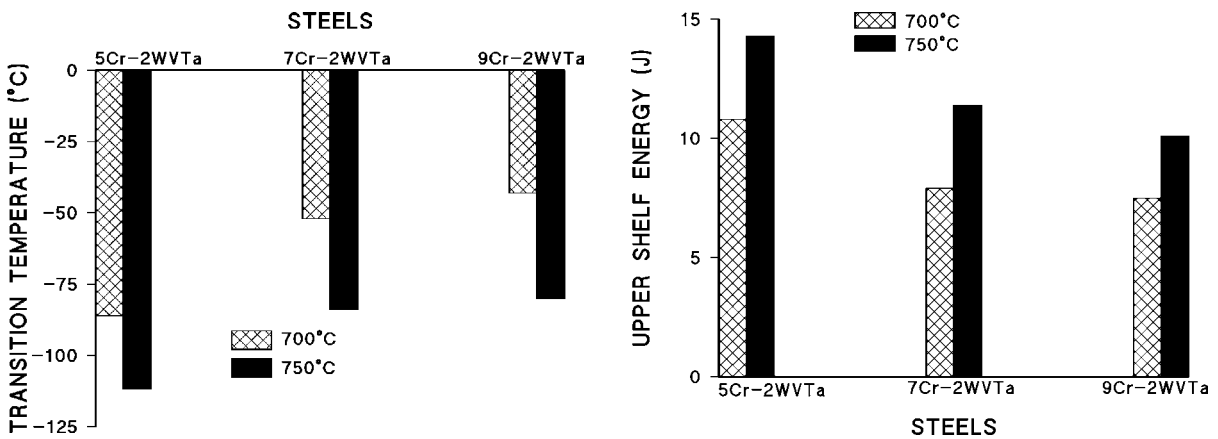


Fig. 10. A comparison of (a) Ductile-brittle transition temperature and (b) upper-shelf energy of 5Cr-2WV Ta, 7Cr-2WV Ta, and 9Cr-2WV Ta steels tempered at 700 and 750°C.

difference in the values for the 7Cr-2WVTa and 9Cr-2WVTa steels, the values for the 7Cr-2WVTa being slightly lower. Similarly, the USE of the 5Cr-2WVTa was the largest after each heat treatment. Again, there was relatively little difference between the 7Cr-2WVTa and 9Cr-2WVTa steels, with a slight advantage for the 7Cr-2WVTa steel [Fig. 10(b)].

## Discussion

Results obtained on the 5 and 9% Cr steels indicates that tantalum has a positive effect on the strength (Figs. 1, 2, and 5). For the 5% Cr steels this was observed for both the 2 and 3% W steels with 0.05% Ta, although there was little difference between the strength of the 5Cr-2WV steel with 0.05 and 0.1% Ta.

Tantalum also favorably affected the DBTT of the 5 and 9Cr steels. For the 5Cr steels with 0.05% Ta, the effect was significant only after a 750°C temper [Fig. 7(a)]; the 5Cr steel with 0.1% Ta showed an effect after both tempers, as was the case for the 9Cr steels [Fig. 9(a)]. The USE did not appear to be affected by tantalum for either the 5Cr [Fig. 7(b)] or 9Cr [Fig. 9(b)] steels.

The use of 3% instead of 2% W in the 5Cr steels had no effect on strength in the absence of tantalum. In the presence of 0.05% Ta, there appeared to be little effect after the 700°C temper, but there was a positive effect on yield stress up to 500°C when tempered at 750°C [Fig. 2(a)]. However, at 600°C, the strength of the 5Cr-3WVTa1 steel deteriorated significantly, thus indicating little or no advantage to the extra tungsten. Furthermore, although the yield stress was highest, there was little difference in the yield stress and ultimate tensile stress, indicating a lack of work-hardening capability. For the 7Cr-2WVTa and 7Cr-3WVTa, the 7Cr-3WVTa steel was generally stronger below 600°C, where there was little difference in strength [Figs. 4(a)].

The presence of 3% W seemed to have a positive effect on the DBTT for the 5% Cr steel after the 750°C [Fig. 7(a)]. There was essentially no effect of tungsten for the 7Cr steel after the 750°C temper, with the appearance of a slight effect after the 700°C temper [8(a)]. The USE appeared little affected by the extra tungsten for either steel [Figs. 7(b) and 8(b)].

The deterioration of the strength at 600°C, especially for the 5Cr steel, would not be favorable for the creep strength. The observation of strength deterioration appears to differ from results obtained by Abe et al.[4,9] for 9Cr-XW steels (X=0, 1, 2, 3, and 4). They found that the creep strength increased with increasing tungsten up to 3%. They did not report the effect of tungsten on tensile properties, but the strength would be expected to parallel the creep strength. The DBTT for the 9Cr-XW steels had a minimum at 1% W.

The tensile and Charpy results from the studies on the 5 and 7% Cr steels provided no reason to use boron in a 5 and 7% Cr steel. In fact the properties of the boron-containing 5 and 7% Cr steels were inferior to those without boron. However, the boron addition to 9Cr-2WVTa steel did favorably affect the impact properties.

The strength comparison of 5Cr-2WVTa, 7Cr-2WVTa, and 9Cr-2WVTa steels indicated that after tempering at 750°C, there was essentially no difference in the strength of the 5Cr-2WVTa and 9Cr-2WVTa, and they were considerably stronger than the 7Cr-2WVTa [Fig. 6(a)]. The ductility of the 5Cr-2WVTa and 9Cr-2WVTa steels were similar. If the apparent minimum in strength between 5 and 9% Cr is an accurate representation of these steels, then 9% Cr steels should be used over one with around 7% Cr. The F82H steel presently being used in an International Energy Agency collaborative program has a nominal composition of Fe-7.5Cr-2W-0.2V-0.03Ta-0.1C.

When the Charpy properties are compared for these three steels, the 5Cr-2WVTa has a clear advantage. In fact, the DBTT [Fig. 10(a)] and USE [Fig. 10(b)] of this steel after tempering at 700°C are as good or better than those for the 7Cr-2WVTa and 9Cr-2WVTa steels tempered at 750°C. Since the 9Cr-2WVTa steel needs to be tempered at 750°C to get adequate toughness, it would appear from the present tests that the 5Cr-2WVTa steel may have advantages in both strength and impact toughness.

## References

- [1] R. L. Klueh and D. J. Alexander, in: *Effects of Radiation on Materials: 18th International Symposium*, ASTM STP 1325, Eds. R. K. Nanstad, M. L. Hamilton, F. A. Garner, and A. S. Kumar (American Society for Testing and Materials, Philadelphia, 1999) 911.
- [2] K. Shiba, I. Ioka, J. E. Robertson, M. Suzuki, and A. Hishinuma, in: *Proceedings, Conference on Materials and Nuclear Power* (The Institute of Materials, London, 1996) 265.
- [3] E. V. van Osch, M. G. Horsten, G. E. Lucas, and G. R. Odette, in: *Effects of Irradiation on Mat. 19<sup>th</sup> International Symposium*, ASTM STP 1366, Eds. M. L. Hamilton, A. S. Kumar, S. T. Rosinski, and M. L. Grossbeck (American Society for Testing and Materials, West Conshohocken, PA, 2000) 612.
- [4] A. Kohyama, Y. Kohno, K. Asakura, and H. Kayano, *J. Nucl. Mater.* 212-214 (1994) 684.
- [5] A. Kohyama, A. Hishinuma, D. S. Gelles, R. L. Klueh, W. Dietz, and K. Ehrlich, *J. Nucl. Mater.* 233-237 (1996) 138.
- [6] H. Kayano, A. Kimura, M. Narui, Y. Sasaki, Y. Suzuki, and S. Ohta, *J. Nucl. Mater.* 155-157 (1988) 978.
- [7] D. S. Gelles, in: *Reduced Activation Materials for Fusion Reactors*, ASTM STP 1047, Eds. R. L. Klueh, D. S. Gelles, M. Okada, and N. H. Packan (ASTM, Philadelphia, 1990) 113.
- [8] F. Abe, T. Noda, H. Araki, and S. Nakazawa, *J. Nucl. Mater.* 179-181 (1991) 663.
- [9] F. Abe, H. Araki, and T. Noda, *Mat. Sci. Tech.* 6 (1990) 714.
- [10] R. L. Klueh and P. J. Maziasz, *Met. Trans.* 20A (1989) 373.
- [11] D. J. Alexander, R. K. Nanstad, W. R. Corwin, and J. T. Hutton, in *Automation Technology to Fatigue and Fracture Testing*, ASTM STP 1092, eds. A. A. Braun, N. E. Ashbaugh, and F. M. Smith (American Society for Testing and Materials, Philadelphia, 1990) p. 83.
- [12] W. R. Corwin and A. M. Hougland, in *The Use of Small-Scale Specimens for Testing Irradiated Material*, ASTM STP 888, eds. W. R. Corwin and G. E. Lucas (American Society for Testing and Materials, Philadelphia, 1986) p. 325.
- [13] D. J. Alexander and R. L. Klueh, in *Charpy Impact Test: Factors and Variables*, ASTM STP 1072, ed. J. M. Molt (American Society for Testing and Materials, Philadelphia, 1990) p. 179.
- [14] M. A. Sokolov and R. K. Nanstad, in *Effects of Radiation on Materials: 17 International Symposium*, ASTM STP 1270, eds. D. S. Gelles, R. K. Nanstad, A. S. Kumar, and E. A. Little (American Society for Testing and Materials, Philadelphia, 1996) p. 384.
- [15] R. L. Klueh, D. J. Alexander, and M. Rieth, *J. Nucl. Mater.*, 273 (1999) 146.

# MICROSTRUCTURAL EVOLUTION OF REDUCED-ACTIVATION 9Cr-STEELS IN HFIR-CTR-62/63 EXPERIMENT - N. Hashimoto and R. L. Klueh (Oak Ridge National Laboratory)

## OBJECTIVE

The objective of this work is to investigate microstructural evolution of nickel-doped and undoped ferritic/martensitic steels irradiated in HFIR-CTR-62/63 experiment in order to clarify the effect of helium generation rate on swelling and the change of the mechanical properties.

## SUMMARY

The microstructures of reduced-activation ferritic/martensitic steels, 9Cr-1MoVNb and 9Cr-1MoVNb-2Ni, irradiated at 400°C up to 12 dpa in the High Flux Isotope Reactor (HFIR), were investigated by transmission electron microscopy. Irradiation-induced cavities were observed in both steels. The cavity number density of the 9Cr-1MoVNb-2Ni was higher than that of 9Cr-1MoVNb due to the higher concentration of helium. The swelling of the 9Cr-1MoVNb and the 9Cr-1MoVNb-2Ni was 0.002% and 0.004%, respectively. Irradiation-induced  $a_0\langle 100 \rangle$  and  $(a_0/2)\langle 111 \rangle$  type dislocation loops were observed in the all irradiated steels; number density and mean diameter of  $a_0\langle 100 \rangle$  type loops was higher and smaller than that of  $(a_0/2)\langle 111 \rangle$  type loops. There was a tendency for the number density of loops in 9Cr-1MoVNb-2Ni to be higher than in 9Cr-1MoVNb. Irradiation-produced precipitates, identified  $M_2X$  phase, were found in the 9Cr-1MoVNb-2Ni.

## PROGRESS AND STATUS

### Introduction

Ferritic/martensitic steels are attractive candidate structural first wall materials for fusion energy systems [1]. The high-energy neutrons produced by the D-T fusion reaction induce displacement damage and generate gas atoms (H and He) in the materials from  $(n,p)$  and  $(n,\alpha)$  reactions. It is considered that the simultaneous production of helium atoms from  $(n,\alpha)$  reactions could strongly influence the nucleation of cavities. Therefore, to clarify the effect of helium atoms on the microstructural development and mechanical property change in martensitic steels under fast neutron irradiation, 9Cr-1MoVNb and 9Cr-1MoVNb doped with 2%Ni (9Cr-1MoVNb-2Ni) were irradiated with neutrons in the High Flux Isotope Reactor (HFIR). Irradiation of Ni-doped steels in a mixed spectrum reactor like the HFIR results in the following transmutation reaction with the thermal neutrons:  $^{58}\text{Ni}(n,\gamma)^{59}\text{Ni}(n,\alpha)^{56}\text{Fe}$ , thus providing the possibility of studying the effects of the simultaneous production of displacement damage and helium production.

### Experimental Procedure

The 9Cr-1MoVNb and 9Cr-1MoVNb-2Ni were normalized by austenitizing 0.5 h at 1050°C followed by rapid cool in blowing helium, and tempered 1 h at 700°C. The compositions are given in Table 1. Standard 3-mm diameter transmission electron microscopy (TEM) disks were punched from 0.25-mm thick sheet stock. Irradiation was at 400°C in the HFIR-CTR-63 capsule in the High Flux Isotope Reactor (HFIR) to a neutron fluence of about  $1.68 \times 10^{22}$  n/cm<sup>2</sup> ( $E > 0.1$  MeV) [2], resulting in a displacement dose of about 12 dpa. The details of the design, construction, and installation of HFIR-CTR-62/63 have been reported [3]. The irradiation conditions and the calculated helium concentrations in the steels are given in Table 2. TEM specimens were thinned using an automatic Tenupol electropolishing unit located in a shielded glove box. TEM disks were examined using a JEM-2000FX (LaB<sub>6</sub>) transmission electron

microscope. The foil thickness was measured using thickness fringes in order to evaluate quantitative defect density values.

Table 1. Chemical compositions of the specimens (wt%)

	9Cr-1MoVNb	9Cr-1MoVNb -2Ni
Cr	8.64	8.54
Ni	0.10	2.18
Mo	0.97	0.97
Nb	0.064	0.068
V	0.21	0.22
Mn	0.35	0.35
W	0.01	< 0.01
Ta	-	-
Al	0.013	0.015
Cu	0.03	0.04
Ti	0.002	0.002
C	0.091	0.070
P	0.008	0.008
S	0.004	0.004
Si	0.07	0.08
B	< 0.001	< 0.001
N	0.050	0.054
Fe	Bal.	Bal.

Table 2. Irradiation conditions and helium concentration

	dpa	appm He	He/dpa
9Cr-1MoVNb	12.1	30	2.5
9Cr-1MoVNb-2Ni	12.3	161	13.1

## Results

### Dislocations and dislocation loops

Figure 1 shows the dislocation segments and loops in the steels after irradiation at 400°C to 12 dpa using the diffraction conditions  $\mathbf{g}=110$ , ( $\mathbf{g},4\mathbf{g}$ ). During irradiation of Fe-Cr binary alloys, dislocation evolution in an initially almost dislocation-free condition proceeds by the formation of interstitial-type dislocation loops with an  $\mathbf{a}_0\langle 100 \rangle$  and/or  $(\mathbf{a}_0/2)\langle 111 \rangle$  Burgers vector [4,5]. Similar loops form in more complicated steels [6,7], such as those used in this experiment. Table 3 summarizes the quantitative results of the dislocation loops observed. The number density and the mean diameter of  $\mathbf{a}_0\langle 100 \rangle$  type loops are higher and smaller than that of  $(\mathbf{a}_0/2)\langle 111 \rangle$  type loops for all the steels. In addition, there is a tendency for a higher number density of  $(\mathbf{a}_0/2)\langle 111 \rangle$  type loops in Ni-doped steels compared to undoped steels.

Table 3. Summary of dislocation structure after irradiation

Steel	$\mathbf{a}_0\langle 100 \rangle$ type loops		$(\mathbf{a}_0/2)\langle 111 \rangle$ type loops	
	Number density ( $\text{m}^{-3}$ )	Mean diameter (nm)	Number density ( $\text{m}^{-3}$ )	Mean diameter (nm)
9Cr-1MoVNb	$5 \times 10^{21}$	21	$4 \times 10^{21}$	25
9Cr-1MoVNb-2Ni	$7 \times 10^{21}$	20	$6 \times 10^{21}$	24
9Cr-2WVTa*	$1 \times 10^{22*}$	18*	$5 \times 10^{21*}$	28*
9Cr-2WVTa-2Ni*	$1 \times 10^{22*}$	17*	$6 \times 10^{21*}$	16*

\* Data in ref. [7]

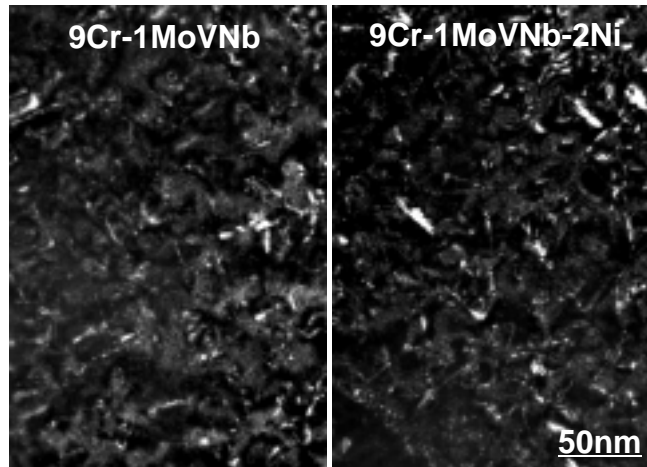


Figure 1 Dislocation segments and loops in 9Cr-1MoVNb and 9Cr-1MoVNb-2Ni after irradiation at 400°C to 12 dpa using the diffraction conditions  $g=110$ ,  $(g,4g)$ .

### Cavities

Figure 2 shows cavities of the specimens irradiated at 400°C to 12 dpa. Distribution of cavities is homogeneous in the matrices, and no cavities were observed on grain boundaries. Neutron irradiation induced tiny cavities (5 nm) with the number densities of  $9 \times 10^{21}$  in 9Cr-1MoVNb-2Ni. In 9Cr-1MoVNb, somewhat larger cavities (9 nm) with the number densities of  $3 \times 10^{21}$  were observed. Swelling of 9Cr-1MoVNb and 9Cr-1MoVNb-2Ni were 0.002% and 0.004%, respectively. Table 4 summarizes the quantitative results of the observations on the cavities.

Table 4. Summary of cavities formed during irradiation

Steel	Mean Size (nm)	Number Density ( $m^{-3}$ )	Swelling (%)
9Cr-1MoVNb	9	$3 \times 10^{21}$	0.002
9Cr-1MoVNb-2Ni	5	$9 \times 10^{21}$	0.004
9Cr-2WVTa*	3*	$1 \times 10^{21}$ *	< 0.001*
9Cr-2WVTa-2Ni*	3*	$3 \times 10^{21}$ *	< 0.001*

\* Data in ref. [7].

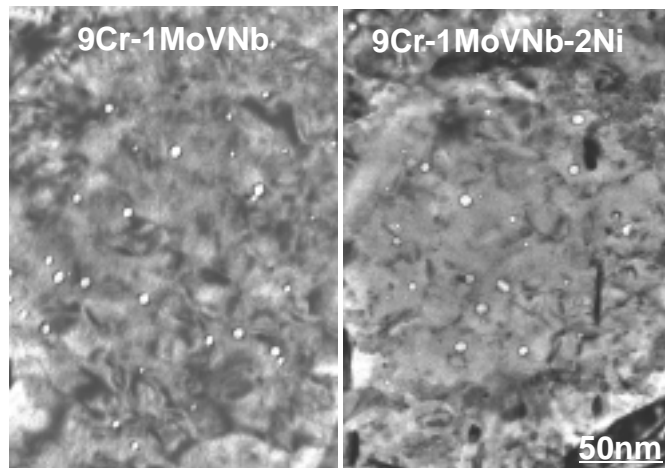


Figure 3 Cavities in 9Cr-1MoVNb and 9Cr-1MoVNb-2Ni irradiated at 400°C to 12 dpa.

## Precipitates

Before irradiation, the precipitates in all the steels used in this study include  $M_{23}C_6$  on grain and/or lath boundaries, with the number density and the mean diameter of  $<1 \times 10^{20} \text{ m}^{-3}$  and about 100 nm, respectively. There was no difference in  $M_{23}C_6$  before and after irradiation in terms of size and distribution, but neutron irradiation did produce precipitates in the matrices of the Ni-doped steels. The spacing of moiré fringes was used to identify the irradiation-produced precipitates, which were identified as  $M_2X$  phase in the 9Cr-1MoVNb-2Ni and  $M_6C(\eta)$ -type carbide in the 9Cr-2VWTa-2Ni. Figure 4 shows the irradiation-induced precipitates in the 9Cr-1MoVNb-2Ni and the 9Cr-2VWTa-2Ni after irradiation at 400 °C to 12 dpa. Precipitation of a Cr- and Ni-rich  $M_6C(\eta)$  has been observed in a number of 8-12Cr steels that contain  $>0.3\text{wt}\%$  Ni during FBR (Fast Breeder Reactor) and HFIR irradiation at about 400°C [8-11]. Table 5 summarizes the quantitative results of precipitates.

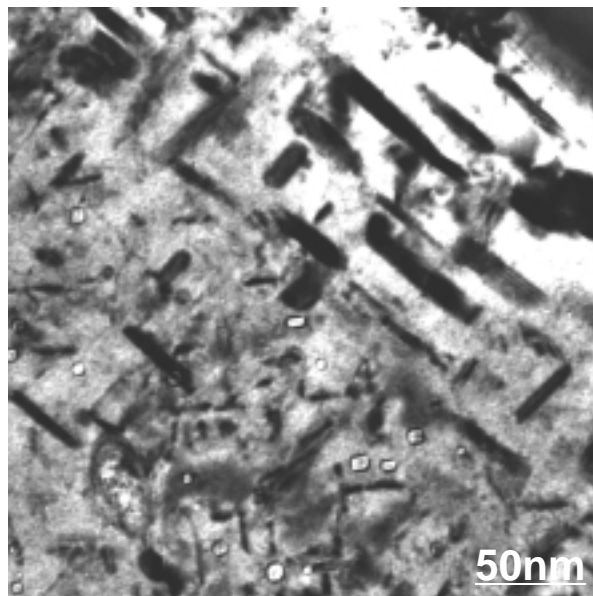


Figure 4 Irradiation-induced precipitates in 9Cr-1MoVNb-2Ni after irradiation at 400°C to 12 dpa

Table 5. Summary of precipitates in the steels after irradiation at 400°C

Steel	$M_{23}C_6$		$M_2X$		$M_6C(\eta)$	
	Mean Size (nm)	Number Density ( $\text{m}^{-3}$ )	Mean Size (nm)	Number Density ( $\text{m}^{-3}$ )	Mean Size (nm)	Number Density ( $\text{m}^{-3}$ )
9Cr-1MoVNb	95	$<1 \times 10^{20}$	-	-	-	-
9Cr-1MoVNb-2Ni	98	$<1 \times 10^{20}$	54	$5 \times 10^{20}$	-	-
9Cr-2VWTa*	95*	$<1 \times 10^{20*}$	-	-	-	-
9Cr-2VWTa-2Ni*	92*	$<1 \times 10^{20*}$	-	-	7*	$2 \times 10^{21*}$

\* Data in ref. [7]

## Discussion

The results from the TEM observations, some of which appear to differ from previous studies, provide information on the effect of composition (W, Mo, N, Ni, etc.) on the irradiation behavior of the steels. Prior to irradiation, the microstructures of the two steels had similar dislocation line densities ( $2\sim 7 \times 10^{14} \text{ m}^{-2}$ ) and analogous precipitates, which were mainly  $\text{M}_{23}\text{C}_6$  ( $\approx 100 \text{ nm}$  in diameter and a number density of  $< 10^{20} \text{ m}^{-3}$ ) with a few MC precipitates, mainly on dislocations.

Results from the present work indicate that the 9Cr-1MoVNb steels have a tendency to swell more than some other ferritic/martensitic steels [12-15]. The results also indicate that composition of elements other than the 9%Cr has an effect on the swelling. Although neither steel showed large amounts of swelling, the swelling in the 9Cr-1MoVNb steel was over twice that in the 9Cr-2WVTa steel. This agrees with previous work [13], where the 9Cr-1MoVNb, 9Cr-2WVTa, and 9Cr-2WV (the same as the 9Cr-2WVTa, but without the tantalum) steels were irradiated in FFTF at  $\approx 420 \text{ }^\circ\text{C}$  to 35 dpa. Swelling for the three steels was estimated as 0.85, 0.33, and 0.2%, respectively, again demonstrating the effect of composition, with the 9Cr-1MoVNb showing the highest swelling. However, it must be noted that the 12Cr-1MoVW steel irradiated in that experiment showed only 0.007% swelling, giving further credence to the conclusion that 9Cr steels have a tendency to swell more than 12Cr steels [12-16]. One reason for the lower swelling resistance of the 9Cr-1MoVNb than the other 9Cr steels might be the nitrogen added to this steel. The 9Cr-1MoVNb with 0.054% N contains twice as much nitrogen as the 12Cr-1MoVW (0.027% N). However, the 9Cr-2WVTa (0.029% N) and the 9Cr-2WV (0.022% N) contain amounts similar to the 12Cr-1MoVW steel, indicating that nitrogen is not the sole determinant for the difference between the 9Cr-1MoVNb and the other 9Cr steels and the 12Cr steel. The previous work for neutron-irradiated austenitic stainless steels reported the effect of nitrogen on swelling [17], the presence of nitrogen resulted in large swelling. Some ion irradiation experiments indicated that oxygen gas affected the cavity pressurization and, therefore, affected the swelling [18]. Nitrogen might be expected to have a similar effect.

The difference in the precipitates after irradiation between 9Cr-1MoVNb-2Ni and 9Cr-2WVTa-2Ni steels is of interest. Whereas the 9Cr-2WVTa-2Ni contained a high number density ( $2 \times 10^{21} \text{ m}^{-3}$ ) of small (7 nm) nickel-rich  $\text{M}_6\text{C}$  particles, the 9Cr-1MoVNb-2Ni steel contained a smaller number density ( $5 \times 10^{20} \text{ m}^{-3}$ ) of larger (54 nm)  $\text{M}_2\text{X}$  particles. A previous investigation found nickel-rich  $\text{M}_6\text{C}$  precipitates in 9Cr-1MoVNb-2Ni and 9Cr-1MoVW-2Ni [12,13] after irradiation in both FFTF and HFIR. Nickel-rich precipitates were also found in ternary Fe-12Cr-1.5Ni alloys irradiated at 300 and 400  $^\circ\text{C}$  in HFIR [19]. The  $\text{M}_6\text{C}$  precipitates in the 9Cr-1MoVNb-2Ni were found after irradiation to 47 dpa at 407  $^\circ\text{C}$  in FFTF and 37 dpa at 400  $^\circ\text{C}$  in HFIR [12,13]. Traces of  $\text{M}_2\text{X}$  were found in the 9Cr-1MoVNb and the 9Cr-1MoVNb-2Ni steels that were irradiated in FFTF but not in those irradiated in HFIR [12,13]. The  $\text{M}_2\text{X}$  is a Cr-rich precipitate with the X generally high in nitrogen, which would be in accord with the 9Cr-1MoVNb steel containing a higher nitrogen concentration than the other steels. The reason for not finding the high density of  $\text{M}_6\text{C}$  in the 9Cr-1MoVNb-2Ni in the present experiment is unknown; it may mean that the  $\text{M}_2\text{X}$  forms first (low dpa) followed by the formation of the  $\text{M}_6\text{C}$ . That is, in the present experiment irradiation was only to 12 dpa, compared to about 40 dpa in the previous experiments [12,13].

In addition to containing TEM specimens of the nickel-doped steels to determine the effect of helium on swelling and microstructure, as discussed in this paper, the irradiation capsule also contained tensile and Charpy impact specimens of 9Cr-1MoVNb, 9Cr-1MoVNb-2Ni, 9Cr-2WVTa, and 9Cr-2WVTa-2Ni steels. Results on the effect of irradiation on the tensile and Charpy properties of the irradiated 9Cr-2WVTa and 9Cr-2WVTa-2Ni steels have been published [20]. The implication of the microstructural observations discussed here on the mechanical properties of those steels will be deferred to a future paper that presents the mechanical properties of the irradiated 9Cr-1MoVNb and 9Cr-2WVTa-2Ni steels.

## **Summary**

To determine the effect of helium on the microstructure of 9Cr-1MoVNb and 9Cr-2WVTa steels, these compositions along with similar compositions except that they contained 2% Ni (9Cr-1MoVNb-2Ni and 9Cr-2WVTa-2Ni) were irradiated in HFIR. Irradiation of Ni-containing steels in HFIR results in the formation of helium from an (n, $\alpha$ ) reaction with thermal neutrons.

Although the amount of swelling was small, there was an effect of helium, especially for the 9Cr-1MoVNb-2Ni and 9Cr-2WVTa-2Ni steels, with the latter steel swelling twice as much as the former (0.004 vs. 0.002%). Swelling for both the 9Cr-2WVTa and 9Cr-2WVTa-2Ni steels was estimated at <0.001 %. Three times as many cavities were observed for the 9Cr-2WVTa-2Ni than for 9Cr-2WVTa, which was similar to the difference in cavity density observed for the 9Cr-1MoVNb-2Ni and 9Cr-1MoVNb steels, indicating the effect of helium on cavity nucleation.

Before irradiation, all four steels contained similar precipitates: mainly  $M_{23}C_6$  with a few MC precipitates. After irradiation, no change in precipitates was observed for the steels without nickel. However, irradiation-induced precipitates were observed in the nickel-containing steels, with the 9Cr-1MoVNb-2Ni containing a low-number density of  $M_6C$ . The  $M_6C$  precipitate has been seen previously in irradiated nickel-containing steels, indicating 9Cr-1MoVNb-2Ni. The presence of  $M_2X$  instead of  $M_6C$  may have been due to the nitrogen in the 9Cr-1MoVNb-2Ni along with a lower fluence of the present experiment compared to previous irradiations where  $M_6C$  was observed.

## **ACKNOWLEDGMENTS**

The authors would like to thank Messrs. J.W. Jones and J.J. Duff for technical support. Particular thanks go to Mr. L.T. Gibson for the preparation of TEM specimens for microstructural examination. This research was supported in part by an appointment to the Oak Ridge National Laboratory Postdoctoral Research Associates Program administered jointly by the Oak Ridge Institute for Science and Education and Oak Ridge National Laboratory.

## **REFERENCES**

- 1) R.L. Klueh, K. Ehrlich, and F. Abe, *J. Nucl. Mater.* **191-194** (1992) 116.
- 2) L.R. Greenwood and C.A. Baldwin, "Neutron Dosimetry and Damage Calculations for the HFIR-CTR-62 and 63 Irradiations", Fusion Reactor Materials Semiannual Report for Period Ending June 30, 1999, DOE/ER-0313/26, 1999, p. 199.
- 3) K.E. Lenox, R.L. Klueh, and R.L. Senn, "Continuing Irradiation of Ferritic Steels: Experiments HFIR-CTR-62 and -63", Fusion Reactor Materials Semiannual Report for Period Ending March 31, 1995, DOE/ER-0313/18, 1995, p. 7.
- 4) N. Yoshida, et al., *J. Nucl. Mater.* **155-157** (1988) 1232.
- 5) D.S. Gelles, in: *Effects of Irradiation on Materials: 14<sup>th</sup> International Symposium*, ASTM STP 1046, Vol. 1, Eds. N.H. Packan, R.E. Stoller, A.S. Kumear (American Society for Testing and Materials, Philadelphia, 1989) p. 73.
- 6) D.S. Gelles, *J. Nucl. Mater.* **233-237** (1996) 293.
- 7) N. Hashimoto and R.L. Klueh, "Microstructural Evolution of 9Cr-2WVTa Steels in HFIR-CTR-62/63 Experiment", Fusion Reactor Materials Semiannual Report for Period Ending June 30, 2000, DOE/ER-0313/28, 2000, p. 147.
- 8) E.A. Little and L.P. Stoter, in: *Effects of Radiation on Materials: 11th Conf.*, ASTM STP-782 (American Society for Testing and Materials, Philadelphia, 1982) p. 207.
- 9) P.J. Maziasz, R.L. Klueh and J.M. Vitek, *J. Nucl. Mater.* **141-143** (1986) 929.

- 10) P.J. Maziasz and R.L. Klueh, in: Effects of Radiation on Materials: 14<sup>th</sup> Conf., ASTM STP-1046 (American Society for Testing and Materials, Philadelphia, 1989) p. 35.
- 11) P.J. Maziasz, J. Nucl. Mater. **169** (1989) 95-115.
- 12) P.J. Maziasz, R.L. Klueh, and J.M. Vitek, J. Nucl. Mater. **141-143** (1986) 929.
- 13) P.J. Maziasz and R.L. Klueh, in: Effects of Irradiation on Materials: 14<sup>th</sup> International Symposium, ASTM STP 1046, Vol. 1, Eds. N.H. Packan, R.E. Stoller, A.S. Kumear (American Society for Testing and Materials, Philadelphia, 1989) p. 35.
- 14) D.S. Gelles, J. Nucl. Mater. **233-237** (1996) 293.
- 15) J.J. Kai and R.L. Klueh, J. Nucl. Mater. **230** (1996) 116.
- 16) D.S. Gelles, J. Nucl. Mater. **212-215** (1994) 714.
- 17) N. Hashimoto, E. Wakai, J.P. Robertson, T. Sawai, and A. Hishinuma, J. Nucl. Mater. **280** (2000) 186.
- 18) E.H. Lee and L.K. Mansur, Phil. Mag. **A61** (1990) 751.
- 19) D.S. Gelles, in: Effects of Irradiation on Materials: 18<sup>th</sup> International Symposium, ASTM STP 1325 (American Society for Testing and Materials, West Conshohocken, PA, 1999) p. 899.
- 20) R.L. Klueh, M.A. Sokolov, K. Shiba, and J.P. Robertson, J. Nucl. Mater. **283-287** (2000) 478.

## **4.0 COPPER ALLOYS**

**TRUE STRESS-STRAIN BEHAVIOR OF AS-IRRADIATED AND POST-IRRADIATION ANNEALED PURE COPPER** - D. J. Edwards (Pacific Northwest National Laboratory)\*, B. N. Singh and Palle Toft (Risø National Laboratory)

**OBJECTIVE**

Post-irradiation annealing has been shown to partially restore the work hardening ability of irradiated pure copper, but not to the levels of the original unirradiated material. True stress-strain behavior for the as-irradiated and post-irradiation annealed samples are compared to that of pure copper to further study the work hardening behavior.

**SUMMARY**

Post-irradiation annealing experiments were conducted on neutron-irradiated pure copper (from 0.01 to 0.3 dpa at 100°C) to explore the possibility of mitigating the effects of radiation hardening on the strength and ductility. The post-irradiation annealing (PIA) condition of 300°C for 50 hours yielded mixed results and did not completely remove the effects of irradiation. However, there were changes brought about in the microstructure that led to the removal of the yield point phenomenon and restored some of the unirradiated ductility and work hardening. The true stress-strain curves have been calculated for both the as-irradiated and the PI annealed Cu and compared to that of the unirradiated pure copper.

The true stresses at which the as-irradiated samples begin to neck (based on the engineering stress-strain curves) are similar for the 0.1 to 0.3 dpa samples and are similar to that of the unirradiated copper. On the other hand, the as-irradiated 0.01 dpa condition and all of the post-annealed conditions begin necking at lower stresses, but at similar strains. The work hardening rate in the as-irradiated copper (0.1 to 0.3 dpa), when compared on Kocks-Mecking plots, shows that after a few percent strain, the macroscopic work hardening behavior mimics that of the unirradiated pure copper in the latter stages of work hardening. The PI annealing does little to restore the elongation compared to the as-irradiated state, yet lowers the yield strength, removes the yield point phenomenon and causes the material to begin necking at a lower stress.

Further work is needed to understand the dislocation interactions (annihilation and storage of dislocations during plastic deformation, sweeping of the defects introduced during irradiation) that produce a situation where the PIA samples neck at similar strains but lower stresses than that of the as-irradiated. Compression testing is offered as a method to extend the mechanical properties testing to minimize the geometrical instabilities inherent in the tensile testing and explore the full range of work hardening up to failure.

**PROGRESS AND STATUS**

Introduction

Over the past 7 years a series of studies [1-7] have been conducted exploring the effects of neutron irradiation at different temperatures on pure copper and various copper alloys, most notably the precipitation strengthened CuCrZr and CuNiBe alloys and the ODS alloy GlidCop Cu-Al<sub>2</sub>O<sub>3</sub>. The irradiation experiments on pure copper included a study directed at using post-irradiation annealing to remove the effects of radiation hardening at 100°C and restore

---

\* Pacific Northwest National Laboratory (PNNL) is operated for the U.S. Department of Energy by Battelle Memorial Institute under contract DE-AC06-76RLO-1830.

both ductility and work hardening to the copper. The results of this post-irradiation annealing experiment were recently reported elsewhere [7], and will only be summarized here for background.

Pure copper, when irradiated at 100°C, hardened such that the yield strength increased by a factor of 6-10 compared to unirradiated pure copper, with a saturation in the change in yield stress occurring at ~0.1 dpa. At doses of 0.01 dpa and higher, a sharply defined yield point or yield point phenomenon with a yield plateau appeared while the uniform strain to necking and total elongation decreased sharply. This radiation hardening and loss of ductility appear to be related to the fine-scale defects produced during irradiation in the form of small dislocations loops and small stacking fault tetrahedra (SFT). Raft-like agglomerates of loops also formed, yielding a microstructure that appeared to have a dislocation network at lower magnifications. Characterization of the deformed microstructure revealed that deformation in the as-irradiated copper samples occurred predominately by a localized deformation mode called dislocation channeling. This mode of deformation involved a finite volume of material (narrow bands) being swept clear of irradiation-produced defects by moving dislocations, with little deformation in the areas between the channels. The as-irradiated materials exhibited good reduction in area and failed in a ductile manner according to the fractography.

Post-irradiation annealing served to remove the upper-lower yield point and restore some measure of the uniform strain and work hardening, but not to the levels of the unirradiated copper. In fact, despite the change in the strength and work hardening, the strains at which necking and failure occurred were only slightly higher than that of the as-irradiated copper. The microstructural characterization revealed that annealing did not remove the defects produced by irradiation, instead it led to a ripening of the SFT defect microstructure and produced large prismatic loops thought to be interstitial in nature. Accompanying the prismatic loops was a dislocation network that presumably evolved from the agglomerated loops formed during irradiation. Annealing also led to the migration of grain and twin boundaries that effectively swept entire regions free of defects, producing soft regions with a low density of dislocations. Deformation in the PIA materials occurred by a mixture of ill-defined channeling and dislocation interactions throughout the bulk of the material. The failure modes were always ductile in nature, often exhibiting good reduction in area.

The following sections detail an analysis aimed at further investigating the work hardening and the overall macroscopic tensile response before and after post-irradiation annealing and comparing it to the unirradiated behavior.

### Experimental

The material used in the present investigation was a thin (0.3 mm) sheet of oxygen-free high conductivity (OFHC) copper containing 10, 3, < 1 and < 1 ppm, respectively, of Ag, Si, Fe and Mg. The oxygen content of this copper was found to be 34 appm.

Tensile samples of OFHC copper were irradiated in the DR-3 reactor at Risø National Laboratory (see reference 1 for tensile geometry). Prior to irradiation, the OFHC copper samples were given a solution annealing treatment of 550°C for 2 hour in a vacuum of  $10^{-6}$  torr. The resulting grain size and dislocation density were about 30  $\mu\text{m}$  and  $\sim 10^{12} \text{ m}^{-2}$ , respectively. The tensile specimens were irradiated at 100°C to different dose levels in the range 0.01 to 0.3 dpa (NRT). All specimens were irradiated with a displacement damage rate of  $\sim 5 \times 10^{-8}$  dpa (NRT)/s. A subset of the irradiated specimens were given a post-irradiation annealing treatment of 300°C for 50 hours under vacuum ( $< 10^{-5}$  torr). Unirradiated, as-irradiated and post-irradiation annealed specimens were tensile tested in an

Instron machine at a strain rate of  $1.2 \times 10^{-3} \text{ s}^{-1}$ . Tensile tests were carried out at  $100^\circ\text{C}$  in vacuum ( $< 10^{-4}$  torr). The test temperature of  $100^\circ\text{C}$  was reached within 30 min.

## Results

### *True Stress-Strain Curves*

For the analysis of the work hardening behavior, the engineering stress-strain curves were converted to true stress-strain using the assumption of constancy of volume and homogeneity of strain along the gage length of the specimen up the point of necking [8]. The true stress  $\sigma$  and true strain  $\epsilon$  are therefore calculated according to the following equations:

$$\sigma = s(e + 1) \quad \text{eq. 1}$$

$$\epsilon = \ln(e + 1) \quad \text{eq. 2}$$

where  $s$  is the engineering stress and  $e$  the engineering strain [8]. These two equations are only valid to the point of necking, after which the actual dimensions of the specimens need to be measured to determine the true stress and strain. In this report, the true stress-strain curves are calculated only to the ultimate stress in the engineering stress-strain curves since the actual reduction in area was not measured once the material began necking. The true stress-strain curves presented in this report reflect the plastic strain only, that is, the machine compliance and Young's modulus have been removed from the curves.

The engineering and true stress-strain curves for the as-irradiated samples are provided in Figures 1 and 2. Both types of curves demonstrate that the as-irradiated samples exhibit a sharp yield point at 0.01 dpa which further evolves into an upper and lower yield point followed by a small yield plateau at 0.1 dpa and higher. In the engineering stress-strain curves the as-irradiated samples harden to much higher levels than the unirradiated material, that is, the yield and ultimate stresses are much higher. However, the true-stress strain curves give a somewhat different perspective in that the ultimate stress of the unirradiated copper matches that of the as-irradiated samples at 0.1 dpa and higher. The macroscopic strain at which the as-irradiated samples begin to neck is considerably lower than that of the unirradiated material. The 0.01 dpa sample necks at a much lower stress, but at a similar strain to that of the higher dose samples.

Post-irradiation annealing alters the tensile behavior as illustrated in Figures 3 and 4. The yield point behavior is clearly removed for all doses and some fraction of the work hardening restored. None of the conditions, however, were completely restored to the unirradiated state for this annealing condition. The true stress-strain curves shown in Figure 4 further demonstrate that annealing leads to little improvement in the strain to necking for those specimens irradiated to 0.1 dpa or higher. The lowest dose specimen did exhibit a significant improvement in the strain to necking. The true stresses at which the PI annealed samples begin to neck are almost identical to the true yield stresses in the as-irradiated samples.

### *Kocks-Mecking Plots ( $\partial\sigma/\partial\epsilon$ versus $\sigma$ )*

Plotting the work hardening rate  $\partial\sigma/\partial\epsilon$  against the true stress  $\sigma$  allows one to compare the work hardening behavior of the unirradiated pure copper, the as-irradiated and PI annealed conditions. These type of plots also show where the instability criterion  $\partial\sigma/\partial\epsilon = \sigma$  takes affect and causes the tensile specimen to begin necking in tension. The intersection of the individual curves with the straight line represents the stress beyond which the material has

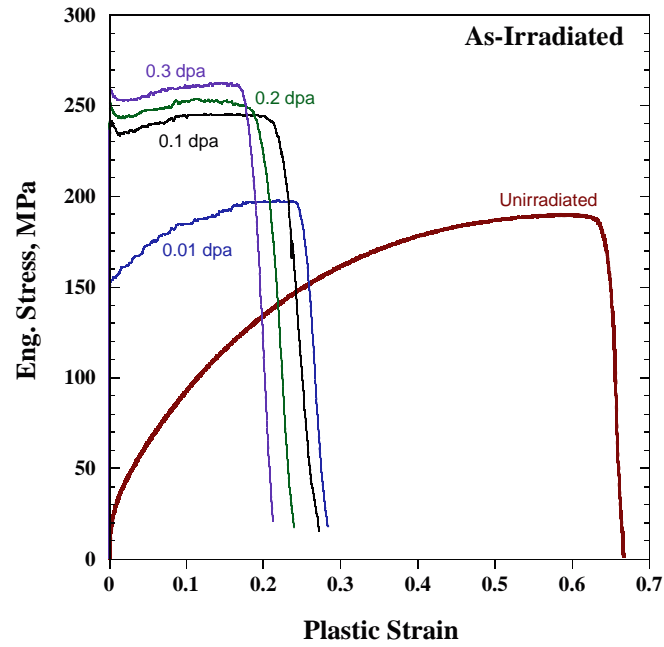


Figure 1. Engineering stress-strain curves for the as-irradiated pure copper and the unirradiated copper.

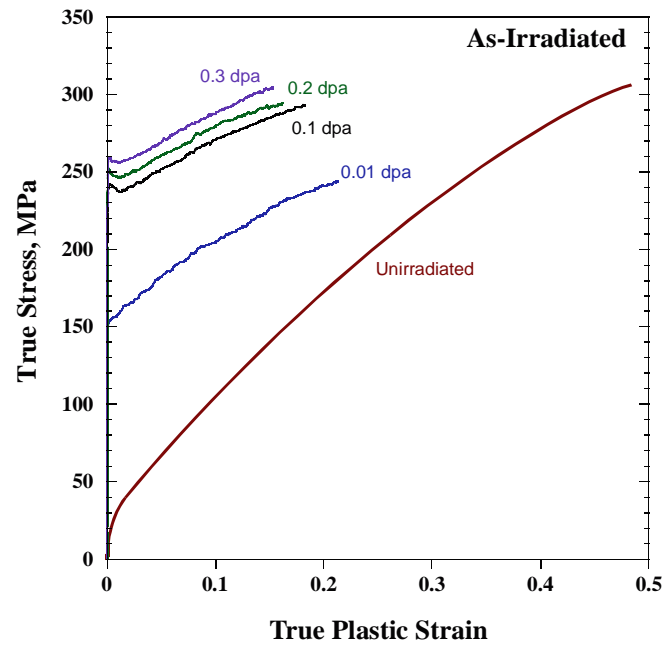


Figure 2. True stress-strain curves derived from the engineering stress-strain curves for the as-irradiated pure copper and the unirradiated copper. The tensile curves demonstrate the as-irradiated samples begin necking at stresses similar to that of the unirradiated copper when irradiated to 0.1 dpa or above.

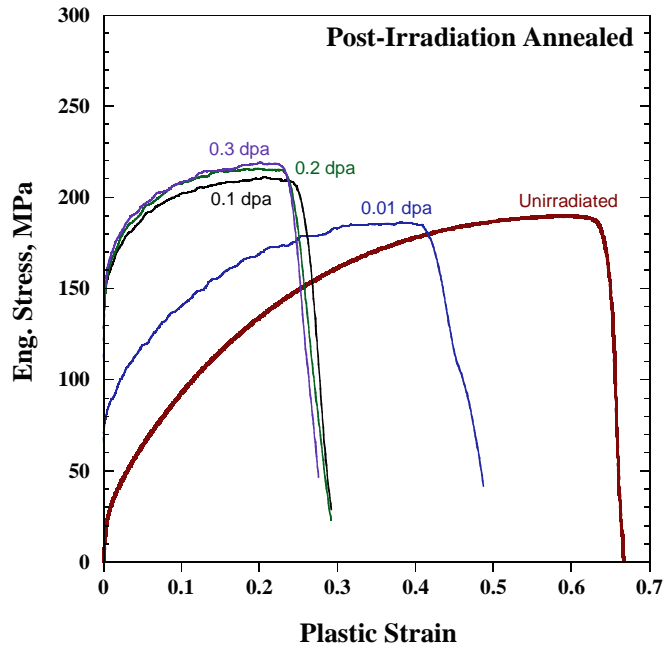


Figure 3. Engineering stress-strain curves for pure copper given a post-irradiation annealing treatment at 300°C for 50 hours.

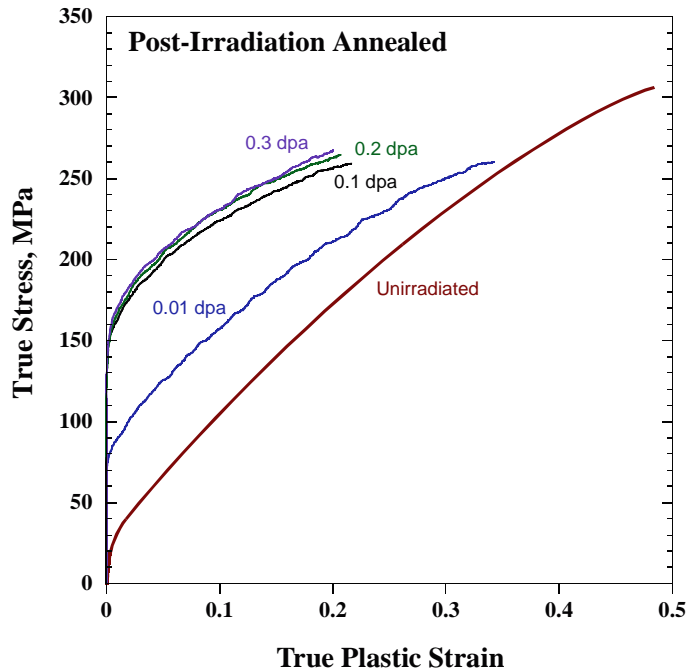


Figure 4. True stress-strain curves after post-irradiation annealing. Annealing lowers the yield stress and removes the yield point phenomenon. Strain to necking is similar to that of the as-irradiated samples, but the stress at which necking occurs is lower.

begun to neck (ultimate stress on the engineering curves). Figures 5 and 6 show these plots for the as-irradiated samples and the PI annealed samples as compared to the work hardening behavior of the unirradiated material.

In the case of the as-irradiated samples (Figure 5), it is clear that significant changes occur between 0.01 dpa and the higher doses. As the dose increases the stress at which necking occurs shifts upward to match that of the unirradiated material and the work hardening rate begins to mimic that of the unirradiated material after a few percent strain. While these curves were generated from a single tensile test result at each condition, and some scatter in the behavior should be expected, the trends are quite clear. The K-M plots show that a few percent strain allows the as-irradiated materials (0.1 dpa and above) to begin behaving macroscopically like unirradiated pure copper in the latter stages of work hardening.

The PI annealed materials (Figure 6) behave differently in that they converge to the same stress point on the instability criterion line, albeit lower than the unirradiated copper and the as-irradiated copper ( $\geq 0.1$  dpa). The work hardening rate for each condition is different in the early stages of deformation, but eventually each converges to follow a common work hardening rate that changes little with dose. Interestingly enough, the work hardening rate in the 0.01 dpa, as-irradiated condition follows roughly the same behavior as that of the PI annealed samples.

For additional comparison, K-M plots were made of several different copper alloys whose tensile properties have been reported in earlier reports [8,9]. These specimens were flat sheet specimens with a somewhat different gage cross-section than those reported for the irradiated pure copper. Figure 7 shows a comparison of the work hardening rate of these various materials and how they compare to the behavior of the as-irradiated conditions and unirradiated copper shown previously. The solution annealed CuCrZr is a solution

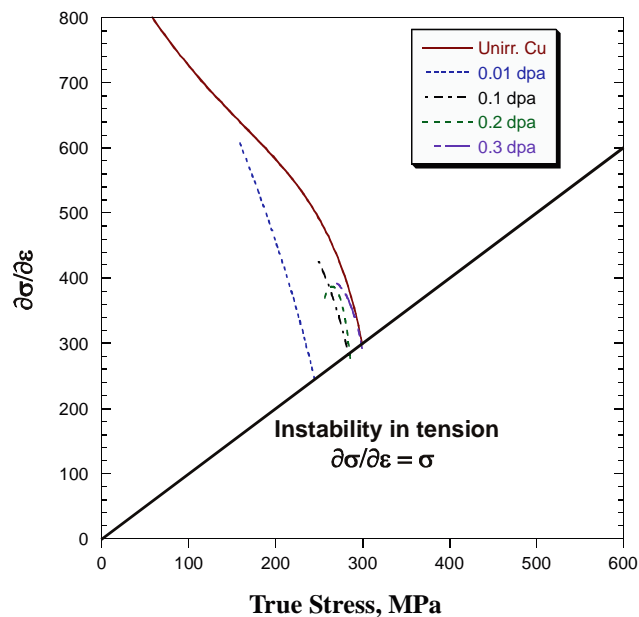


Figure 5. The Kocks-Mecking plots reveal the changes in work hardening with increasing stress in the as-irradiated materials. As the neutron dose increases, the macroscopic work hardening rate begins to match that of the pure copper in the unirradiated state.

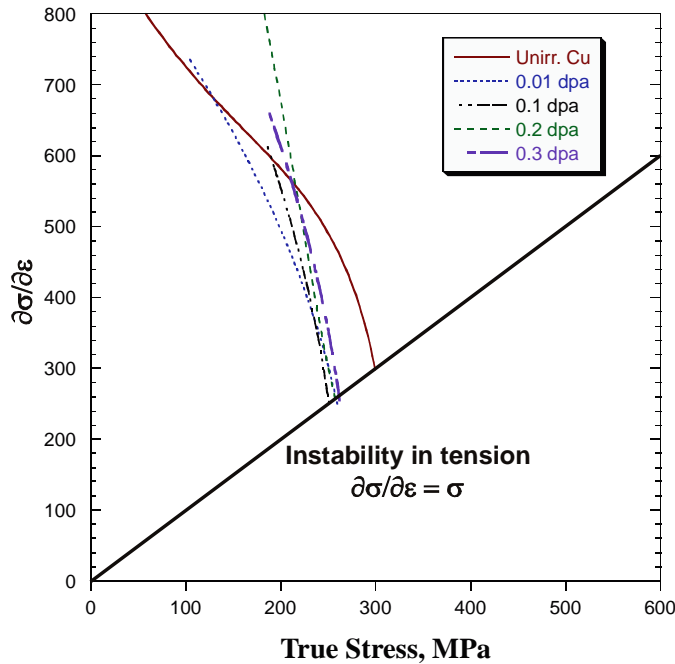


Figure 6. The Kocks-Mecking plots reveal the changes in work hardening with increasing stress after post-irradiation annealing. The work hardening rate is somewhat lower compared to the high dose as-irradiated samples and unirradiated samples, and all samples converge to the same necking stress.

strengthened alloy that possesses a higher yield strength than the pure copper, but work hardens to roughly the same levels. Ageing of the CuCrZr shows that the precipitation strengthening changes the overall response in regard to both the yielding, the work hardening rate and stress at which necking occurs. The CuNiBe alloy (AT condition) is a much higher strength copper alloy far removed from the behavior of the other materials. The final alloy is the oxide dispersion strengthened GlidCop Al25, which behaves in much the same manner as the aged CuCrZr. The main conclusion to draw from these comparisons is that irradiation, despite leading to large increases in the yield strength, does not produce obstacles that are close to the effectiveness of the precipitate particles or oxide dispersions.

### Discussion

The true stress-strain behavior and the K-M plots appear to indicate that despite a dramatic difference in yield strength and yielding behavior in the as-irradiated copper, the irradiated materials are “conditioned” in the early stages of deformation such that a few percent strain allows the as-irradiated materials to behave similarly to the unirradiated copper. This is based on the macroscopic behavior as measured from the tensile test and assumes that the strain is distributed homogeneously over the specified gage length of the sample. These plots demonstrate that the influence of highly localized deformation (dislocation channeling) is not so easy to distinguish from a macroscopic work hardening standpoint. The 0.2 mm/mm plastic strain (20% elongation) present in the as-irradiated samples (up to necking) implies considerable dislocation motion, yet the deformed microstructures reported by Singh et al. [7] did not show any significant dislocation motion in many areas of the sample. Therefore questions arise concerning the reconciliation of the apparently small degree of homogeneous dislocation motion and the relatively large strains to necking. The answers likely are found in

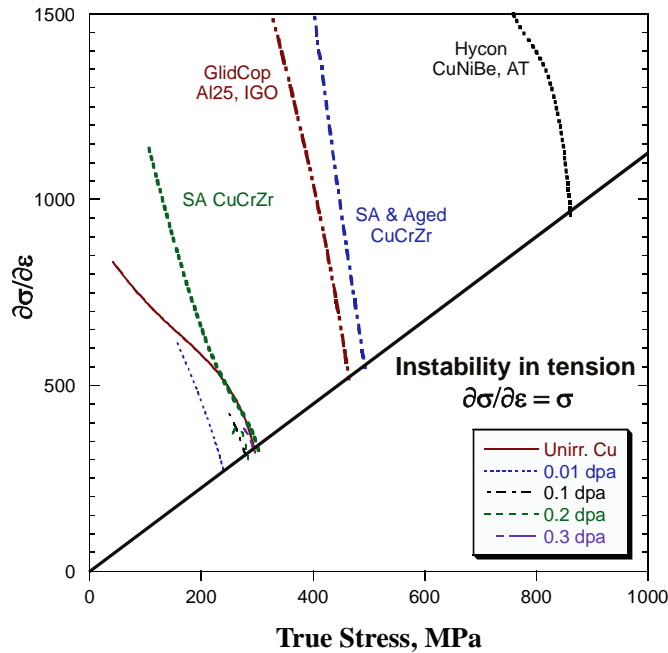


Figure 7. These K-M plots compare the work hardening rates of the as-irradiated pure copper and the unirradiated pure copper to that measured for several different unirradiated copper alloys. Precipitation and oxide dispersion strengthening are clearly more effective in altering the stress-strain response by providing more stronger obstacles that cannot be easily annihilated.

the details of the dislocation storage and annihilation mechanisms that operate once yielding begins and how the clearing of the channels occurs and relates to the dislocation evolution. Since unirradiated copper will form a cellular dislocation network whereas the as-irradiated copper does not, it seems obvious that the mechanisms are different, yet appear to result in the same macroscopic response.

The PI annealed samples and the lowest dose as-irradiated samples raise additional questions since these materials exhibit a decidedly different tensile response. The cause for the onset of necking at lower strains and somewhat lower stresses is not yet known, but bears further investigation. The microstructural characterization of the deformed PI annealed samples ( $\geq 0.1$  dpa) indicated that deformation occurred via a mixture of channeling and deformation in-between the channels. The 0.01 dpa PI annealed sample exhibited a deformation substructure similar to that of the unirradiated copper, that is, it contained a strongly developed cellular dislocation structure. The removal of the yield point phenomenon was attributed to a decrease in the degree of dislocation decoration by small loops and any impurities in the system. This allowed a more homogeneous production of dislocations, but the presence of channeling even in the PI annealed samples indicates that the dislocation sources still remain pinned to some degree.

The data shown here illustrate that considerable uncertainty exists concerning the exact mechanisms that occur during deformation after yielding. It seems that the tensile test introduces a further complication since the onset of necking disguises any further work hardening that may occur. The data tends to suggest that in a macroscopic sense work softening does not occur in this materials when irradiated at  $100^{\circ}\text{C}$ , but different tests are

needed to further study this. As compression testing does not lead to necking or tensile instability, this test method may provide more information on the work hardening behavior to much higher strains.

One final point to consider is that at a lower irradiation temperature of 47°C pure copper was observed to begin necking after yielding with no measurable uniform strain [1]. It is interesting to note that the maximum stress in this case was around 320 MPa, similar to the stresses found to cause necking in the tensile samples irradiated at 100°C that are reported in this study. This suggests that at lower temperatures, radiation hardening increases the yield strength to the point that upon yielding, the tensile specimens have already reached the instability criteria at small strains and will therefore neck.

### **FUTURE WORK**

The preliminary analysis shown here of the true stress-strain behavior of the as-irradiated copper and PI annealed copper indicates that further analysis of the mechanism of channeling and its effects on the macroscopic strain response to the material bear further investigation. Attempts will be made to relate microstructural observations to the tensile behavior to explain the conditions that lead to necking at lower stresses in the post-irradiation materials for strains similar to that observed in the as-irradiated materials.

### **ACKNOWLEDGEMENTS**

D. J. Edwards would like to thank J. D. Embury and R. G. Hoagland for their helpful discussions regarding the work hardening analysis. The present work was partly funded by the European Fusion Technology Programme. The authors wish to thank B. F. Olsen for the tensile testing in the original experiment. D.J. Edwards' work was also partly supported by the U.S. Department of Energy under contract DE-AC06-76RLO 1830 with the Battelle Memorial Institute at the Pacific Northwest National Laboratory.

### **REFERENCES**

- [1] B. N. Singh, A. Horsewell, P. Toft, and D. J. Edwards, *J. of Nucl. Mater.*, 224, (1995), p. 131.
- [2] B. N. Singh, D. J. Edwards and P. Toft, *J. Nucl. Mater.* 238 (1996) 244.
- [3] B. N. Singh, D. J. Edwards, M. Eldrup and P. Toft, *Journal of Nucl. Matls.* 249 (1997), p. 1.
- [4] B. N. Singh, D. J. Edwards, M. Eldrup and P. Toft, Effect of Bonding and Bakeout Thermal Cycles on the Properties of Copper Alloys Irradiated at 350°C, Risø-R-971 (EN), Risø National Laboratory, Roskilde, Denmark, September (1997).
- [5] D. J. Edwards, B. N. Singh, P. Toft, and M. Eldrup, *J. Nucl. Mater.* 258-263 (1998) 978.
- [6] B. N. Singh, D. J. Edwards, M. Eldrup and P. Toft, *Journal of Nucl. Matls.* 295 (2001) pp. 1-15.
- [7] B. N. Singh, D. J. Edwards and P. Toft, accepted for publication in the *Journal of Nuclear Materials*, 2001.

- [8] G. E. Dieter, Mechanical Metallurgy, 3<sup>rd</sup> Edition, McGraw-Hill, 1986, pp. 284-290.
- [9] D. J. Edwards, Fusion Materials Semiannual Progress Report for the Period ending December 31, 1997, DOE/ER-0313/23, (Oak Ridge National Laboratory), p. 213.
- [10] D. J. Edwards, Fusion Materials Semiannual Progress Report for the Period ending December 31, 1998, DOE/ER-0313/25, (Oak Ridge National Laboratory), p. 185.

## **5.0 REFRACTORY METALS AND ALLOYS**

No contributions.

## **6.0 AUSTENITIC STAINLESS STEELS**

**DETERMINATION OF THE LOWER TEMPERATURE LIMIT OF VOID SWELLING OF STAINLESS STEELS AT RELATIVELY LOW DISPLACEMENT RATES** - S.I. Porollo, Yu.V. Konobeev, A.M. Dvoriashin, and V.M. Krigan (Institute of Physics and Power Engineering, Russia), F. A Garner (Pacific Northwest National Laboratory)\*

**OBJECTIVE**

The purpose of this effort is to determine the lower temperature limit of void swelling in austenitic steels.

**SUMMARY**

An issue of current interest to PWRs is the possibility that void swelling of austenitic near-core internal components may exert some deleterious effect on component functionality, particularly during extended operation to 60 years. A similar concern has also been raised for water-cooled fusion devices. One question of particular interest is the range of temperature over which void swelling can occur, since the internal components experience temperatures from ~290 to perhaps as high as 390°C in some limited locations. This question was addressed using a flow restrictor component from the low-flux breeder zone of the BN-350 fast reactor in Kazakhstan. This component was constructed of annealed 12X18H10T, an alloy similar to AISI 321 which is used in Russian reactors for applications where AISI 304L would be used in comparable Western and Japanese reactors. Extensive sectioning to produce 114 separate specimens, followed by examination of the radiation-induced microstructure showed that void swelling in the range of temperatures and dpa rates of PWR interest occurs down to ~305°C. At 330°C the swelling reached ~1% at 20 dpa. Comparison of these data with other published results from Russian LWR reactors at <10 dpa confirms that the lowest temperature that stainless steels can begin swelling appears to be ~300°C. Since fusion and PWR spectra generate similar levels of hydrogen and helium, it is expected that these conclusions are also applicable to fusion devices operating at comparable dpa rates.

**INTRODUCTION**

Voids as a new type of radiation defect were discovered in 1967 to form in austenitic stainless steel fuel pin cladding after irradiation in the Dounreay Fast Reactor [1]. Since that time thousands of scientific papers have been written on this subject, with most data derived from fast reactors, some high-flux thermal reactors and experiments utilizing charged particle irradiations at very high damage rates. An extensive summary of swelling data for stainless steels is presented elsewhere [2].

For a long time it was assumed that neutron-induced void formation was characteristic only of fast reactor or test reactor irradiation with very high atomic displacement rates and elevated irradiation temperatures of 370 to 650°C. Recently, however, new insight and data became available showing that void formation may occur in the internal structural components of Western PWR and Russian VVER internals, which operate at lower temperatures (280 to 430°C) and significantly lower neutron fluxes [3-12]. In spite of these low fluxes these components can accumulate damage exposures during typical reactor life times (30-40 years) as high as 50-100 dpa. Similar conditions can be found in some fusion device designs.

---

\* Pacific Northwest National Laboratory (PNNL) is operated for the U.S. Department of Energy by Battelle Memorial Institute under contract DE-AC06-76RLO-1830.

In addition to dimensional changes, the swelling in structural materials of PWR and VVER internals (in particular, austenitic stainless steels such as AISI 304 in PWRs and X18H10T in VVERs) may lead to the generation of mechanical stresses caused by the non-uniformity of swelling over each component, and also to severe void-induced embrittlement for swelling levels above approximately 10% [2, 13].

The upper temperature limit of void formation is related to the lower supersaturations of vacancies at high temperatures. The lower temperature limit of void formation is thought to arise from low vacancy mobility and/or to the inability of vacancies to aggregate and nucleate voids. It is the lower temperature limit that is of interest to PWRs and VVERs. Is it possible that void swelling can occur over all or a large portion of the PWR, and VVER fusion operating temperature range?

Available data at high damage exposure on swelling of AISI 304 stainless steel in fast reactors are in general limited to temperatures above 380°C, reflecting the relatively high inlet coolant temperature of Western fast reactors. It is therefore very desirable to collect high fluence data at lower PWR-relevant temperatures and hopefully at lower PWR-relevant damage rates. Since the overwhelming majority of data on AISI 304 and 304L were generated in EBR-II with an inlet temperature of 370°C, no additional PWR-relevant data can be obtained without destructively examining actual PWR components. However, it is possible to examine X18H10T components removed from both fast reactors and VVER reactors from the former states of the Soviet Union, choosing components that operated at PWR-relevant conditions. Since the overall swelling behaviors of all stainless steels are in general similar (2), it is thought possible to use data on this Russian steel to infer the lower temperature limit of swelling of AISI 304L in PWRs of Western or Japanese design.

The present paper presents the final results of a microstructural study designed to determine the swelling of type 12X18H9T austenitic stainless steel after long-term irradiation at PWR-relevant damage rates in the BN-350 fast reactor in Kazakhstan at temperatures ranging from 280°C to 334°C to doses from 4 to 56 dpa. A previous paper presented the initial results of this experiment [12]. A comparison will also be made with results from other Russian reactors at comparable irradiation conditions.

The path chosen in this experiment was to assess the lowest temperature at which swelling could occur over a range of dpa rates and temperatures relevant to PWR internals and some fusion conditions. Transmission electron microscopy of many small specimens was used to determine the swelling, even at very low levels, avoiding resolution problems associated with bulk measurement techniques such as immersion density.

#### 1. *Material and irradiation conditions.*

To study the swelling of type 12X18H9T steel after low-temperature neutron irradiation, one of the out-of-core components of BN-350 was chosen. This component served as a flow restrictor to the sodium coolant in the breeder zone. The component was a hexagonal tube of 96 mm flat-to flat size, having a central cylindrical hole 65 mm in diameter. The total length of the flow restrictor component equals the 3.435 m length of reference driver subassemblies of the BN-350 fast reactor.

This flow restrictor component was made from annealed type 12X18H9T austenitic stainless steel of the following nominal specification (wt. %): C ≤ 0.12; Cr, 17-19; Ni, 8-9.5; Mn ≤ 2; Si ≤ 0.8; Ti, 0.5-0.7. The nearest Western equivalent to this steel is AISI 321 stainless steel. The composition of the examined component was confirmed using an "Kamebax" x-ray

micro-analyzer in scanning mode on an irradiated specimen and found to have the following composition (wt.%): Cr, 18.5; Ni, 9.5; Mn, 1.5; Si, 0.6-0.8; Ti, 0.6-0.7. Thus, the measured composition falls within the specification.

The component was exposed without removal or rotation for 46,536 h (November, 1972 till June, 1984) in the breeder zone of the BN-350 reactor at a radial distance of 94.5 cm from the core axis. The maximum neutron fluence at the core midplane was equal to  $3.3 \times 10^{23}$  n/cm<sup>2</sup> (E>0) or  $1.6 \times 10^{23}$  n/cm<sup>2</sup> (E>0.1 MeV). This fluence in the softer neutron spectra of the out-of-core region corresponds to a neutron damage dose of 56 dpa. Hence, the maximum dose rate was  $1.56 \times 10^{-7}$  dpa/s, comparable to the damage rate experienced by the re-entrant corners of many PWR baffle plates at mid-core levels. The lowest dose regions of the restrictor explored in this experiment reached ~4 dpa at  $1.12 \times 10^{-8}$  dpa/s, a damage rate comparable to that experienced by many regions of PWR former plates and core barrel.

The distribution of irradiation temperatures for both the inboard and outboard flats of the flow restrictor are shown in Table 1. The irradiation temperatures in the component were calculated at the average 60% nominal reactor capacity for the period from 1973 to 1984. The inlet sodium temperature in the core was 280°C. All calculated temperatures are judged to be accurate within  $\pm 3^\circ\text{C}$ .

There is a somewhat complicated distribution of neutron fluence, dose, and irradiation temperature throughout the component. Due to different cooling conditions the maximum difference of temperature between internal and outer component surfaces reaches 30°C, the neutron fluence and dose between two arbitrary points in a cross section of the component might differ by roughly a factor of two.

## 2. Specimen preparation

In the hot cell of the BN-350 facility the flow restrictor component was cut into 5 pieces, each of 300 mm length. Sections #1, 3 and 5 (see Fig. 2) corresponding to the bottom, middle and top parts of the component were transported to the IPPE laboratory in Obninsk, Russia. Fig. 1 illustrates the range of dose-temperature irradiation conditions for each component piece. The areas of the map corresponding to absent pieces are shaded. As shown in Fig. 1, the accessible area of dpa values and irradiation temperatures has a complicated form, and is bounded by doses of 4 and 56 dpa, and irradiation temperatures of 282 and 335°C. The dpa-temperature areas corresponding to the three different pieces of the component overlap partially, allowing one to get some information which might have been obtained from absent pieces #2 and #4.

Table 1: The distribution of irradiation temperature (°C) in different cross sections of the flow restrictor component

Distance from midplane, mm	Outer surface, inboard flat	Internal surface, inboard flat	Outer surface, outboard flat	Internal surface, outboard flat
-750	282	282	281	281
-450	290	287	288	286
-150	306	296	303	293
0	317	302	313	299
+150	324	304	321	301
+450	334	307	333	306
+750	337	307	336	306

To obtain the most complete information on swelling the cutting scheme of the TEM-specimens shown in Fig. 2 was chosen. First, the section was sectioned to produce several slices of ~0.6 cm thickness. To prepare specimens for the electron microscopy investigation (disks of 3 mm in diameter and of 0.3-0.4 mm in thickness) several samples were cut from each edge of the component (7 sets of two specimens) and from the middle of each face (5 sets of two specimens). The scheme of cutting of microscopy specimens shown in Fig. 2 was utilized for the three cross sections located with their centers at distances of 0, -150 and +590 mm from the core midplane. For the cross section with its center located at -670 mm, TEM specimens were cut from only three faces. Such a cutting scheme allowed us to fill rather uniformly the area of the dpa-irradiation temperature map with experimental points (shown as crosses in Fig. 1). A total of 114 specimens were examined by microscopy.

### 3. Microstructure and swelling of the 12X18H9T stainless steel

Data on irradiation conditions and swelling for the cross sections located at distances of -670, -150 and 0 mm from the core midplane are shown in Table 2. Voids were observed in sections -150, 0 and +590 (examples in Fig. 4), but no voids were detected in sections -670 and -450 mm. Fig. 3 shows the dose-irradiation temperature map of void formation observed in the 12X18H9T stainless steel flow restrictor.

Voids, dislocation loops, dislocation segments, two types of precipitates, and deformation stacking faults characterize the microstructure of 12X18H9T steel in the specimens investigated. The dislocation structure of the irradiated steel consists of both faulted and perfect dislocation loops, and also linear dislocations (Fig. 5). The total length of dislocations per unit volume depends slightly on the irradiation temperature.

In the irradiated steel two types of precipitates were observed. The first type was cubical with mean diameter of 59 nm and a rather low concentration of  $5 \times 10^{14} \text{ cm}^{-3}$ . The volume fraction of these precipitates equals 0.72%. From electron diffraction patterns it was determined that these are TiC precipitates, which probably formed in the steel during crystallization, but new precipitates appear to have formed during irradiation. It should be noted that this type of precipitate was observed in all examined sections of the flow restrictor component regardless of temperature or damage dose. The other type of precipitate is very small, finely dispersed precipitates in the grain interior (Fig. 6). An analysis has shown that these precipitates are G-phase. These did not exist prior to irradiation and are well known to be a radiation-induced phase, especially in Ti-modified stainless steels [2]. As shown in Table 3, the diameter of G-phase particles increases in general and the concentration decreases with increasing irradiation temperature.

Along with the defects mentioned above, long stacking faults were often observed in the irradiated steel (Fig. 7), probably due to deformation of TEM specimen foils during preparation.

### 4. Results and discussion

In Figs. 8-10 the temperature dependence is shown of the mean void diameter  $\langle dv \rangle$ , void concentration  $N_v$ , and swelling. Despite the range of dpa and dpa rates in this dose/temperature range it is seen that the mean void diameter increases monotonically with increase of irradiation temperature, with an activation energy of about 1 eV. In contrast

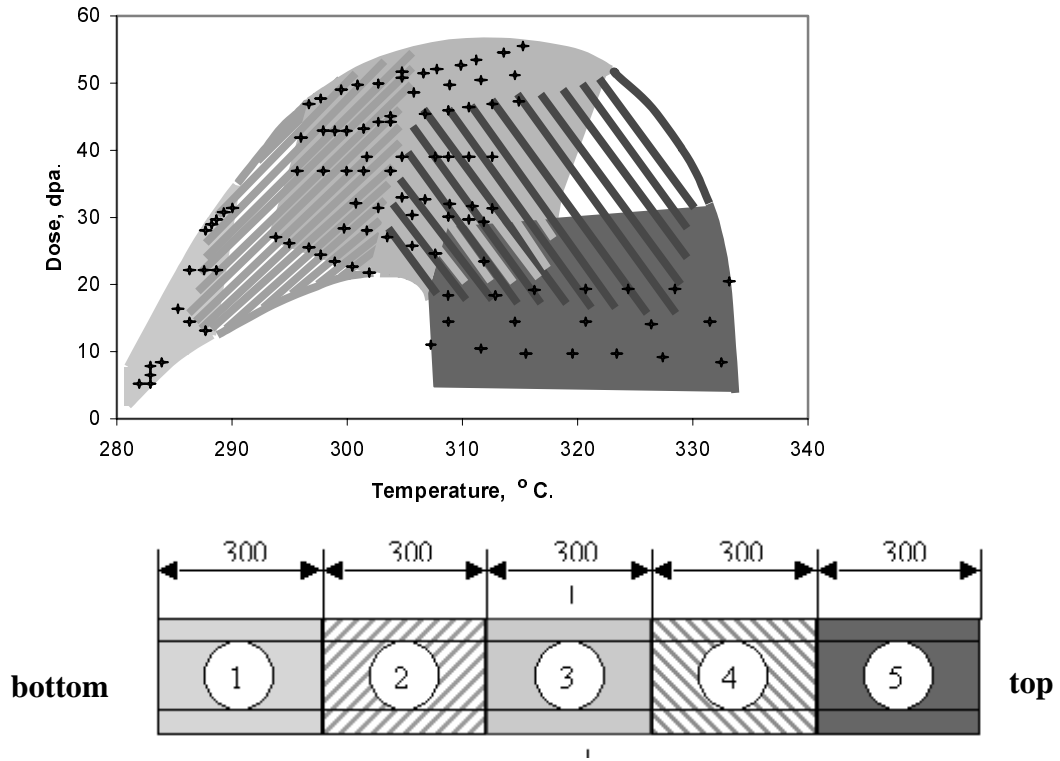


Figure 1. Dose-temperature map of irradiation conditions and the scheme of initial cutting of the flow restrictor component. Dimensions are in mm. The middle of section 3 corresponds to the core midplane. Crosses represent the conditions at which microscopy was performed.

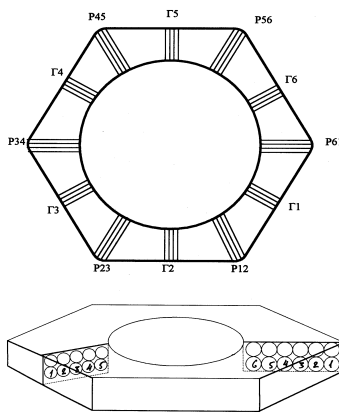


Figure 2. Cutting scheme of microscopy specimens for component cross sections with centers located at distances of 0, -150 and +590 mm from the core midplane. P and  $\Gamma$  are derived from the Russian terms for corner and flat, respectively.

Table 2: Microstructural data

Sample number	Dose, dpa	Temperature, °C	Mean void diameter, nm	Void concentration, $10^{14} \text{ cm}^{-3}$	Void volume fraction, %
-150_P34.1	21.6	302	4.4	Voids in single grains	
-150_P56.3	43.4	302	4.9	0.82	0.0008
-150_P56.3	43.6	302	4.9	0.8	0.001
-150_P61.3	50.3	302	5.1	1.2	0.001
-150_P56.2	43.8	303	4.9	1.9	0.002
-150_P56.2	44	303	4.9	1.9	0.002
-150_P56.1	42.2	304	4.4	1.4	0.00144
-150_P61.2	51.2	304	5.0	1.4	0.02
-150_P56.1	44.5	305	4.4	1.4	0.0014
-150_P61.1	52.1	305	4.8	1.7	0.02
0_P34.4	25.7	306	7.9	1.5	0.006
0_Г4.3	30.5	306	5.2	0.5	0.001
0_P23.4	32.5	307	6.4	0.78	0.002
0_P56.5	45.5	307	4.7	1.96	0.002
0_P61.5	51.7	307	4.7	1	0.001
590_P34.7	10.0	308	9.4	8.4	0.06
+590_P34.7	10.3	308	9.4	8.4	0.06
0_P34.3	24.8	308	9.2	3.1	0.02
0_Г2.3	39.2	308	5.4	0.84	0.001
0_Г5.3	39.2	308	5.3	0.52	0.001
0_P61.4/5	52.1	308	4.9	0.9	0.001
590_Г5.5	13.7	309	9.5	6	0.04
590_Г2.5	13.7	309	8.0	6	0.03
+590_Г2.5	14.1	309	8.3	6	0.03
+590_Г5.5	14.1	309	9.5	6.3	0.04
590_61.7	17.5	309	9.0	8	0.05
+590_P61.7	18	309	9.0	7.9	0.05
0_Г4.2	29.9	309	6.0	0.91	0.002
0_P23.3	32.0	309	8.1	1.2	0.006
0_Г2.2/5	39.2	309	5.4	0.78	0.001
0_P56.4	45.9	309	6.2	4.7	0.01
0_Г1.3	49.8	309	6.0	1.08	0.002
0_P61.4	52.6	310	5.0	1.4	0.002
0_Г4.1/5	29.5	311	7.0	2.1	0.007
0_P23.2	31.6	311	8.5	2.9	0.013
0_Г2.2	39.2	311	6.6	1.7	0.004
0_Г5.2	39.2	311	6.6	1.8	0.005
0_P56.3	46.4	311	6.2	4.75	0.01
+590_P34.6	9.9	312	9.0	21	0.12
0_P34.1	23.0	312	9.0	7.1	0.044
0_Г3.1	29.2	312	8.7	0.28	0.001
0_Г4.1	29.2	312	8.0	2.6	0.012
0_Г1.2	50.6	312	6.6	2.7	0.006
0_P61.3	53.6	312	5.9	4.5	0.009
+590_P61.6	18.3	313	10.1	22	0.19

0_P23.1	31.1	313	9.1	2.1	0.013
0_Г2.1	39.2	313	8.7	0.85	0.004
0_Г5.1	39.2	313	7.2	8.6	0.024
0_P56.2	46.8	313	6.9	13.9	0.037
0_P61.2	54.5	314	6.7	10	0.026
+590_Г2.4	14.1	315	9.0	15	0.09
+590_Г5.4	14.1	315	10.4	18	0.16
0_P56.1	47.3	315	7.0	15.8	0.049
0_Г6.1	51.4	315	7.1	7.9	0.021
+590_P34.5	9.6	316	11.0	38	0.4
0_P61.1	55.4	316	7.1	9.2	0.024
+590_P61.5	18.6	317	11.4	20	0.24
+590_P34.4	9.3	320	13.1	37	0.65
+590_Г2.3	14.1	321	10.4	19	0.18
+590_Г5.3	14.1	321	11.8	22	0.3
560	16.8	321	12.4	12	0.17
+590_P61.4	19	321	12.5	27.5	0.44
+590_P34.3	8.9	324	14.0	27	0.6
+590_P61.3	19.3	325	14.2	22	0.5
+590_Г2.2	14.1	327	11.1	29	0.32
+590_Г5.2	14.1	327	12.8	21	0.35
+590_P34.2	8.6	328	18.0	25	0.95
590_P34.2	8.4	329	18.0	25	0.96
+590_P61.2	19.6	329	14.0	21	0.45
+590_P34-Г4	8.4	332	16.9	22	0.69
+590_Г5.1	14.1	332	15.0	24	0.67
+590_Г2.1	14.1	332	13.8	22	0.47
590	14.5	332	17.3	6.4	0.28
590_P34.1	8.1	333	18.0	18	0.77
+590_P34.1	8.3	333	17.0	20	0.70
590_Г2.1	13.7	333	14.0	22	0.50
590_Г5.1	13.7	333	15.0	24	0.70
590_P61-Г1.1.4	18.8	334	16.7	18	0.65
590_P61-Г1.1.3	19.0	334	14.4	22	0.50
590_61.1	19.4	334	17.0	14	0.50
+590_P61.1	19.9	334	17.0	14	0.49

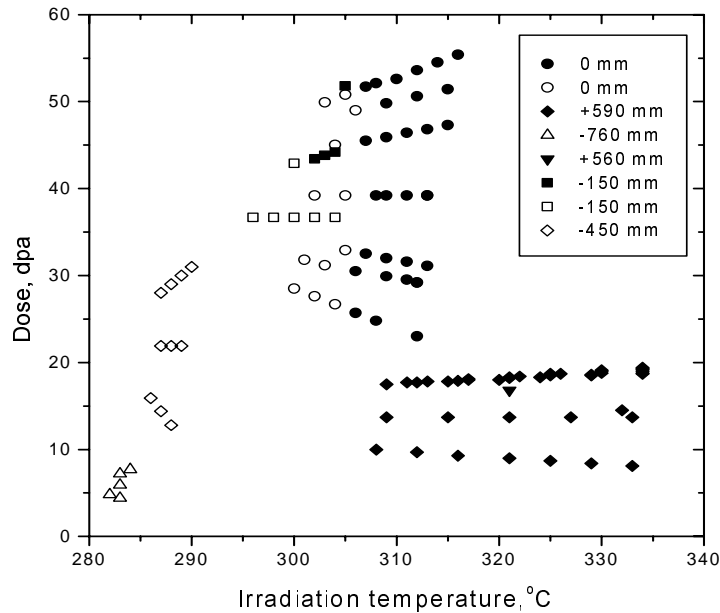


Figure 3. The dose-irradiation temperature map of void formation in the 12X18H9T steel irradiated in BN-350. Solid symbols denote that voids were observed. Open symbols denote the absence of observable voids.

to the mean void diameter, the void concentration appears to behave non-monotonically with increasing temperature. This behavior is thought to reflect primarily the shape of the dose-temperature space shown in Fig. 1, however, rather than any parametric sensitivity of swelling. The range of swelling shown in Figs. 3 and 10 is clearly bounded on the lower temperature side at about  $\sim 305^{\circ}\text{C}$  over the full range of dpa rates examined. Below this temperature no voids were observed, even at  $\sim 50$  dpa.

At a temperature of  $\sim 330^{\circ}\text{C}$  and doses ranging from 8 to 20 dpa the swelling level ranges from  $\sim 0.3$  to 1.0 %, depending on both the dpa and dpa rate. At the highest temperature examined,  $\sim 334^{\circ}\text{C}$ , the swelling ranged from 0.5 to 0.8% at  $\sim 19$  dpa. Most significantly, swelling below  $\sim 305^{\circ}\text{C}$  did not occur even for doses on the order of 50 dpa, indicated that some thermal barrier exists to void nucleation that can not be overcome by continued irradiation, at least to dpa levels that reach a very large fraction of the exposure expected in operating PWRs and VVERs. On the other hand, the region of the PWR baffle/former assembly operating above  $305^{\circ}\text{C}$  comprises a very large fraction of the total.

Neustroev and co-workers have recently published a series of swelling data on this same steel from several LWR reactors, with all data derived at comparably low dpa rates [14]. Fig. 11 shows a comparison of these data with those of the current study. In general, the two

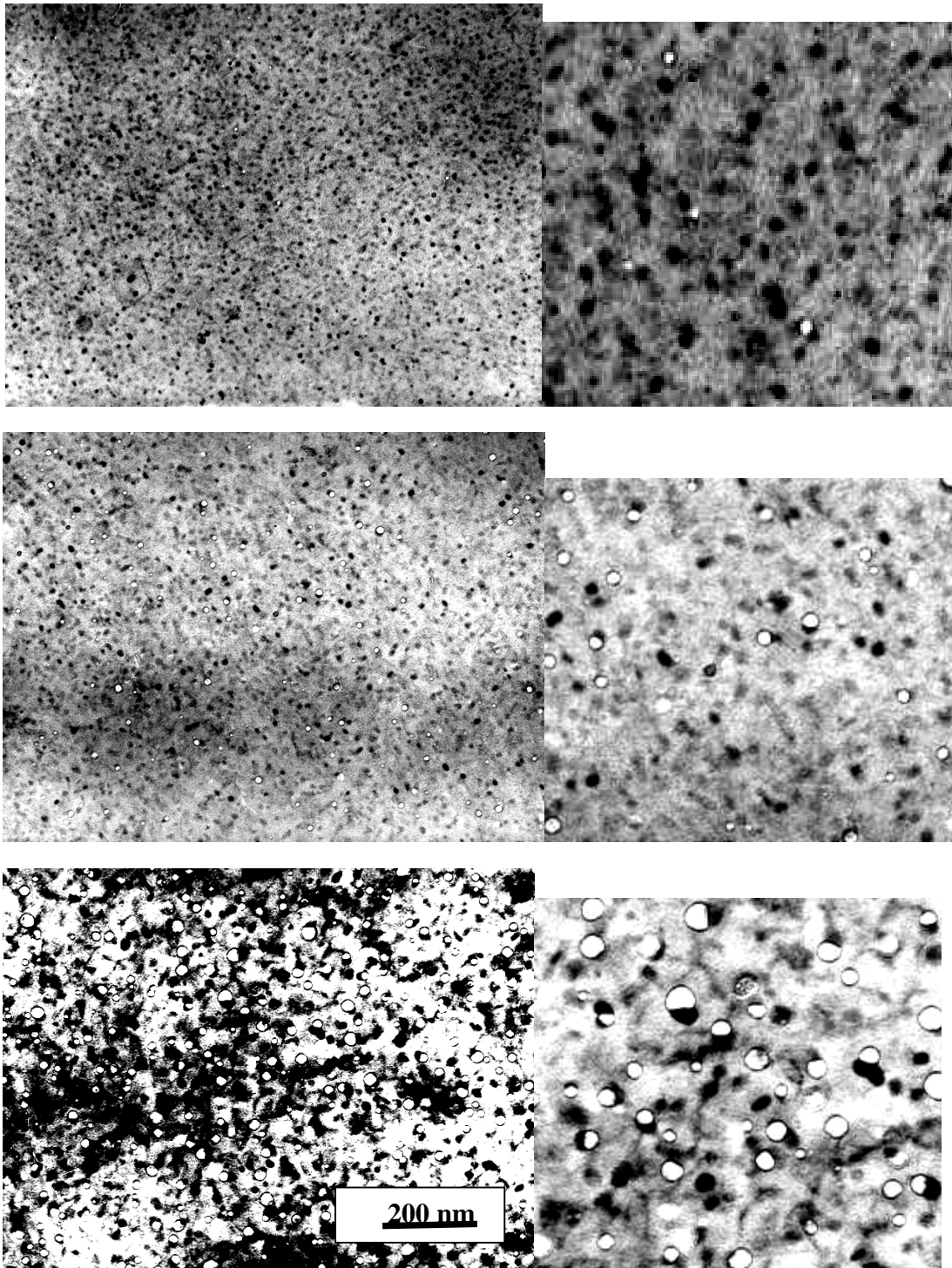


Figure 4. Voids observed in the 12X18H9T steel after neutron irradiation: 1) barely observable at 302°C to 50.3 dpa, 2) more visible at 308°C to only 10.3 dpa, and 3) at 324°C to 8.9 dpa. TiC precipitates are also visible in all conditions. Enlarged views of the central sections are placed on the right side to show finer detail of typical cavities.

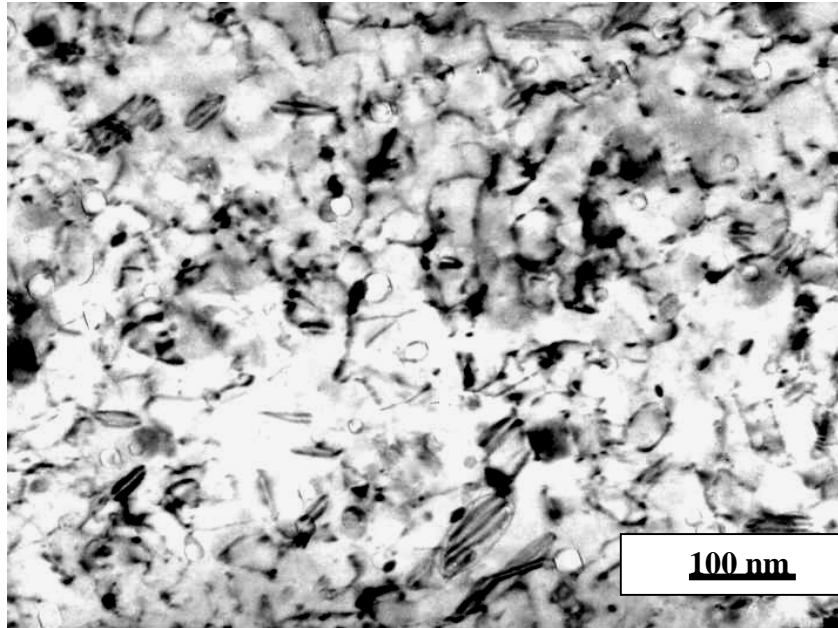


Figure 5. Dislocation structure of 12X18H9T steel after neutron irradiation at 329°C to 19.6 dpa (cross section at +590 mm). Some voids are also visible.

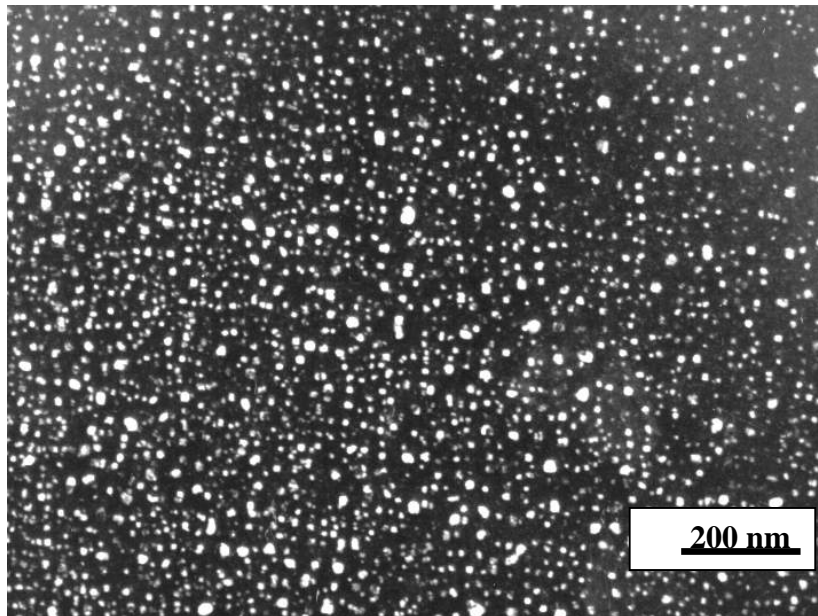


Figure 6. Dark-field image of G-phase precipitates in the 12X18H9T steel after neutron irradiation: at 302°C to 27.6 dpa (cross section at 0 mm).

Table 3. Microstructural data on G-phase

Temperature, °C	Dose, dpa	Mean diameter, nm	Concentration, $10^{16} \text{ cm}^{-3}$	Volume fraction, %
289	30.5	5.5	3.0	0.5
299	23.4	8.0	2.0	0.9
302	27.6	5.0	11.0	0.3
308	24.8	8.0	1.0	0.4
311	10.3	11.0	1.0	1.0
313	10.3	12.0	0.7	0.7
319	9.4	11.0	0.3	0.3
327	9.5	15.0	0.6	0.6

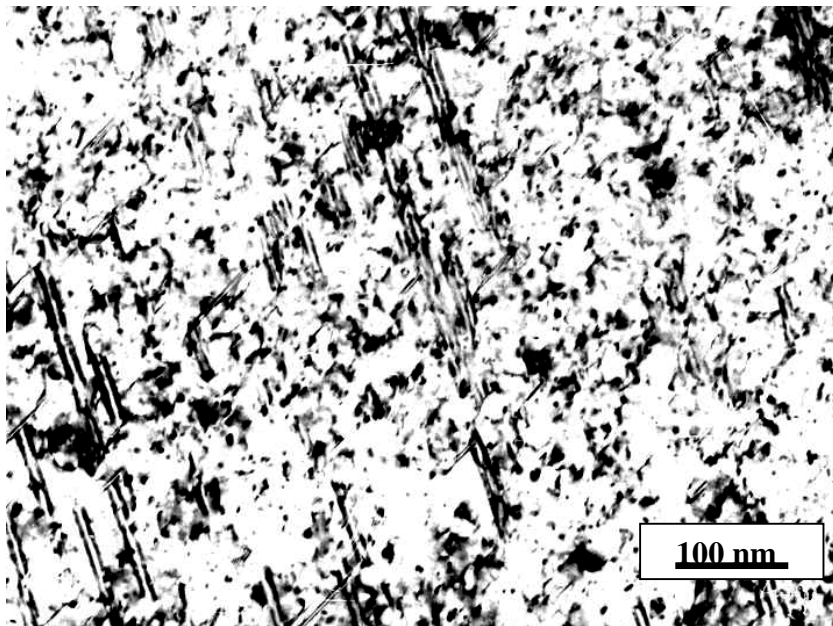


Figure 7. Bright-field image of stacking faults in the 12X18H9T steel after neutron irradiation at 314°C to 54.5 dpa (cross section at 0 mm).

data sets are very consistent, especially in extending the ~305°C swelling/no swelling boundary to lower dpa levels. Once again it appears that 305°C is the lower limit of void formation for this steel at doses of 10 dpa or greater, and that voids can form at doses perhaps as low as 7 dpa at temperatures above the 305°C boundary.

Garner and co-workers have also published swelling data on various Russian stainless steels from both fast reactors and water-moderated reactors operating at PWR-relevant dpa rates [3,6-12]. Many of these data also support a low temperature boundary in the vicinity just above 300°C.

Neustroev also has published data on the X18H9T steel after irradiation at  $1.3 \times 10^{-7}$  dpa/s in the reflector region of the BOR-60 fast reactor [8]. At ~345°C, 1.4% swelling was reached at

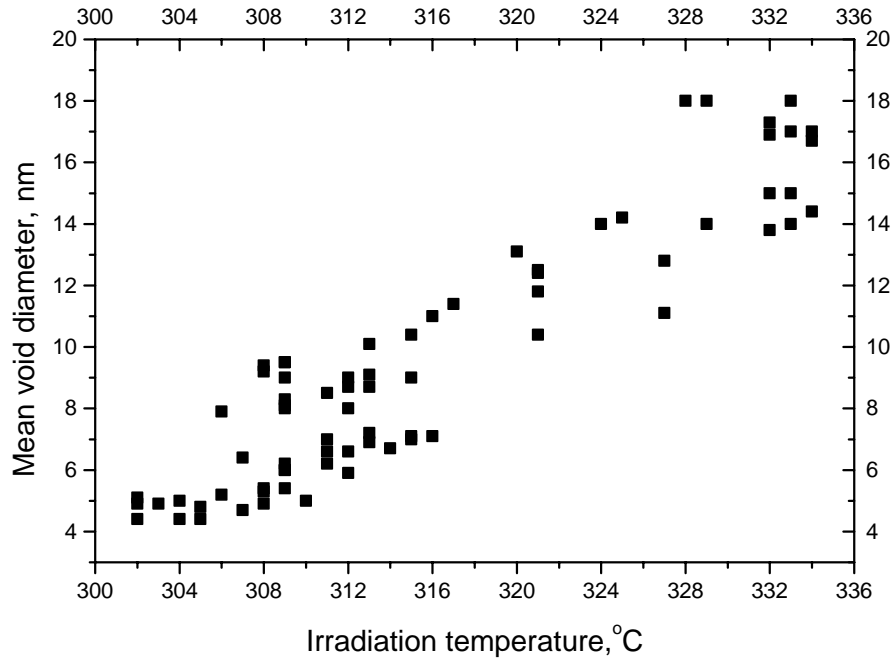


Figure 8. Temperature dependence of the mean void diameter.

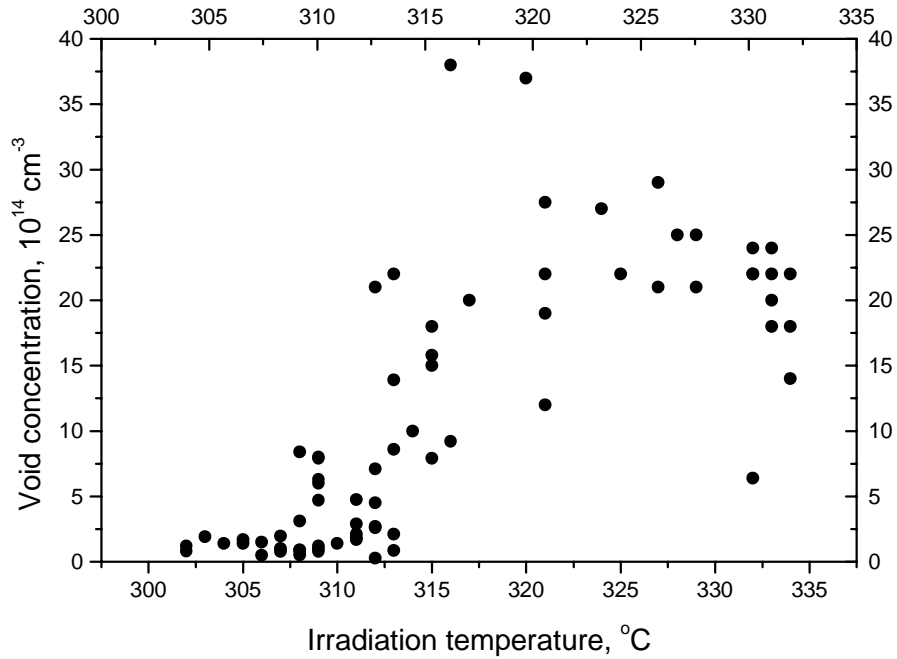


Figure 9. The temperature dependence of the void concentration.

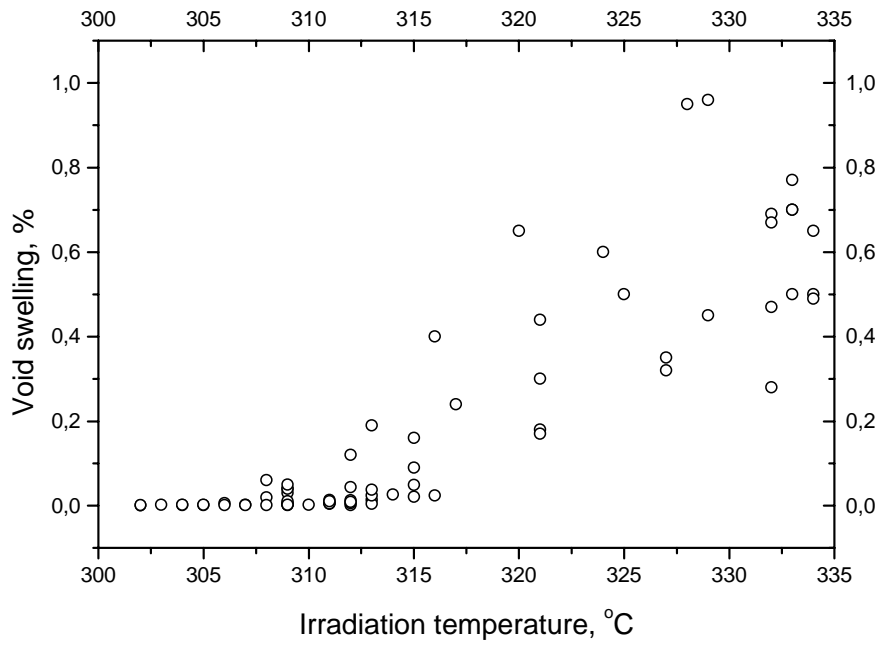


Figure 10. The temperature dependence of void swelling.

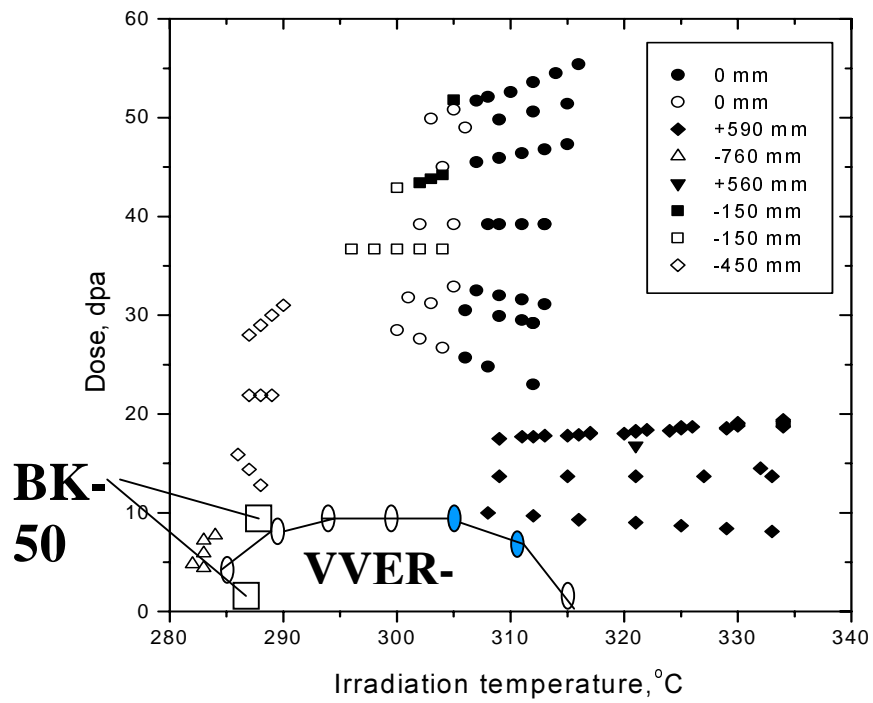


Figure 11. Comparison of results by Neustroev et al. (14) and those of this study. BK-50 is a BWR located in Dimitrovgrad Russia, and the VVER-1000 is a Russian PWR in Rovenskaya, Ukraine.

only 38 dpa, with a significantly smaller incubation dose than observed in comparable irradiations conducted at higher dpa rates. As shown by Edwards et al., voids are already forming in some PWR baffle bolts made with cold-worked 316 stainless steel irradiated to only 8-12 dpa at temperatures in the range 330-345°C [15]. This steel is normally considered to be rather swelling resistant, especially when compared to annealed 304 stainless steel.

### Conclusions

On the basis of the present microstructural study it is possible to make the following conclusions.

1. Voids in type 12X18H9T austenitic steel irradiated in the BN-350 fast reactor at dose rates ranging from  $1.1 \times 10^{-8}$  to  $1.6 \times 10^{-7}$  dpa/s are observed in the temperature range of 305-334°C at doses ranging from 8 to 56 dpa. At irradiation temperatures below ~305°C voids resolvable in an electron microscope were not found.
2. The ~305°C lower boundary of swelling appears to be relatively insensitive to dpa rate in the range examined, and also insensitive to the differences in neutron spectra found between fast reactors and water-moderated reactors.
3. The ~305°C boundary also appears to be consistent with observations on other Russian steels, providing some confidence in predicting that such a boundary may also apply to the AISI 304 and 316 steels employed in Western and Japanese PWRs.
4. It is anticipated that the above conclusions are also applicable to fusion spectra irradiation of 300 series stainless steels.

### **ACKNOWLEDGEMENTS**

The Offices of Fusion Energy, Basic Energy Sciences and Nuclear Energy, Science and Technology, U.S. Department of Energy provided support for the U.S. portion of this research under contract DE-AC06-76RLO 1830 with Battelle Memorial Institute. The Civilian Research and Development Foundation under Grants RE2-123 and GAP Project RPO-649 sponsored the Russian portion.

### **REFERENCES**

- [1] C. Cawthorne and J. E. Fulton, *Nature* 216 (1967) 515-517.
- [2] F. A. Garner, Chapter 6: "Irradiation Performance of Cladding and Structural Steels in Liquid Metal Reactors", Vol. 10A of Materials Science and Technology: A Comprehensive Treatment, VCH Publishers, 1994, pp. 419-543.
- [3] F. A. Garner and M. B. Toloczko, "Irradiation Creep and Void Swelling of Austenitic Stainless Steels at Low Displacement Rates in Light Water Energy Systems", J. of Nucl. Mater., 251 (1997) 252-261.
- [4] F. A. Garner, L. R. Greenwood and D. L. Harrod, "Potential High Fluence Response of Pressure Vessel Internals Constructed from Austenitic Stainless Steels", Proc. Sixth Intern. Symp. on Environmental Degradation of Materials in Nuclear Power Systems - Water Reactors, San Diego, CA. August 1-5, 1993, pp. 783-790.

- [5] F. A. Garner, "Materials Issues Involving Austenitic Pressure Vessel Internals Arising From Void Swelling and Irradiation Creep", Trans. Am. Nucl. Soc., 71 (1994) 190.
- [6] F. A. Garner, M. B. Toloczko, S. I. Porollo, A. N. Vorobjev, A. M. Dvoriashin and Yu. V. Konobeev, "Potential Irradiation Creep and Void Swelling of Stainless Steels in PWR Internals", Proceedings Eighth International Symposium On Environmental Degradation of Materials in Nuclear Power Systems-Water-Reactors, Amelia Island, Florida, Aug 10-14, 1997, pp. 839-845.
- [7] S. I. Porollo, A. N. Vorobjev, Yu. V. Konobeev, A. M. Dvoriashin, V. M. Krigan, N. I. Budylnkin, E. G. Mironova and F. A. Garner, "Void-Induced Embrittlement of Austenitic Stainless Steel Irradiated to 73-82 dpa at 335-360°C", J. of Nucl. Mater., 258-263 (1998), pp. 1613-1617.
- [8] V. S. Neustroev, V. K. Shamardin, Z. E. Ostrovsky, A. M. Pecherin, and F. A. Garner, "Temperature-Shift of Void Swelling Observed at PWR-Relevant Temperatures in Annealed Fe-18Cr-10Ni-Ti Stainless Steel Irradiated in the Reflector Region of BOR-60", Effects of Radiation on Materials: 19th International Symposium, ASTM STP 1366, M. L. Hamilton, A. S. Kumar, S. T. Rosinski and M. L. Grossbeck, Eds., American Society for Testing and Materials, 2000, pp. 792-800.
- [9] F. A. Garner, S. I. Porollo, A. N. Vorobjev, Yu. V. Konobeev, A. M. Dvoriashin, V. M. Krigan, N. I. Budylnkin, and E. G. Mironova, "Void-Induced Swelling and Embrittlement in the Russian Equivalent of AISI 316 Stainless Steel at PWR-Relevant End-of-Life Conditions", International Symposium on "Contribution of Materials Investigation to the Resolution of Problems Encountered in Pressurized Water Reactors, 14-18 Sept. 1998, Fontevraud, France, pp. 249-260.
- [10] S. I. Porollo, A. M. Dvoriashin, A. N. Vorobjev, V. M. Krigan, Yu. V. Konobeev, F. A. Garner, N. I. Budylnkin and E. G. Mironova, "Neutron-Induced Swelling and Embrittlement Behavior of Two Russian Stainless Steels at PWR-Relevant Temperatures and 65-85 dpa", 9<sup>th</sup> International Conference on Environmental Degradation of Materials in Nuclear Power Systems – Water Reactors, 1999, pp. 1061-1068
- [11] G. M. Bond, B. H. Sencer, F. A. Garner, M. L. Hamilton, T. R. Allen and D. L. Porter, "Void Swelling of Annealed 304 Stainless Steel at ~370-385°C and PWR-Relevant Displacement Rates", 9<sup>th</sup> International Conference on Environmental Degradation of Materials in Nuclear Power Systems – Water Reactors, 1999, pp. 1045-1050.
- [12] F. A. Garner, S. I. Porollo, A. N. Vorobjev, Yu. V. Konobeev and A. M. Dvoriashin, "Void Swelling at Low Displacement Rates in Annealed X18H10T Stainless Steel at 30-56 dpa and 280-332°C", 9<sup>th</sup> International Conference on Environmental Degradation of Materials in Nuclear Power Systems – Water Reactors, 1999, pp. 1051-1059.
- [13] M. L. Hamilton, F. H. Huang, W. J. S. Yang and F. A. Garner, "Mechanical Properties and Fracture Behavior of 20% Cold-Worked 316 Stainless Steel Irradiated to Very High Exposures", Effects of Radiation on Materials: Thirteenth International Symposium (Part II) Influence of Radiation on Material Properties,

ASTM STP 956, F. A. Garner, N. Igata and C. H. Henager, Jr., Eds., ASTM Philadelphia, PA, 1987, pp. 245-270.

- [14] V. S. Neustroev, V. N. Golovanov, Z. Ye. Ostrovsky, A. M. Pecherin, and V. K. Shamardin, "Radiation Effects in 18Cr-10Ni-Ti Steel Irradiated in Different Reactors under Conditions Close to VKU VVER Reactors Operating Conditions", Proceedings of the Fourth International Ural Seminar on Radiation Damage Physics of Metals and Alloys, Feb. 25 – Mar. 3, 2001. Snezhinsk, Russia, in press.
- [15] D. J. Edwards, F. A. Garner, B. A. Oliver and S. M. Bruemmer, "Microstructural Evaluation of a Cold-Worked 316SS Baffle Bolt Irradiated in a Commercial PWR", Proc. of Tenth Intern. Conf. on Environmental Degradation of Materials in Nuclear Power Systems - Water Reactors, Aug. 5-9, 2001, in press.

**GENERATION AND RETENTION OF HELIUM AND HYDROGEN IN AUSTENITIC STEELS IRRADIATED IN A VARIETY OF LWR AND TEST REACTOR SPECTRAL ENVIRONMENTS** - F. A. Garner, B. M. Oliver, L. R. Greenwood, D. J. Edwards and S.M. Bruemmer (Pacific Northwest National Laboratory)\* M. L. Grossbeck, (Oak Ridge National Laboratory)

## **OBJECTIVE**

The purpose of this effort is to explore the possibility that both helium and hydrogen influence the behavior of stainless steels during neutron irradiation.

## **SUMMARY**

In fission and fusion reactor environments stainless steels generate significant amounts of helium and hydrogen by transmutation. The primary sources of helium are boron and nickel, interacting with both fast and especially thermal neutrons. Hydrogen arises primarily from fast neutron reactions, but is also introduced into steels at often much higher levels by other environmental processes. Although essentially all of the helium is retained in the steel, it is commonly assumed that most of the hydrogen is not retained. It now appears that under some circumstances, significant levels of hydrogen can be retained, especially when helium-nucleated cavities become a significant part of the microstructure.

A variety of stainless steel specimens have been examined from various test reactors, PWRs and BWRs. These specimens were exposed to a wide range of neutron spectra with different thermal/fast neutron ratios. Pure nickel and pure iron have also been examined. It is shown that all major features of the retention of helium and hydrogen can be explained in terms of the composition, thermal/fast neutron ratio and the presence or absence of helium-nucleated cavities. In some cases, the hydrogen retention is very large and can exceed that generated by transmutation, with the additional hydrogen arising from either environmental sources and/or previously unidentified radioisotope sources that may come into operation at high neutron exposures.

## **INTRODUCTION**

It is well known that helium and hydrogen are formed in stainless steels, as well as in other metals and alloys, by neutron-induced transmutation. Hydrogen is also introduced into metals during irradiation by a variety of other mechanisms. Examples are corrosion, recoil injection of protons after neutron-water collisions, radiolytic decomposition of water in light water reactors, and the equilibrium dissociation arising from hydrogen overpressures used in PWRs. Although essentially all of the helium is retained in the steel, it is commonly assumed that most of the hydrogen cannot be retained at high concentrations and will therefore diffuse out of the steel.

Both of these gases are known to exert deleterious effects on the properties of stainless steels, but two potential degradation processes are of current interest. First, it is well known that helium and other gases stabilize small vacancy clusters to form bubbles and void cavities, and thereby accelerate the onset of void swelling. It has recently been suggested that hydrogen may possibly serve a similar role [1]. Second, hydrogen has also been

---

\* Pacific Northwest National Laboratory (PNNL) is operated for the U.S. Department of Energy by Battelle Memorial Institute under contract DE-AC06-76RLO-1830.

occasionally suggested to play a role in irradiation-assisted stress corrosion cracking, but no convincing evidence of hydrogen's direct role has yet been provided.

To date no systematic attempt has been made to measure the concentrations of both gases in highly neutron-irradiated stainless steels, or to investigate the possible interaction of the two gases. This paper first presents a summary of such measurements on a variety of stainless steel specimens irradiated in PWRs and BWRs. Second, a series of specimens from several test reactors are used to address specific questions arising from the LWR results. The specimens examined in these two groups were therefore exposed to a wide range of neutron spectra. Third, and finally, pure nickel and pure iron wires used as dosimeters and irradiated in HFIR were also measured to address issues related to transmutation sources of helium and hydrogen.

#### Transmutant sources of helium and hydrogen

Virtually all elements in stainless steel produce helium to some degree during neutron irradiation via  $(n,\alpha)$  reactions with neutrons with energies above  $\sim 4$  MeV. The majority of the helium from such reactions is formed from the five isotopes of natural nickel (primarily  $^{58}\text{Ni}$ ), with all other major elements typically used in steels having much smaller cross sections [2]. The range of alpha particles from this type of reaction is rather small, typically less than a micron, leading to minimal energetic losses across the specimen surfaces.

Helium is also formed by interactions with low energy or thermal neutrons that exist at high fluxes in water-moderated reactors. There are two important reactions of this type. The first is the  $(n,\alpha)$  reaction with  $^{10}\text{B}$ , which comprises 19.9% of natural boron. This contribution to helium production is generally quite small ( $\ll 50$  appm) and normally saturates quickly with the rapid burnout of this isotope in most reactor neutron spectra having a significant thermal component. Note that  $^6\text{Li}$  also has a higher thermal neutron  $(n,\alpha)$  cross-section, but  $^6\text{Li}$  comprises  $\sim 7\%$  of natural lithium, however, and lithium is generally not a significant impurity in steel.

The second major contribution arises from the  $^{58}\text{Ni}(n,\gamma)^{59}\text{Ni}(n,\alpha)$  reaction sequence, which is essentially unsaturable within the range of conditions relevant to LWRs and fusion devices [3].  $^{59}\text{Ni}$  is a radioactive isotope not found in natural nickel. It is important to note that this two-step generation reaction is non-linear with exposure, involving the buildup of  $^{59}\text{Ni}$  as the first step. Therefore, this contribution exhibits a delay in its production and continuously accelerates in rate with increasing exposure, only saturating at thermal neutron fluences  $> 10^{23} \text{ n/cm}^2$ , well above the range of LWR and fusion interest. Most importantly, the degree of acceleration is directly proportional to the thermal-to-fast neutron ratio, which can vary strongly with position both within and especially outside of LWR cores. The thermal-to-fast ratio increases strongly as the local water to fuel (or metal) ratio increases. Usually there is a strong increase in the ratio just outside the core boundary. Both within and especially outside of LWR cores, this contribution soon becomes the dominant source of helium in nickel-bearing alloys.

Both of these thermal neutron reactions are very exothermic and yield energetic helium atoms with ranges on the order of several microns. Therefore the energetic losses of helium across specimen surfaces are somewhat larger. For samples with minimum dimensions comparable to the recoil distance, the near-surface regions of specimens must be removed before measurement of helium proceeds.

Helium is both very immobile and chemically inert. Therefore it has no driving force for significant diffusional migration or segregation, leading to near total trapping within the specimen. Since it does not further transmute, it can be used as a fluence and spectral monitor for retrospective dosimetry. This means that an estimation of the neutron exposure can be made for specimens whose exposures are not well known, especially when other measurements are also used that measure radioactivation or isotopic shifts for selected elements.

Hydrogen is also generated by transmutation, but it is important to remember that hydrogen can be introduced into steels by other environmental processes. Examples are corrosion, radiolytic decomposition of water, direct injection from proton recoil following collisions of neutrons with the H in water, and from equilibrium dissociation of the hydrogen overpressure maintained in PWR reactors. Another example arises from diffusion of transmutant hydrogen produced at large levels in adjacent materials.

In steels, hydrogen arising from transmutation is formed primarily from the various nickel isotopes, especially  $^{58}\text{Ni}$ , interacting with fast neutrons above  $\sim 1$  MeV. The production rate via this reaction is essentially linear with accumulating exposure. Other constituents of typical steels also generate hydrogen by (n,p) reactions, but the cross sections are much smaller than those of nickel. Due to the lower (n,p) threshold (1 MeV) compared to the  $\sim 4$  MeV threshold for alpha production, the H/He ratio due to fast neutrons is usually on the order of 14-20, depending on the details of the fast portion of the neutron spectra. However, there is also a  $^{58}\text{Ni}(n,\gamma)^{59}\text{Ni}(n,p)$  reaction, with a thermal cross section that is about one-sixth of the  $^{59}\text{Ni}$  helium production cross section [4]. The total hydrogen production rate in nickel-bearing alloys is therefore also non-linear with increasing exposure, but at only  $1/6^{\text{th}}$  the rate of helium.

Hydrogen is thought to be very mobile in steels at LWR-relevant and fusion-relevant temperatures, and therefore it might be expected that very little would be retained. There is some evidence, however, that hydrogen can be stored in highly irradiated steels under certain conditions [1, 5]. In particular, hydrogen retention appears to be accelerated when large amounts of helium are cogenerated [1]. More importantly, hydrogen arising from non-transmutation sources might also be stored. This is a particularly important consideration in LWRs with water coolant, but not necessarily in sodium-cooled fast reactors.

In summary, the major source of helium at high neutron exposure is nickel, and the production rate is proportional to the nickel content and the local thermal-to-fast neutron ratio, but in a non-linear manner with increasing exposure. Transmutant hydrogen is similarly dependent on the Ni content and the thermal-to-fast ratio, but the non-linearity is less pronounced due to the lower (n,p) thermal cross section. The production of helium by boron occurs very quickly, saturating at a rate that is strongly dependent on the thermal neutron flux.

#### Gas measurement procedures

Smaller sections on the order of milligrams were first cut from each sample. These sections were then etched to remove  $\sim 0.013$  mm or more of surface material. This etching step was done to remove material that may have been affected by  $\alpha$ -recoil either out of the sample or into the sample from adjacent materials during irradiation. After etching, smaller specimens were cut from each section for duplicate helium analysis. The specimens were cut using small wire cutters. Before each use, the cutters were cleaned by wiping several times with a dry lint-free paper cloth (Kimwipe). Replicate helium analyses are routinely performed to

give an indication of the analysis reproducibility and helium homogeneity in each sample. Prior to analysis, each specimen was cleaned in alcohol and air-dried. The mass of each specimen was determined to an accuracy of  $\pm 0.002$  mg using a calibrated microbalance traceable to the National Institute of Standards and Technology (NIST).

The helium content of each specimen was determined by isotope-dilution mass spectrometry following vaporization in a resistance-heated graphite or tungsten-wire crucible in one of the mass spectrometer system's high-temperature vacuum furnaces [6,7]. The absolute amount of  $^4\text{He}$  released was measured relative to a known quantity of added  $^3\text{He}$  "spike". The helium spike was obtained by expanding and partitioning a known quantity of gas through a succession of calibrated volumes. The mass spectrometer was calibrated for mass sensitivity during each series of runs by analyzing known mixtures of  $^3\text{He}$  and  $^4\text{He}$ .

Hydrogen analyses were also conducted by gas mass spectrometry using a newly developed H analysis system [8]. The analysis procedure involved dropping the individual specimens, under vacuum, into a small cylindrical ceramic crucible heated to approximately  $1200^\circ\text{C}$ . During initial vacuum pumping, the sample chamber and crucible volume were subjected to a low-pressure ( $\sim 200$  mm Torr) argon gas discharge to aid in desorption of water or hydrated-oxide surface layers that could be dissociated by the hot crucible during analysis, and thus contribute to the measured H release. The sample chamber was then connected to the high-vacuum analysis chamber, and the analysis crucible was pre-heated to approximately  $1000^\circ\text{C}$  for several days. The crucible temperature was increased to  $1200^\circ\text{C}$  a few hours prior to analysis. During the pre-heating and subsequent analysis procedure, the sample chamber was maintained at room temperature.

Hydrogen release was measured as a function of time using a quadrupole mass spectrometer connected to the analysis chamber. The total hydrogen was determined from the integral of the hydrogen release curve. Calibration of the system sensitivity was accomplished using a calibrated H leak source of  $\sim 1 \times 10^{-10}$  mole  $\text{H}_2/\text{sec}$ , with a stated absolute uncertainty of  $\pm 15\%$  ( $3\sigma$ ). Calibration measurements were conducted before and after each sample analysis, and showed an overall standard deviation of  $\sim 2$  to  $3\%$ . Measurements were also conducted on milligram-sized specimens of a standard hydrogen-containing steel maintained in the laboratory. Variability in numerous replicate measurements of this steel is currently averaging approximately  $20\%$  ( $1\sigma$ ), and is believed to represent actual heterogeneity in the hydrogen content for these small samples.

#### LWR specimens examined

Four sets of LWR specimens were investigated. In the first set Types 304 and 316SS heats with previously characterized IASCC response were selected from an extensive ABB-Atom testing program [9]. In this program three different 304SS and three different 316SS heats were irradiated to dose levels of  $\sim 0.4$  to  $9 \times 10^{21}$   $\text{n}/\text{cm}^2$  ( $\sim 0.6$  to  $13.3$  dpa) in a commercial BWR (Barsebäck) at a temperature of  $\sim 275^\circ\text{C}$ . The compositions are shown in Table 1. A total of 38 specimen conditions were chosen to span the range of irradiation doses shown in Table 2. Unirradiated archive materials were also available for each heat.

The second LWR set of specimens examined were sections cut from two different locations of the top guide of the core shroud from the KWW Wurgassen BWR reactor. This component was constructed from Type 347 stainless steel, as described in Table 3. One specimen was extracted above the center of the core with an estimated fluence of  $1.4 \times 10^{21}$   $\text{n}/\text{cm}^2$   $E > 0.1$  MeV ( $\sim 2$  dpa). The second, lower dose piece was obtained from another section away from the core center at an estimated fluence of  $5 \times 10^{19}$   $\text{n}/\text{cm}^2$  ( $\sim 0.07$  dpa).

Table 1. Bulk compositions of ABB-Atom heats, wt%

	304-B	304-C	304-E	316-F	316-K	316-P
C	0.035	0.014	0.015	0.009	0.055	0.040
Cr	18.3	18.6	18.5	16.7	16.5	16.7
Ni	8.5	10.2	10.9	11.6	12.4	12.2
Mo	0.4	0.3	0.1	2.7	2.3	2.6
Mn	1.4	1.3	0.8	1.4	1.7	1.8
Si	0.65	0.43	0.05	0.26	0.64	0.59
P	0.031	0.023	0.006	0.021	0.016	0.024
S	0.029	0.006	0.009	0.001	0.006	0.007
B	<0.0004	<0.0004	<0.0004	0.0010	<0.0004	0.0013
N	0.067	0.077	0.039	0.062	0.029	0.058

Table 2. CIR Materials from the ABB-Atom IASCC Program, indicating Sample Numbers and Dose Conditions ( $n/cm^2$ ,  $E>1MeV$ )

304SS Heat B	304SS Heat C	304SS Heat E	316SS Heat F	316SS Heat K	316SS Heat P
#B15 $0.5 \times 10^{21}$	#C36 $0.4 \times 10^{21}$				
#B27 $0.8 \times 10^{21}$	#C35 $0.6 \times 10^{21}$	#E6 $0.8 \times 10^{21}$	#F6 $0.8 \times 10^{21}$	#K4 $0.7 \times 10^{21}$	#P28 $0.8 \times 10^{21}$
#B21 $1.1 \times 10^{21}$	#C5 $1.2 \times 10^{21}$	#E1 $1.2 \times 10^{21}$	#F1 $1.1 \times 10^{21}$	#K3 $1.1 \times 10^{21}$	#P14 $1.1 \times 10^{21}$
#B74 $2.2 \times 10^{21}$	#C69 $2.5 \times 10^{21}$	#E18 $2.2 \times 10^{21}$	#F12 $2.3 \times 10^{21}$	#K10 $2.6 \times 10^{21}$	#P64 $2.0 \times 10^{21}$
#B79 $3.4 \times 10^{21}$	#C62 $3.4 \times 10^{21}$	#E15 $3.1 \times 10^{21}$	#F10 $3.3 \times 10^{21}$	#K9 $4.0 \times 10^{21}$	#P51 $3.4 \times 10^{21}$
#B132 $5.9 \times 10^{21}$	#C106 $5.8 \times 10^{21}$	#E24 $6.0 \times 10^{21}$	#F16 $6.6 \times 10^{21}$	#K18 $5.0 \times 10^{21}$	#P79 $5.5 \times 10^{21}$
#B124 $9.2 \times 10^{21}$	#C87 $9.3 \times 10^{21}$	#E22 $9.0 \times 10^{21}$	#F15 $9.0 \times 10^{21}$	#K15 $9.3 \times 10^{21}$	#P83 $9.2 \times 10^{21}$

The third set of LWR specimens were several heats of 304 and 348 stainless steels irradiated in the control rod guide tube of a standard 14X14 fuel assembly of the KWO Obrigheim PWR as part of a swelling-mandrel test program [10]. It is important to note that the  $B_4C$  in these mandrels probably lowered the thermal-to-fast neutron ratio significantly,

Table 3. Composition and fabrication history of the top guide for the Wurgassen KWW Nuclear Power Plant

Heat # 71836	Semi-finished Product (Solution Annealed 1020°C/WQ) Room Temperature Tensile Properties				Stabilization Ratio Nb/C			
	0.2%YS	UTS	%TE	%RA				
	295 MPa	630 MPa	50.7	60.7				
Measured Bulk Chemistry (wt%)					10			
C	Si	P	S	Cr	Mn	Fe	Ni	Nb + Ta
0.049	0.65	0.02	0.014	18.4	1.3	68.5	10.6	0.49

and thereby the  $^{59}\text{Ni}$  helium production. This complication does not allow us to specify the thermal neutron spectrum very accurately.

The fourth set of LWR specimens were cut from a cold-worked 316 baffle bolt removed from the Tihange 1 PWR. While the major element composition is known, there is no knowledge of the boron content of this bolt. As shown in Figure 1, three sections were cut at 1, 25 and 55 mm from the bolt head surface, with doses of 19.5, 12.2 and 7.5 dpa, respectively, as determined by retrospective dosimetry. This bolt and its full characterization are presented in another paper in this symposium [5].

#### Results: LWR specimens

The measured helium values for the ABB and 304/308 PWR specimens are shown in Figure 2. Helium concentrations increase consistently with increasing dose for each heat. The rate

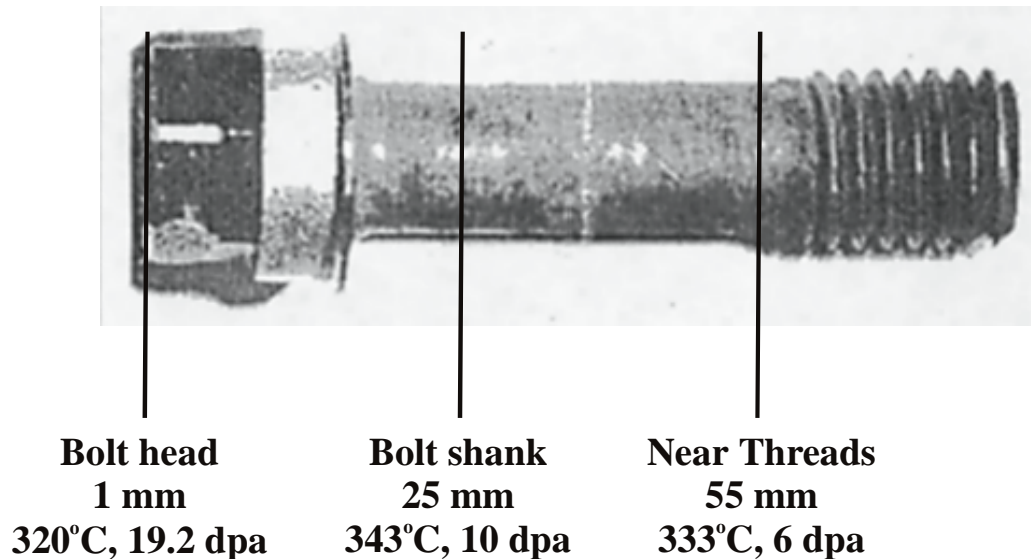


Figure 1. Location of specimens cut from baffle bolt. The dpa levels have recently been revised to 19.5, 12.2 and 7.5 dpa based on retrospective dosimetry.

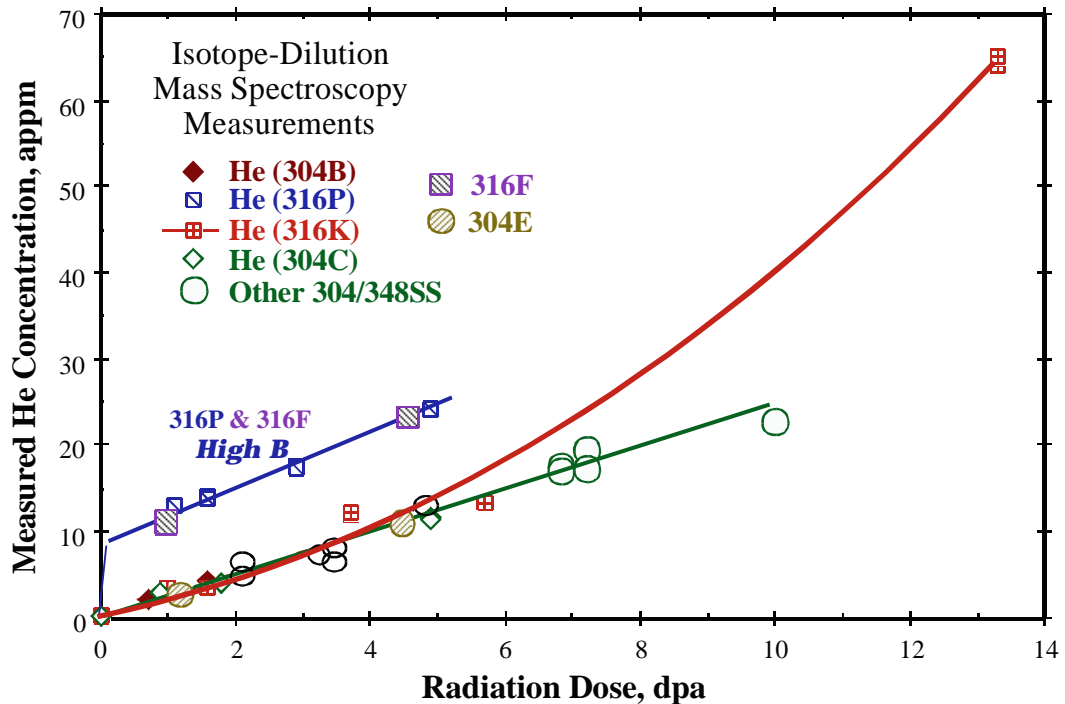


Figure 2. Helium concentrations measured in various 300 series stainless steels after irradiation in various LWRs.

of increase is approximately 2.5 appm per dpa for 316 heats until ~10 dpa. From fast neutron reactions only, the calculated helium generation rate is only about 1 appm/dpa, so the apparently linear 2.5 appm/dpa rate represents the combined effect of the time-varying boron, fast neutron and  $^{59}\text{Ni}$  contributions. As expected, there is a more obvious acceleration in helium production rate indicated by heat K at high dose as the  $^{59}\text{Ni}$  contribution continues to accelerate.

The largest difference among the ABB heats is seen for 316 heats P and F when compared with the others. Both of these heats show an initial offset in helium content (~10 appm) at the lowest dose investigated. This occurs due to higher boron levels in these two heats that burns out by ~1 dpa. Since  $^{10}\text{B}$  comprises ~20% of natural boron, the bulk concentration of this element in heat P can be estimated to be ~55 appm, and ~40 appm in heat F. These numbers agree quite well with predicted values based on the bulk concentrations listed in Table 1.

The increasing rate of helium generation at high neutron exposure is consistent with the buildup of  $^{59}\text{Ni}$ . The much lower rate of increase in the 304SS Heat B and 348SS PWR specimens most likely reflects both their lower nickel content compared to 316 heats and a lowering of the local thermal neutron flux by the  $\text{B}_4\text{C}$  inside the mandrels. The continued apparent linearity of helium generation at higher dpa is also consistent with a lower thermal neutron contribution.

Using a typical in-core LWR spectrum, and removing the boron contributions, it is possible to reproduce all features of the measured helium behavior, as shown in Figure 3. Only the

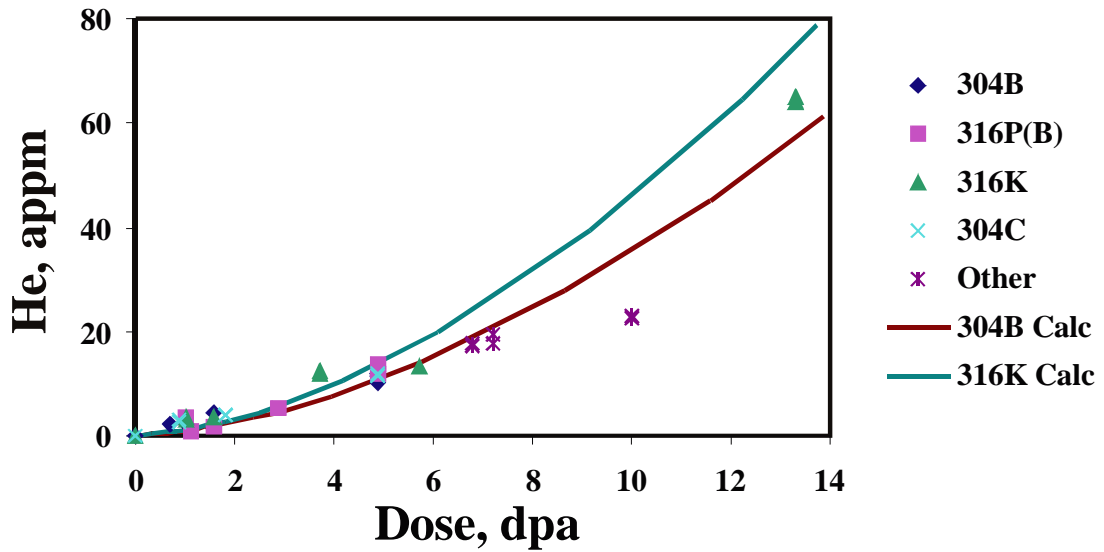


Figure 3. Comparison of predicted and measured helium levels after removal of boron contributions.

Obrigheim PWR data on 304/348 stainless fall below the prediction, as expected by the  $B_4C$  suppression of the local thermal neutron population.

With the exception of ABB heat C the retained hydrogen concentrations in the ABB heats shown in Figure 4 appear to be relatively low and perhaps increasing at a relatively low rate.

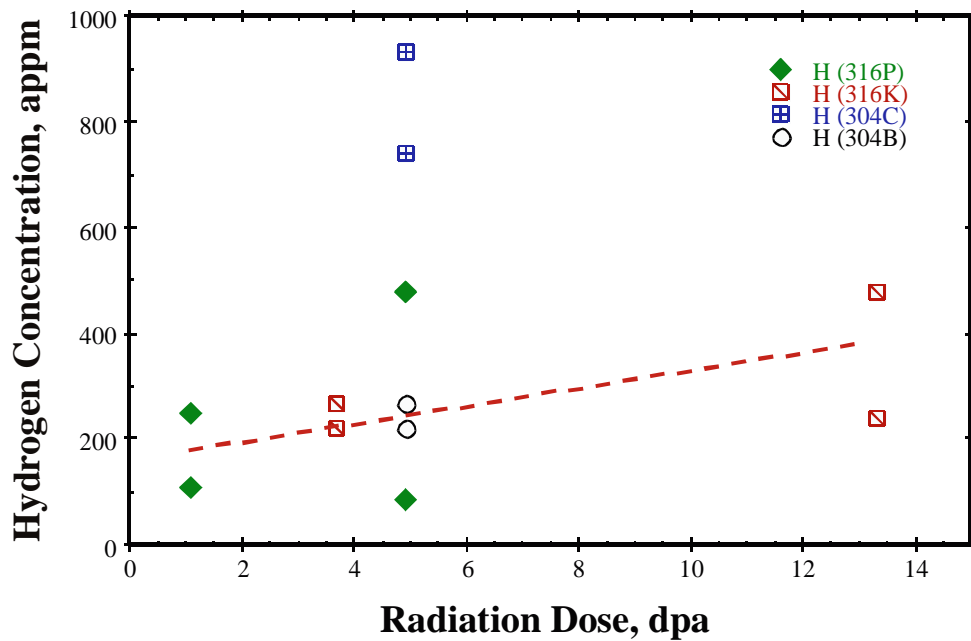


Figure 4. Hydrogen concentrations measured in ABB heats.

Using the same spectra employed for the helium above, calculations of the predicted concentrations of transmutation-induced hydrogen in the ABB specimens are significantly lower than those measured, indicating that environmental sources must be the dominant sources.

The helium measurements shown in Figure 5 compare the differences between the two Wurgassen conditions relative to the ABB-Atom materials. The much lower helium content at the 0.07 dpa condition compared to the 2 dpa condition is primarily due to the lower overall flux at this position. Compared to the ABB-Atom materials, the higher thermal-to-fast ratio in the out-of-core region produces significant increases in the He/dpa ratio. Although not as noticeable without close inspection of Figure 5, the 0.07 dpa condition also has a higher helium content than the low-boron ABB-Atom materials at comparable doses. The boron content of this material is unknown, however, so how much helium is derived from transmutation of  $^{10}\text{B}$  cannot be predicted.

The hydrogen concentrations shown in Figure 6 are surprising in that, for reasons that remain unclear, the 0.07 dpa condition has much higher hydrogen than measured in the 2 dpa condition. Compared to the ABB-Atom materials, the Wurgassen plate appears to have higher hydrogen concentrations at both doses, but the concentration at 0.07 dpa exceeds that of the ABB-Atom materials by a significant margin.

Table 4 lists the results of the gas measurements on the Tihange bolt. Figure 7a shows the helium measured at three positions along the Tihange baffle bolt, with all data points connected to each other. At first glance, it appears that the data imply a very large level of boron in the steel, on the order of 150 ppm. This is an incorrect conclusion, however, and is

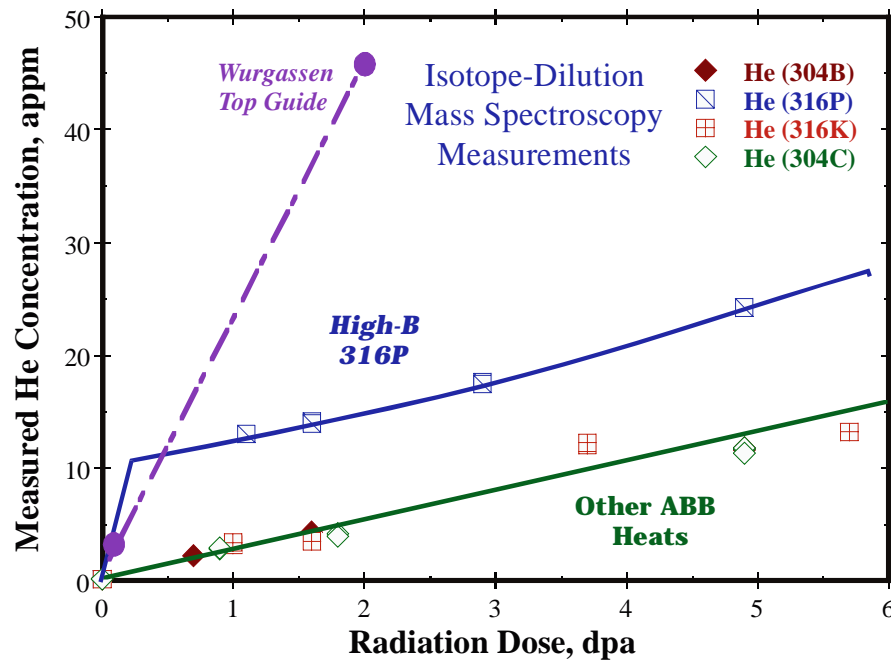


Figure 5. Helium concentration in two Wurgassen samples compared to those of the ABB materials.

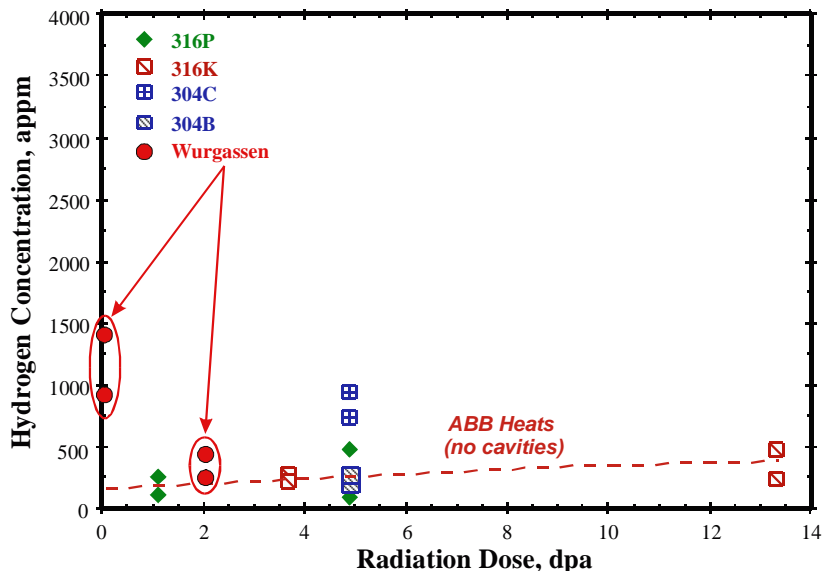


Figure 6. Hydrogen concentration in two Wurgassen samples compared to those of the ABB materials.

predicated on an assumption that the thermal-to-fast ratio is the same everywhere along the bolt axis.

Whereas the ABB heats occupied an in-core position without significant variations in thermal-to-fast ratio, the bolt head is only millimeters from a fuel element which absorbs thermal neutrons strongly, while the shaft of the bolt experiences a significant change in this ratio along the bolt axis as it penetrates into areas where water surrounds the former plate in which it is buried.

By using the known power history of the reactor, measuring the activity of  $^{60}\text{Co}$  and  $^{54}\text{Mn}$ , and also measuring the cobalt and iron compositions using EDXRF, the neutron exposure of these three bolt positions can be determined. Such a process is called retrospective dosimetry and was employed on this bolt. Dpa levels calculated with this procedure agree rather well (19.5 vs. 19.2 dpa at the bolt head surface) with calculated values provided by the Tihange vendor, Tractebel. Figure 8 shows that the thermal-to fast ratio increased about a factor of two between the 1 and 55 mm positions. Figure 7b shows the correct interpretation of the helium data, using a baffle bolt spectrum previously used to calculate gas generation [11], but modified to fit the thermal-to-fast ratios obtained from the retrospective dosimetry analysis. Indeed, the predictions match the measurements almost exactly. Such a match was reached without including any boron contribution, and therefore implies that the boron content of the bolt is rather low, perhaps 5 appm or less.

The first observation is that the hydrogen levels vary somewhat from one repeat measurement to the next. Unfortunately, these measurements were made from the small sections left between punched-out microscopy disks, and there is no record of where these measurements correspond with respect to the bolt radius. The hydrogen levels measured in the 1 mm position are consistent, however, with the range of those for the ABB heats shown in Figure 2.

Table 4. Helium and Hydrogen Concentrations in the Tihange Baffle Bolt 2K1R5

Specimen	Material	Mass <sup>a</sup> (mg)	Measured Gas Release			
			(10 <sup>14</sup> atoms)		(appm) <sup>b</sup>	
			<sup>4</sup> He	<sup>1</sup> H	<sup>4</sup> He	<sup>1</sup> H
1-mm Position	Tihange	0.312	2.426		71.3	
		0.595	4.645		71.6	
		1.005	-	54.0		493
		1.598	-	129		743
25-mm Position	Tihange	0.477	2.784		53.6	
		0.204	1.186		53.8	
		0.264	1.444		50.7	
		1.188		85.0		660 <sup>c</sup>
		1.314		233		1620
		0.740		102		1260
		0.181		73.3		3710
		1.295		101		720 <sup>c</sup>
55-mm Position	Tihange	0.448	2.378		48.7	
		0.510	2.726		49.0	
		1.358		553		3740
		1.701		341		1840

<sup>a</sup> Mass of specimen for analysis. Mass uncertainty is  $\pm 0.002$  mg.

<sup>b</sup> Gas concentration in atomic parts per million ( $10^{-6}$  atom fraction) with respect to the total number of atoms in the specimen.

<sup>c</sup> Crucible temperature of  $\sim 1000^\circ\text{C}$  instead of  $\sim 1200^\circ\text{C}$ .

However, the 25- and 55-mm positions contain concentrations of hydrogen 3 to 7 times that measured in the 1-mm bolt head position, even though the dpa levels are lower. The variations in estimated mid-cycle temperatures of the three positions ( $320, 343, 333^\circ\text{C}$  for 1, 25, 55 mm, respectively) are not large enough to justify such differences in hydrogen content.

Our current interpretation is that the "extra" hydrogen is stored, possibly as  $\text{H}_2$  gas in cavities. As shown in Figure 9, there is approximately 0.2% swelling in the form of cavities in the 25 and 55 mm positions. In the 1 mm position, there is only a few, much smaller density and sizes of cavities, yielding less than 0.01% swelling. Although there is a little more helium in the 1 mm position, most of it must still be in solution or in unresolvable ( $< 1$  nm) bubbles and cavities.

#### Discussion: LWR results

It has been proposed based on the results of other studies [1,12] that helium-nucleated bubbles or voids may allow the storage of hydrogen at LWR-relevant temperatures. From the bolt study, the retention of hydrogen only in those regions where measurable swelling exists lends support for the association of hydrogen with cavities. It is clear, however, that the large levels of hydrogen found in the bolt shank positions cannot be generated from

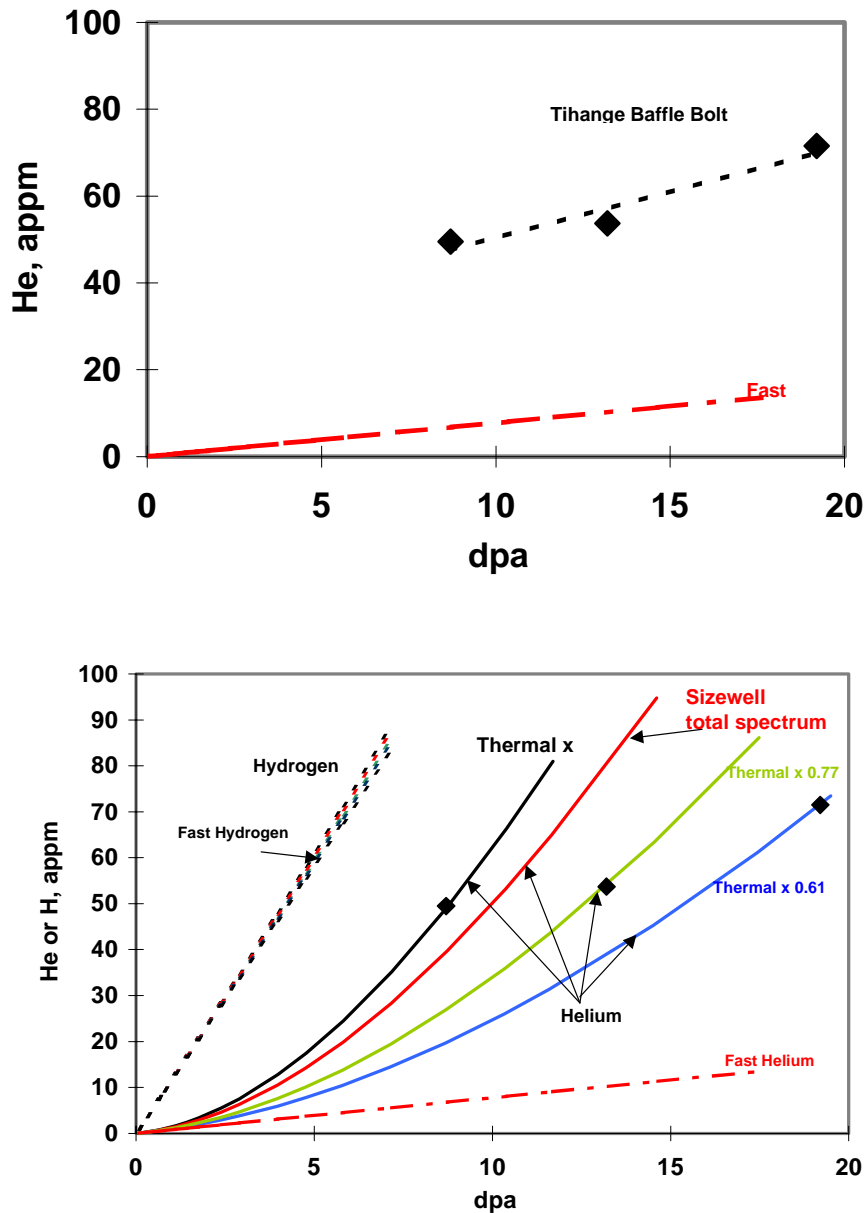


Figure 7. a) Helium measurements from the Tihange baffle bolt, assuming all positions experience the same thermal-to-fast neutron ratio. b) Correct interpretation of helium data showing the contributions of fast neutrons and varying thermal-to-fast ratio. Hydrogen generation is also shown.

Figure 7. b) also shows the transmutant hydrogen levels that would be predicted from the three spectra associated with the three bolt positions. For these relatively low thermal-to-fast ratios, the hydrogen generation is not enhanced significantly in this dpa range by the  $^{59}\text{Ni}(n,p)$  reaction. Even more importantly, the predicted transmutant hydrogen levels are rather low (~100-200 appm) compared to the measured values shown in Table 4.

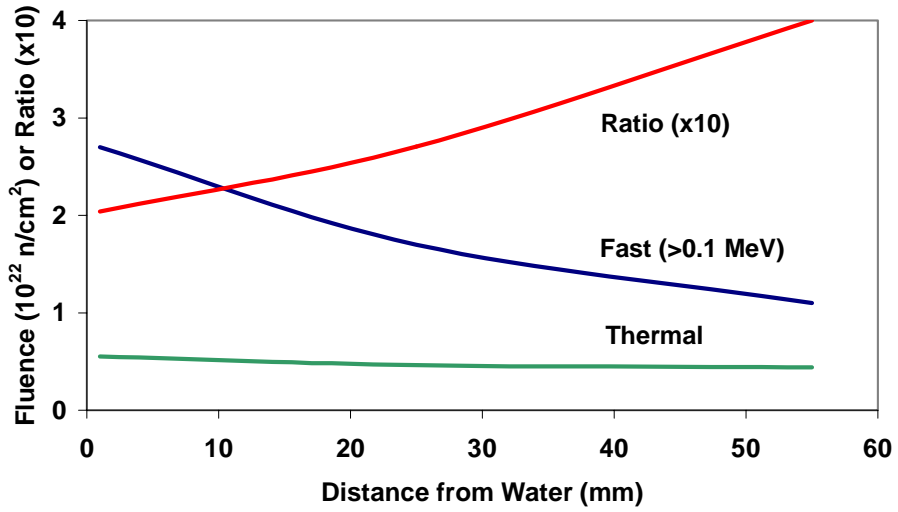


Figure 8. Neutron fluxes and thermal-to-fast ratio for the various positions on the baffle bolt as determined by retrospective dosimetry.

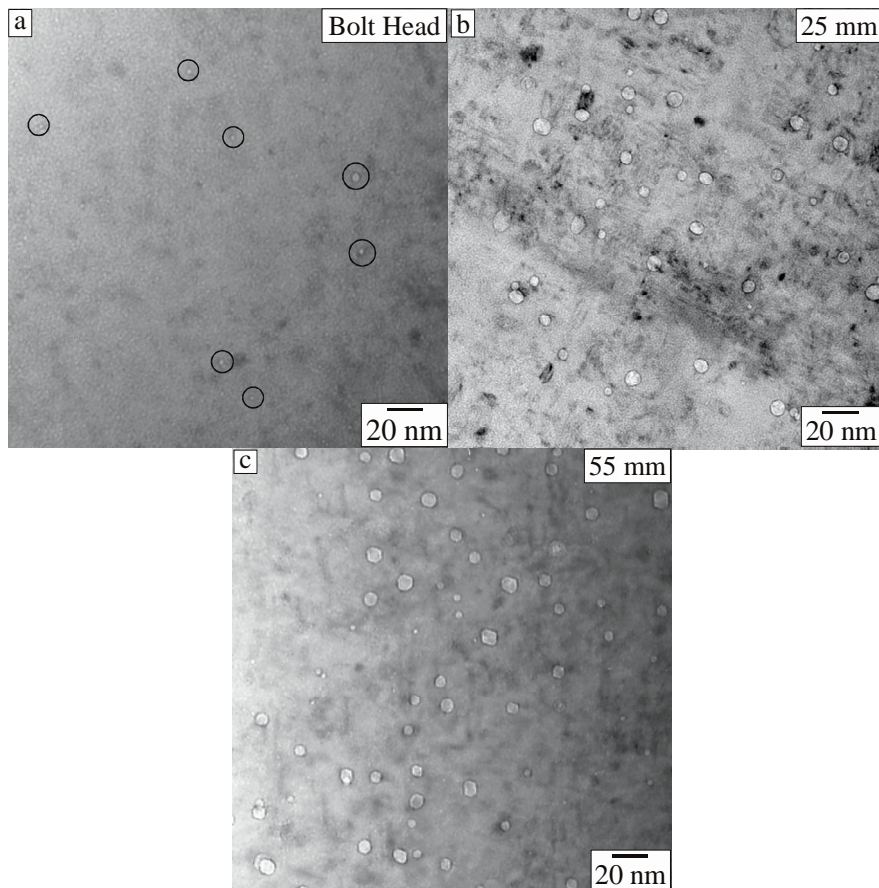


Figure 9. Cavities observed in the baffle bolt sections.

transmutation reactions only, but must result from environmental sources. Note that no cavities exist in the ABB specimens, and cavities exist only in very low densities in the 1-mm position. In both cases the hydrogen levels are correspondingly smaller, lending further credibility to the association between the cavities and retained hydrogen. Several specific questions are raised by these results.

- 1) Are voids by themselves sufficient to store large amounts of hydrogen?
- 2) Are there any other examples of significant hydrogen storage in cavities, either bubbles or voids?
- 3) Have all sources of helium and hydrogen been identified?
- 4) Is there any evidence for direct association of helium and hydrogen retention?

In order to address these questions the following experiments were performed.

#### Stainless steels irradiated in FFTF

Three cold-worked 316 stainless specimens irradiated in the FFTF fast reactor were chosen to see if voids *per se* would store hydrogen when hydrogen was generated primarily by transmutation. These specimens were in contact with the sodium coolant. The FFTF core is an oxide-fueled core with a rather soft neutron spectra (mean neutron energy of ~0.5 MeV, and no thermal neutrons), so both the helium and hydrogen generated per dpa are less than that generated by LWR spectra.

Two of the specimens had ~8% swelling, as determined by immersion density measurements and confirmed by electron microscopy [13]. One of these was irradiated to 88 dpa at 400-430°C, and the other to 60 dpa at 550°C. Although the swelling was approximately the same, the cavity densities were very different, at  $2.1 \times 10^{21}$  and  $0.15 \times 10^{21} \text{ m}^{-3}$ , respectively. Thus, the two specimens had very different void surface areas. The third specimen was part of the 400-430°C irradiation series, but was exposed to only 17.5 dpa, producing only 0.28% swelling. The first two specimens had primarily network dislocations and the low exposure specimen had a Frank loop and network structure.

As shown in Table 5, the measured helium contents in the three samples ranged from 4.99 to 36.8 appm, in good agreement with predictions. Reproducibility between the duplicate analyses averaged ~3%, somewhat higher than the analysis system reproducibility of 0.5%, suggesting some low level of heterogeneity in the helium contents.

Measured hydrogen levels in the irradiated samples ranged from 322 to 570 appm. Given the relatively high irradiation temperatures seen by the samples, however, the fact that hydrogen still exists even at these rather low levels suggests some trapping mechanism may be operating. Reproducibility between the duplicate hydrogen analyses averaged ~38%, which is not inconsistent with the level of variability observed in measurements of our standard hydrogen-containing steel. Most significantly, there was no elevated retention of hydrogen as a function of dislocation structure, total void volume or void surface area.

#### Model alloys irradiated in FFTF

Four model Fe-15Cr-XNi alloy specimens were irradiated in FFTF in the  $^{59}\text{Ni}$  isotopic tailoring experiment in the below-core assembly, at damage levels of either 10.2 or 24 dpa [14,15]. The irradiation temperature was 365°C, which is more prototypic of PWR conditions. Several variables were investigated in this experiment; the effect of nickel level (25 and 45 wt.%) and the effect of He/dpa ratio. The latter was accomplished by doping one half of the alloys with  $^{59}\text{Ni}$  extracted from material irradiated in a highly thermalized neutron

Table 5. Measured gas concentrations in 316 stainless steel

Specimen	Mass <sup>a</sup> (mg)	Measured Gas Release (10 <sup>13</sup> atoms)		Gas Concentration (appm) <sup>b</sup>	
		<sup>4</sup> He	<sup>1</sup> H	Measured	Average <sup>c</sup>
MAEZ	0.857	4.813	-	5.201	4.99
	0.497	2.569	-	4.786	±0.29
	0.398	-	139	322	-
RAEZ	0.500	19.84	-	36.83	-
	0.620	-	419	626	493
	1.087	-	423	360	±188
PAE7	0.677	12.81	-	17.52	17.6
	0.333	6.343	-	17.64	±0.1
	1.143	-	515	417	570
	0.806	-	629	723	±216

<sup>a</sup>Mass of specimen for analysis. Mass uncertainty is ±0.002 mg.

<sup>b</sup>Gas concentration in atomic parts per million (10<sup>-6</sup> atom fraction) with respect to the total number of atoms in the specimen.

<sup>c</sup>Mean and standard deviation (1σ) of duplicate analyses.

spectrum. Thus, a side-by-side comparison could be made of the single variable influence of low and high He/dpa rates. The swelling levels were not greatly altered by <sup>59</sup>Ni doping, but in general, the swelling was distributed on a much finer scale in the doped alloys. The alloys were swelling 0.2-0.4% at 10.2 dpa and several percent at 24 dpa.

At 10.2 dpa the undoped and doped 25 wt% Ni alloys were previously measured to have 7.1 and 165 appm respectively in the absence of doping. The 45 wt% Ni alloys had 41.6 and 317 appm at 24 dpa. As shown in Table 6, the measured hydrogen levels in the irradiated samples were rather low, ranging from 184 to 545 appm. It should be noted, however, that several hundred appm would be expected to have been present in the materials prior to irradiation.

In effect, there appears to be no storage of excess hydrogen in these specimens, regardless of nickel content, helium level or swelling level.

#### Ti-modified stainless steel in HFIR

Two stainless steel specimens of US PCA, a modified 316 stainless steel were irradiated in the JP-12 experiment at 400°C in HFIR in the late 1980's, with the specimens contained in an aluminum block, which was surrounded by a stainless steel canister, without any possibility to contact water. Microscopy was reported on these and other specimens in 1988 and showed the specimens to be densely packed (~10<sup>17</sup> cm<sup>13</sup>) with small (10-20 nm) "helium-filled cavities" [16,17]. The calculated helium level for these specimens was 2835 appm at 33 dpa, produced by the very high thermal-to-fast ratio (~2) in this reactor.

Thirteen years later, identical specimens from the same capsule were retrieved from dry storage and measurements made of the helium and hydrogen. The measured helium levels were 2979 and 3012 appm, within 5% of the calculated values. This agreement provides

Table 6. Hydrogen concentrations in FFTF-MOTA model alloys

Specimen	Material	Mass <sup>a</sup> (mg)	Measured <sup>1</sup> H (10 <sup>16</sup> atoms)	Hydrogen Concentration (appm) <sup>b</sup>	
				Measured	Average <sup>c</sup>
ZXLN-2	Fe-15Cr-25Ni 10.2 dpa	3.416	1.53	416	395
		3.478	1.40	373	±30
Z1LN-2	Fe-15Cr-45Ni 10.2 dpa	2.284	0.514	211	293
		2.756	1.10	375	±116
Z3LN-1	Fe-15Cr-25Ni 24 dpa, <sup>59</sup> Ni.	3.117	1.70	506	545
		3.422	2.15	583	±54
Z5LN-1	Fe-15Cr-45Ni (d 24 dpa, <sup>59</sup> Ni.	3.261	0.724	208	184
		3.082	0.522	159	±35

<sup>a</sup>Mass of specimen for analysis. Mass uncertainty is ±0.002 mg.

<sup>b</sup>Hydrogen concentration in atomic parts per million (10<sup>-6</sup> atom fraction) with respect to the total number of atoms in the specimen. Uncertainty is estimated to be ±20 %.

<sup>c</sup>Mean and standard deviation (1σ) of duplicate analyses.

confidence in our knowledge of the neutron spectrum, and allowed the opportunity to calculate the neutron-induced hydrogen generated, which was predicted to be 884 appm.

Surprisingly, the measured hydrogen values were 3864 and 3790 appm, indicating that the retained hydrogen was more than four times the predicted total generation. In effect, these cavities contain as much hydrogen as helium, assuming that both are largely contained in the cavities. Examination of all details of the experiment revealed no obvious environmental sources of hydrogen strong enough to account for this “excess” hydrogen. While this highly voided microstructure has been clearly storing hydrogen for more than a decade, the major hydrogen source is unknown. Therefore to address the source question in this HFIR experiment, the next experiment was conducted.

#### Pure metal dosimeters irradiated in HFIR

In the absence of an identifiable environmental source, the possibility of unrecognized transmutant sources must be investigated. Perhaps the various (n,p) and (n,α) cross sections have been underestimated or perhaps some previously unidentified radioisotope source similar to <sup>59</sup>Ni is contributing.

Therefore, it was decided that the thin wire dosimeters that were used to determine the spectrum in the JP-12 and follow-on JP-15 experiments were examined. Only the nickel and iron dosimeters were measured. These dosimeters were chosen not only from the 400°C canister used to irradiate the stainless steel specimens discussed above, but also from the 300, 500 and 600°C canisters as well, with dpa levels ranging from 34 to 59 dpa. Some of these dosimeters had not been removed from their original sealed aluminum packets, guaranteeing that the wires had not been exposed to moist air or other potential sources of hydrogen over the last decade.

The hydrogen levels measured for the two metals are shown in Figures 10 and 11. The iron dosimeters showed, with the exception of the 300°C specimen, that the iron specimens had relatively low hydrogen levels, and were comparable to the predicted transmutation level. In such a comparison, however, it is not possible to judge the original hydrogen content or the amount lost during or after the irradiation. In any event, the hydrogen levels were not large enough to identify iron as a transmutant contributor to the “extra” hydrogen. In addition, iron has a relatively high solubility for hydrogen, and the low hydrogen levels tend to support the absence of other environmental sources. The solubility of hydrogen in nickel is known to be lower than that of iron.

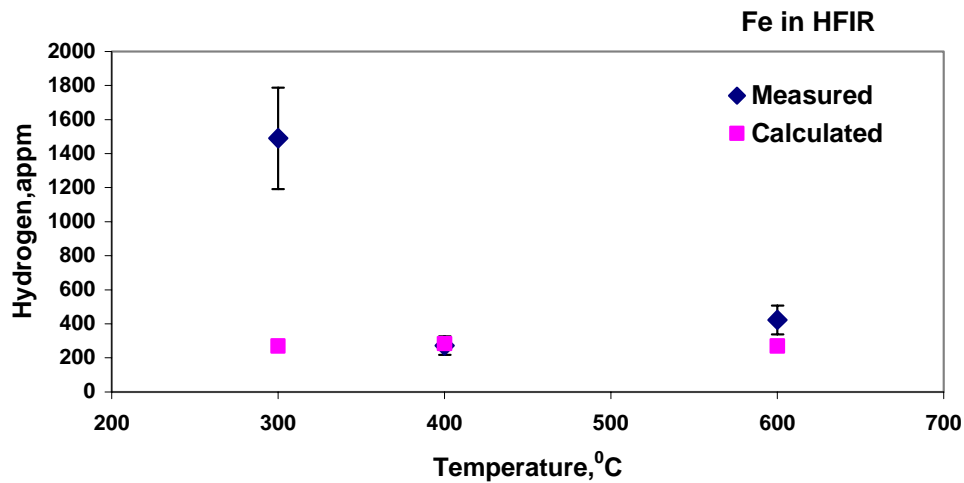


Figure 10. Hydrogen levels measured in pure iron dosimeters from the JP-12 and JP-15 experiments in HFIR.

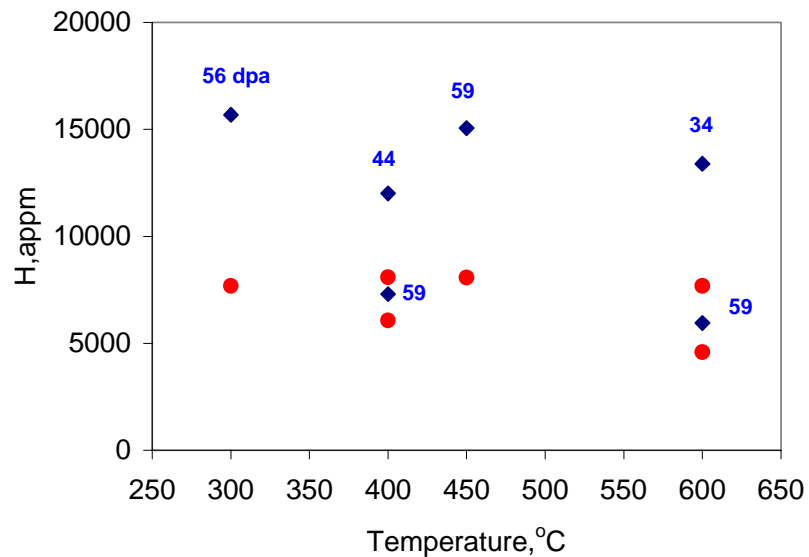


Figure 11. Hydrogen levels measured in pure nickel dosimeters from the JP-12 and JP-15 experiments in HFIR. Diamonds denote measured values; circles denote predictions.

The nickel dosimeters, however, were found to possess very large amounts of hydrogen at levels ranging from 6,000 to 16,000 appm, even at 600°C. Most interestingly, the levels were not strongly dependent on irradiation temperature or dpa level. In effect, these specimens retained more hydrogen than was calculated to have been formed by transmutation. If any diffusional losses have occurred during or after irradiation, the original hydrogen content would have been even larger.

Since nickel demonstrated such an unexpected response with hydrogen, it was decided to measure the helium content as well, since the predictive correlation was developed for total thermal neutron exposures significantly smaller than those explored in this study. Once again, as shown in Figure 12, we are surprised to see the unexpected. It appears measurements are progressively rising with accumulated dpa above the predictive correlation in a manner that is suggestive of another, previously unanticipated, late-term contribution to the helium production.

It therefore appears that nickel or more appropriately, one of its numerous radioactive daughters and granddaughters, may be responsible for both the "excess" hydrogen and helium. Currently, the most likely candidates are thought to be  $^{58}\text{Co}$  and  $^{65}\text{Zn}$ , since these isotopes are multiple-step in their formation and appear to have favorable Q-values for both (n,p) and (n, $\alpha$ ) reactions with thermal neutrons. In fact,  $^{65}\text{Zn}$  has a very large thermal

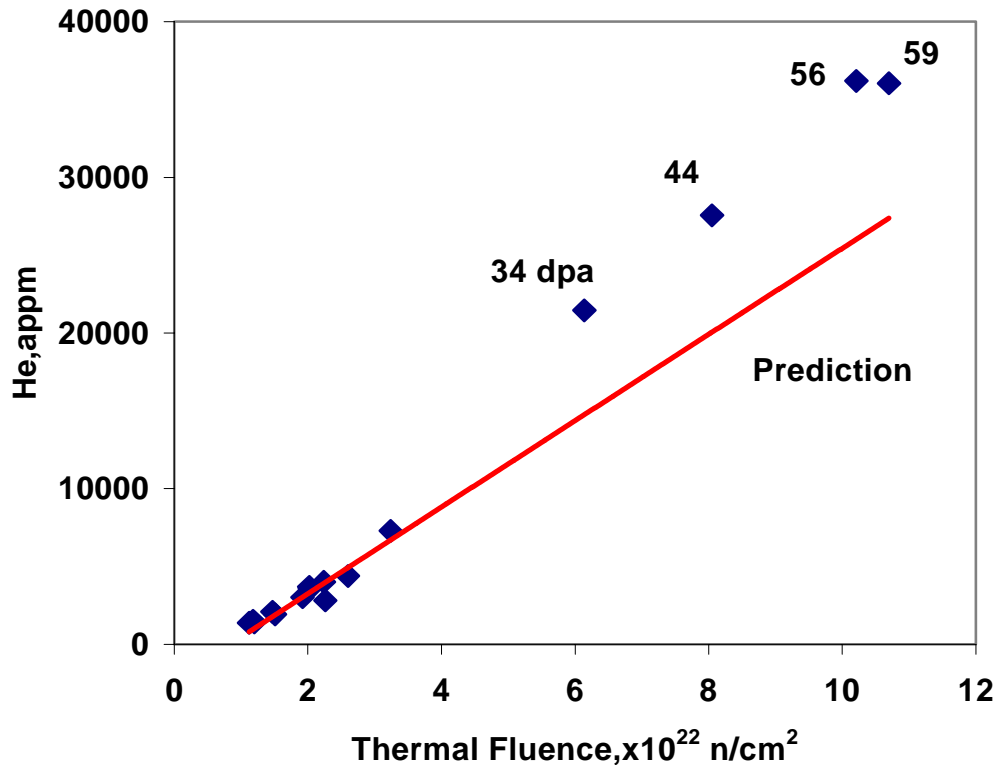


Figure 12. Comparison of measured helium and predictions as a function of thermal fluence. Dpa values are also shown. Data at lower fluences were used to establish the original predictive correlation.

(n, $\alpha$ ) cross section of 4.7 barns, so it would not be surprising if it also has a large thermal (n,p) cross section as well [18].

#### Discussion: Test reactor results

The several sets of FFTF studies show that the accumulation of voidage *per se* is insufficient to store hydrogen if there are not large sources of transmutant or environmental hydrogen to store. On the other hand, the two HFIR studies confirm that the simultaneous presence of voids and strong non-equilibrium concentrations of hydrogen can combine to store hydrogen, regardless of the nature of the hydrogen sources. One additional factor may be the temperature that the specimens experience at the end of the irradiation. In HFIR the temperature quickly drops to the coolant temperature of  $\sim 50^{\circ}\text{C}$ , while in FFTF the sodium coolant in MOTA requires  $\sim 15$  hours to cool and never drops below  $\sim 230^{\circ}\text{C}$  thereafter.

While the nickel dosimeter results indicate that some nickel daughter or granddaughter isotope may be providing unexpected contributions to helium and especially hydrogen production, this experiment has not shown clearly that the storage in nickel was in cavities. The wires were too small to measure swelling and were destroyed during gas measurement.

However, nickel is well known to exhibit void swelling throughout the  $300\text{-}600^{\circ}\text{C}$  range [19-21]. One aspect of swelling in this material is its strong tendency to saturate in swelling at a level that is not only independent of temperature, but also cannot exceed  $\sim 8\%$  swelling. If hydrogen is stored in cavities, then perhaps the saturation of both hydrogen and swelling may be directly related.

There is another potential explanation for the dosimeter results, however. If it is allowed that the cumulative uncertainties in the  $^{59}\text{Ni}(n,\alpha)$  and  $^{58}\text{Co}$  cross sections can be as large as 20-30%, the disparity in helium production might be explained without resort to invoking unidentified transmutant sources. This weakens the argument for an unidentified (n,p) source, however.

Note also that at  $300^{\circ}\text{C}$  the iron dosimeter had an apparently anomalous high hydrogen concentration. It has recently become known that pure iron, especially when cold-worked and irradiated at low temperatures, can exhibit substantial void swelling [21-23]. This suggests that void storage may be in progress in iron at  $300^{\circ}\text{C}$ . Additional measurements are planned to investigate this possibility.

Finally, this line of reasoning leads us back to the possibility of an environmental source of hydrogen to provide the "excess". Perhaps the source is transmutant hydrogen generated in the large aluminum block that surrounds both the stainless steel specimens and the dosimeter packages. This possibility will be investigated in future studies.

#### Conclusions

It appears that until exposure levels in excess of typical LWR levels are reached, it is possible to predict the helium production and retention on the basis of alloy composition and neutron flux-spectra. A similar expectation should apply to fusion environments. The prediction of hydrogen retention is more difficult, however, especially since hydrogen appears to become trapped in cavities such as bubbles and voids. Significant trapping in cavities requires strong non-equilibrium concentrations that can arise from either transmutation or environmental sources. The impact of such storage on degradation

processes such as void swelling and irradiation assisted stress corrosion cracking remains to be studied, however.

## ACKNOWLEDGEMENTS

The Offices of Basic Energy Sciences, Fusion Energy, and Nuclear Energy, Science and Technology, U.S. Department of Energy provided support for this research under Contract DE-AC06-76RLO 1830. Pacific Northwest National Laboratory is operated for DOE by Battelle Memorial Institute.

## REFERENCES

- [1] F. A. Garner and L. R. Greenwood, "Neutron Irradiation Effects on Fusion or Spallation Structural Materials: Some Recent Insights Related to Neutron Spectra", in Radiation Effects and Defects in Solids, 144 (1998) 251-283.
- [2] L. R. Greenwood, "Neutron Interactions and Atomic Recoil Spectra", J. of Nucl. Mater. 216 (1994) 29-44.
- [3] L. R. Greenwood, J. of Nucl. Mater. 116 (1983)137.
- [4] L. R. Greenwood and F. A. Garner, J. of Nucl. Mater. 233-237 (1996) 1530.
- [5] D. J. Edwards, F. A. Garner, B. A. Oliver and S. M. Bruemmer, "Microstructural Evaluation of a Cold-worked 316SS Baffle Bolt Irradiated in a Commercial PWR", Proc. Of Tenth Intern. Conf. on Environmental Degradation of Materials in Nuclear Power Systems – Water Reactors, Aug. 5 –9, 2001, in press.
- [6] H. Farrar and B. M. Oliver, "A Mass Spectrometer System to Determine Very Low Levels of Helium in Small Solid and Liquid Samples", J. Vac. Sci. Technol. A4, 1740 (1986).
- [7] B. M. Oliver, J. G. Bradley, and H. Farrar, "Helium Concentration in the Earth's Lower Atmosphere", Geochim. Cosmochim. Acta **48**, 1759 (1984).
- [8] B. M. Oliver, F.A. Garner, and L.R. Greenwood, "Quadrupole Mass Spectrometer for the Determination of Low to high Levels of Hydrogen in Irradiated Materials", J. of Nucl. Mater. 283-287 (2000) 1006-1010.
- [9] A. Jenssen and L. G. Ljungberg, Final Report: Irradiation Assisted Stress Corrosion Cracking Studies, ABB Atom, SDA-95-1262, (1995).
- [10] S. M. Bruemmer, D. J. Edwards, B. W. Arey and L. A. Charlot, "Microstructural, Microchemical and Hardening Evolution in LWR-Irradiated Austenitic Stainless Steel", Proceedings, Ninth International Symposium on Environmental Degradation in Nuclear Power Systems - Water Reactors, (1999) pp. 1079-1087.
- [11] F. A. Garner, L. R. Greenwood and D. L. Harrod, "Potential High Fluence Response of Pressure Vessel Internals Constructed from Austenitic Stainless Steels", Proc. Sixth Intern. Symp. on Environmental Degradation of Materials in Nuclear Power Systems - Water Reactors, San Diego, CA. August 1-5, 1993, pp. 783-790.
- [12] T. Matsuoka, T. Yonezawa, K. Nakamura, H. Myojin, J. Shimizu and T. Nagata, Proc. Of ICONE-4, Vol. 4, pp. 249-256.
- [13] G. L. Hankin, "Radiation-Induced Evolution of Microstructure and Mechanical Properties of Stainless Steels", Ph. D. Thesis, Loughborough University, U.K., 1999.

- [14] L. R. Greenwood, F. A. Garner and B. M. Oliver, J. of Nucl. Mater. 212-215 (1994) 492.
- [15] F. A. Garner, M. L. Hamilton, L. R. Greenwood, J. F. Stubbins and B. M. Oliver, "Isotopic Tailoring with <sup>59</sup>Ni to Study the Effect of Helium on Microstructural Evolution and Mechanical Properties of Neutron Irradiated Fe-Cr-Ni Alloys", Proceedings of 16th ASTM International Symposium on Effects of Radiation on Materials, ASTM STP 1175, Denver, CO, June 22-24, 1992, pp. 921-939.
- [16] M. P. Tanaka, S. Hamada, A. Hishinuma and P. J. Maziasz, J. of Nucl. Mater. 155-157 (1988) 801-805.
- [17] S. Hamada, P. J. Maziasz, M. P. Tanaka, S. Suzuki and A. Hishinuma , J. of Nucl. Mater. 155-157 (1988) 838-834.
- [18] D. W. Kneff, L. R. Greenwood, B. M. Oliver, R. P. Skowronski and E. L. Callis, Radiation Effects 92-93 (1986) 553-556.
- [19] F. A. Garner, J. of Nucl. Mater. 205 (1993) 98-117.
- [20] F. A. Garner, in Fusion Reactor Materials Semiannual Report for period ending March 31, 1990, DOE/ER-0313/8, pp.125-135.
- [21] N. I. Budylnkin, E. G. Mironova, V. A. Krasnoselov, S. I. Porollo and F. A. Garner, "Void Swelling and Embrittlement of Pure Iron and Pure Nickel in the BN-350 and BOR-60 Fast Reactors", to be published in the Proc. of ICFRM-10, Oct, 2001 in Baden-Baden, Germany.
- [22] S. I. Porollo, A. M. Dvoriashin, A. N. Vorobyev and Yu. V. Konobeev, J. of Nucl. Mater. 256 (1998) 247.
- [23] A. M. Dvoriashin, S. I. Porollo, Yu. V. Konobeev and F. A. Garner, J. of Nucl. Mater. 283-287 (200) 157.

**NEUTRON-INDUCED MICROSTRUCTURAL EVOLUTION OF Fe-15Cr-16Ni ALLOYS AT ~ 400°C DURING NEUTRON IRRADIATION IN THE FFTF FAST REACTOR** - T. Okita, T. Sato and N. Sekimura (University of Tokyo), F. A. Garner and L. R. Greenwood (Pacific Northwest National Laboratory)\*, W. G. Wolfer (Lawrence Livermore National Laboratory), Y. Isobe (Nuclear Fuel Industries Ltd., Japan)

## **OBJECTIVE**

The purpose of this effort is to determine the influence of dpa rate on void swelling of fcc alloys.

## **SUMMARY**

An experiment conducted at ~400°C on simple model austenitic alloys (Fe-15Cr-16Ni and Fe-15Cr-16Ni-0.25Ti, both with and without 500 appm boron) irradiated in the FFTF fast reactor at seven different dpa rates clearly shows that lowering of the atomic displacement rate leads to a pronounced reduction in the transient regime of void swelling. While the steady state swelling rate (~1%/dpa) of these alloys is unaffected by changes in the dpa rate, the transient regime of swelling can vary from <1 to ~60 dpa when the dpa rate varies over more than two orders of magnitude. This range of dpa rates covers the full span of fusion, PWR and fast reactor rates.

The origin of the flux sensitivity of swelling arises first in the evolution of the Frank dislocation loop population, its unfauling, and the subsequent evolution of the dislocation network. There also appears to be some flux sensitivity to the void nucleation process. Most interestingly, the addition of titanium suppresses the void nucleation process somewhat, but does not alter the duration of the transient regime of swelling or its sensitivity to dpa rate. Side-by-side irradiation of boron-modified model alloys in this same experiment shows that higher helium generation rates homogenize the swelling somewhat, but do not significantly change its magnitude or flux sensitivity.

The results of this study support the prediction that austenitic alloys irradiated at PWR-relevant displacement rates will most likely swell more than when irradiated at higher rates characteristic of fast reactors. Thus, the use of swelling data accumulated in fast reactors may possibly lead to an under-prediction of swelling in lower-flux PWRs and fusion devices.

## **INTRODUCTION**

The void swelling phenomenon was the life-limiting aging phenomenon of austenitic stainless steels in fast reactors (1). Until very recently it was not thought that void swelling would occur in the austenitic internal components of light water reactors (LWRs). Similar predictions have been made for some fusion devices operating at lower dpa rates and lower temperatures. The two reactor concepts share many similarities, including high generation rates of helium and hydrogen.

It was predicted in 1994, however, that the 316 and especially 304 stainless steels used in the baffle-former-barrel assembly of pressurized water reactors (PWRs) were probably already swelling at relatively low levels and would continue to swell at accelerating rate as the nuclear plants continued to age (2,3). Due to the accelerating development of swelling

---

\* Pacific Northwest National Laboratory (PNNL) is operated for the U.S. Department of Energy by Battelle Memorial Institute under contract DE-AC06-76RLO-1830.

rate at higher exposures it was suggested that void swelling might become an important issue in plant life extension of PWRs. Stainless steels used in boiling water reactors (BWRs) experience much lower neutron exposures and are not expected to develop significant amounts of swelling.

Even more importantly, it was predicted that not only would the higher rates of gamma heating and helium generation characteristic of LWRs tend to somewhat accelerate the onset of void swelling, but the lower neutron fluxes and atomic displacement rates of PWRs, compared to those of fast reactors, would strongly accelerate the onset of swelling. The acceleration was predicted both in lowering the threshold neutron dose and the threshold irradiation temperature, pushing the swelling temperature regime down toward the PWR inlet temperature (2).

Subsequent papers published by Garner and co-workers have examined void development in various Russian steels irradiated at very low neutron fluxes in either fast reactors or PWRs (4-9). These studies demonstrate the onset of swelling at very low temperatures and neutron exposures, down to  $\sim 300^{\circ}\text{C}$  and at doses below 10 dpa (displacements per atom). Voids have also recently been found in cold-worked 316 and 347 bolts removed from various Western reactors at unexpectedly low temperatures and neutron exposures (10,11). Even charged particle irradiation experiments conducted at higher atomic displacement rates have shown that void swelling can occur in 300 series steel at temperatures as low as  $300^{\circ}\text{C}$  (12-14). Since the majority of the PWR baffle-former assembly that is exposed to high neutron exposures exists at temperatures above  $300^{\circ}\text{C}$ , this implies that the potential for swelling at some level exists throughout the assembly. It is only the magnitude of swelling that is uncertain under PWR conditions.

Garner proposed, however, that the most important environmental variables for swelling in PWRs would be the irradiation temperature and especially the rate of atomic displacement, the latter being roughly linear with the fast neutron flux (2). The dependence of swelling on atomic displacements per atom per second (dpa/sec) is somewhat more difficult to study, but one recent study indicated that the swelling of annealed 304 stainless steel at  $\sim 380^{\circ}\text{C}$  appeared to accelerate as the dpa rate decreased through the PWR-relevant range (15).

A number of comprehensive experiments have been initiated to study the separate effects of dpa rate and helium generation. The first of these is a fast reactor study on annealed 304 stainless steel, which clearly shows an acceleration of void swelling with decreasing dpa rate (16). Unfortunately, this study on 304 stainless does not provide strong clues illuminating the microstructural origins of the sensitivity of swelling to dpa rate. The second flux-effect study is the current study, which not only confirms the flux-sensitivity of swelling, but also provides evidence of the microstructural origins of the flux dependency of void swelling during neutron irradiation. A companion study on the same alloy using charged particle irradiation at much higher dpa rates reaches similar conclusions while providing additional insight on the microstructural origins of the flux sensitivity of swelling (17).

Okita and coworkers earlier published the first small fraction of the results from the current neutron irradiation experiment (18). The large specimen matrix of this experiment is still being analyzed but the major results of the experiment are presented here.

#### Experimental Details

Simple model austenitic alloys, ternary Fe-15Cr-16Ni and quaternary Fe-15Cr-16Ni-0.25Ti (atomic %) and boron-doped (500 appm natural boron) variants of each were prepared by

arc melting from very pure Fe, Ni, Cr and Ti. Microscopy showed that no titanium or boron-containing precipitates were present, indicating that these elements were well dispersed.

The alloys were rolled to sheets of 0.2 mm thickness. Afterward, standard 3 mm microscopy disks were punched and then annealed for 30 minutes at 1050°C in a very high vacuum. Each specimen was marked with a unique identification code by laser engraving. The specimens were then loaded in a well-defined order into sealed, helium-filled tubes of 0.88 in length. The tubes were helium leak-checked to insure tube integrity. All alloys of interest in a given experiment were placed side-by-side into the same tube to insure that there were no differences in environmental history between the various alloys. Multiple tubes with identical contents and packing order were placed at all positions and irradiation conditions of interest.

Each tube was placed in one of canisters of the Materials Open Test Assembly (MOTA) at one of seven axial locations ranging from below the core of the Fast Flux Test Facility (FFTF) to far above the core. In the FFTF-MOTA experiment the temperature of each canister was measured by thermocouples and was actively controlled to  $\pm 5^\circ\text{C}$  of the target temperature throughout the irradiation. The target temperatures of the individual canisters varied over a limited range, 390 to 444°C.

The first irradiation sequence occurred in Cycle 11 of FFTF operation in MOTA-2A, and a subset of tube packets was then removed. Other identical tube packets continued in Cycle 12 with irradiation in MOTA-2B, and then the packets were removed. With one exception all tube packets remained at the same canister level during the transition to MOTA-2B. One set moved from Level 3 to level 2 with a slight increase in dose rate.

The irradiation exposure was determined by extensive dosimetry measurements involving radioactivation of a number of pure metals. The dpa rates specified in this paper were determined for the midpoint of the tube packet length and for the various packets ranged from  $8.9 \times 10^{-9}$  to  $1.7 \times 10^{-6}$  dpa/sec. The mid-point dpa levels varied from 0.23 to 43.8 dpa in MOTA-2A and 0.38 to 24.0 dpa in MOTA-2B. Wherever possible, two identical packets were placed in MOTA-2A and one of them moved to MOTA-2B at essentially identical dpa rates. In some out-of-core canisters, however, the position and associated dpa rate of individual packages changed somewhat when moved from MOTA-2A to MOTA-2B, and consideration of such changes is necessary in interpretation of the swelling data.

Even more importantly, the packets near or outside of the core boundary will have a gradient along their length. Although the ternary and quaternary alloys were usually side-by-side in the tube packet with little potential difference in dpa rate, this was not necessarily always the case for the comparable boron-doped alloys, with some consequences in the interpretation of the influence of boron addition. In general the boron-doped alloys were 0.5 to 0.7 cm away from the undoped alloys. Thus the swelling will be subject to the combined effects of both boron and dpa rate.

The exposures were calculated in displacements per atom (dpa) using the standard NRT model (19). The target irradiation temperatures, dpa levels and dpa rates experienced by each specimen group are listed in Table 1. Spectral-dependent calculations were performed to assess the production of helium in both the base alloys and B-doped alloys. The fractional burnup of  $^{10}\text{B}$  per dpa was highly dependent on the location in the core, being larger at the out-of-core locations where the neutron spectra are softer. Table 1 also provides the helium levels reached in the alloys.

Table 1. Irradiation Conditions in MOTA-2A and 2B

MOTA		Dose, dpa			dpa/sec		Temperature		appm He	
2A	2B	2A	2B	Total	2A	2B	2A	2B	without B	with 500appm B
Yes	No	0.23	-----	0.23	8.90E-09	-----	436	-----	0.013	3.59
Yes	Yes	0.23	0.38	0.61	8.90E-09	2.20E-08	436	444	0.021	6.1
Yes	No	0.71	-----	0.71	2.74E-08	-----	434	-----	0.23	7.84
Yes	Yes	0.71	1.16	1.87	2.74E-08	6.60E-08	434	437	0.35	12.6
Yes	No	2.36	-----	2.36	9.11E-08	-----	430	-----	0.45	12.2
Yes	Yes	2.36	3.7	6.36	9.11E-08	2.10E-07	430	431	0.7	19
Yes	No	8.05	-----	8.05	3.11E-07	-----	411	-----	1.84	27.5
Yes	Yes	5.69	5.36	11.1	2.20E-07	3.00E-07	411	410	3.22	37.6
Yes	No	14	-----	14	5.41E-07	-----	430	-----	3.06	14.1
Yes	Yes	14	14.8	28.8	5.41E-07	8.40E-07	430	424	5.48	22.7
Yes	No	20	-----	20	7.80E-07	-----	390	-----	6.64	19.6
Yes	Yes	15.6	16.8	32.4	6.00E-07	9.50E-07	390	387	10.9	31.1
Yes	No	43.8	-----	43.8	1.70E-06	-----	427	-----	8.96	22.3
Yes	Yes	43.8	24	67.8	1.70E-06	1.40E-06	427	408	15.5	38.2

After removal of the TEM specimens from the tube packet, they were cleaned and then measured by one and sometimes two methods to determine the swelling. The first method involved the use of an immersion density technique known to be accurate to ~ 0.2%, but which is incapable of discriminating between void swelling and other contributions to density change. This technique is especially effective in determining the volume-averaged swelling at large levels. The second technique involved the use of electropolishing and transmission electron microscopy (TEM), which is very effective to determine low levels of void swelling, but cannot easily discriminate between swelling variations that are rather heterogeneously distributed. TEM is not particularly effective to measure swelling at large levels where significant intersection of voids with the electropolished surfaces occurs. In some cases both methods were used to determine the swelling. Usually, there is only one TEM determination from a single specimen, but often there are two, three or four separate disks measured for density.

## Results

Microscopy examination reveals that voids, occasional bubbles, Frank interstitial loops and unfaulted perfect dislocation loops, and finally network dislocations are the only microstructural features observed. There were no pre-existing or radiation-induced precipitates observed in any sample.

Figure 1 shows typical void microstructures of quaternary Fe-15Cr-16Ni-0.25Ti, both without and with 500 appm boron, after irradiation to 28.8 dpa at 430/424°C in MOTA-2A and 2B. Figure 2 shows typical loop and dislocation microstructures of Fe-15Cr-16Ni-500appmB after irradiation to 0.61 dpa at 436/444°C in MOTA-2A and 2B. Note that most of the loops are already unfaulted and/or heavily decomposed into network dislocations.

When more than one specimen was measured by density change, the swelling was remarkably consistent between specimens. Figures 3 and 4 show that the ternary and quaternary alloys exhibit remarkably similar behavior, with the transient regime of swelling progressively increasing in duration as the dpa rate increases, ranging from less than 1 dpa to greater than 50 dpa. Figure 4 expands the scale in order to better visualize the behavior of the two alloys at the lowest two displacement rates. It is very clear from Figures 3 and 4

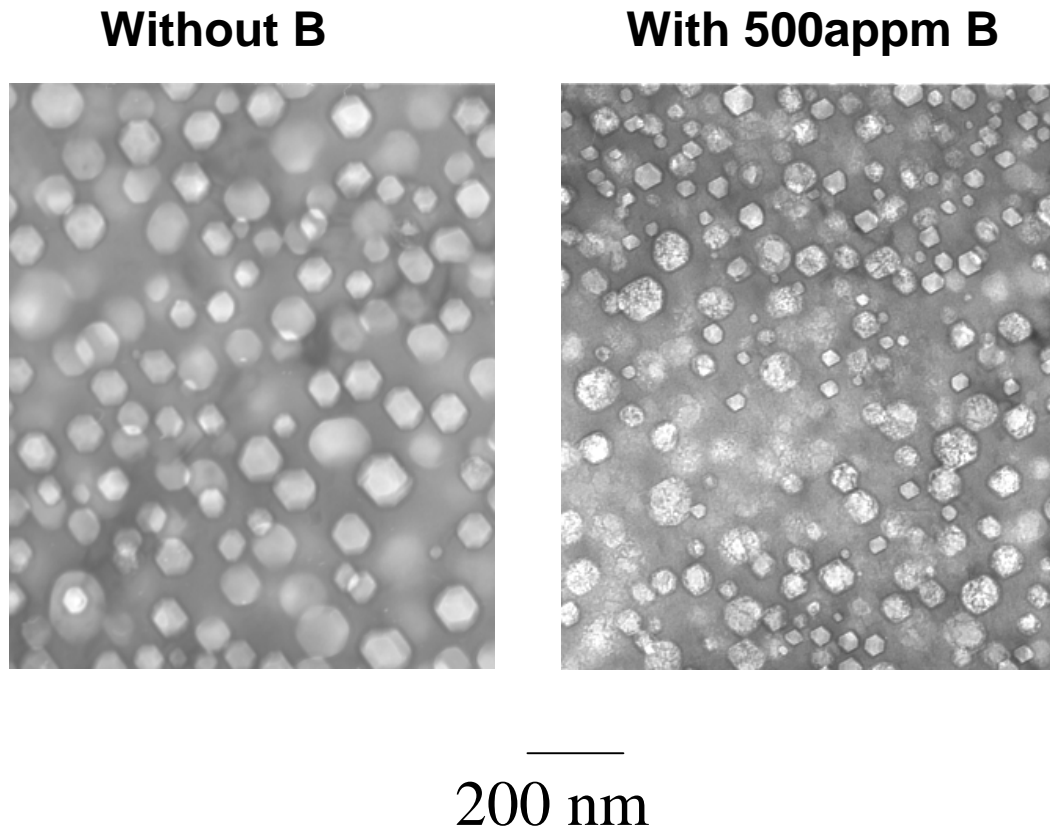
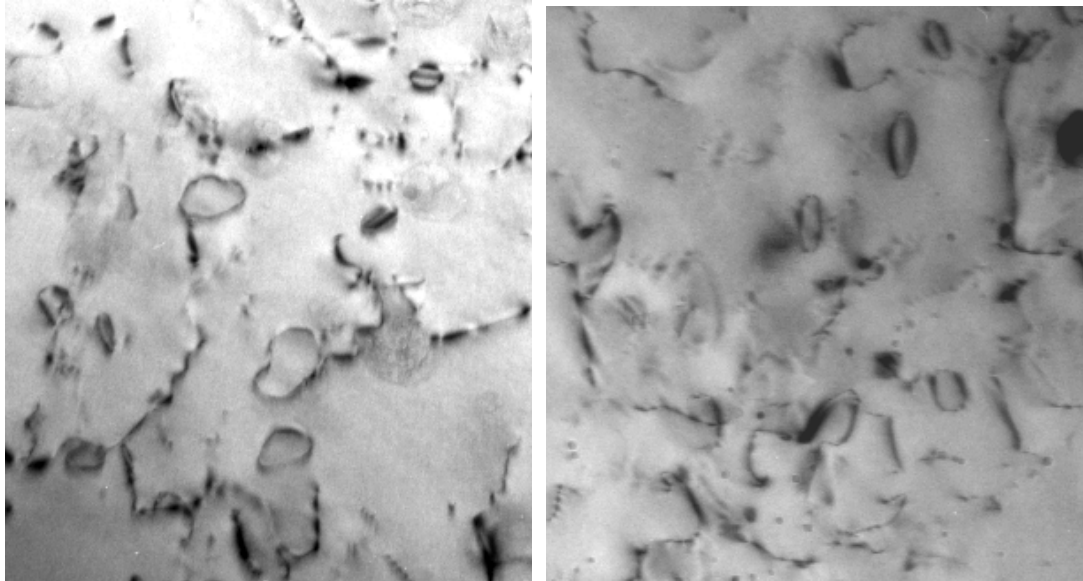


Figure 1. Void microstructures observed in Fe-15Cr-16Ni-0.25Ti after irradiation to 28.8 dpa at 430/424°C in MOTA-2A and 2B. Note that addition of 500 appm boron caused a slight increase in void density as a result of increasing the helium content from 5.5 to 22.7 appm.

that the steady-state swelling rate over the entire range of dpa rates is  $\sim 1\%/dpa$ , in agreement with earlier results on ternary model alloys irradiated in the EBR-II reactor (20-21) and all austenitic stainless steels irradiated in a variety of reactors (1, 22).

Figure 5 presents a comparison for the ternary and quaternary alloys at several irradiation conditions to emphasize that titanium addition made very little difference in the macroscopic swelling behavior at this irradiation temperature. On the microscopic level, however, there were distinct differences in behavior with titanium appearing to suppress somewhat the nucleation of voids as shown in Figure 6, with compensating increases in void sizes, as shown in Figure 7.



200 nm

Figure 2. Dislocation loop microstructure of Fe-15Cr-16Ni-500appmB at 0.61dpa and 436/444°C after irradiation in MOTA-2A and 2B. Note that, even at this low dose, most of the loops are unfaulted and dislocation network evolution is well in progress.

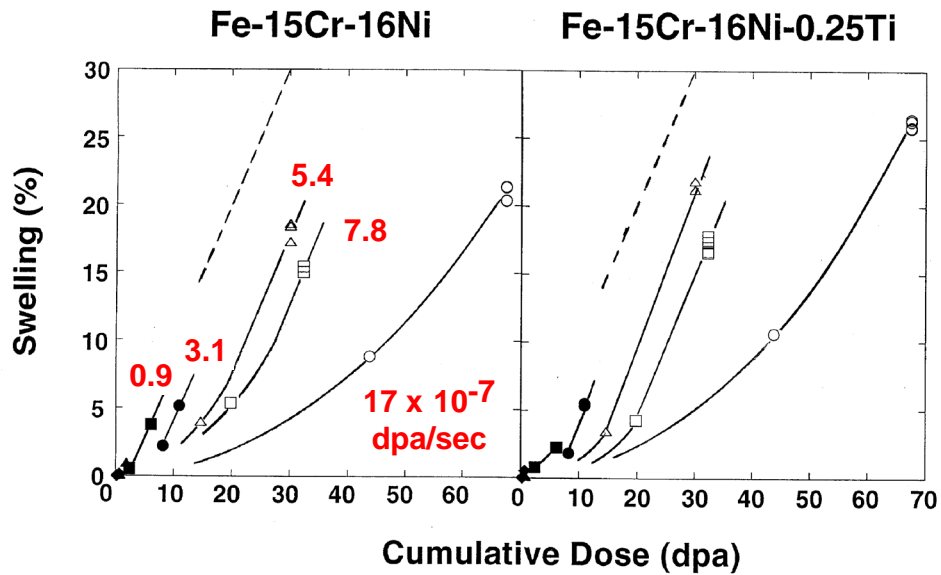


Figure 3. Swelling observed at ~400°C in the ternary and quaternary alloys as a function of dpa rate. In these comparisons the ternary and quaternary alloys are side-by-side with no significant gradient in dpa rate.

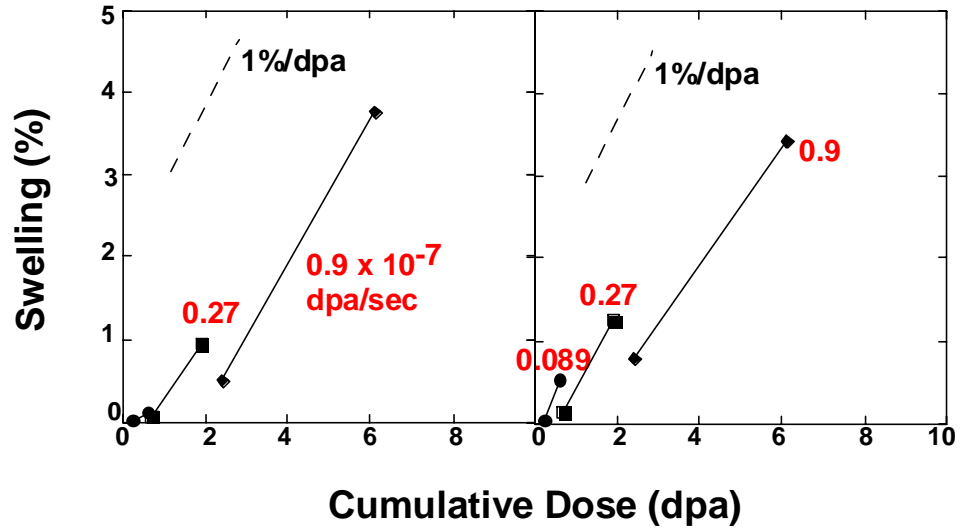


Figure 4. Expand version of Figure 3 to more clearly show swelling at the lowest three dpa rates.

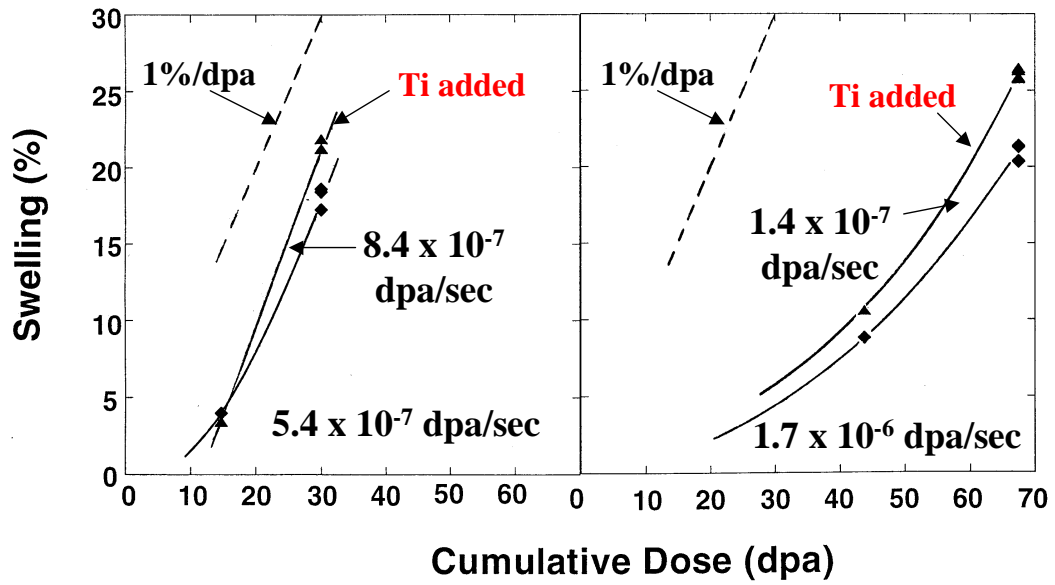


Figure 5. Small influence of titanium on void swelling at  $\sim 400^\circ\text{C}$  for two conditions where the dpa rates changed somewhat.

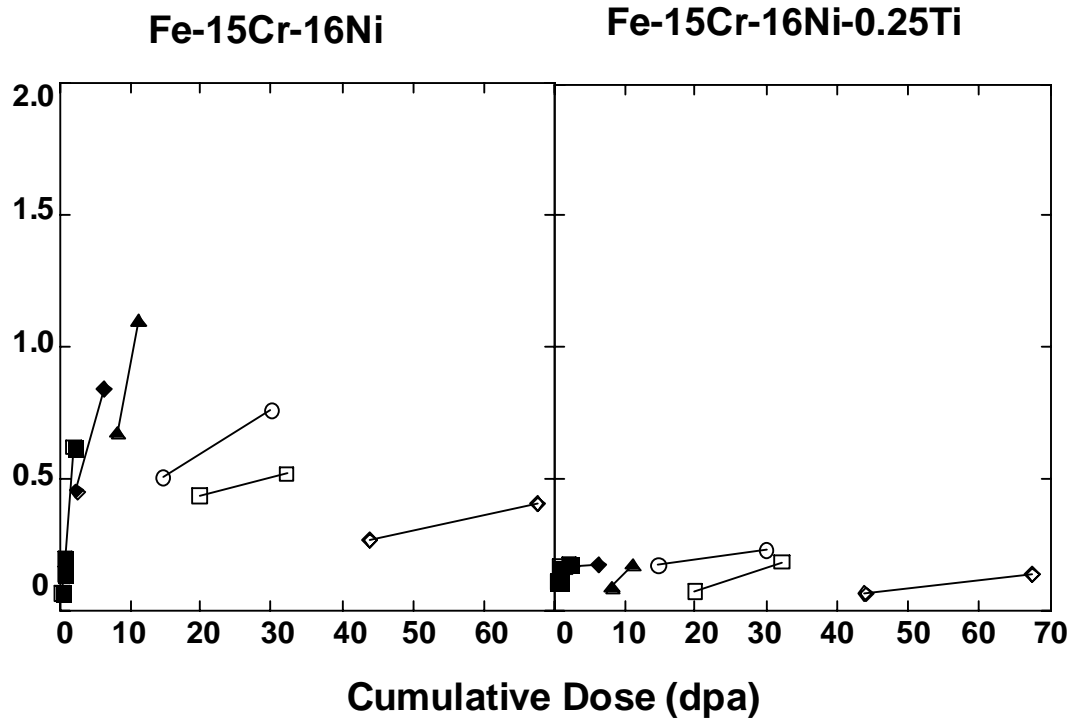


Figure 6. Dose dependence of cavity density in the two alloys.

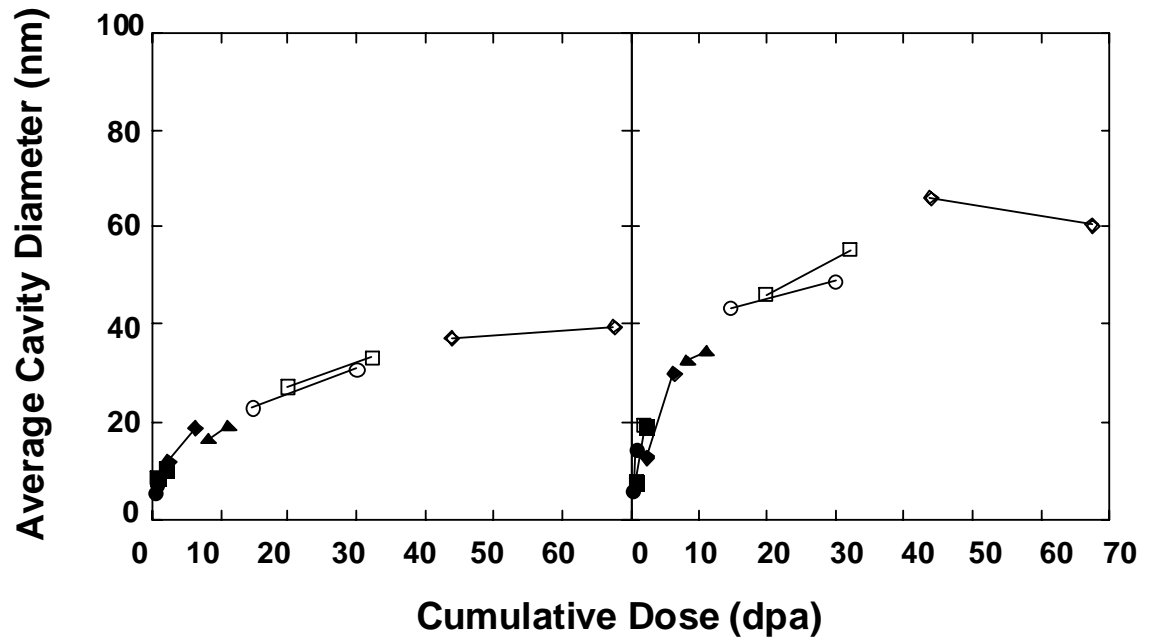


Figure 7. Dose dependence of average cavity diameter in the two alloys.

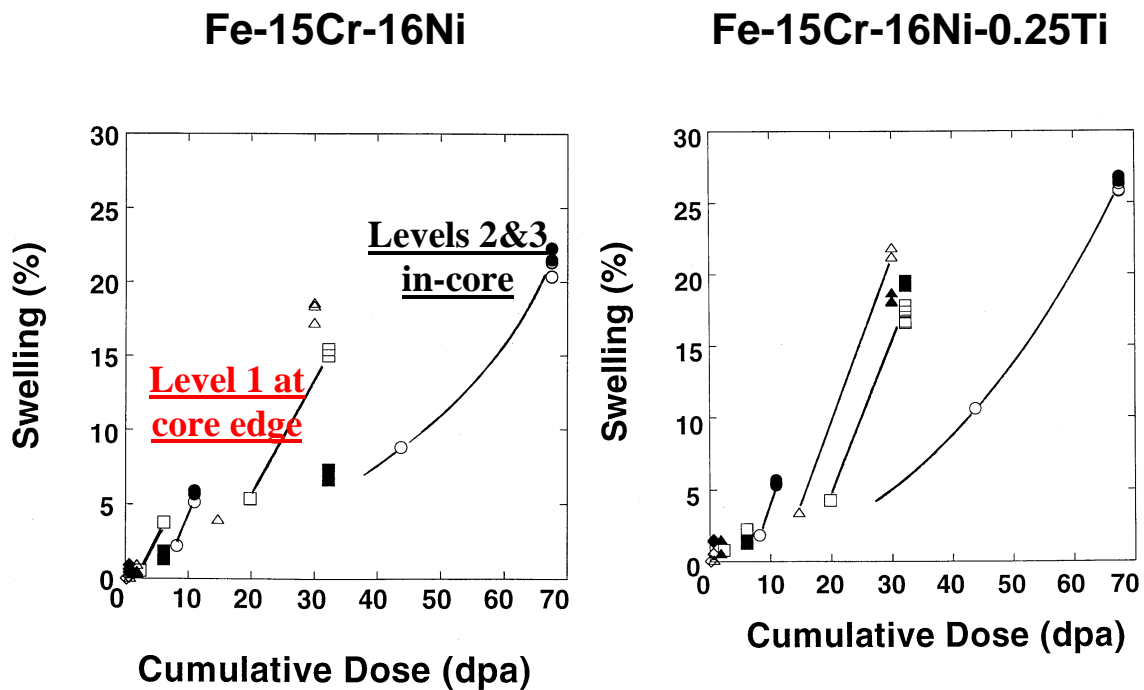


Figure 8. Influence of 500 appm boron addition (solid symbols) on total swelling of the ternary and quaternary alloys. The sometimes large apparent depression of swelling with boron addition (e.g. Level 1) results from the spatial separation of the B-doped and undoped alloys along a gradient in dpa rate, with the depression actually arising from a slightly higher dpa rate. When the gradient is very small such as in levels 2 and 3, there is very little effect of boron on swelling. The ternary alloy seems to be more sensitive to such spatial variations compared to the quaternary.

Figure 8 shows that, with a few striking exceptions, the macroscopic swelling of both alloys is not appreciably affected by boron addition that produces both He and Li via the  $^{10}\text{B}(n,\alpha)^6\text{Li}$  reaction. However, it appears that in those several cases where the boron appeared to strongly depress swelling, there was a small but significant difference in dpa rate of the boron-doped and undoped alloys due to their 0.5 to 0.7 cm separation in the packing order. Once again the dpa rate effect overshadowed the action of composition and transmutation.

Remember that the helium levels are dependent on both the dpa level and on the position in the reactor, thereby exerting different influence at different dpa rates. In Figure 1 an increase from 5.5 to 22.7 appm/dpa caused a slight increase in the void density with concurrent reduction in void size, and the swelling was reduced by several percent.

It is important to note that  $^{11}\text{B}$  is 89% of natural boron and is not transmuted, so any variations in swelling behavior as a result of boron addition cannot be attributed to He alone, but to the combined effect of He, Li and retained B. It has shown that both He and Li tend to increase void nucleation in boron-doped austenitic steels (23, 24).

Figure 9 at first glance appears to imply that the loop density of the ternary alloy at the four lowest dpa rates is insensitive to dpa rate, tending toward saturation with increasing dpa.

This conclusion is misleading, however. Note that loops are absent at the highest three dpa rates, indicating that loop unfaulting and network formation now completely dominates the dislocation microstructure. As shown in Figure 10 it is obvious that loop unfaulting and network formation was occurring even more strongly at the lowest dpa rates. One strong consequence of the flux-sensitivity of loop unfaulting is a progressive delay of network dislocation evolution with increasing dpa rate. As shown in Figure 11 titanium addition appears to slightly depress the nucleation of Frank loops, but the mean loop size is slightly larger, leading to no large change in the total loop line length or the evolution of the dislocation network. Thus titanium's influence on both voids and dislocation evolution appears to be similar, with a reduction in number density that is almost exactly offset by an increase in size.

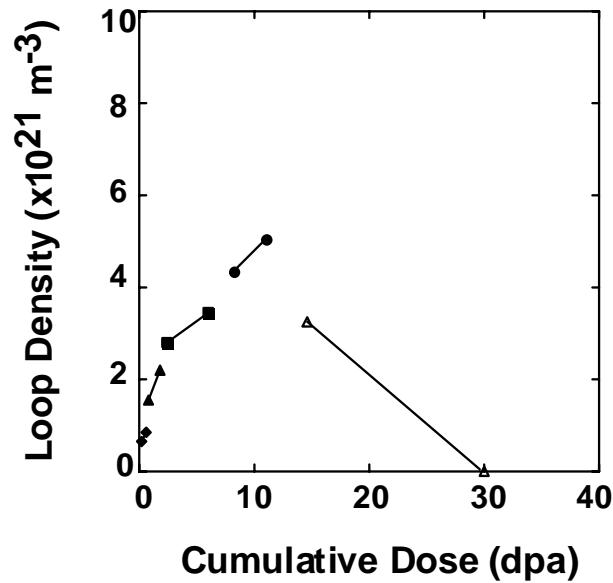


Figure 9. Dose dependence of loop density in the ternary alloy.

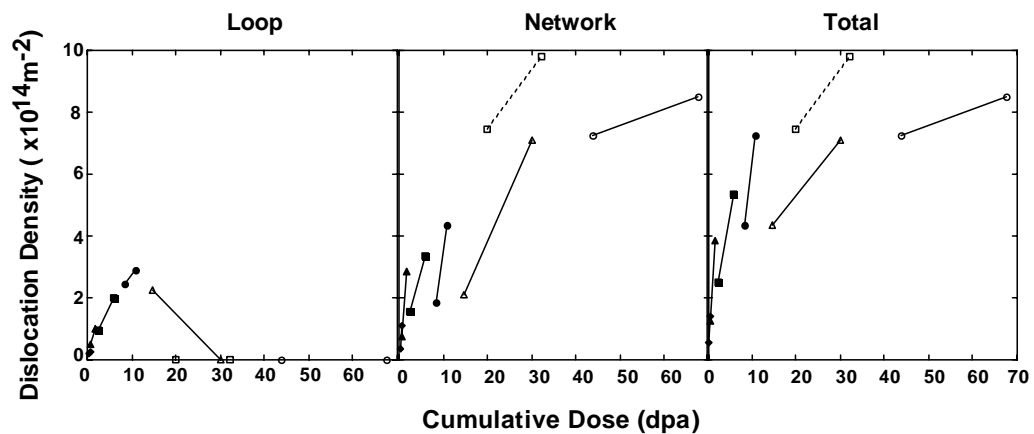


Figure 10. Evolution of the components of the dislocation line length in the ternary alloy.

## Discussion

One interesting aspect of these results is the influence of titanium at  $\sim 400^\circ\text{C}$  was its effect to reduce somewhat both the loop density and the void density, but having no effect on the aggregate dislocation or swelling behavior. Similar behavior was observed in several similar experiments also conducted in the JOYO or FFTF fast reactors at  $\sim 400^\circ\text{C}$  (25-27). In these constant dpa rate irradiations both Fe-13Cr-14Ni (0.12Ti) and Fe-15Cr-16Ni (0.25Ti), the addition of titanium had no influence on total swelling at  $400^\circ\text{C}$ , but caused an increasing suppression of swelling at higher temperatures (500,  $600^\circ\text{C}$ ).

Such a solute-induced dependence of void nucleation on temperature in simple model Fe-Cr-Ni alloys is consistent with the addition of a fast diffusing solute (28, 29). Indeed titanium is a fast diffusing species, diffusing in  $\gamma$ -iron at a rate 4.2 times faster than that of iron (30).

Yoshiie and co-workers note, however, that 0.25% titanium addition to Fe-15Cr-16Ni slowed down Frank loop growth, and that was a consequence of a titanium-induced decrease in vacancy diffusivity (31), and that this view was supported by electrical resistivity measurements by Dimitrov and co-workers showing that mobility is decreased with titanium addition (34). Is it possible that addition of a fast-diffusing element can suppress the overall vacancy diffusivity of the alloy?

Such a proposal has merit and will require further study. While it is frequently assumed that addition of a faster or slower-diffusing solute will speed up or slow down overall vacancy diffusion of the alloy, this is not always a safe assumption. For example, addition of more fast-diffusing Cr actually depresses overall vacancy diffusion in Fe-Cr-Ni alloys, while addition of additional slower-diffusing Ni actually elevates vacancy diffusion of the alloy matrix (33). Perhaps Cr and Ti are very similar in this respect.

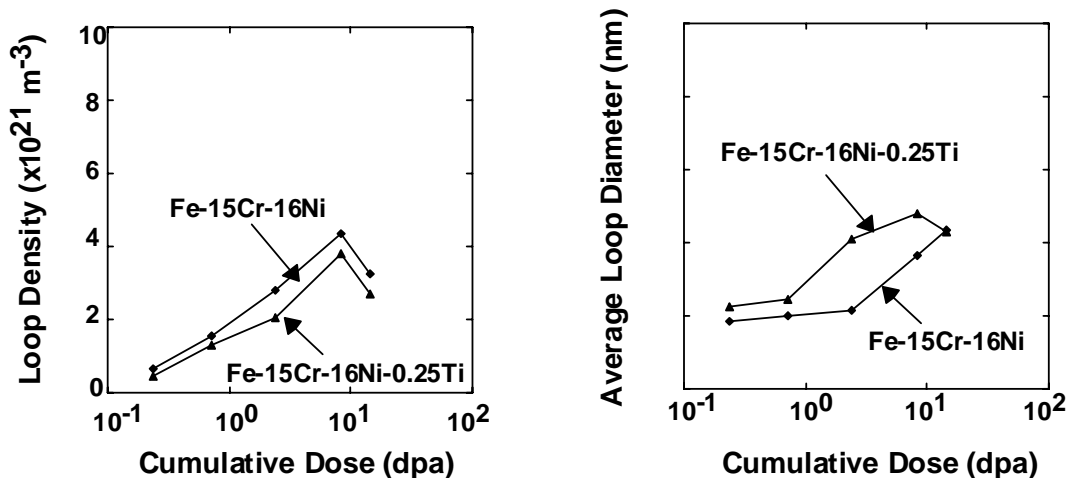


Figure 11. Influence of titanium addition on loop evolution, as observed in MOTA-2A specimens.

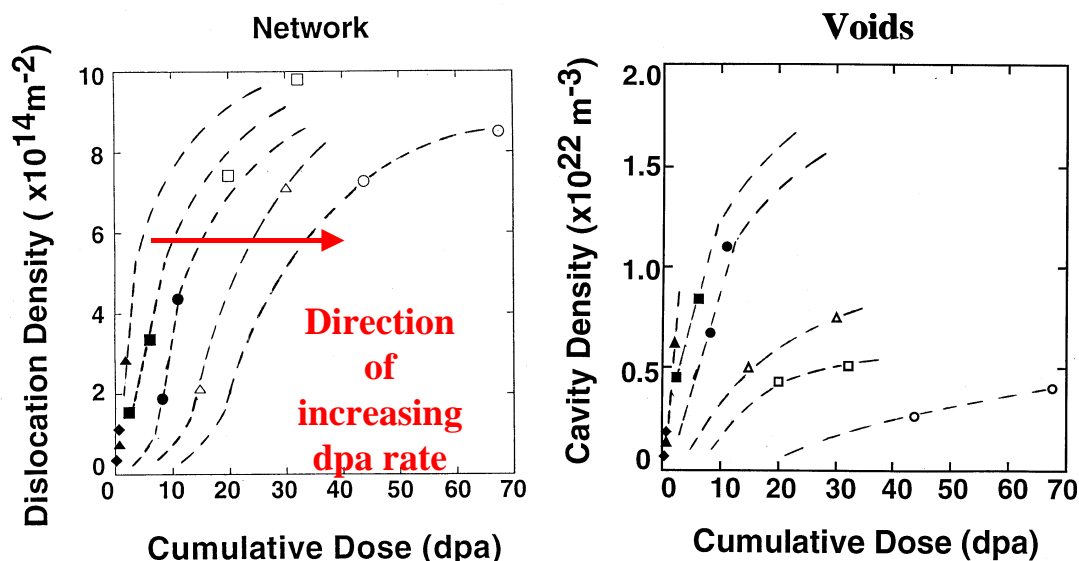


Figure 12. Interpretation of the trends exhibited by the microstructural data.

An alternate interpretation of the effect of titanium to reduce the void density would focus on the potential of this element to act as a getter for gases, especially any residual oxygen, and thereby reducing void nucleation somewhat.

The most significant observation of this study is the very clear and progressive reduction in the transient regime of swelling in both the ternary and quaternary alloys, approaching zero dpa at the lowest dose rates. Secondly, the results of this study reconfirm the universally observed steady-state swelling rate of  $\sim 1\%/dpa$  that is characteristic of all austenitic steels over a very wide range of dpa rates, temperatures and other environmental or material variables. It is significant that the approach to this rate can be very languid at dpa rates much higher than relevant to PWR operation.

It appears, that in this irradiation series, the effect of dpa rate overwhelms the influence of boron, lithium, helium and titanium, even though each has significant but different impacts on modifying the void density. In general, it has been shown that the steady-state swelling rate is expected to be relatively independent of cavity density, providing cavity densities are reached in excess of  $\sim 10^{14} \text{ cm}^{-3}$  (34).

The strong onset of unfauling and dislocation evolution at very low dpa rates erases any meaningful evidence of the dependence of Frank loop nucleation on dpa rate in this experiment, but the charged particle companion experiment (17) mentioned earlier clearly shows that Frank loop nucleation is strongly sensitive to dpa rate. This conclusion is in agreement with a more comprehensive series of experiments by Muroga and co-workers (35) where the saturation density of Frank interstitial loops increased with  $(dpa \text{ rate})^{1/2}$  over more than three orders of magnitude in dpa rate. In general, higher densities of loops develop concurrently with smaller loop sizes and therefore different probabilities of intersection, interaction and unfauling.

It appears that the primary flux-sensitivity of the microstructural evolution resides in the development of the Frank interstitial loop population, followed by a flux-dependent delay in the unfauling and network formation processes. Following the formation of the dislocation network it is expected that void nucleation will also exhibit sensitivity to dpa rate (36). The flux-sensitive delay in the onset of void swelling appears to first involve a delay in the formation of the dislocation network. Figure 12 presents our interpretation of the network and void nucleation of Fe-15Cr-16Ni when viewed in this context. Theoretical modeling of these results is in progress and will be presented in a later paper.

Conventional wisdom holds that there is a “temperature shift” in the temperature regime inhabited by void swelling (37). This shift envisions that void swelling would respond similarly to decreases in temperature and increases in dpa rate. One anticipated consequence of the temperature shift concept would be that decreasing dpa rates ought to bring decreases in void nucleation, since the irradiation would proceed at a higher effective temperature. As can be seen from Figure 12, however, exactly the opposite behavior is observed in void nucleation as a function of dpa rate.

In previous papers Garner and co-workers showed that the dependence of the transient regime of swelling on displacement rate has been observed in both 304 and 316 stainless steels, and also in model Fe-Cr ferritic steels (16, 38, 39). Ongoing studies on pure nickel and V-Cr alloys also indicate a strong flux sensitivity of the transient regime, leading to the conclusion that the flux effect might be a universal aspect of the swelling phenomenon, independent of crystal system or composition.

The results of these other studies and the current study support the prediction that austenitic alloys irradiated at PWR-relevant displacement rates will most likely swell more than when irradiated at higher rates characteristic of fast reactors. A similar concern exists for some regions of various fusion concepts. Thus, the use of swelling data accumulated in fast reactors will most likely lead to an under-prediction of swelling in PWRs and lower-flux fusion devices.

## ACKNOWLEDGEMENTS

The authors are pleased to acknowledge the contributions of PNNL employees Gary Whiting for density measurements, and Ruby Ermi and Elaine Dieffenbacher for specimen retrieval and preparation. This work was supported by Monbusho, the Japanese Ministry of Education, Science and Culture under the FFTF-MOTA collaboration and the JUPITER program (Japan-USA Program for Irradiation Testing for Fusion Research), the U.S. Department of Energy, Office of Fusion Energy, and Office of Basic Energy Sciences, under Contract DE-AC06-76RLO 1830 at Pacific Northwest National Laboratory, and by the Lawrence Livermore National Laboratory under contract No W-7405-ENG-48 with the DOE. Additional financial support for T. Okita was provided by Nuclear Fuel Industries Ltd.

## REFERENCES

- [1] F. A. Garner, Chapter 6: “Irradiation Performance of Cladding and Structural Steels in Liquid Metal Reactors”, Vol. 10A of Materials Science and Technology: A Comprehensive Treatment, VCH Publishers, 1994, pp. 419-543.
- [2] F. A. Garner, L. R. Greenwood and D. L. Harrod, “Potential High Fluence Response of Pressure Vessel Internals Constructed from Austenitic Stainless Steels”, Proc. Sixth

Intern. Symp. on Environmental Degradation of Materials in Nuclear Power Systems - Water Reactors, San Diego, CA. August 1-5, 1993, pp. 783-790.

- [3] F. A. Garner, "Materials Issues Involving Austenitic Pressure Vessel Internals Arising From Void Swelling and Irradiation Creep", Trans. Am. Nucl. Soc., 71 (1994) 190.
- [4] F. A. Garner and M. B. Toloczko, "Irradiation Creep and Void Swelling of Austenitic Stainless Steels at Low Displacement Rates in Light Water Energy Systems", J. of Nucl. Mater. 251 (1997) pp. 252-261.
- [5] S. I. Porollo, A. N. Vorobjev, Yu. V. Konobeev, A. M. Dvoriashin, and F. A. Garner, "The Influence of PWR-Relevant Atomic Displacement Rates and Temperatures on Void Swelling in the Russian Equivalent of AISI 304 Stainless Steel", International Symposium on "Contribution of Materials Investigation to the Resolution of Problems Encountered in Pressurized Water Reactors, 14-18 Sept. 1998, Fontevraud, France, pp. 271-280.
- [6] V. S. Neustroev, V. K. Shamardin, Z. E. Ostrovsky, A. M. Pecherin, and F. A. Garner, "Temperature-Shift of Void Swelling Observed at PWR-Relevant Temperatures in Annealed Fe-18Cr-10Ni-Ti Stainless Steel Irradiated at High and Low Dpa Rates in BOR-60", International Symposium on Contribution of Materials Investigation to the Resolution of Problems Encountered in Pressurized Water Reactors, 14-18 Sept. 1998, Fontevraud, France, pp. 261-269.
- [7] F. A. Garner, S. I. Porollo, A. N. Vorobjev, Yu. V. Konobeev and A. M. Dvoriashin, "Void Swelling at Low Displacement Rates in Annealed X18H10T Stainless Steel at 30-56 dpa and 280-332°C", 9<sup>th</sup> International Conference on Environmental Degradation of Materials in Nuclear Power Systems – Water Reactors, 1999, pp. 1051-1059.
- [8] S. I. Porollo, Yu. V. Konobeev, A. M. Dvoriashin, V. M. Krigan, and F. A. Garner, "Determination of the Lower Temperature Limit of Void Swelling of Stainless Steels at PWR-relevant Displacement Rates", Proc. of Tenth Inter. Conf. on Environmental Degradation of Materials in Nuclear Power Systems – Water Reactors, August 5-9, 2001, in press.
- [9] V. S. Neustroev V. N. Golovanov, Z. Ye. Ostrovsky, A. M. Pecherin, and V. K. Shamardin, "Radiation Effects in 18Cr-10Ni-Ti Steel Irradiated in Different Reactors under Conditions Close to VKU VVER Reactors Operating Conditions", Proceedings of the Fourth International Ural Seminar on Radiation Damage Physics of Metals and Alloys, Feb. 25 – Mar. 3, 2001. Snezhinsk, Russia, in press.
- [10] D. J. Edwards, F. A. Garner, B. A. Oliver and S. M. Bruemmer, "Microstructural Evaluation of a Cold-Worked 316SS Baffle Bolt Irradiated in a Commercial PWR", Proc. of Tenth Inter. Conf. on Environmental Degradation of Materials in Nuclear Power Systems – Water Reactors, August 5-9, 2001, in press.
- [11] J. M. Conermann, R. P. Shogan, D. R. Forsyth, Ian L. W. Wilson and H. T. Tang, "Characterization of Baffle-Former Bolts Removed from Service in U.S. PWRs – 50", Proc. of Tenth Inter. Conf. on Environmental Degradation of Materials in Nuclear Power Systems – Water Reactors, August 5-9, 2001, in press.

- [12] T. Aoki, T. Fukuda, Y. Isobe, A. Hasegawa, M. Sato, K. Abe, K. Matsueda and Y. Nishida, "Comparison of Radiation Induced Degradation in Several Austenitic Stainless Steels Used for Core Internals in LWR", 9<sup>th</sup> International Conference on Environmental Degradation of Materials in Nuclear Power Systems – Water Reactors, 1999, pp. 1045-1050.
- [13] T. Fukuda, M. Sagisaka, Y. Isobe, A. Hasegawa, M. Sato, K. Abe, Y. Nishida, T. Kamada and Y. Kaneshima, "Microstructural Changes of Austenitic Steels Caused by Proton Irradiation Under Various Conditions", J. of Nucl. Mater. 283-287 (2000) 263-267.
- [14] M. Sagisaka, T. Fukuda, Y. Isobe, G. S. Was, F. A. Garner, B. H. Sencer, T. Kamada and G. M. Bond, "Evaluation of Potential Void Swelling Behavior in PWR Core Internals Using Light Ion Bombardment – 83", Proc. of Tenth Inter. Conf. on Environmental Degradation of Materials in Nuclear Power Systems – Water Reactors, August 5-9, 2001, in press.
- [15] G. M. Bond, B. H. Sencer, F. A. Garner, M. L. Hamilton, T. R. Allen and D. L. Porter, "Void Swelling of Annealed 304 Stainless Steel at ~370-385°C and PWR-Relevant Displacement Rates", 9<sup>th</sup> International Conference on Environmental Degradation of Materials in Nuclear Power Systems – Water Reactors, 1999, pp. 1045-1050.
- [16] F. A. Garner, M. L. Hamilton, D. L. Porter, T. R. Allen, T. Tsutsui, M. Nakajima, T. Kido, T. Ishii, G. M. Bond and B. H. Sencer, in preparation for submission to J. of Nucl. Mater.
- [17] T. Okita, N. Sekimura, T. Iwai and F. A. Garner, "Investigation of the Synergistic Influence of Irradiation Temperature and Atomic Displacement Rate on the Microstructural Evolution of Ion-Irradiated Model Austenitic Alloy Fe-15Cr-16Ni", Proc. of Tenth Inter. Conf. on Environmental Degradation of Materials in Nuclear Power Systems – Water Reactors, August 5-9, 2001, in press.
- [18] T. Okita, T. Kamada and N. Sekimura, "Effects of Dose Rate on Microstructural Evolution and Swelling in Austenitic Steels Under Irradiation", J. of Nucl. Mater. 283-287 (2000) 220-223.
- [19] M. J. Norgett, M. T. Robinson and I. M. Torrens, Nuclear Engineering Design, 33 (1975) 50.
- [20] F. A. Garner and H. R. Brager, "Swelling of Austenitic Fe-Cr-Ni Ternary Alloys During Fast Neutron Irradiation", Effects of Radiation on Materials: Twelfth International Symposium, ASTM STP 870, F. A. Garner and J. S. Perrin, Eds., ASTM, Philadelphia, PA, 1985, pp. 187-201.
- [21] F. A. Garner and A. S. Kumar, "The Influence of Both Major and Minor Element Composition on Void Swelling on Simple Austenitic Steels", Effects of Radiation on Materials: Thirteenth International Symposium (Part 1) Radiation-Induced Changes in Microstructure, ASTM STP 955, F. A. Garner, N. H. Packan and A. S. Kumar, Eds., ASTM, Philadelphia, PA, 1987, pp. 289-314.
- [22] F. A. Garner, "Recent Insights on the Swelling and Creep of Irradiated Austenitic Alloys", Invited Paper, J. of Nucl. Mater. 122 and 123, (1984), pp. 459-471.

- [23] D. S. Gelles and F. A. Garner, "An Experimental Method to Determine the Role of Helium in Neutron-Induced Microstructural Evolution", J. of Nucl. Mater. 85 and 86 (1979) pp. 689-693.
- [24] W. J. S. Yang, F. A. Garner and A. Kumar, "The Lithium Shell Effect and its Impact on Microscopy Determinations of Swelling Behavior", J. of Nucl. Mater. 122 and 123, (1984), pp. 242-245.
- [25] T. Muroga, K. Araki, Y. Miyamoto and N. Yoshida, "Void Swelling in High Purity Fe-Cr-Ni and Fe-Cr-Ni-Ti Alloys irradiated in JOYO", J. of Nucl. Mater. 155-157 (1998) pp. 1118-1122.
- [26] N. Sekimura and S. Ishino, "The Effect of Titanium Addition on Microstructural Evolution in Stainless Steel Irradiated with Fast Neutrons in FFTF", J. of Nucl. Mater. 179-181, (1991)pp. 542-545.
- [27] N. Sekimura, K. Hamada and S. Ishino, "The Observation and Interpretation of Microstructural Evolution and Swelling in Austenitic Steels Under Irradiation", Effects of Radiation on Materials; 16<sup>th</sup> International Symposium, ASTM STP 1175, 1994, pp. 992-1000.
- [28] F. A. Garner and W. G. Wolfer, "The Effect of Solute Additions on Void Nucleation", J. of Nucl. Mater. 102, (1981), pp. 143-150.
- [29] B. Esmailzadeh, A. S. Kumar and F. A. Garner, "The Influence of Silicon on Void Nucleation in Irradiated Alloys", J. of Nucl. Mater. 133 & 134, (1985), pp. 590-593.
- [30] H. Oikawa, "Review on Lattice Diffusion of Substitutional Impurities in Iron; A Summary Report", Technology Reports, Tohoku University, 47, No. 2. (1982), pp. 215-224.
- [31] T. Yoshiie, S. Kojima, Y. Sato, N. Yoshida and M. Kiritani, "A Study of Point Defect Processes in Candidate and Model Alloys for Fusion Reactor First Wall by HVEM", J. of Nucl. Mater. 133-134 (1985) pp. 390-394.
- [32] C. Dimitrov and O. Dimitrov, J. Physics F 14 (1984) p. 793.
- [33] S. J. Rothman, L. J. Nowicki and G. E. Murch, "Self-diffusion in Austenitic Fe-Cr-Ni Alloys", J. Physics F: Metal Physics 10 (1980) pp. 383-398.
- [34] F. A. Garner and W. G. Wolfer, "Factors Which Determine the Swelling Behavior of Austenitic Stainless Steels", J. of Nucl. Mater. 122 and 123, (1984), pp. 201-206.
- [35] T. Muroga, H. Watanabe and N. Yoshida, "Correlation of Fast Neutron and Electron Irradiations Based on the Dislocation Loop Density", J. of Nucl. Mater. 174 (1990) pp. 282-288.
- [36] W. A. Coghlan and F. A. Garner, "Effect of Nickel Content on the Minimum Critical Void Radius in Ternary Austenitic Alloys", Effects of Radiation on Materials: Thirteenth International Symposium (Part 1) Radiation-Induced Changes in Microstructure, ASTM

STP 955, F. A. Garner, N. H. Packan and A. S. Kumar, Eds., ASTM, Philadelphia, PA, 1987, pp. 315-327.

- [37] L. K. Mansur, "Correlation of Neutron and Heavy Ion Damage, II. The Predicted Shift of Swelling with Changes in Radiation Dose Rate", J. of Nucl. Mater. 78 (1978) pp. 156-160.
- [38] D. L. Porter and F. A. Garner, "Swelling of AISI Type 304L Stainless Steel in Response to Simultaneous Variations in Stress and Displacement Rate", Effects of Radiation on Materials: Twelfth International Symposium, ASTM STP 870, F. A. Garner and J. S. Perrin, Eds., ASTM, Philadelphia, PA, 1985, pp. 212-220.
- [39] F. A. Garner, M. B. Toloczko and B. H. Sencer, "Comparison of Swelling and Irradiation Creep Behavior of fcc-Austenitic and bcc-Ferritic/Martensitic Alloys at High Neutron Exposure", J. of Nucl. Mater. 276 (2000) pp. 123-142.

**INVESTIGATION OF THE SYNERGISTIC INFLUENCE OF IRRADIATION TEMPERATURE AND ATOMIC DISPLACEMENT RATE ON THE MICROSTRUCTURAL EVOLUTION OF ION-IRRADIATED MODEL AUSTENITIC ALLOY Fe-15Cr-16Ni – T. Okita, T. Iwai and N. Sekimura (Tokyo University), F. A. Garner (Pacific Northwest National Laboratory)\***

**OBJECTIVE**

The purpose of this effort is to determine the influence of dpa rate and irradiation temperature on void swelling of fcc alloys.

**SUMMARY**

A comprehensive experimental investigation of microstructural evolution has been conducted on Fe-15Cr-16Ni irradiated with 4.0 MeV nickel ions in the High Fluence Irradiation Facility of the University of Tokyo. Irradiations proceeded to dose levels ranging from ~0.2 to ~26 dpa at temperatures of 300, 400 and 500°C at displacement rates of  $1 \times 10^{-4}$ ,  $4 \times 10^{-4}$  and  $1 \times 10^{-3}$  dpa/sec. This experiment is one of two companion experiments directed toward the study of the dependence of void swelling on displacement rate. The other experiment proceeded at seven different but lower dpa rates in FFTF-MOTA at ~400°C. In both experiments the swelling was found at every irradiation condition studied to monotonically increase with decreases in dpa rate.

The microstructural evolution under ion irradiation was found to be very sensitive to the displacement rate at all three temperatures. The earliest and most sensitive component of microstructure to both temperature and especially displacement rate was found to be the Frank loops. The second most sensitive component was found to be the void microstructure, which co-evolves with the loop and dislocation microstructure. These data support the prediction that void swelling will probably be higher in lower-flux fusion devices and PWRs at a given irradiation temperature when compared to irradiations conducted at higher dpa rates in fast reactors.

**INTRODUCTION**

It has recently come to the attention of the light water reactor community that void swelling is probably occurring in the austenitic components of pressure vessel internals, especially in pressurized water reactors (1). Similar concerns have been raised for fusion devices, especially those that will experience lower atomic displacement rates than found in fast reactors. Questions exist however, concerning the magnitude of swelling that might occur and what might be the effect of the major irradiation variables. These variables are the irradiation temperature, the rate of atomic displacements in dpa/sec and the generation rates of helium and hydrogen gas. A number of comprehensive irradiation experiments are in progress to quantify the answers to these questions and to provide microstructural data that will allow extrapolation to and prediction of swelling under conditions of lower dpa rate.

The experiment described in this paper is one of two companion experiments directed toward the study of the dependence of void swelling on displacement rate in particular, with additional information to be gained on the action of the other two variables. The other experiment proceeded at seven different but lower neutron-induced dpa rates in FFTF-

---

\* Pacific Northwest National Laboratory (PNNL) is operated for the U.S. Department of Energy by Battelle Memorial Institute under contract DE-AC06-76RLO-1830.

MOTA at  $\sim 400^\circ\text{C}$  (2). This range of dpa rates spanned the full set of dpa rates relevant to fusion devices, PWRs and fast reactors. In the neutron experiment the swelling was found at every irradiation condition studied to monotonically increase with decreases in dpa rate.

With some limitations the neutron experiment explored the effect of helium generation but it was conducted at only one irradiation temperature,  $400^\circ\text{C}$ , which lies just above or at the higher end of the PWR range of interest. The current experiment must of necessity proceed at dpa rates that or higher than that explored in fast reactors, but is capable of studying temperatures from the lower limit of fusion or PWR interest,  $300^\circ\text{C}$  and higher. The higher temperatures are necessary to explore the interaction of the two most important variables, that of dpa rate and temperature.

The on-going ion experiment is very large in scope, involving three alloys and simultaneous injection of helium and in some cases, helium and hydrogen. In the current paper we focus only on one alloy, the ternary Fe-15Cr-16Ni with very low levels of other solutes, irradiated without gas injection in the annealed condition.

### Experimental Details

The model austenitic alloy, ternary Fe-15Cr-16Ni was prepared by arc melting from very pure Fe, Ni and Cr. The alloy was rolled to sheets of 0.2 mm thickness. Afterward, standard 3 mm microscopy disks were then punched and annealed for 30 minutes at  $1050^\circ\text{C}$  in a very high vacuum. The specimens used in the two companion experiments were identical in every way.

Irradiation proceeded with 4.0 MeV  $\text{Ni}^{3+}$  ions in the High Fluence Irradiation Facility operated by the University of Tokyo and located at Tokai-Mura, Japan. In this first series of irradiations no gas atoms were preinjected or simultaneously injected.

The irradiation conditions chosen are listed in Table 1. The damage vs. depth profile was calculated using the TRIM code (3) and the results are shown in Figure 1. After irradiation the specimens were electrochemically thinned to reach a depth of 600 to 700 nm, a depth chosen to avoid a strong influence of the "injected interstitial" effect (4) and also minimize the influence of the specimen surface. Analysis was conducted using a JEOL 200CX electron microscope operating at 200 KeV.

### Results

In general, the radiation-induced microstructures were dense, especially at the lower temperatures, but rather simple, being comprised primarily of Frank interstitial loops, some unfaulted perfect loops, some network dislocations and faceted voids.

As shown in Figure 2, the swelling of Fe-15Cr-16Ni increases as the atomic displacement rate is lowered at all three irradiation temperatures studied. While swelling appears to increase with increasing temperature, it is significant to note that swelling occurs at  $300^\circ\text{C}$ , the lowest temperature relevant to PWR internals.

Figure 3, shows that there is a tendency for the cavity density to increase somewhat as the dpa rate decreases, although the cavity density also increases as the irradiation temperature falls. The Frank loop density also increases with decreasing temperature and decreasing dpa rate, as shown in Figure 4.

Table 1. Irradiation conditions studied to date

Temperature	Dose Rate	Dose
300°C	$1 \times 10^{-4}$ dpa/sec	0.17-0.21 dpa 1.6-1.9 dpa
400°C	$4 \times 10^{-4}$ dpa/sec	
500°C	$1 \times 10^{-3}$ dpa/sec	
300°C	$4 \times 10^{-4}$ dpa/sec	15.2-17.4 dpa
400°C		
500°C		
300°C	$4 \times 10^{-4}$ dpa/sec	26.2 dpa

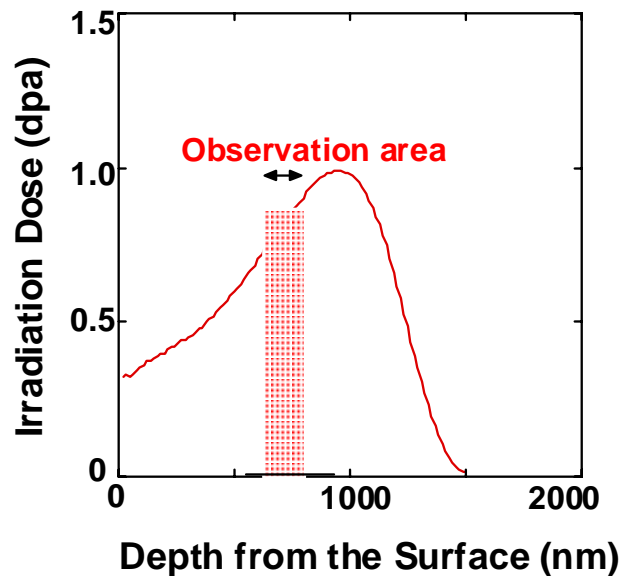


Figure 1. Depth distribution of ion-induced damage as calculated by the TRIM code, showing range of depths chosen for observation by microscopy.

#### Discussion

The most significant observation from this study is that swelling can occur at temperatures as low as 300°C, even in the absence of injected gases. This result appears to agree with the results of Porollo et al. (5) and Neustroev et al. (6). The second important observation is that void swelling is accelerated at lower dpa rates at every temperature studied, similar to the results of the companion irradiation study using fast neutrons.

When comparing the results of the ion and neutron studies (2) it becomes apparent that the level of swelling obtained at a given dpa level at the very high ion-induced dpa rates is much less than that obtained at lower neutron-induced dpa rates, confirming that dpa rate effects appear to be very consistent. It must also be recognized, however, that ion-induced swelling tends to be additionally retarded by the combined influence of the surface and the injected interstitial.

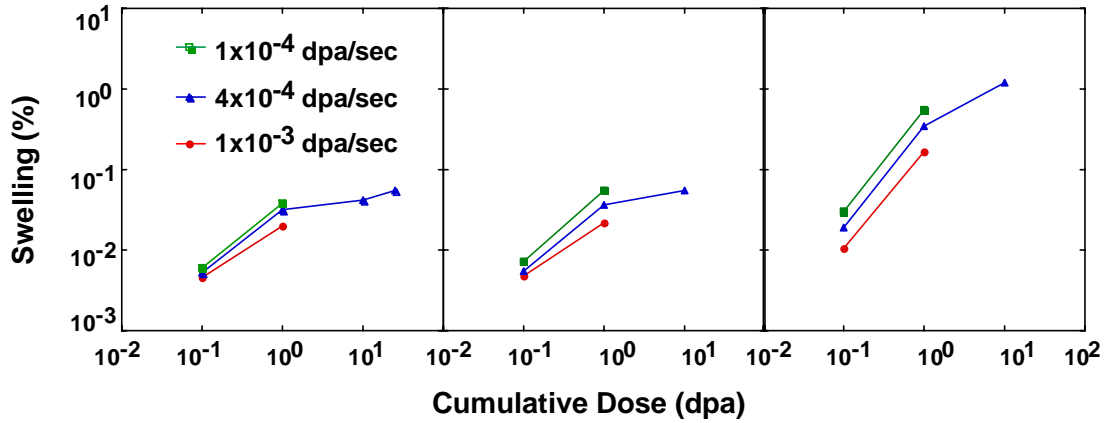


Figure 2. Dependence of swelling of annealed Fe-15Cr-16Ni on temperature, dpa and dpa rate. The irradiation temperatures are 300, 400 and 500°C, moving from left to right.

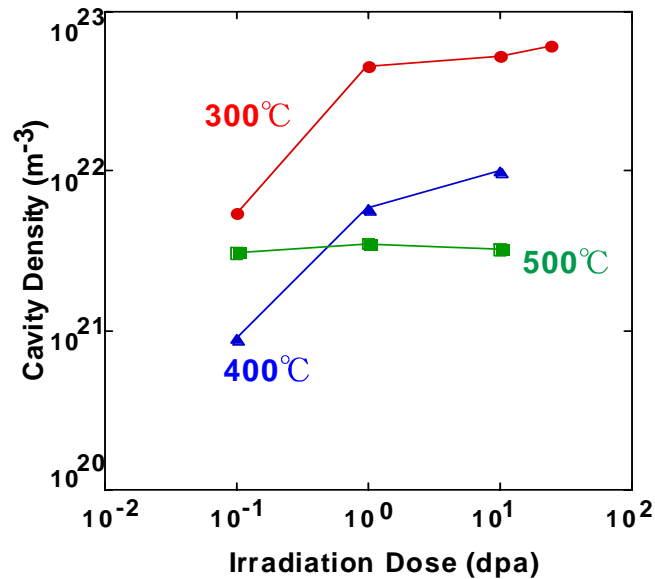


Figure 3. Dependence of cavity density of annealed Fe-15Cr-16Ni on temperature and dpa at  $4 \times 10^{-4}$  dpa/sec.

The swelling levels attained in the ion experiment have not yet reached large enough levels where it can be determined if changes in dpa rate are expressed primarily in the duration of the transient regime of swelling, as clearly observed in the neutron experiment. However, the ion experiments allow us the opportunity to test the conclusion of the neutron study

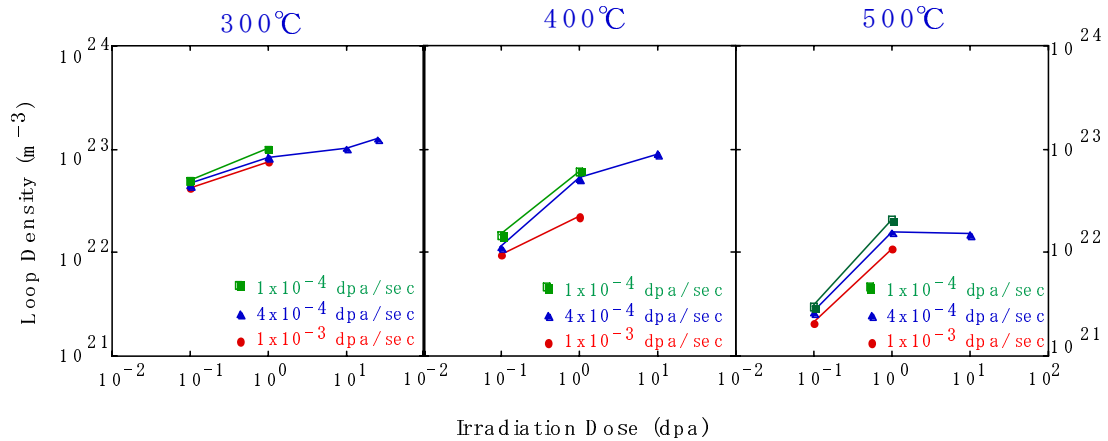


Figure 4. Dependence of loop density of annealed Fe-15Cr-16Ni on temperature, dpa and dpa rate.

concerning the origin of the transient shift. In the neutron study it appeared that the primary flux sensitivity was expressed in the evolution of the Frank loop population and its subsequent unfauling. At all the neutron-induced dpa rates studied, however, most of the loops had already unfauled and network formation was well in progress at even the lowest doses studied. In the ion experiment the specimens at lowest doses still retained most of the Frank loops.

As shown in Figure 5, however, it appears that the saturation loop population is temperature-dependent and also scales with the dpa rate to the  $\frac{1}{2}$  power, as predicted by the model of Watanabe et al. (7) and Muroga and co-workers (8). Figures 6 and 7 shows the evolution of loop evolution in simple austenitic Fe-Cr-Ni model alloys observed by Watanabe, indicating the strong role of temperature and dpa rate to determine the saturation density of Frank loops. Figure 8 shows the measured dependence of the saturation density as measured by Muroga in these same alloys.

A detailed model is now being constructed that incorporates the combined observation of the two companion studies. The model will describe how the microstructural evolution under both neutron and ion irradiation was found to be very sensitive to the displacement rate at all three temperatures. The earliest and most sensitive component of microstructure to both temperature and especially displacement rate was found to be the Frank loops, whose rate of unfauling determines when the dislocation network starts to evolve. The second most sensitive component was found to be the void microstructure, which co-evolves with the loop and dislocation microstructure.

The data from these two companion experiments are very consistent and support the prediction that void swelling will probably be higher in lower-flux PWRs and fusion devices at a given irradiation temperature and dpa level when compared to irradiations conducted at higher dpa rates in fast reactors.

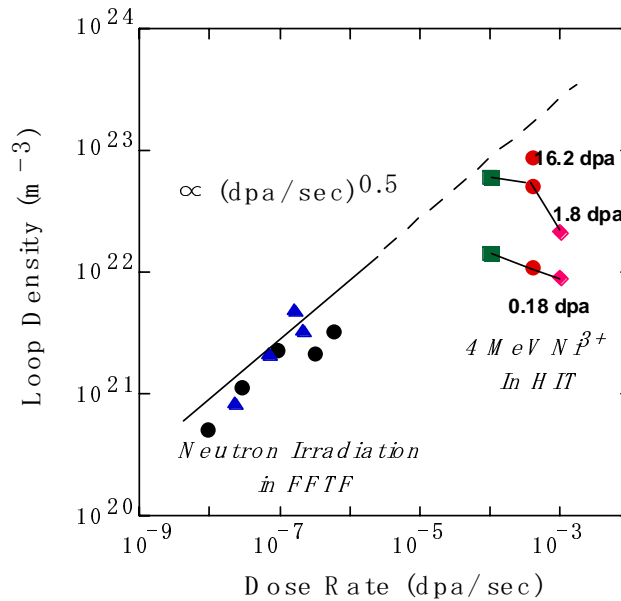


Figure 5. Dependence of loop density on dpa rate to the 1/2 power, as observed in this experiment and the companion neutron experiment in FFTF. Note that the ion-induced loop density moves toward the  $(\text{dpa}/\text{sec})^{1/2}$  trend line with increasing dpa, indicating that ion-induced loop saturation requires relatively high dpa levels.

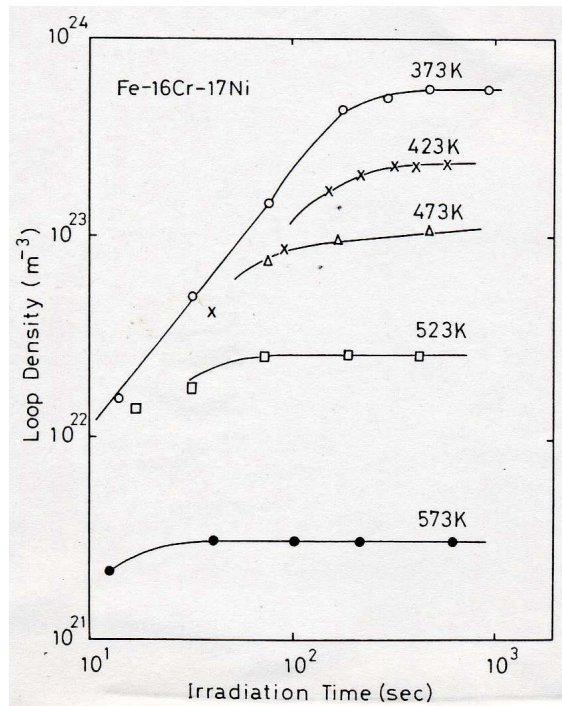


Figure 6. Development of Frank loop density vs. irradiation time and temperature, as observed during electron irradiation of simple ternary austenitic alloys by Watanabe and co-workers (7).

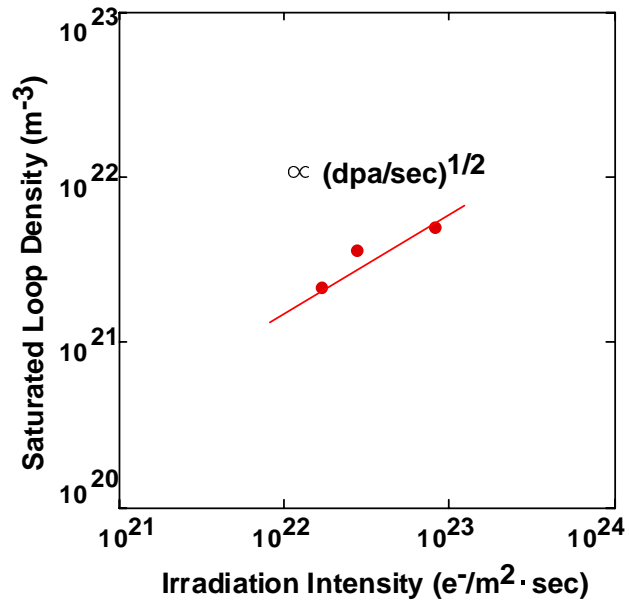


Figure 7. Flux dependence of Frank loop density vs. dpa rate, as observed by Watanabe and co-workers (7).

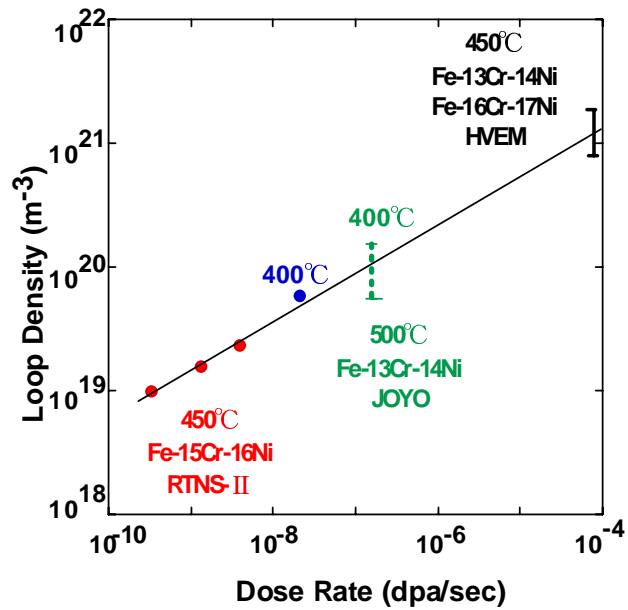


Figure 8. Dose rate dependence of saturated loop density in simple ternary austenitic alloys, as observed by Muroga and co-workers (8).

## ACKNOWLEDGEMENTS

This work was supported by Monbusho, the Japanese Ministry of Education, Science and Culture under the FFTF-MOTA collaboration and the JUPITER program (Japan-USA Program for Irradiation Testing for Fusion Research), and the U.S. Department of Energy, Office of Fusion Energy, and Office of Basic Energy Sciences, under Contract DE-AC06-76RLO 1830. Pacific Northwest National Laboratory is operated for DOE by Battelle Memorial Institute.

## REFERENCES

- [1] F. A. Garner, L. R. Greenwood, and D. L. Harrod, "Potential High Fluence Response of Pressure Vessel Internals Constructed from Austenitic Stainless Steels", Proc. Sixth Intern. Symp. on Environmental Degradation of Materials in Nuclear Power Systems - Water Reactors, San Diego, CA. August 1-5, 1993, p. 783-790.
- [2] T. Okita, N. Sekimura, F. A. Garner, L. R. Greenwood, W. G. Wolfer, and Y. Isobe, in this semi-annual report.
- [3] J. P. Biersack and L. G. Hagmark, *Nucl. Instr. And Meth.* 174 (1980) 257.
- [4] F. A. Garner, "Impact of the Injected Interstitial on the Correlation of Charged Particle and Neutron-Induced Radiation Damage", J. of Nucl. Mater. 117, (1983), p. 177-197.
- [5] S. I. Porollo, Yu. V. Konobeev, A. M. Dvoriashin, V. M. Krigan, and F. A. Garner, "Determination of the Lower Temperature Limit of Void Swelling of Stainless Steels at PWR-relevant Displacement Rates", *Proc. of Tenth Inter. Conf. on Environmental Degradation of Materials in Nuclear Power Systems – Water Reactors*, August 5-9, 2001, in press.
- [6] V. S. Neustroev, V. N. Golovanov, Z. Ye. Ostrovsky, A. M. Pecherin, and V. K. Shamardin, "Radiation Effects in 18Cr-10Ni-Ti Steel Irradiated in Different Reactors under Conditions Close to VKU VVER Reactors Operating Conditions", *Proceedings of the Fourth International Ural Seminar on Radiation Damage Physics of Metals and Alloys*, Feb. 25 – Mar. 3, 2001. Snezhinsk, Russia, in press.
- [7] H. Watanabe et al., J. of Nucl. Mater. 155-157 (1988) 815.
- [8] T. Muroga, H. Watanabe and N. Yoshida, "Correlation of Fast Neutron and Electron Irradiations Based on the Dislocation Loop Density", J. of Nucl. Mater. 174 (1990) 282-288.

**7.0 MHD INSULATORS, INSULATING CERAMICS AND  
OPTICAL MATERIALS**

## **STUDY OF THE LONG-TERM STABILITY OF MHD COATINGS FOR FUSION REACTOR APPLICATIONS -- B. A. Pint and J. R. DiStefano (Oak Ridge National Laboratory)**

### **OBJECTIVE**

The objective of this task is to assess the long-term, high-temperature compatibility of high electrical resistance coatings with lithium at high temperatures. Electrically insulating, magnetohydrodynamic (MHD) coatings on the first wall of magnetic confinement reactors are essential to reduce the MHD force that would otherwise inhibit the flow of the lithium coolant. Initial experimental work is being conducted on bulk ceramics to determine basic lithium compatibility and maximum-use temperatures of candidate ceramics such as AlN and CaO.

### **SUMMARY**

Bulk specimens of two candidate compositions, CaO and AlN+0.04wt.%Y, for insulating coatings in a lithium-cooled fusion reactor have been exposed to lithium in 1000 h isothermal tests at 500°-800°C to determine the maximum temperature at which acceptable compatibility is likely. Because high mass losses for AlN were observed at 700°C, additional testing has focused on this temperature in order to examine what changes may slow the rate of dissolution. Changing from a vanadium alloy test capsule to a Mo capsule appears to have the largest effect at 700°C. For single crystal specimens of CaO, high mass losses have been observed after exposure at 600°C. In this case, changing to a Mo capsule or adding Ca or O to the lithium have not consistently showed a beneficial effect. For testing at 700°C, neither doping the Li with Ca or O altered the high mass losses. These results suggest that CaO may be limited to exposure temperatures of less than 600°C but that AlN may be able to operate above 600°C.

### **PROGRESS AND STATUS**

#### **Experimental Procedure**

Current work focused on two compositions of bulk specimens. High purity AlN (0.9wt%O, 0.04wt% Y) from Tokuyama Corp (Shapal SH-50) was made by nitriding Al<sub>2</sub>O<sub>3</sub>. The AlN specimens measured 2x8x12mm, had an average grain size of 7-8µm and a density of 3.25g/cm<sup>3</sup>. Single crystals of CaO were obtained from Commercial Crystal Laboratories (Naples, FL) and measured 2x6x12mm. Previous work on these materials had used AlN with 5wt%Y<sub>2</sub>O<sub>3</sub> and polycrystalline CaO specimens.<sup>1</sup> Specimen dimensions and mass were measured before and after exposure. The mass change accuracy was 0.01mg/cm<sup>2</sup>.

The experimental procedure for lithium exposures has been outlined elsewhere<sup>2,3</sup>. Bulk ceramic specimens were exposed for 1000h at 500°-800°C. In some tests, additions of Li<sub>3</sub>N, Li<sub>2</sub>O or Ca (99.5% purity) granules were made to increase the impurity levels in the lithium to nominally 1000ppmw of nitrogen, 1000-2000ppmw oxygen or 1-10wt%Ca, respectively. In order to explore the effect of the vanadium inner capsule on the experiment, a molybdenum capsule that was expected to be more inert to reactions of interstitial impurities in the lithium was used for some experiments. After exposure to Li, specimens were distilled in vacuum at 500-550°C to remove any residual Li from the specimen. Additional characterization was performed on selected specimens.

## Results and Discussion

Previous work on AlN showed relatively low mass gains at 600°C but much higher mass losses (indicating dissolution) at 700°C. Thus the focus in these experiments was on altering the dissolution rate at the higher temperature. Figure 1 summarizes the mass change results for AlN. With a V alloy capsule, the addition of 1000ppm nitrogen did not significantly change the mass loss at 700°C. However, switching to a Mo capsule did reduce the mass loss after 1000h to 1.7mg/cm<sup>2</sup>. The reason for this difference is believed to be the gettering of N by the V alloy capsule. Previous work<sup>1</sup> showed the Al content of the Li increased with exposure temperature but not the N content. If nitrogen from dissolved AlN is continually getterred from the lithium into the V capsule, then the rate of dissolution may be higher than might be expected in a reactor environment where the AlN coating would separate the lithium from the vanadium.

Table I shows the composition of the lithium after several recent exposures. Unfortunately, two of the samples were contaminated prior to spectrographic analysis and contained very high N levels. However, the available data appears to support a hypothesis that N is getterred by a V alloy capsule but not by a Mo capsule. In particular, the nitrogen level was only 120ppm when 1000ppm N was added prior to the test with a V capsule at 700°C, Table I. In contrast, with a Mo capsule at 700°C, 330ppm N was measured in the lithium after exposure. The Al levels likewise reflected the reduced attack at 700°C when a Mo capsule was used.

For single crystal CaO, high mass losses were observed at 600°C. Therefore, additions were made to the lithium in an effort to improve performance at this temperature. Figure 2 summarizes the results for various test conditions. In this case, neither V or Mo would be expected to getter O from Li; therefore, no effect of capsule type was expected and virtually none was observed. Based on earlier work<sup>4</sup>, it was hoped that O or Ca doping of the lithium would reduce the rate of

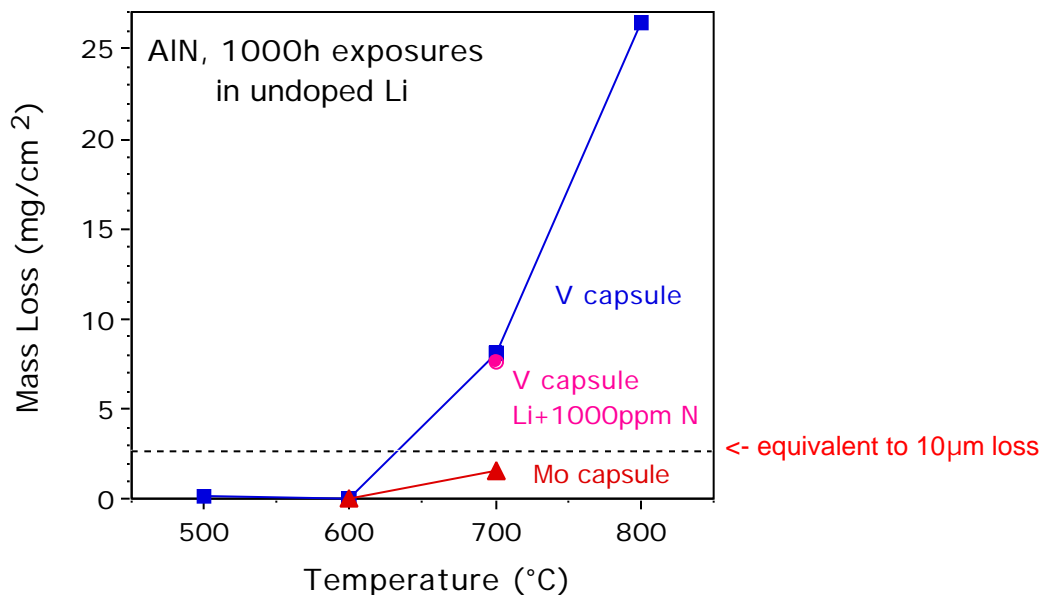


Figure 1. Mass losses for AlN+0.04Y after 1000h at various temperatures. At 700°C, switching from a V alloy capsule to a Mo capsule had a more significant effect than the addition of 1000ppm N to the lithium. A mass loss of 3.2 mg/cm<sup>2</sup> corresponds to a 10µm loss in material thickness.

Table I. Lithium composition determined by spectrographic analysis.

<u>Conditions</u>	<u>Nitrogen</u> (wppm)	<u>Aluminum</u> (wppm)	<u>Yttrium</u> (wppm)
Starting Lithium*	140	<0.3	<0.3
500°C V can	150	1	<0.3
600°C Mo can	contaminated	1	<0.4
700°C V can	contaminated	110	<0.4
700°C V can + 1000ppm N	120	160	<0.4
700°C Mo can	330	3	<0.4

\* 40 metallic elements examined, only Cu (15wppm) was above detectability limit

dissolution at 600°C. The addition of 1000 or 2000ppm O resulted in a modest reduction in the amount of dissolution. However, the mass losses were still equivalent to more than a 10 $\mu$ m loss in material after 1000h. An addition of 1wt%Ca in two separate tests resulted in a mass gain rather than a mass loss without Ca. The reason for the mass gain is not known but may be the result of Ca remaining on the specimen after distillation of the lithium after the test. Unexpectedly, the addition of more Ca (3 and 5wt%) resulted in specimen mass losses, Figure 2. The specimen broke after exposure to Li + 10wt.%Ca preventing an accurate mass change measurement. The results with higher Ca levels suggests that Ca doping may not be an effective strategy.

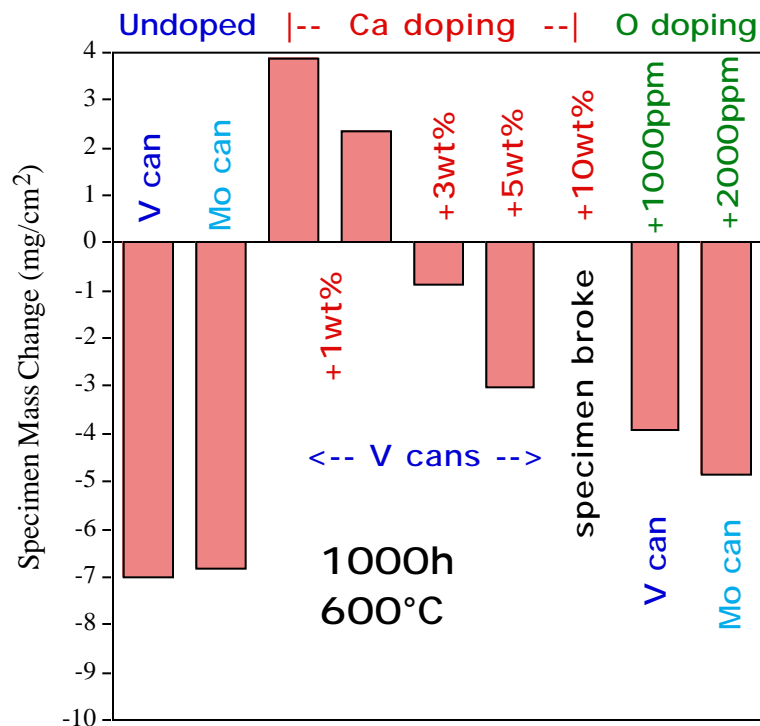


Figure 2. Mass changes for single crystal CaO after 1000h at 600°C with various additives to the lithium and both V and Mo capsules. A mass loss of 3.2 mg/cm<sup>2</sup> corresponds to a 10 $\mu$ m loss in material thickness.

Similar doping tests also were performed at 700°C. In this case, the addition of 1wt.%Ca had very little effect on the mass loss. An addition of 1000ppm O reduced the mass loss compared to undoped Li but a significant amount of material was still lost during the 1000h exposure. As noted previously, these rates of dissolution are consistent with the high equilibrium levels of Ca and O in solution in Li at these temperature.<sup>4</sup>

Because of the desire for operating temperatures as high as 750°-800°C,<sup>5,6</sup> new ceramic candidates are being tested in bulk form. Single crystals of  $\text{Sc}_2\text{O}_3$  and  $\text{Y}_2\text{O}_3$  are being exposed at 600°-800°C as are polycrystalline samples of  $\text{Er}_2\text{O}_3$  and  $\text{YScO}_3$ . The latter two compositions were not available in single crystal form so they were produced by conventional ceramic processing from powders (cold compacted and sintered). These tests should indicate if they would be possible candidates for higher temperature operation.

## REFERENCES

1. B. A. Pint, L.D. Chitwood, J. H. DeVan and J. R. DiStefano, DOE/ER-0313/28 (2000) 26.
2. B. A. Pint, L.D. Chitwood, J. H. DeVan and J. R. DiStefano, DOE/ER-0313/27 (2000) 49.
3. B. A. Pint, L. D. Chitwood and J. R. DiStefano, J. Nucl. Mater. 289 (2001) 52.
4. B. A. Pint, L.D. Chitwood, J. H. DeVan and J. R. DiStefano, DOE/ER-0313/29 (2001) 3
5. D.L. Smith, M.C. Billone, S. Majumdar, R.F. Mattas and D.-K. Sze, J. Nucl. Mater. 258-263 (1998) 65.
6. Y. Gohar, S. Majumdar and D. Smith, Fusion Eng. Design 49-50 (2000) 551.

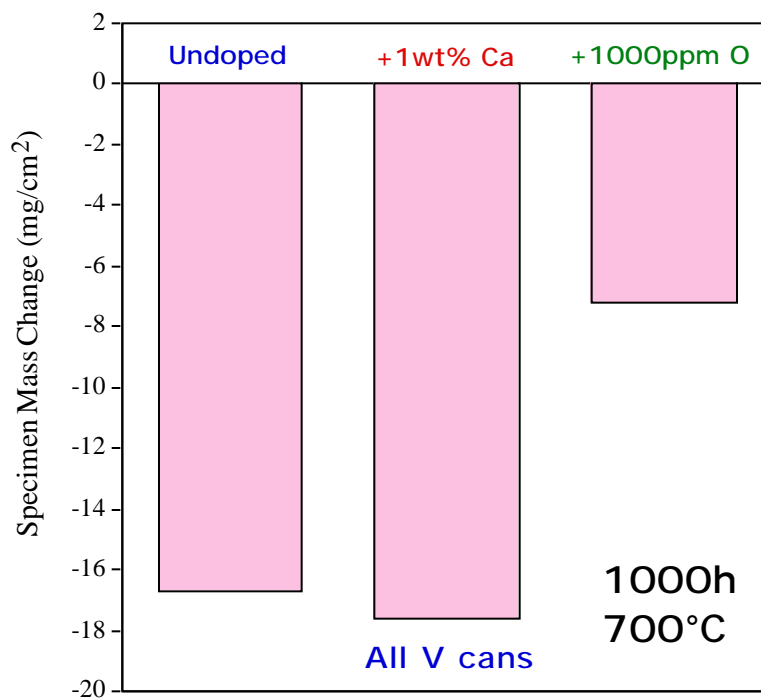


Figure 3. Mass changes for single crystal CaO after 1000h at 700°C with lithium and lithium doped with Ca or O. Neither addition prevented very high levels of dissolution at this temperature.

## IN-SITU FORMATION OF CaO INSULATOR COATINGS ON VANADIUM ALLOYS

D.L. Smith, J-H. Park, and K. Natesan (Argonne National Laboratory)

### OBJECTIVE

The objectives of this task are (1) to define the thermodynamic and kinetic parameters required to form electrically insulating coatings on vanadium alloy by in-situ exposure of the vanadium alloy substrate to lithium with controlled chemistry, and (2) to evaluate the performance characteristics of the coatings.

### SUMMARY

A key issue for the self-cooled lithium blanket concept with a vanadium alloy structure is the development of an electrically insulating coating on the coolant channel walls to mitigate the magneto-hydrodynamic pressure drop in a high magnetic field. A systematic investigation of the thermodynamics and kinetics of oxygen and calcium interactions in the vanadium alloy/lithium system is being conducted to define the system parameters required for in-situ formation of a CaO coating on vanadium alloys. This paper presents results of theory and modeling as well as experimental results on the formation of CaO coatings on vanadium alloys after exposure at temperatures of 600 - 700°C to lithium with a small fraction of Ca added. Coatings of 10 - 30  $\mu\text{m}$  with high electrical resistivity have been formed.

### BACKGROUND

The self-cooled lithium blanket with a vanadium alloy structure offers a potential for high performance with attractive safety and environmental features [1-4]. Features include high heat load capability, high operating temperature, potential for long lifetime, design simplicity, low operating pressure and use of low activation materials. Key remaining issues for the lithium/vanadium blanket concept include effects of fusion-relevant helium transmutation rates on the properties of neutron irradiated vanadium alloys and development of electrically insulating coolant channels to mitigate the magneto-hydrodynamic (MHD) pressure drop in the lithium coolant. Formation of electrically insulating coatings on channel walls is the proposed approach to mitigate the MHD effects. In-situ formation of the coatings after fabrication of the blanket appears necessary and self-healing of any defects in the coatings that might occur during operation is considered essential to provide acceptable reliability. The temperature range of primary interest for the lithium blanket with the reference V-4Cr-4Ti alloy structure is 400 - 750°C.

Design analyses have been conducted previously to define the performance requirements for insulator coatings under projected fusion system conditions [5-6]. These analyses indicate that only modest electrical resistivities or very thin coatings are adequate to suppress the MHD pressure drop. A value of  $100 \text{ } \Omega\text{-cm}^2$  for the product of the electrical resistivity and the thickness will reduce the MHD pressure drop to negligible levels. This corresponds to a coating thickness of 1  $\mu\text{m}$  for an electrical resistivity of  $10^6 \text{ } \Omega\text{-cm}$ . A coating thickness of  $\sim 10 \mu\text{m}$  is considered desirable.

Oxide, nitride and carbide coatings have all been considered; however, only a few oxides are stable in lithium and many nitrides, carbides and silicides do not exhibit adequate electrical resistivities [7]. CaO has been selected as the leading candidate coating material for the lithium/vanadium system on the basis of its properties and the requirements for the coating. This paper presents a status of in-situ formed CaO coatings on V-alloy substrates by exposure of V-alloy specimens to lithium containing small amounts of Ca. Related investigations are also being conducted on CaO coatings produced by thermal-physical vapor deposition and chemical vapor deposition techniques [8].

## COATING REQUIREMENTS - CAO

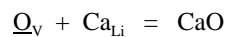
The requirements for the coating material are quite complex. CaO has been selected as the leading candidate for the coating material because it appears to best meet the stringent requirements for the insulator coating for the Li/V system application. Key considerations for the selection of candidate coating materials include the following:

- reasonably high electrical resistivity
- chemical stability/compatibility with Li at elevated temperatures
- potential for coating complex channel configurations
- potential for in-situ self-healing of any defects that might occur
- mechanical integrity/thermal expansion match with V-alloy
- safety/environmental characteristics, e.g., low activation
- materials availability/cost
- favorable neutronic properties
- resistance to irradiation damage

The reported electrical resistivity of monolithic CaO is among the highest of the potential candidate coating materials, varying from  $\sim 10^{16}$   $\Omega\text{-cm}$  at 300°C to  $\sim 10^9$   $\Omega\text{-cm}$  at 750°C compared to a minimum requirement of  $\sim 10^6$   $\Omega\text{-cm}$  [ ]. Based on fundamental thermodynamic data, CaO is one of the most stable oxides and is predicted to be stable in low-oxygen lithium as indicated in Fig. 1. The thermal expansion mismatch for the CaO/V-alloy interface is fairly low since the coefficient of thermal expansion for CaO ( $\sim 12 \times 10^{-6}/^\circ\text{C}$ ) is fairly close to that for vanadium ( $\sim 10 \times 10^{-6}/^\circ\text{C}$ ). As discussed in detail later, the CaO system with vanadium exhibits favorable properties with respect to in-situ coating and self-healing. The neutronic, environmental and safety-related characteristics of calcium are generally favorable, the resources are ample and the cost is low. The radiation response has not been determined, but the margin for electrical resistivity is quite large and self-healing should also mitigate some of the radiation effects. Overall, CaO exhibits characteristics that are favorable to the proposed coating application.

## IN-SITU COATING PROCEDURE

The approach for in-situ coating under investigation involves a reaction of calcium dissolved in the lithium with oxygen dissolved in the vanadium alloy to form CaO at the solid/liquid interface as indicated schematically in Fig. 2.



The vanadium alloys under investigation for the structure typically contain about 300 wppm oxygen; however, the solubility of oxygen in vanadium is over 1 wt. % at the temperatures of interest. Oxygen is also relatively mobile in vanadium with a diffusivity of  $\sim 10^{-9}$   $\text{cm}^2/\text{s}$  at 600°C. Therefore, at temperatures of primary interest, 500-700°C, oxygen is sufficiently mobile to diffuse to the surface of the V-alloy. Additional oxygen is precharged into the surface of the alloy to provide sufficient oxygen to form the desired CaO coating thickness. The amount of oxygen precharge can be varied to obtain the desired coating thickness, e.g., the oxygen required for a 10  $\mu\text{m}$  CaO coating corresponds to  $\sim 0.94$   $\text{mg}/\text{cm}^2$  of oxygen in the V-alloy. The oxygen precharge involves exposure of the V-alloy to a low-pressure oxygen environment at  $\sim 700^\circ\text{C}$  for time sufficient to pickup the desired amount of oxygen, typically 10-20 hr. The V-alloy is then conditioned, e.g.,  $750^\circ\text{C}$  for  $\sim 17$  hr, to diffuse the oxygen into the subsurface region and to reduce any vanadium oxide on the surface. Reduction of any V-oxide is necessary to avoid the formation of a Ca-V-O complex oxide, since the calcium vanadates typically do not exhibit high electrical resistivity. For the case of the reference V-4Cr-4Ti alloy, internal oxidation of the Ti in the alloy occurs, which maintains the oxygen in the near-surface regions as indicated in Fig. 3. The calculated oxygen profile based on an internal oxidation model is in good agreement with the hardness profile, which is related to the oxygen content. Similar calculations and experimental results for vanadium and V-alloys with lower Ti

concentrations show deeper penetration of the oxygen into the metal. Retention of the oxygen in the near-surface regions facilitates the subsequent coating formation.

The oxygen precharged V-alloy specimens are then exposed to lithium containing small amounts of calcium to form the CaO coating. Calcium is highly soluble in lithium with a eutectic at ~ 8 at. % Ca with a melting temperature ~ 40°C below the melting point of lithium. Any oxygen in the lithium preferentially reacts with the Ca to form CaO, which reduces the oxygen activity in the Li-Ca alloy as indicated by the calculated distribution of oxygen between Li and Ca indicated in Fig. 4. Nitrogen reacts with calcium in a similar manner such that the nitrogen activity in the Li-Ca alloy is also very low. In past studies on lithium corrosion, Ca additions to the Li have been shown to decrease the nitrogen content of the lithium to very low levels by cold trapping the calcium nitride. Earlier investigations on in-situ formation of CaO coatings were conducted at temperatures of 350 - 500°C in Li-Ca alloys with a wide range of Li-Ca compositions [ ]. Recent investigations have been focused on higher temperature exposures of V-alloys, typically 600 - 700 °C, in Li with 2.8 at. % Ca.

## RESULTS OF IN-SITU FORMED COATINGS

Figure 5 shows EDS analysis of coatings formed on vanadium and V-5Cr-5Ti alloy exposed to Li-2.8 at.% Ca at 600°C for 120 hrs. The transition from the base metal to the calcium-rich surface coating is evident. Similar results are shown in Fig. 6 for V-4Cr-4Ti alloys that were precharged to different oxygen concentrations and then exposed to Li-2.8 at. % Ca at 700°C for 50 hrs. Figure 7 is a plot of the hardness profile for the two V-4Cr-4Ti alloys with oxygen precharged to levels similar to those for specimens indicated in Fig. 6. The solid symbols indicate the hardness profiles after oxygen charging and the open symbols indicate the hardness profiles after exposure to the Li-Ca alloy. The reduction in the surface hardness of the V-alloy represents the oxygen that has diffused out to form the coating. The coating thicknesses indicated by the EDS profiles in Fig. 6 correlate well with the predicted CaO coating thickness corresponding to the amount of oxygen precharge. Figure 8 shows micrographs of the coating formed on the V-5Cr-5Ti alloy exposed at 600°C. The coating thickness indicated in the micrograph in Fig. 8a correlates well with the EDS profile in Fig 5 and the backscattered electron image in Fig. 8b shows the uniformity of the coating in a lower magnification. Additional analyses are in progress to further characterize these coatings. Electrical resistance measurements have also been performed on the coatings at temperatures up to 500°C. Liquid gallium has been used for the electrical contact on the coating surface. Previous experiments on resistance measurements performed by exposure of the coatings to liquid gallium indicated that micron-sized defects in the coatings could be readily detected [ ]. Electrical resistivity values in excess of  $10^8$  -cm were obtained at temperatures to 500°C for the coatings formed on the V-4Cr-4Ti alloy at 700°C.

## CONCLUSIONS

The approach for in-situ coating involves an interfacial reaction of calcium dissolved in lithium with oxygen dissolved in the V-alloy to form a CaO coating on the V-alloy substrate. Factors that aid the coating formation include a high solubility of Ca in Li relatively high solubility and mobility of oxygen in V-alloys, and the stability of CaO.

Calcium oxide coatings have been successfully formed on V-alloy substrates by exposure of oxygen-charged V-alloys to Li with small additions of Ca for a range of conditions. Oxygen charging of V-alloys was varied from 0 to ~2.5 mg/cm. The V-alloys were conditioned at ~750°C to dissolve surface oxide into metal to avoid formation of complex Ca-V-O compounds that exhibit low electrical resistivity. V-alloy specimens were exposed to Li-2.8 at. % Ca at 600°C for ~120 hr and at 700°C for ~50 hr. Coating thicknesses up to ~ 30  $\mu\text{m}$  were obtainable with a thickness of ~ 10  $\mu\text{m}$  desired. The coating thickness correlated with oxygen pre-charge and varied with exposure time and temperature. The coatings appear to be adherent and relatively uniform, and they exhibit high electrical resistivity ( $\sim 10^8$  -cm at 500°C). Further characterization of the

coating is in progress. The coating parameters indicated above, viz., the temperatures and times for coating formation; are acceptable for practical applications; however, further effort is required to define the complete range of conditions for obtaining satisfactory coatings.

#### REFERENCES

- [1] D. L. Smith et al., *Fusion Technology*. 8(1985)10-44.
- [2] D-K. Sze, et al., *Fusion Engr. & Design* 41(1998)371-376.
- [3] I. R. Kirillov, et al., *Fusion Engr. & Design* 39-40(1998)669-674.
- [4] Y.Gohar, S. Majumdar, and D. Smith, *Fusion Engr. & Design* 49-50(2000)551-558.
- [5] T. Q. Hua and Y. Gohar, *Fus. Engr. & Design* 27(1995)696-702.
- [6] S. Malang and L. Buhler, MHD pressure drop in ducts with imperfectly insulating coatings, Argonne National Laboratory report ANL/FPP/TM-269, August 1994.
- [7] Y. Y. Liu and D.L. Smith, *J. Nucl. Mater.* 141-143(1986)38-43.
- [8] K. Natesan, M. Uz, Z. Zeng, and D. L. Smith, Development of electrically insulating coatings by thermal/vapor deposition, (this proceedings).
- [9] K. Natesan, M. Uz, Z. Zeng, and D.L. Smith, Development of electrically insulating coatings by thermal/vapor deposition, (this proceedings).
- [10] J-H. Park et al., *Fus. Engr. & Design* 27(1995)682-695.
- [11] J-H. Park and T.F. Kassner, *J. Nucl. Mater.* 233-237(1996)476-481.
- [12] D.L. Smith, et al., *Fus. Engr. & Design* 51-52(2000)185-192

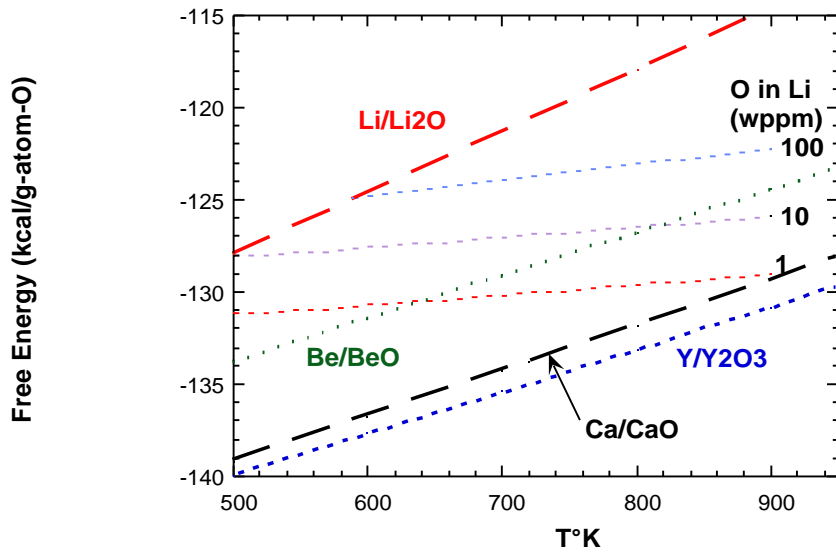


Fig. 1. Calculated thermodynamic stability of selected oxides relative to lithium with various oxygen concentrations

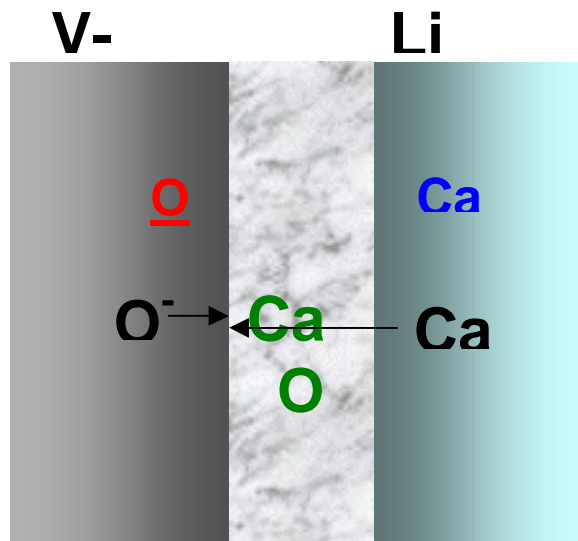


Fig. 2. Schematic diagram of reaction of oxygen in vanadium alloy with calcium in lithium to form CaO coating.

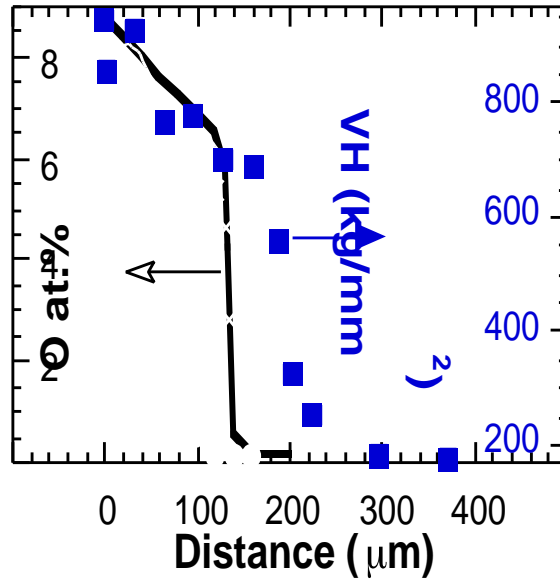


Fig. 3. Calculated oxygen profile and hardness profile in V-4Cr-4Ti alloy after precharging in low-pressure oxygen and homogenizing at 750°C for ~17 hr.

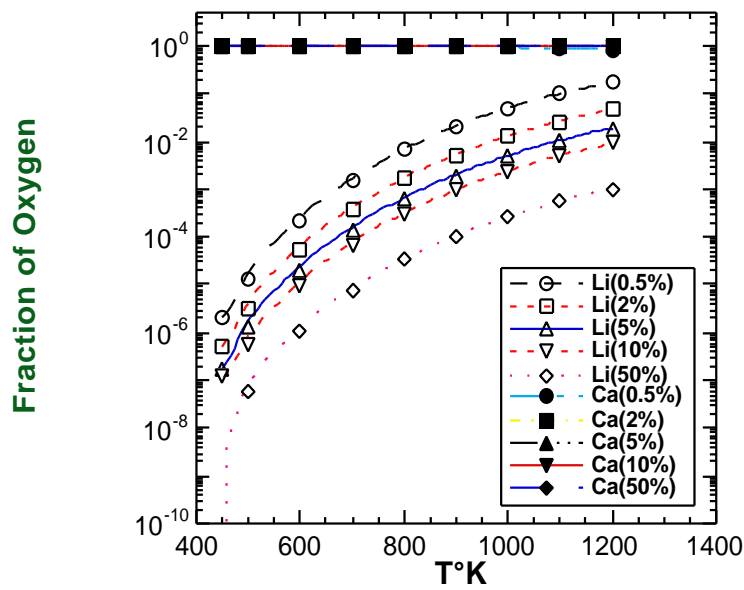


Fig. 4. Calculated distribution of oxygen between Ca and Li in LiCa alloy as a function of composition and temperature.

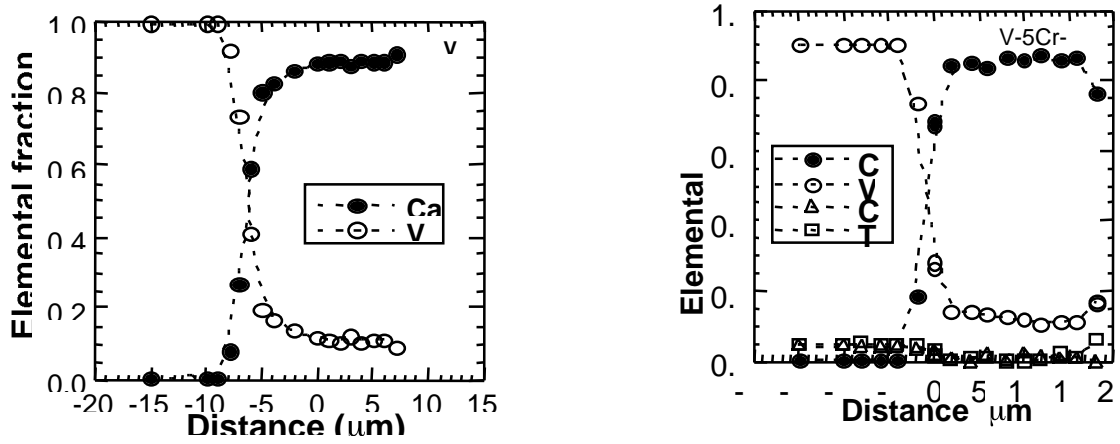


Fig. 5. EDS analysis of coatings on V and V-5Cr-5Ti alloy after oxygen charging and exposure to Li - 2.8 at. % Ca at 600°C for 120 hrs.

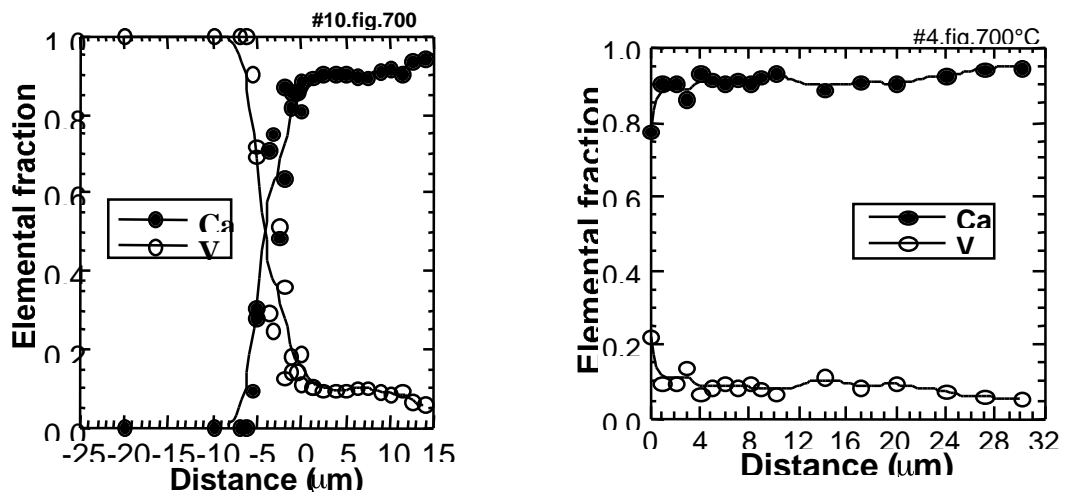


Fig. 6. EDS analysis of coating formed on V-4Cr-4Ti alloy after oxygen precharge to ~ 5000 wppm and ~9000 wppm oxygen and exposure to Li - 2.8 at. % Ca at 700°C for 50 hrs.

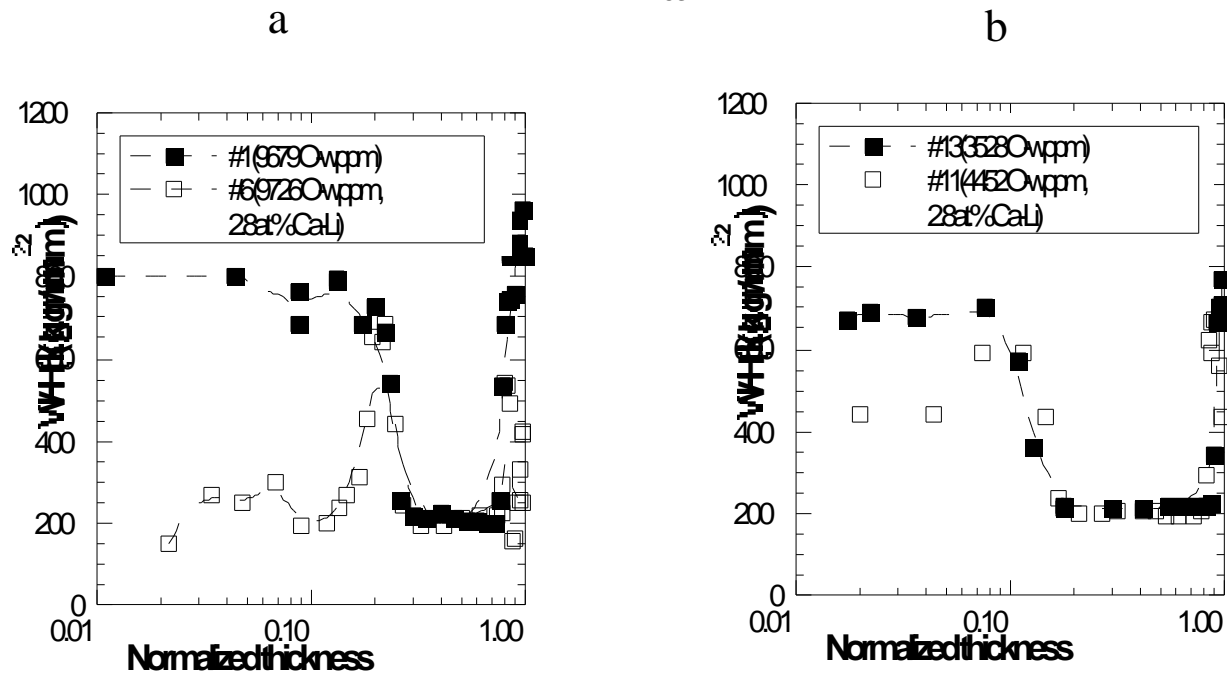


Fig. 7. Hardness profile of V-4Cr-4Ti alloys (a) after oxygen precharging to ~9000 wppm oxygen before (solid symbols) and after exposure to Li - 2.8 at. % Ca at 700°C for 50 hr (open symbols), and (b) similar plot for specimens after oxygen precharge to ~ 5000 wppm oxygen.

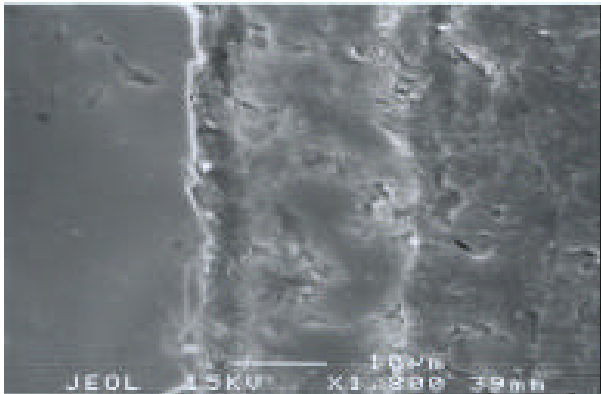


Fig. 8. (a) SEM of in-situ formed coating of CaO on V-5Cr-5Ti after exposure to Li - 2.8 at. % Ca at 600°C for 120 hr and (b) low-magnification backscattered electron image of same coating.

**DEVELOPMENT, CHARACTERIZATION, AND Li COMPATIBILITY OF AN ELECTRICALLY INSULATING CaO COATING ON V-4Cr-4Ti ALLOY**

K. Natesan, M. Uz, D. L. Rink, and D. L. Smith (Argonne National Laboratory)

**OBJECTIVE**

The objectives of this study include (a) development of an electrically insulating CaO coating on V-4Cr-4Ti alloy; (b) evaluation of the coating's long-term Li compatibility; (c) characterization of the coating before and after exposure to Li; and (d) establishment of optimal processing procedures from the standpoint of sample preparation, exposure time and temperature, and sequence of operations in order to obtain reliable and reproducible coatings with adequate electrical resistance for use in an Li environment.

**SUMMARY**

Vanadium (V), alloyed with chromium (Cr), and/or titanium (Ti), V-4 Cr-4 Ti alloy in particular, has been the primary candidate for various fusion reactor structural applications, including the first-wall structure/blanket. The outside of the first wall will be in contact with liquid Li coolant, and electrical conductivity across the wall will lead to magnetohydrodynamic pressure losses during flow of the conducting liquid in the magnetic field. Hence, it is essential that a coating be applied to the alloy, and that it be electrically insulating and compatible with a liquid Li environment at temperatures of 400-700°C. More information on the material requirements of fusion reactors is reported in Ref. 1. As part of the U.S. Department of Energy's Fusion Program, research is being conducted to develop an electrically insulating and liquid-Li-compatible CaO coating on V-4Cr-4Ti alloy. CaO has been identified as the primary coating candidate for this application, based on its high electrical resistivity and thermodynamic stability in Li at the temperatures of interest.<sup>1</sup> This report deals with the development and characterization of a CaO coating deposited on V-4Cr-4Ti alloy specimens by a vapor transport process that uses double Ca-deposition/oxidation steps. The specimen surfaces were analyzed after each step during the process, and the surfaces, along with their cross-sections, were analyzed after exposure to liquid Li. The analysis and characterization were done by one or more techniques, including scanning electron microscopy, energy-dispersive X-ray analysis, X-ray diffraction, and measurement of electrical resistivity external to Li. Here, we present the new developments and results obtained since the last reporting period that ended on December 31, 2000.

**EXPERIMENTAL**

Details of the experimental aspects of the processes utilized in depositing a CaO coating on V-4Cr-4Ti alloy specimens, including materials, system details, and procedure are provided in Ref. 2. Therefore, only brief information on materials and experimental procedure is discussed below.

Two approaches, an He-flow process and a vacuum process, were successfully used to coat V-4Cr-4Ti alloy coupons and rods with CaO. Both processes utilized transport of Ca through the vapor phase and deposition onto the samples.

In the He-flow process, the samples (tabs and/or rods) were hung vertically from the top of the wire screen inner chamber, which was placed inside a steel or alumina outer chamber with a porous bottom and top. A granular Ca charge was placed between the inner and outer chambers. The first Ca deposition step was carried out by heating the entire assembly in a flowing He environment at 775-800°C for 100-150 h. The resulting Ca-coated specimens were then oxidized in a vertical quartz tube furnace in a flowing Ar environment at 700°C for 130-200 h. The sequence of Ca deposition followed by oxidation was repeated to complete the double Ca deposition/oxidation process in He flow to fully coat the samples with CaO.

In the vacuum process, the samples held inside a cylindrical wire screen basket were sealed in a quartz tube with a pressure  $10^{-4}$  torr. A granular Ca charge was placed around the inner chamber and in a cylindrical wire basket at the bottom. The entire assembly was then heated for 100-150 h at 775-800°C in a muffle furnace. The resulting Ca-deposited samples were oxidized as described in the He-flow process above. Development of stable CaO on sample surfaces via double Ca deposition/oxidation in vacuum was accomplished by repeating the Ca deposition and oxidation steps.

The alloy used in this study had a nominal composition of V-4 wt.% Cr-4 wt.% Ti. The samples were either 1-mm-thick tabs or 5-mm diameter rods. All specimens were annealed for 1 h at 1000°C at a pressure  $10^{-7}$  torr before use. The Ca metal was redistilled -6 mesh size granules with a purity of 99.5% on metals basis.

Results obtained from the CaO-coated samples exposed to Li at 500, 600, and 700°C for up to 100 h were reported in Refs. 1-5. During the current reporting period, several samples coated with CaO by either the He-flow or vacuum process were exposed to Li at 600 and 700°C for up to 500 h. Tables 1 and 2 show the experimental conditions and the process details for samples exposed to Li at 600°C and 700°C, respectively. It will be noted from Table 1 that the sample 44Tab29 was given an Mg step instead of the second Ca step. Also, the sample 44Rod11S in Table 2 was given a third Ca deposition step followed by a third oxidation step. The reasons for these deviations in processes and their effects are discussed below in the Results and Discussion section. All other samples listed in these tables were coated by the double Ca-deposition/oxidation processes.<sup>2</sup>

## RESULTS AND DISCUSSION

In earlier reports,<sup>2-6</sup> it was noted that the CaO coatings on the V-4Cr-4Ti coupon and/or rod samples remained intact after exposure to Li at 500 and 600°C for 100 h. It was also reported that the electrical resistivity measurements (external to Li) on these samples showed that they had electrical insulation properties in excess of the design requirements of a fusion device that uses an Li blanket at temperatures of up to 700°C.<sup>1</sup>

During the present reporting period, V-4Cr-4Ti specimens in the form of both tabs and rods were coated with CaO via the He-flow or vacuum process and exposed to Li for 137 h at 600°C (see Table 1) and for about 145, 282 and 500 h at 700°C (see Table 2). The Li used for all exposures

Table 1. Experimental conditions for the Ca deposition and Li exposure at 600°C

Sample ID	Process Step	Environment or Method	Temperature (°C)	Time (h)	Tab Dimensions (mm)
44Tab12	Anneal	P 10 <sup>-6</sup> torr	1000	1	11.6 x 7.4 x 1
	Ca Step 1	He flow	795	140	
	Ox. Step 1	UHP Ar	695	160	
	Ca Step 2	He flow	800	120	
	Ox. Step 2	UHP <sup>2</sup> Ar	692	140	
	Li Exposure <sup>1</sup>	Liquid Li	600	137	
44Tab14SB <sup>3</sup>	Anneal	P 10 <sup>-6</sup> torr	1000	1	11.9 x 7.65 x 1
	Ca Step 1	He flow	795	140	
	Ox. Step 1	UHP Ar	695	160	
	Ca Step 2	He flow	800	120	
	Ox. Step 2	UHP <sup>2</sup> Ar	692	140	
	Li Exposure <sup>1</sup>	Liquid Li	600	137	
44Tab29	Anneal	P 10 <sup>-6</sup> torr	1000	1	12.1 x 9.4 x 1
	O Precharge	P 5x10 <sup>-4</sup> torr O <sub>2</sub>	600	50	
	Ca Step 1	Vac./Quartz	790	140	
	Ox. Step 1	UHP <sup>2</sup> Ar	690	160	
	Mg Step 1	Vac./Quartz	600	116	
	Ox. Step 2	UHP <sup>2</sup> Ar	410	120	
	Li Exposure <sup>1</sup>	Liquid Li	600	137	
44Rod13L <sup>4</sup>	Anneal	P 10 <sup>-6</sup> torr	1000	1	
	Ca Step 1	He flow	795	140	
	Ox. Step 1	UHP <sup>2</sup> Ar	695	160	
	Ca Step 2	He flow	800	120	
	Ox. Step 2	UHP <sup>2</sup> Ar	692	140	
	Li Exposure <sup>1</sup>	Liquid Li	600	137	

<sup>1</sup>Li-2 wt.% Ca solution maintained at 600°C during exposure.

<sup>2</sup>Argon gas used was ultrahigh purity (UHP) grade with a 99.999% purity.

<sup>3</sup>This tab was slightly sandblasted.

<sup>4</sup>L designates long rod 60 mm in length.

contained ~2.8 at.% Ca dissolved in it. It was possible to obtain data on the weight change after each step during the CaO coating of the tab samples, and also after their exposure to Li. This was not possible for the rod samples because the screws used to hold the samples were often self-welded in during the Ca deposition and/or oxidation steps.

The bar graphs in Figure 1 show the weight change data for the V-4Cr-4Ti tab samples after each step during the CaO coating process and also after Li exposure at 600°C. The bar graphs in Figure 2 show similar data for samples exposed to Li at 700°C. From these figures, it is not

possible to compare the rate of weight change during similar steps of the He-flow and vacuum processes. However, it is clear that either process can be used to successfully coat V-4Cr-4Ti alloy samples with stable CaO. The lack of weight loss after Li exposure in Figures 1 and 2 indicates that CaO is stable in an Li/Li-Ca environment, as predicted by thermodynamic data.

Table 2. Experimental conditions for Ca deposition and Li exposure at 700°C

Sample ID	Process Step	Environment or Method	Temperature (°C)	Time (h)	Tab Dimensions (mm)
44Tab9	Anneal	P $10^{-6}$ torr	1000	1	12.8 x 7.5 x 1
	O Precharge	P $5 \times 10^{-4}$ torr O <sub>2</sub>	600	50	
	Ca Step 1	He flow	790	140	
	Ox. Step 1	UHP <sup>2</sup> Ar	690	160	
	Ca Step 2	He flow	775	146	
	Ox. Step 2	UHP <sup>2</sup> Ar	693	157	
	Li Exposure <sup>1</sup>	Liquid Li	700	145	
44Tab24	Anneal	P $10^{-6}$ torr	1000	1	11.9 x 8.9 x 1
	Ca Step 1	Vac./Quartz	780	150	
	Ox. Step 1	UHP <sup>2</sup> Ar	700	140	
	Ca Step 2	Vac./Quartz	775	146	
	Ox. Step 2	UHP <sup>2</sup> Ar	693	157	
	Li Exposure <sup>1</sup>	Liquid Li	700	145	
44Rod1S <sup>3</sup>	Anneal	P $10^{-6}$ torr	1050	1	
	O Precharge	P $5 \times 10^{-4}$ torr O <sub>2</sub>	600	124	
	Ca Step 1	Vac./Quartz	780	150	
	Ox. Step 1	UHP <sup>2</sup> Ar	700	140	
	Ca Step 2	Vac./Quartz	775	146	
	Ox. Step 2	UHP <sup>2</sup> Ar	693	157	
	Li Exposure <sup>1</sup>	Liquid Li	700	145	
44Rod3S <sup>3</sup>	Anneal	P $10^{-6}$ torr	1000	1	
	O Precharge	P $5 \times 10^{-4}$ torr O <sub>2</sub>	600	200	
	Ca Step 1	Vac./Quartz	780	166	
	Ox. Step 1	UHP <sup>2</sup> Ar	705	190	
	Ca Step 2	Vac./Quartz	775	146	
	Ox. Step 2	UHP Ar	693	157	
	Li Exposure <sup>1</sup>	Liquid Li	700	145	
44Rod10L <sup>4</sup>	Anneal	P $10^{-6}$ torr	1000	1	
	O Precharge	P $5 \times 10^{-4}$ torr O <sub>2</sub>	600	50	
	Ca Step 1	Vac./Quartz	790	140	
	Ox. Step 1	UHP <sup>2</sup> Ar	690	160	
	Ca Step 2	Vac./Quartz	775	142	
	Ox. Step 2	UHP <sup>2</sup> Ar	700	161	
	Li Exposure <sup>1</sup>	Liquid Li	700	282	
44Rod11S <sup>3</sup>	Anneal	P $10^{-6}$ torr	1000	1	
	Ca Step 1	Vac./Quartz	780	135	
	Ox. Step 1	UHP <sup>2</sup> Ar	700	145	
	Ca Step 2	Vac./Quartz	775	142	
	Ox. Step 2	UHP <sup>2</sup> Ar	700	158	
	Ca Step 3	He flow	780	100	
	Ox. Step 2	UHP <sup>2</sup> Ar	675	120	
Li Exposure <sup>1</sup>	Liquid Li	700	500		

<sup>1</sup>Li-2 wt.% Ca solution maintained at 700°C during exposure.

<sup>2</sup>Argon gas used was ultrahigh purity (UHP) grade with 99.999% purity.

<sup>3</sup>S designates short rod 20 mm in length.

<sup>4</sup>L designates long rod 60- mm in length.

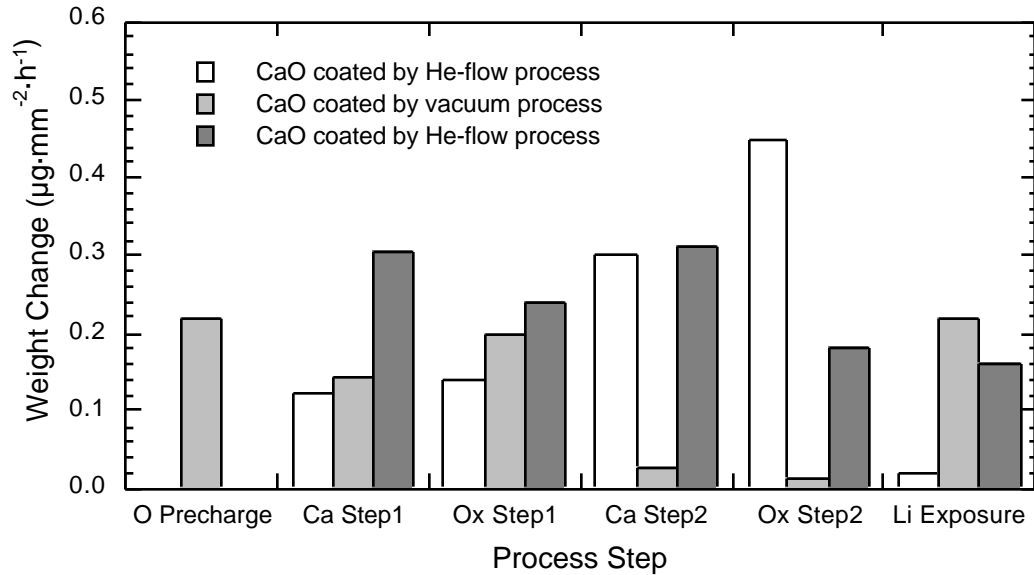


Fig. 1. Weight change during CaO deposition steps and 137-h Li exposure at 600°C of V-4 Cr-4 Ti alloy tabs coated by He-flow or vacuum process (also see Table 1).

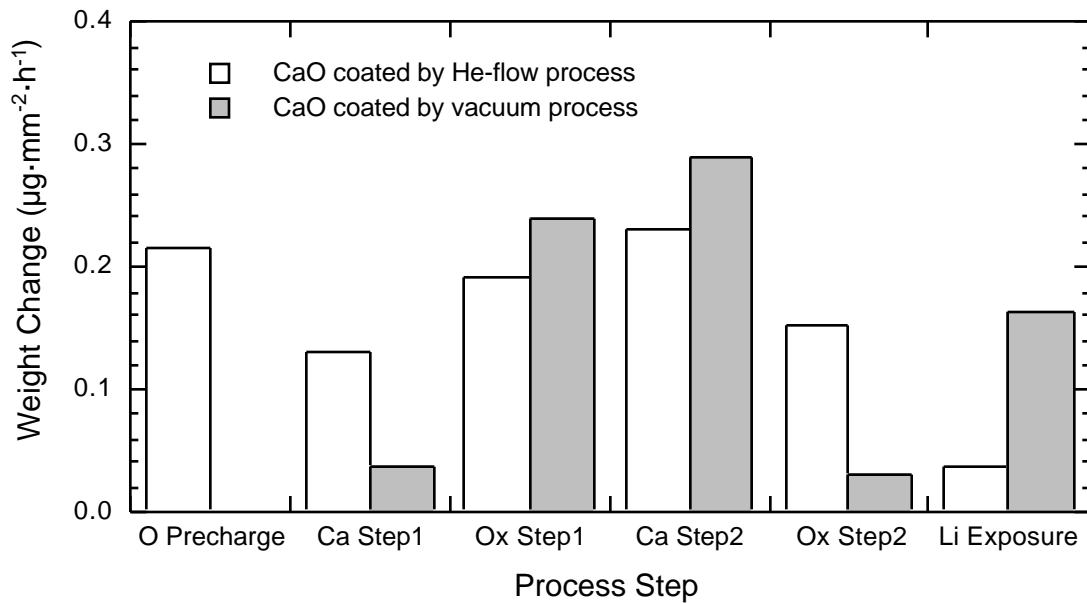


Fig. 2. Weight change during CaO deposition steps and 145-h Li exposure at 700°C for V-4 Cr-4 Ti alloy tabs coated by He-flow or vacuum process (see Table 1).

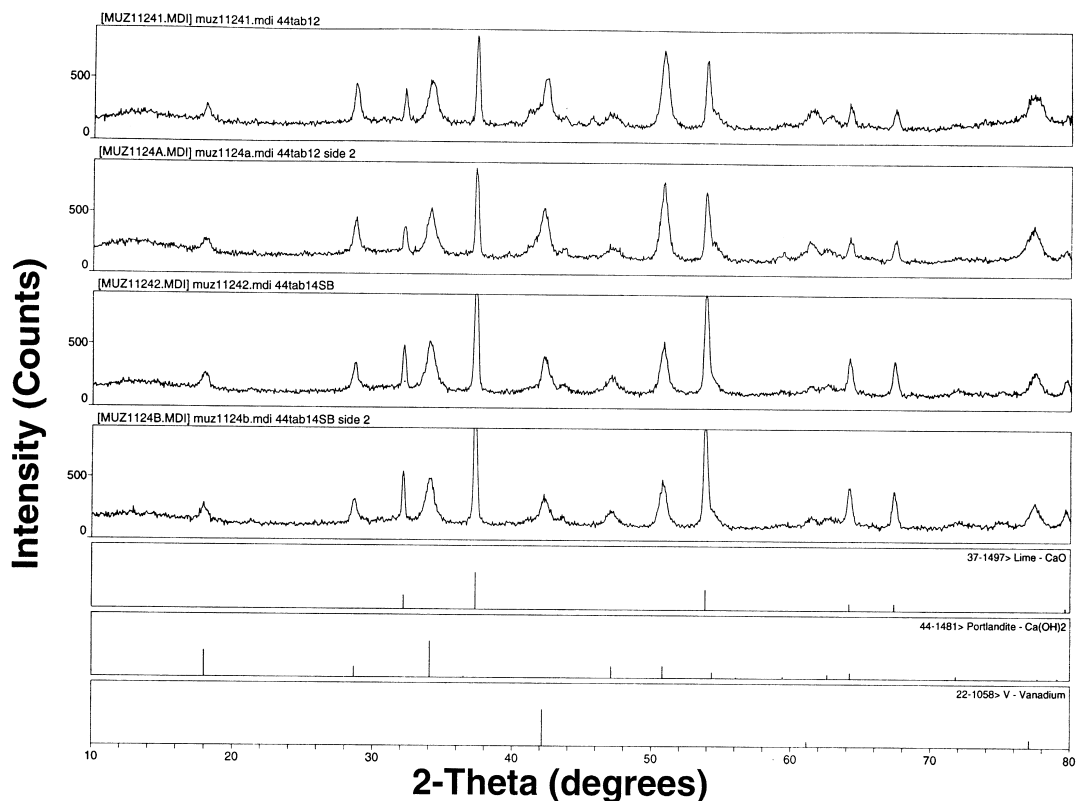


Fig. 3. X-ray diffraction patterns obtained from both surfaces of CaO-coated V-4 Cr-4 Ti tabs after 137-h Li exposure at 600°C (both samples were coated by He-flow process; see Table 1 for process histories of samples).

Figure 3 shows X-ray diffraction (XRD) results of the two surfaces of the tab samples (44Tab12 and 44Tab14SB), that were exposed to Li for 137 h at 600°C. Figure 4 shows similar results for 44Tab24 and 44Tab9, which were exposed to Li at 700°C. All patterns in both figures give strong indications of the presence of CaO on these samples after Li exposure.  $\text{Ca(OH)}_2$  is expected because it forms readily from CaO in a humid environment. The presence of the V peak in all these patterns (less so in samples exposed to Li at 700°C) should be due to sampling of the matrix during the X-ray analysis. The presence of CaO in these tabs, as well as in other samples exposed to Li, and hence indicating Li compatibility with CaO, was also verified by energy-dispersive X-ray analysis (EDX) using scanning electron microscope (SEM). The photomicrographs of 44Rod13L after exposure to Li for 137 h at 600°C and of 44Rod3S after exposure to Li for 145 h at 700°C are shown in Figures 5 a and b, respectively. These photomicrographs, which were typical of other samples listed in Tables 1 and 2, indicate that the CaO coating maintained its integrity during exposure to Li.

Characterization of the 60-mm-long rod 44Rod10L (see Table 2), which was exposed to Li for 282 h at 700°C, is in progress. This sample will have to be cut before it can be analyzed by XRD. However, preliminary examination of this sample by SEM and SEM/EDX indicate that CaO is still present on the sample surface.

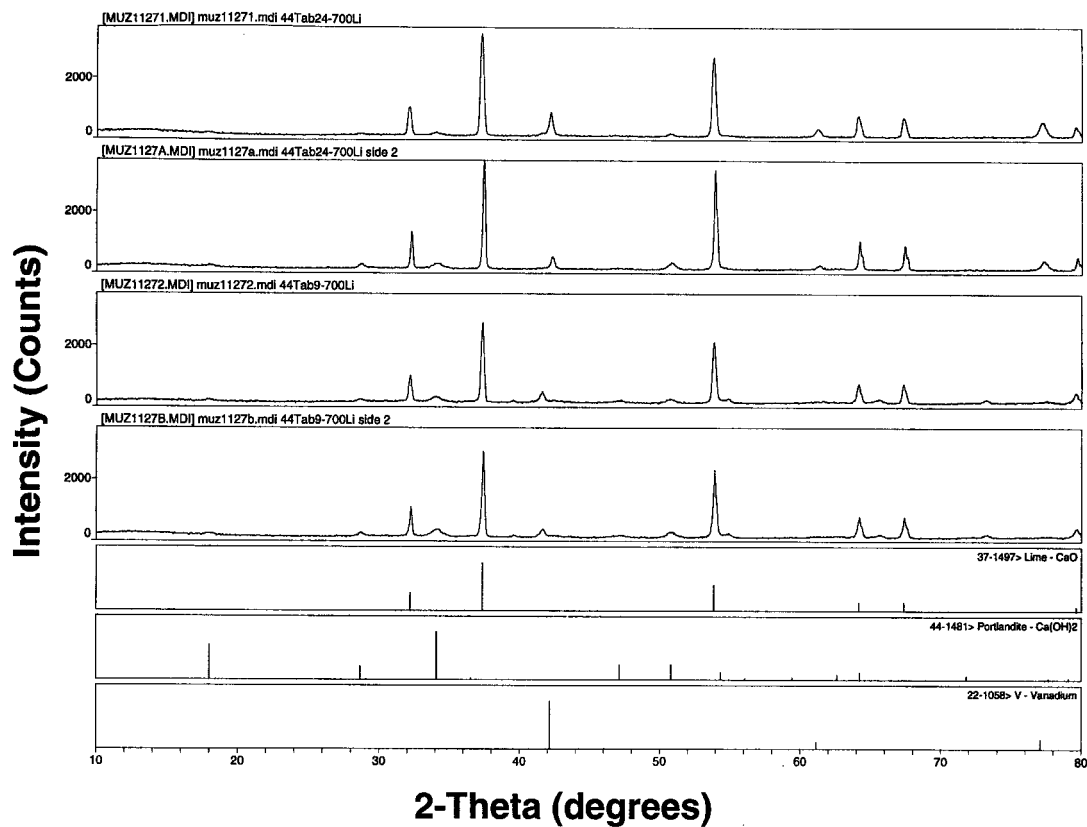


Fig. 4. X-ray diffraction patterns obtained from both surfaces of CaO-coated V-4 Cr-4 Ti tabs after 145-h Li exposure at 700°C. (44Tab9 was coated by He-flow, and 44Tab24 was coated by vacuum process; see Table 1 for process histories of samples).

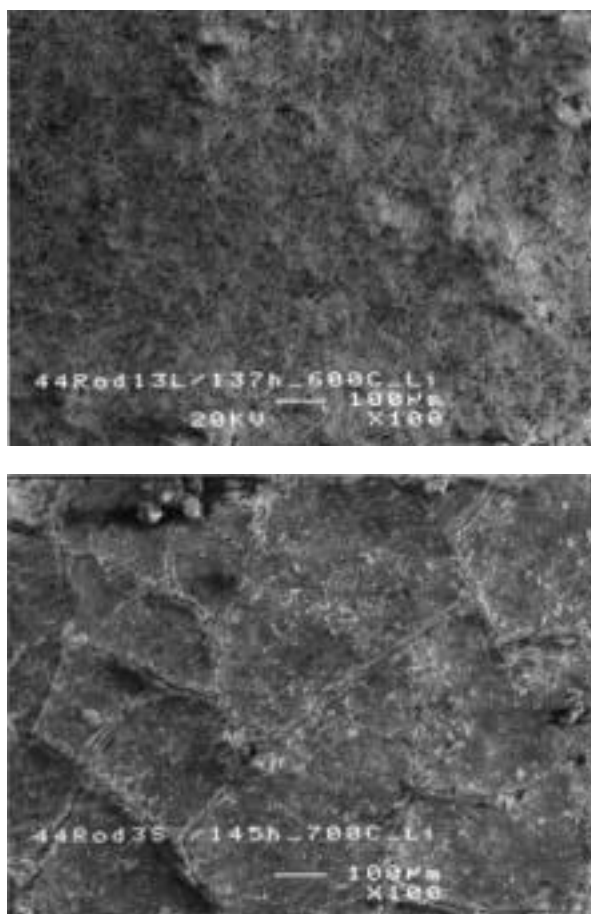


Fig. 5. SEM photomicrographs of V-4 Cr-4 Ti rod samples after Li exposure, showing Li compatibility of CaO coating developed by double Ca-deposition/oxidation processes: (left) 44Rod13L CaO coated by He-flow process and exposed to Li for 137 h at 600°C, and (right) 44Rod3S CaO coated by vacuum process and exposed to Li for 145 h at 700°C.

The 44Rod11S sample was recently removed from Li after 500-h exposure at 700°C. To minimize the deleterious effects of the humid ambient environment, this sample was analyzed by XRD at several spots on its surface. The peaks were not sharp due to the curvature and uneven nature of the sample surface. But there was clear evidence of CaO in this sample. Other compounds detected on this sample included V, as sampled from beneath the coating, and some Li compounds because the sample was analyzed without removing all the Li in order to avoid alterations on the coating due to exposure to ambient environment. Environmental effects on the coating after removal from Li was accomplished to some extent as evidenced by the absence of  $\text{Ca}(\text{OH})_2$  in this sample. Coating scraped from various locations on the surface of this specimen was also analyzed with a Debye-Scherrer camera and the results indicated presence of CaO. Further evidence of the presence of CaO on this sample after 500 h in Li at 700°C can be seen in Figures 6 a and b. These patterns are obtained from EDX analysis at two different locations on the sample surface using SEM. The Ca and O peaks are sharp, and there seems to be no

appreciable V peak. Along with other results, this indicates that CaO is stable in Li-2 wt.% Ca solution at 700°C.

#### WORK IN PROGRESS

Cross sectional areas of the samples listed in this report will be further analyzed by SEM and SEM/EDX. Depth profiles for various elements, including Ca, O, V, Cr, and Ti, will be determined from the outer surface of the coating to the interior of the substrate alloy.

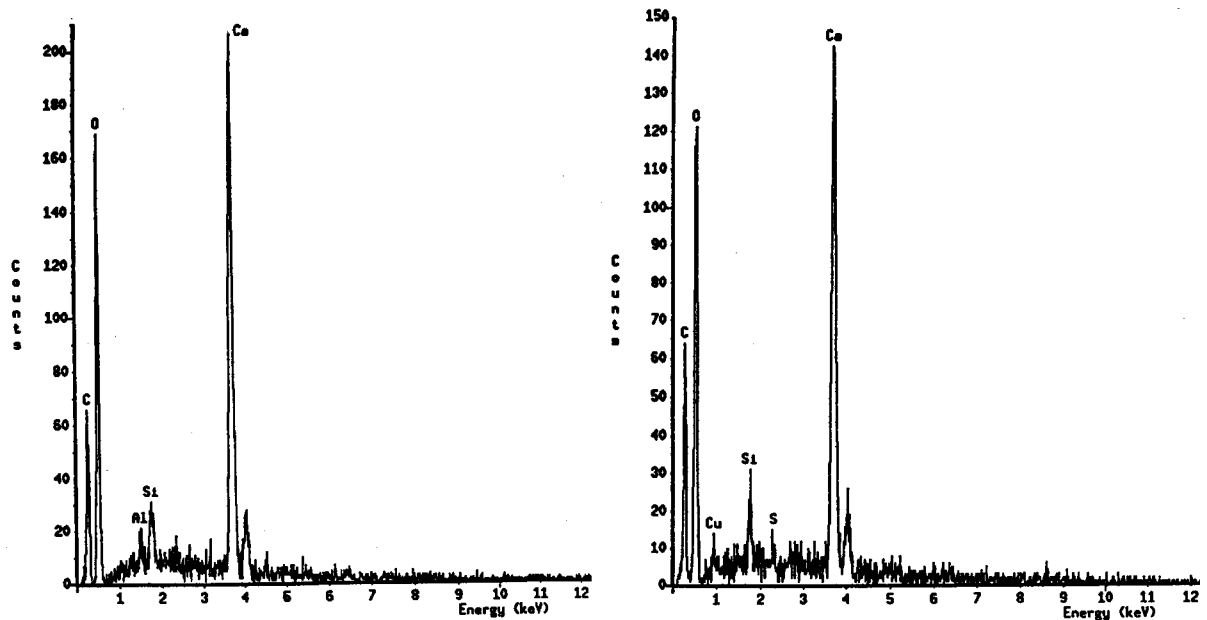


Fig. 6. Energy-dispersive X-ray patterns obtained from (left) light gray area, and (right) dark gray area on surface of 44Rod11S after 500-h Li exposure at 700°C (see Table 2 for processing history of sample).

#### REFERENCES

1. K. Natesan, C. B. Reed, M. Uz, J. H. Park, and D. L. Smith, "Electrically Insulating Coatings for V-Li Self-Cooled Blanket in a Fusion System," Argonne National Laboratory Report ANL/TD/TM00-10, May 2000.
2. K. Uz, D. L. Rink, and D. L. Smith, "Development and Characterization of Electrically Insulating CaO Coatings," Fusion Reactor Materials Progress Report for the Period Ending December 31, 2001, Argonne National Laboratory, DOE/ER-0313/29, , pp. 9-18, Sept. 2000.
3. K. Natesan, Z. Zeng, W. E. Luther, M. Uz, and D. L. Smith, "Development of Electrically Insulating CaO Coatings," Fusion Reactor Materials Progress Report for the Period Ending June 30, 2000, Argonne National Laboratory, DOE/ER-0313/28, Sept. 2000.

4. K. Natesan, C. B. Reed, M. Uz, and D. L. Rink, "Development of Electrically Insulating CaO Coatings," Fusion Reactor Materials Progress Report for the Period Ending June 30, 1998, Argonne National Laboratory, DOE/ER-0313/24, p. 82, Sept. 1998.
5. K. Natesan, M. Uz, and S. Weider, "Development of Electrically Insulating CaO Coatings," Fusion Reactor Materials Progress Report for the Period Ending December 31, 1998, Argonne National Laboratory, DOE/ER-0313/25, p. 69, April 1999.
6. K. Natesan, M. Uz, and S. Weider, "Development of Electrically Insulating CaO Coatings For Service In a Lithium Environment," J. Nuclear Materials, 283-287, pp. 1277-1281, 2000.

## DEVELOPMENT OF ELECTRICALLY INSULATING COATINGS BY MOCVD TECHNIQUE

Z. Zeng and K. Natesan (Argonne National Laboratory)

### OBJECTIVE

The objectives of this task are to (a) develop electrically insulating coatings by the metallorganic vapor deposition (MOCVD) technique, with emphasis on understanding the basic thermodynamic conditions and kinetic processes needed to develop stable coatings that are compatible with an Li/Li-Ca environment; (b) perform detailed postexposure analysis of the surface layers by several electron/optical techniques to characterize the elemental and phase compositions, quantify stratification in the layers, and establish the roles of compositional changes in the coating and microstructure; and (c) measure the electrical resistance of the coatings before and after exposure to Li.

### SUMMARY

As part of the U.S. Department of Energy's Fusion Reactor Program, studies have been in progress at Argonne National Laboratory (ANL) to develop electrically insulating coatings on V-Cr-Ti alloys, in particular on V-4Cr-4Ti, the primary candidate for use in various structural applications, including in the first-wall structure/blanket of a fusion reactor. The first wall will be in contact with liquid Li coolant, and electrical conductivity across the wall will lead to magnetohydrodynamic pressure losses during flow in the magnetic field. Hence, among the critical requirements of the rather stringent design criteria for the first wall material are that the coating on it be nonporous, tenacious, electrically insulating, and capable of maintaining its structural integrity while in use in a liquid Li environment at temperatures of 400-700°C. More information on the material requirements of fusion reactors is reported in Ref. 1.

This report addresses the development and characterization of CaO and Y<sub>2</sub>O<sub>3</sub> coatings that were applied on V-4Cr-4Ti alloy by an MOCVD process. Several coupon specimens were coated with CaO or Y<sub>2</sub>O<sub>3</sub> by the process developed at ANL. The specimens were analyzed and the coatings were characterized before exposure to a liquid Li environment. The analysis and characterization used one or more of scanning electron microscopy (SEM), energy-dispersive X-ray analysis (EDX), and X-ray diffraction (XRD) techniques. Results are presented, with emphasis on microstructural analysis and electrical resistivity of the coatings. We plan to expose the coated specimens in liquid Li of varying chemistry at temperatures of 500-700°C.

### BACKGROUND

A review of available information on electrical resistivity values for several oxides, nitrides, and mixed oxides showed that oxides such as CaO, MgO, BeO, Y<sub>2</sub>O<sub>3</sub>, and MgAl<sub>2</sub>O<sub>4</sub>, and nitrides such as BN, AlN, and Si<sub>3</sub>N<sub>4</sub> exhibit resistivities of  $>10^6$  Ω·cm at temperatures below 700°C.<sup>1</sup> The requirement is that the product of the electrical resistivity of the insulator coating and the

thickness of the coating should exceed a nominal value of  $100 \text{ } \mu\text{m}^2$  under operating conditions. This translates to a

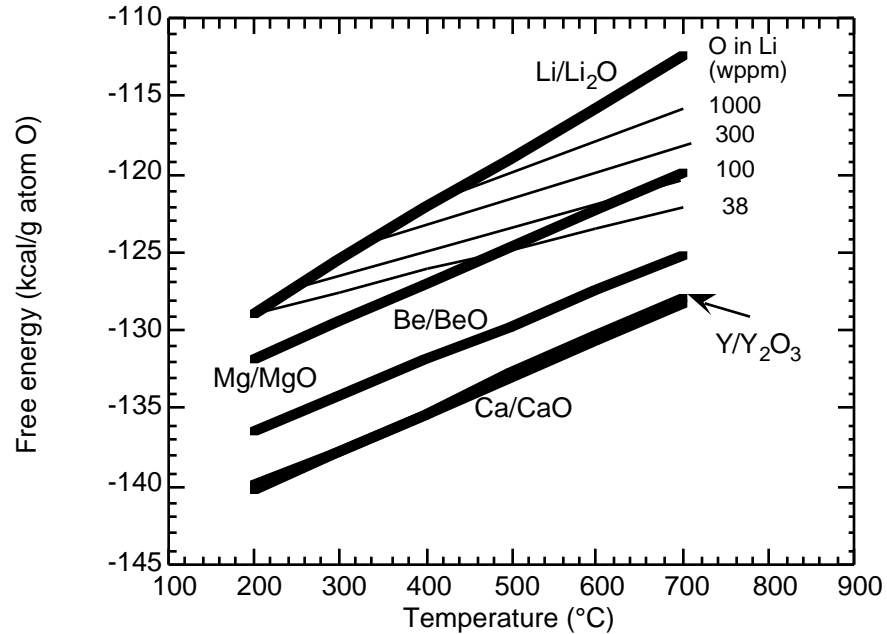


Fig. 1. Thermodynamic stability of several candidate oxide coatings in Li environment.

minimum resistivity value of  $10^6 \text{ } \Omega\cdot\text{cm}$  for a coating thickness of  $1 \text{ } \mu\text{m}$ , or  $10^5 \text{ } \Omega\cdot\text{cm}$  for a coating thickness of  $10 \text{ } \mu\text{m}$ . Based on the resistivity values of materials listed above, a coating layer of  $<1 \text{ } \mu\text{m}$  in thickness of any of these materials would be adequate from the insulating standpoint, provided that resistivity is not reduced during operation, e.g., by irradiation.

A majority of oxides that form from the constituents (e.g., V, Cr, Ti, Si, Al, etc.) of structural materials are unstable in an Li environment. The distribution coefficient for O between these metals and Li is such that O will transfer from the metals into Li and that O concentration in Li has no consequence in the corrosion performance of these metals and their alloys. Therefore, from the standpoint of stable oxides in an Li environment, very few candidates are feasible. Figure 1 shows the thermodynamic stability of several oxides (CaO, MgO, Y<sub>2</sub>O<sub>3</sub>, BeO) that are possible candidates for insulator application in an Li environment. It is evident that all four oxides are stable in O-saturated Li at temperatures of  $>200^\circ\text{C}$ . Also shown in the figure are free energy values for Li that contains various concentrations (1000, 300, 100, and 38 wppm) of O. The lowest value of 38 wppm O corresponds to an O concentration that is established by cold-trapping Li at  $200^\circ\text{C}$ . Under these conditions, all except MgO are thermodynamically stable over the wide temperature range ( $200\text{--}700^\circ\text{C}$ ) of interest for fusion systems.

Coating approaches such as the physical vapor deposition (PVD) technique and in-situ coating in a Ca/Li environment have been investigated to prepare CaO coating on vanadium alloys<sup>2</sup> which

are candidate materials for structural application in a fusion system. In both approaches, a layer of calcium is deposited on the surface of V alloys by vapor- or liquid-phase transport methods. CaO

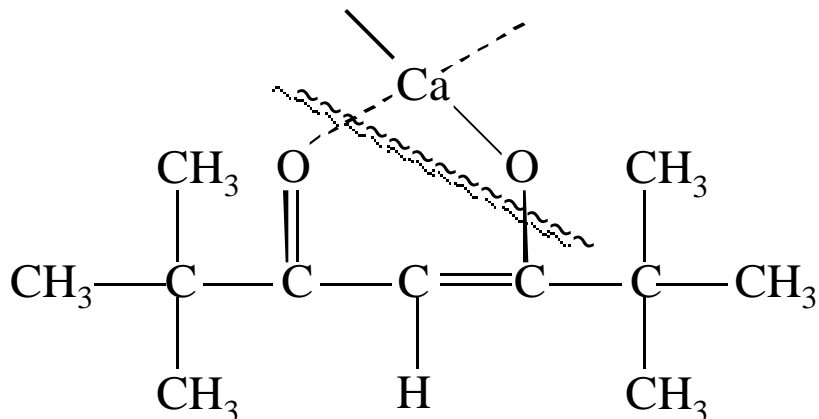


Fig. 2. Diagram of bond breaks in Ca precursor used in MOCVD technique.

coatings were obtained after oxidation of the deposited Ca layer. There may be a small amount of V in the film since Ca-deposited specimens were oxidized at elevated temperature to obtain the electrically insulating coating. Vanadium enrichment can decrease the resistance of the coating, especially if it is bound with oxygen, since the O will transfer to Li thereby leaving V metal in the coating. Furthermore, oxidation of the deposited Ca layer to CaO can lead to volume increase and may debond the coating from the substrate. To overcome these problems, an alternate method (MOCVD) was examined for the development of electrically insulating coatings.

The MOCVD technique allows preparation of a CaO film on the surface of a V alloy without using the two-step Ca deposition/oxidation process. CaO can be directly deposited on the surface of V alloy by MOCVD. For example, when the Ca precursor, calcium bis(2,2,6,6-tetramethyl-3,5-heptanedionate), is heated to high temperature, the C and O bonds will break as shown in Fig. 2.

The MOCVD approach will not only reduce the concentration of V and O enrichment in the coatings, but will also minimize the possibility of cracking during oxidation of deposited Ca. The method also has an additional advantage in that coatings can be applied in structures with complex geometry. In this report, we discuss the preparation of CaO and Y<sub>2</sub>O<sub>3</sub> coatings by MOCVD.

#### EXPERIMENTAL PROGRAM

Calcium bis(2,2,6,6-tetramethyl-3,5-heptanedionate) [Ca(TMHD)<sub>2</sub>] was selected as the precursor to prepare the CaO coating by the MOCVD method. However, [Ca(TMHD)<sub>2</sub>] has a low vapor pressure and decomposes easily. To obtain a reasonable rate of film growth, the precursor must be heated to a high temperature (usually above 200°C) for a suitable vapor pressure, whereas significant decomposition of this compound is observed at 240°C. Therefore, only a narrow

temperature window is available for vaporizing the precursor. To accomplish the precursor vaporization and deposition of the coating in a narrow temperature range, we developed an MOCVD system in which the residence time and temperature for the process were controlled better than that possible with commercial MOCVD equipment.

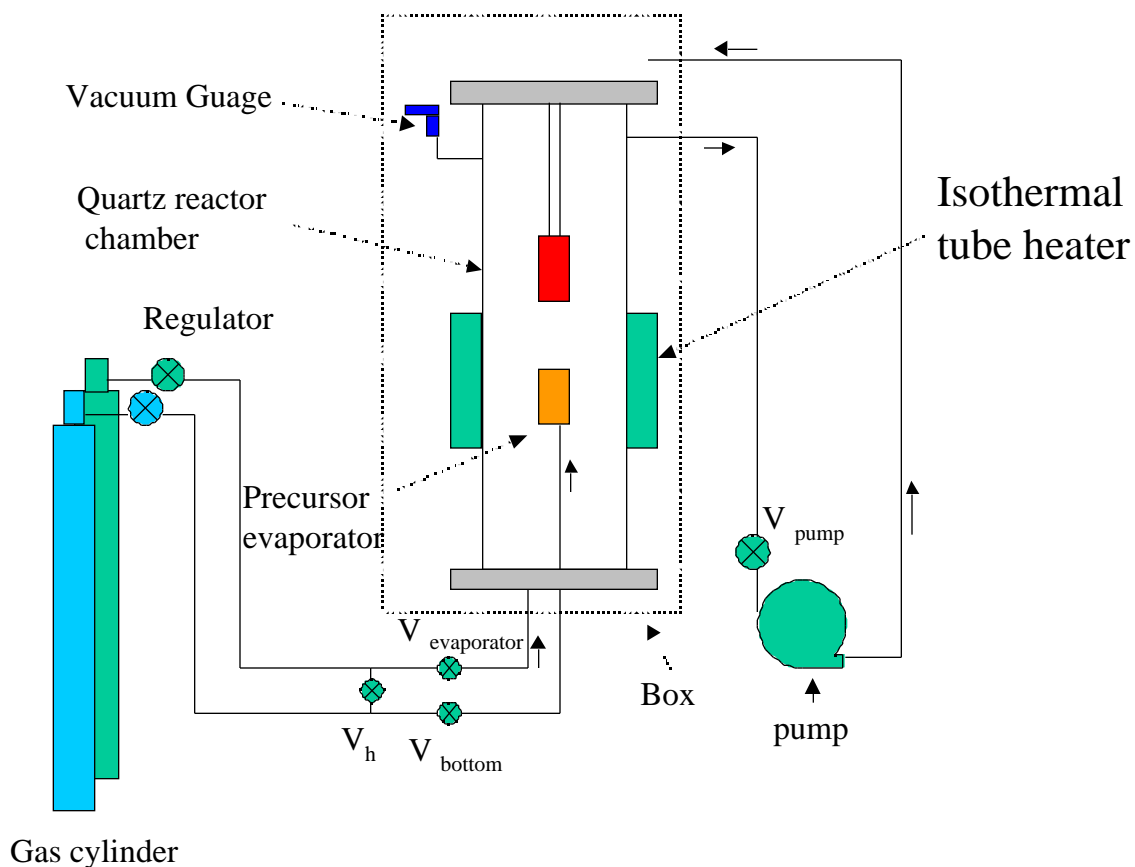


Fig. 3. Schematic of MOCVD system with assembled reactor and precursor evaporator.

The system we developed at Argonne National Laboratory consists of gas supply lines, precursor evaporator, isothermal tube heater, quartz reactor chamber, sample heater, vacuum meter, and pump. Figure 3 is a schematic representation of the entire system. The difference between this system and commercial MOCVD equipment is that the precursor evaporator is located within the quartz reaction chamber. Since the distance between the precursor evaporator and the sample heater is short, it is easy to control the temperature over this short distance with the isothermal tube heater, so that the precursor will not condense or decompose before it reaches the sample heater. The sample holder is made of a Ni-base alloy with a resistance heater. The precursor evaporator is covered by Al foil and 99.999% purity He is introduced into the precursor evaporator to minimize oxidation of the precursor. Oxygen flow enters from the bottom of the quartz reactor chamber.

Vanadium alloy coupons were glued to the sample heater by Ag paste.  $[\text{Ca}(\text{TMHD})_2]$  was positioned in the precursor evaporator. 99.999% purity Ar was introduced into the chamber from bottom at the beginning to prevent precursor from oxidation. The reactor chamber was evacuated to 0.5 torr by a mechanical pump. The isothermal tube heater was kept at 220-240°C, the samples were heated to 650-850°C, and the precursor evaporator was heated to 200-240°C. After all temperatures were stabilized, Ar was introduced into the precursor evaporator from the bottom of the chamber and then the flow was switched to O gas. The O reacted with  $\text{Ca}(\text{TMHD})_2$  and deposited CaO on the surface of each V alloy coupon.

## RESULTS

Figure 4 is an SEM image of the coating developed by MOCVD. The surface of the V alloy specimen is covered by condensed fine particles (1  $\mu\text{m}$  in size) of CaO. The SEM cross-sectional photomicrograph of the CaO coating shows that the thickness of CaO layer is 20  $\mu\text{m}$  (Fig. 5). Figure 6 shows the X-ray diffraction pattern of the coating and clearly indicates the coating to be pure CaO. Figure 7 shows the concentration of Ca and V as a function of distance from surface. There is almost no V in the CaO layer.

A two-probe method was used to measure the electrical resistance of these specimens by deposition of Au film over areas of 2 x 2 mm and use of Pt wire for electrical leads. The specimen assembly was inserted in a furnace and resistance measurements were made in an Ar environment between room temperature and 700°C. The variation in the product of resistance times area (i.e.,  $R \times A$ , which is equivalent to the product of resistivity times coating thickness) as a function of temperature obtained on specimens of V-4Cr-4Ti alloy was measured. For some of the specimens, the measurements were conducted during several heating and cooling cycles to establish the mechanical integrity of the coatings under thermal cycling. The  $R \times A$  value of the coating decreases with increasing temperature (see Fig. 8). The value is  $>10^7 \text{ } \Omega \cdot \text{cm}^2$  at 700°C, which is much higher than the minimum requirement of  $100 \text{ } \Omega \cdot \text{cm}^2$  for fusion application.

## REFERENCES

1. K. Natesan, C. B. Reed, M. Uz, J. H. Park, and D. L. Smith, "Electrically Insulating Coatings for V-Li Self-Cooled Blanket in a Fusion System," Argonne National Laboratory Report ANL/TD/TM00-10, May 2000.
2. K. Natesan, Z. Zeng, W. E. Ruther, M. Uz, and D. L. Smith, "Development of Electrically Insulating CaO Coatings," Fusion Reactor Materials Progress Report for the Period Ending June 30, 2000, Argonne National Laboratory, DOE/ER-0313/28, p. 30, Sept. 2000

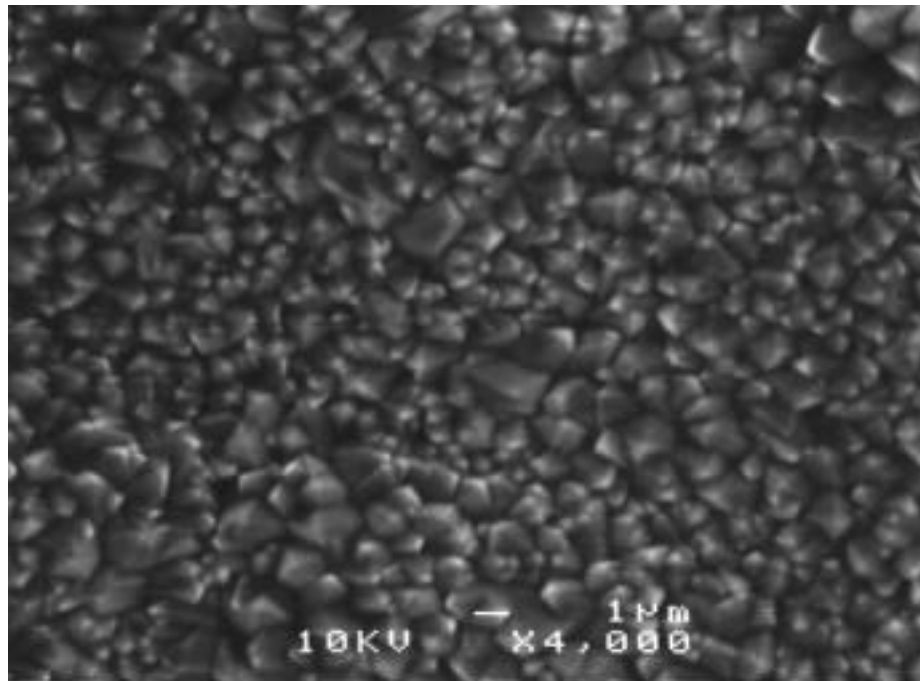


Fig. 4. SEM photomicrograph of surface of CaO coating developed by MOCVD.

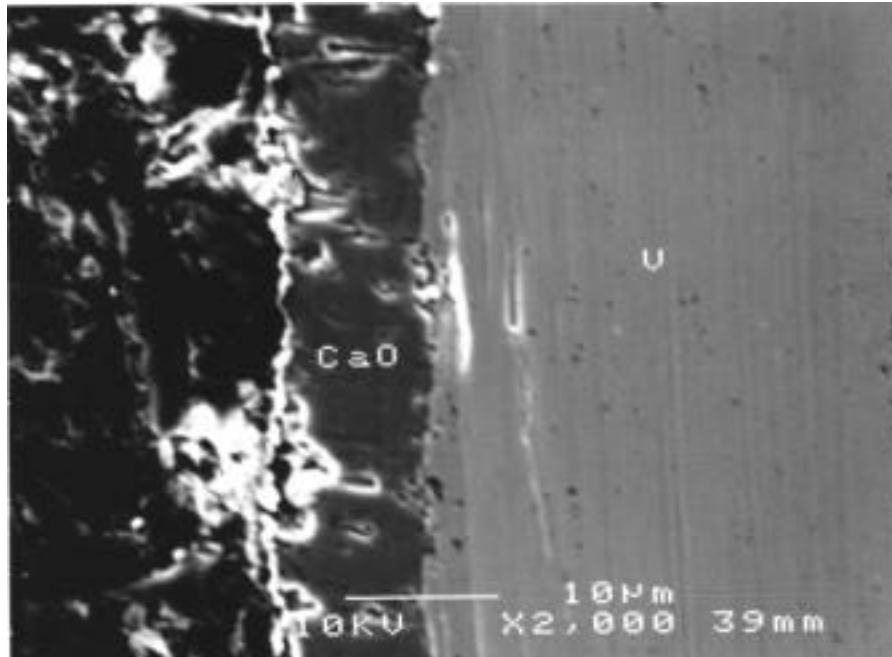


Fig. 5. SEM photomicrograph of cross section of CaO coating developed by MOCVD.

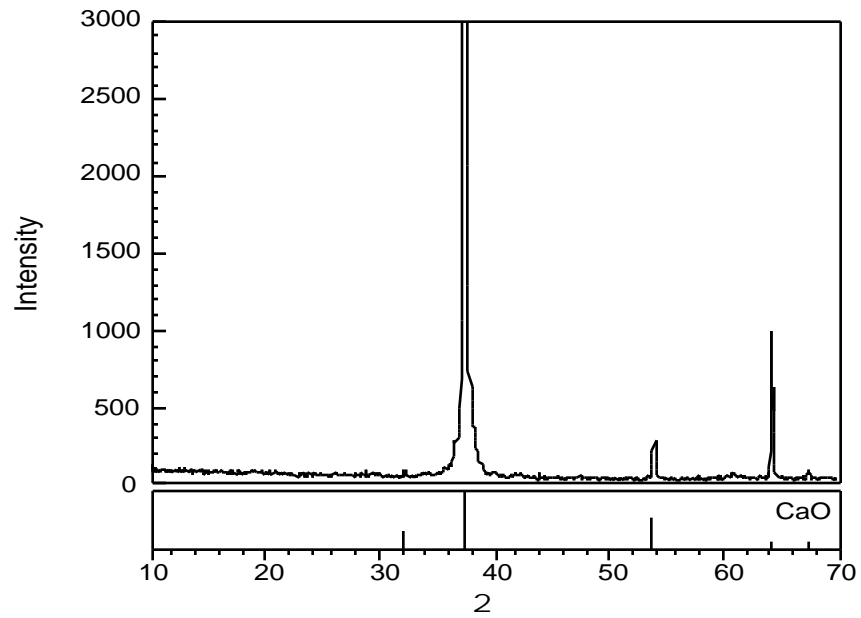


Fig. 6. XRD pattern of coating developed by MOCVD, indicating a composition of CaO.

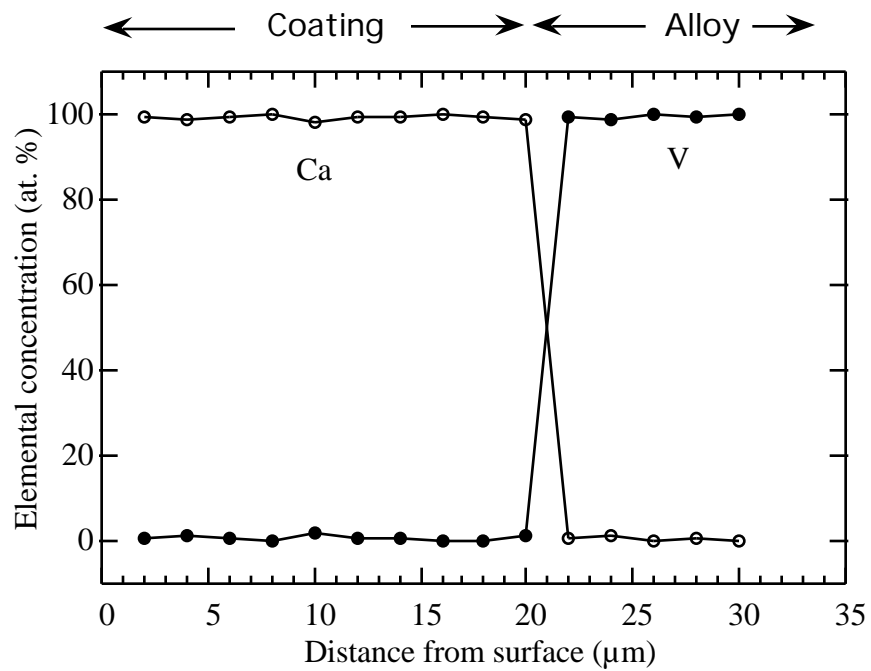


Fig. 7. Concentration of Ca and V as a function of distance from surface of CaO coating developed by MOCVD.

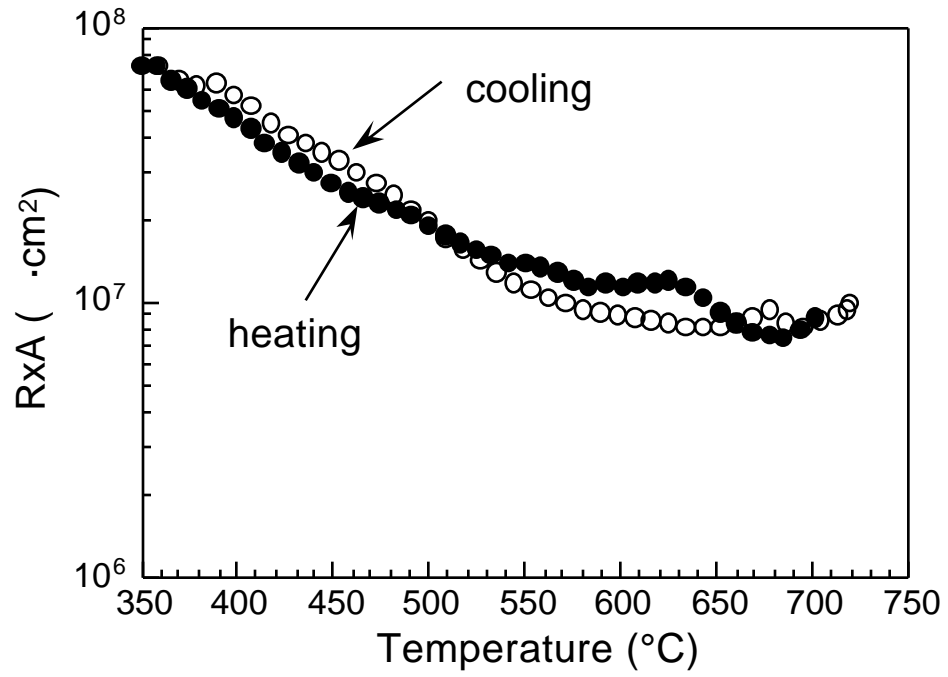


Fig. 8. Resistance times area (R x A) as a function of temperature for CaO coating developed by MOCVD.

## **8.0 BREEDING MATERIALS**

No contributions.

**9.0 RADIATION EFFECTS, MECHANISTIC STUDIES,  
AND EXPERIMENTAL METHODS**

## Atomistic Simulation of Dislocation-Defect Interactions in Cu

B. D. Wirth<sup>a</sup>, V. V. Bulatov and T. Diaz de la Rubia, Chemistry and Materials Science Directorate, Lawrence Livermore National Laboratory, Livermore, CA 94550

### OBJECTIVE

The mechanisms of dislocation-defect interactions are of practical importance for developing quantitative structure-property relationships, mechanistic understanding of plastic flow localization and predictive models of mechanical behavior in metals under irradiation. In copper and other face centered cubic metals, high-energy particle irradiation produces hardening and shear localization. Post-irradiation microstructural examination in Cu reveals that irradiation has produced a high number density of nanometer sized stacking fault tetrahedra. Thus, the resultant irradiation hardening and shear localization is commonly attributed to the interaction between stacking fault tetrahedra and mobile dislocations, although the mechanism of this interaction is unknown. In this work, we present a comprehensive molecular dynamics simulation study that characterizes the interaction and fate of moving dislocations with stacking fault tetrahedra in Cu using an EAM interatomic potential. This work is intended to produce atomistic input into dislocation dynamics simulations of plastic flow localization in irradiated materials.

### SUMMARY

It is well established that irradiation of metals by high-energy neutrons and ions produces significant changes in material microstructure and mechanical properties [1-5]. In low stacking fault energy face centered cubic (fcc) metals, stacking fault tetrahedra (SFT) are the primary defect observed following high-energy particle irradiation. For example, post-irradiation microstructural examination of copper irradiated at temperatures between 20 and 100 °C and doses between  $10^{-4}$  and  $10^2$  dpa reveals that approximately 90% of the high number density (about  $10^{23} \text{ m}^{-3}$ ) of radiation-induced defects are SFTs and that the average SFT size remains constant at about  $2.5 \pm 0.5$  nm [3,6]. When deformed after irradiation, Cu and other low stacking fault energy fcc metals exhibit significant mechanical property degradation, including a sharp increase in yield stress, a decrease in ductility and often, plastic flow localization in the form of defect-free dislocation channels [2,5]. The formation of dislocation channels is commonly attributed to dislocation absorption of the vacancies contained in SFTs [7]. However, a concise atomistic picture of the SFT absorption mechanism is lacking. Thus, the objective of this work is to obtain atomistic insight into the interaction of SFTs with dislocations, necessary to understand radiation-induced mechanical property changes.

---

<sup>a</sup> Corresponding author contact information: phone (925) 424-9822, fax (925) 423-7040, wirth4@llnl.gov

Computer simulation studies have been used to successfully model the production and accumulation of damage in irradiated Cu [8-13] and some key results of our work are briefly summarized here. Molecular dynamics (MD) simulations of displacement cascade evolution in Cu reveal the formation of large vacancy and self-interstitial loops [8-10]. The self-interstitial cluster loops undergo easy, one-dimensional transport [11] and are assumed to rapidly migrate away from the vacancy rich cascade region. The clustered vacancies then collapse to form SFTs, which occurs within a few picoseconds at room temperature by a dislocation mechanism [12], consistent with that first proposed by Silcox and Hirsch [14]. Interestingly, a number of MD simulations predict that the SFT structure will not consist of perfect tetrahedron, but in most cases, will actually consist of truncated tetrahedron [12,15] and in some cases, overlapping, truncated SFTs<sup>1</sup> [12].

## SIMULATION METHODOLOGY

MD simulations of the interaction and fate of moving edge dislocations in Cu were performed using the MDCASK code [16] and an embedded atom method (EAM) potential [17,18]. The elastic constants and stacking fault energy obtained with the EAM potential are provided in Table 1. The simulations were performed in a cubic cell bounded by  $\langle 111 \rangle$ ,  $\langle 110 \rangle$  and  $\langle 112 \rangle$  faces, as sketched in Figure 1. Periodic boundary conditions are applied in the  $Y=[110]$  and  $Z=[\bar{1}\bar{1}2]$  directions, while the  $X=[\bar{1}11]$  faces are free surfaces. An edge dislocation is introduced in the simulation cell by removing two (220) half-planes and equilibrating the system at 100 K to allow the edge dislocation,  $\mathbf{b}=a/2\langle 110 \rangle\{111\}$ , to split into two Shockley partial dislocations,  $\mathbf{b}=a/6\langle 112 \rangle\{111\}$ , separated by a stacking fault. SFT and overlapping, truncated SFTs were also inserted into the simulation cell on the  $(\bar{1}11)$  glide plane ahead of the dissociated edge

Table 1 – Elastic constants and stacking fault energy obtained from the EAM Cu potential [17,18] used in this work.

$C_{11}$	176 GPa
$C_{12}$	129 GPa
$C_{44}$	82.3 GPa
$\mu$	58.8 GPa
Stacking fault energy	11.4 mJ/m <sup>2</sup>

<sup>1</sup> A triangular vacancy platelet on a  $\{111\}$  plane bounded by three  $\langle 110 \rangle$  directions forms a single SFT. A triangular vacancy platelet bounded by two  $\langle 110 \rangle$  and one  $\langle 112 \rangle$  directions forms two partial (truncated) SFTs, one above and one below the initial plane; we define this as an overlapping truncated SFT.

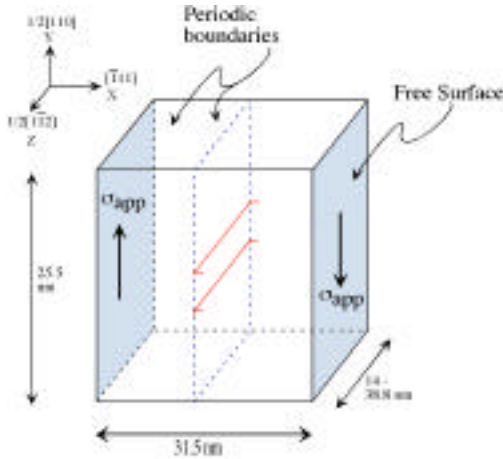


Figure 1 = Schematic view of the simulation cell and dimensions used in this work.

dislocation. Following equilibration at 100 K, a constant shear stress,  $\sigma_{yx}$ , is applied by superimposing a constant force in the  $[110]$  direction on the atoms in the two  $(\bar{1}11)$  surfaces.

In the results reported here, the simulation cell was 31.2 nm in X, 25.5 nm in Y and either 14.0 or 38.8 nm in Z (along the dislocation line), corresponding to a dislocation density of about  $8 \times 10^{14} \text{ m}^{-2}$  and a SFT density of 3 to  $9 \times 10^{22} \text{ m}^{-3}$ . The dislocation and SFT are visualized by plotting the location of atoms with high potential energy.

## RESULTS AND DISCUSSION

Figure 2 shows a series of MD simulation snapshots of the  $(\bar{1}11)$  glide plane (in  $[\bar{1}11]$  projection) of the interaction between a moving, dissociated edge dislocation and a SFT which lies across the dislocation glide plane. The simulation was performed at an initial temperature of 100 K and an applied shear stress of 300 MPa. It is important to mention some additional details regarding this simulation. First, as shown in Table 1, the Cu EAM potential gives a stacking fault energy which is lower than experimental values ( $30\text{-}40 \text{ mJ/m}^2$ ) and results in a large equilibrium separation ( $\sim 7\text{-}8 \text{ nm}$ ) between the two Shockley partials. Second, the applied stress is significantly higher than the yield stress of copper and is used to study the fate of the interaction within readily accessible MD simulation times. Additional simulations are ongoing to characterize the effect of these (and other) variables on the results.

Figure 2a shows the initial configuration of the edge dislocation, which is split into the two Shockley partial dislocations, and the SFT, which consists of 6 stair-rod dislocations when viewed using high potential energy atoms. Although not seen in this projection, the SFT overlaps the glide plane of the edge dislocation. Following application of the shear stress, the two Shockley partial dislocations are driven towards

the SFT. Figure 2b shows the position of the partial dislocations 9 ps after applying the 300 MPa shear stress. By this time, the leading Shockley partial dislocation has reached the SFT, felt a repulsive force and bowed back away from the SFT. As the trailing partial approaches, the leading partial is forced to enter the SFT (Figure 2c). The SFT acts as a hard barrier to dislocation motion and in order for the leading partial to move past the SFT, it must noticeably bow around it, finally releasing at a critical angle of about  $80^\circ$  (Figure 2d). By 15.5 ps (Figure 2e) the trailing partial enters the SFT, as the leading partial continues to move ahead with significant remaining curvature along its line. Interestingly, the SFT provides less resistance to the passage of the trailing partial and the shape of the trailing partial shows only a slight perturbation immediately after passing the SFT (Figure 2f).

Surprisingly, the SFT is not absorbed by the moving edge dislocation, but instead acts as a hard obstacle to dislocation motion. Following passage of the dislocation, the SFT has been sheared along the dislocation glide plane, and thus has a surface step (ledge) along three of its four  $\{111\}$  faces, but remains largely intact. Qualitatively similar results are observed in simulations of the edge dislocation – SFT interaction performed with a range of applied stress from 50 to 300 MPa, different SFT separation along the dislocation line and slightly different interaction geometry. In all cases, the SFT acts as a hard barrier and despite the formation of surface steps, remains intact following dislocation passage.

However, dislocation absorption of an SFT-type defect has been observed in the case where the SFT is not perfect, but rather consists of overlapping, truncated SFTs. Figure 3 shows the results of one such simulation at 100 K in Cu. In this simulation, an overlapping, truncated SFT such as formed by aging displacement cascades [12], with a spacing of 14 nm (along the dislocation line), is placed on the glide plane of a dissociated edge dislocation which moves under an applied shear stress of 300 MPa. Figure 3a shows the initial configuration of the edge dislocation, split into two Shockley partial dislocations, and the overlapping, truncated SFT (most easily visualized in  $\langle 110 \rangle$  projection), as represented through visualization of the atoms with high potential energy. Figure 3b shows that upon contact, the leading partial absorbs vacancies from part of the overlapping truncated SFT and climbs, forming a pair of superjogs that effectively pin the leading partial as the trailing partial approaches. Figure 3c shows that the trailing partial catches the leading partial at the location of the overlapping SFT and superjog pair, climbs through absorption of the remaining vacancies in the defect and constricts at the location of the superjogs. Following defect absorption, the dislocation continues to move (Fig. 3d), but with a decreased mobility associated with the superjogs.

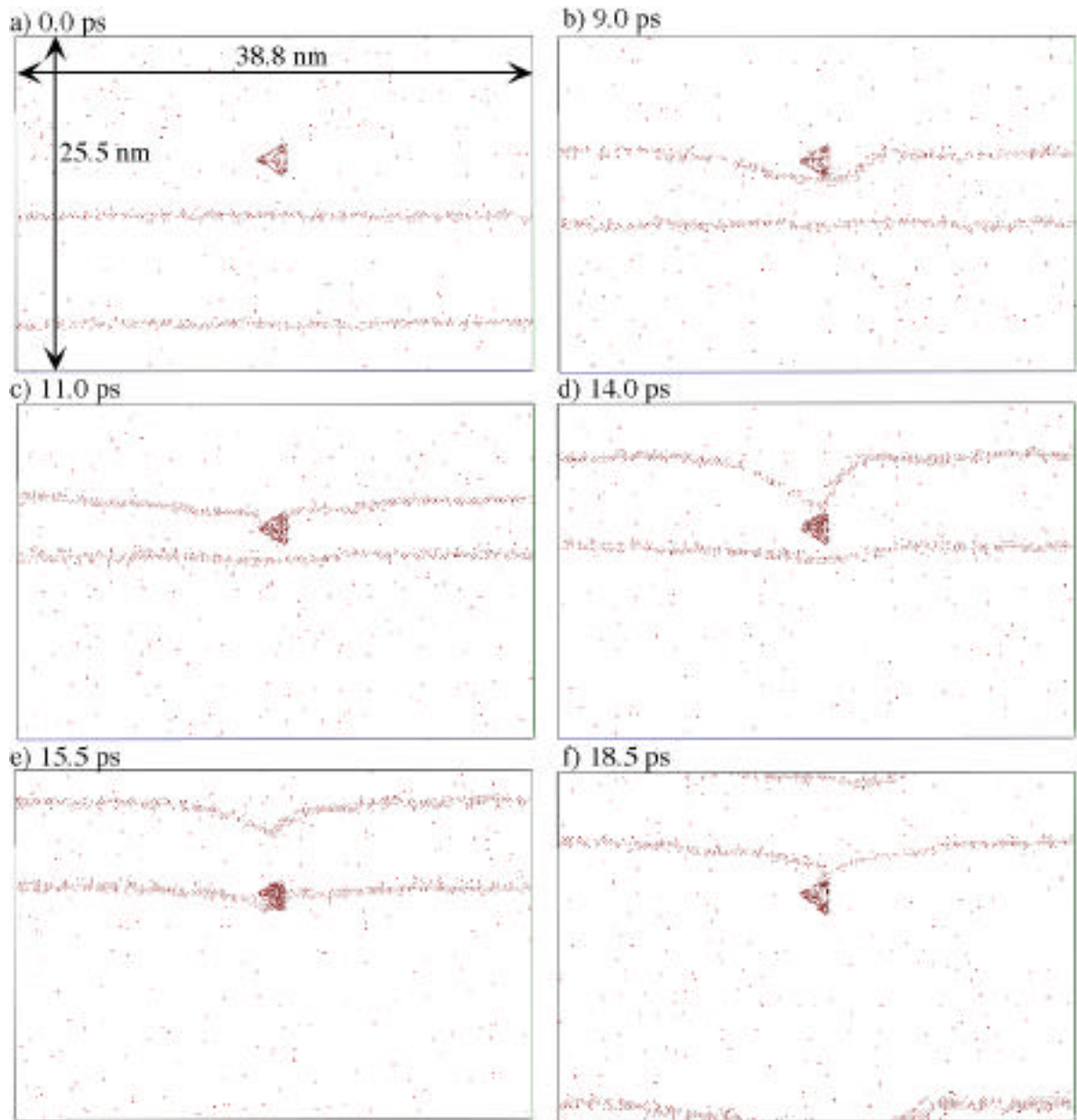


Figure 2 –  $[\bar{1}11]$  projection of MD simulation snapshots showing the interaction between a moving, dissociated edge dislocation and an SFT which overlaps the dislocation glide plane, as visualized by plotting atoms with high potential energy. Dislocation positions are shown at a) 0.0 ps, b) 9.0 ps, c) 11.0 ps, d) 14.0 ps, e) 15.5 ps and f) 18.5 ps after applying a 300 MPa shear stress. Note, the use of high potential energy atoms for visualization introduces thermal noise (isolated points) into the snapshots.

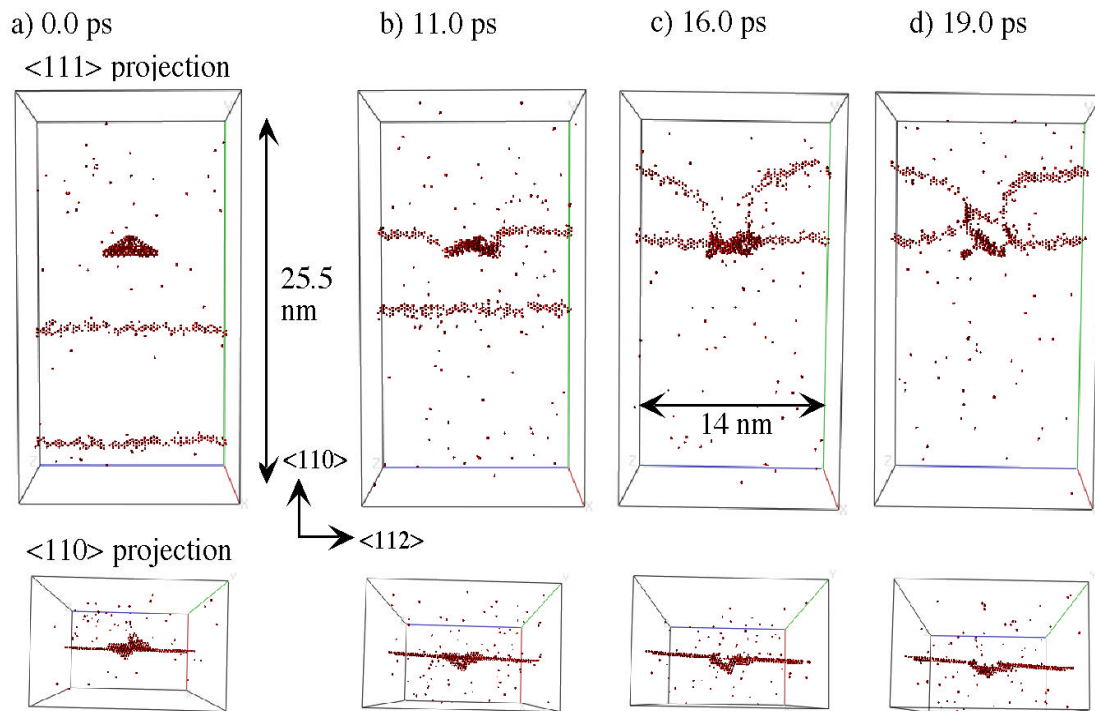


Figure 3 – MD simulation snapshots showing the interaction between a moving, dissociated edge dislocation and an overlapping, truncated SFT in Cu. The high potential energy atoms are visualized in  $\langle 111 \rangle$  (top) and  $\langle 110 \rangle$  (bottom) projections and show the motion of the two Shockley partials and interaction with the overlapping, truncated SFT at a) 0, b) 11.0, c) 16.0 and d) 19.0 ps after application of a 300 MPa shear stress. See text for additional details.

The detailed absorption mechanism is complicated and has not yet been completely analyzed. It is clear that passage of a single dislocation through a perfect SFT will not lead to its absorption, but it is not yet known how many dislocations are required to completely shear a SFT, or what degree of SFT truncation will result in absorption. However, it is clear that defect absorption produces dislocation climb and the formation of superjog pairs, which have decreased mobility. One of the superjogs is initially constricted, presumably in the form of a Lomer segment, as discussed by Rodney and Martin for the case of dislocation climb associated with self-interstitial cluster absorption [19]. The constricted superjog is essentially sessile, but can transform to a more favorable (glissile) configuration through the incorporation of three self-interstitials, as discussed in Ref. 19. This process occurred just prior to the snapshot shown in Fig. 3c, and indeed, the small cluster of high energy atoms seen below the left superjog in Fig. 3d has been identified to consist of three vacancies.

## CONCLUSIONS

Selected results from a MD simulation study of the interaction between a moving edge dislocation and stacking fault tetrahedra defects have been presented. The results show that a perfect SFT acts as a hard obstacle for dislocation motion and, although the SFT is sheared by the dislocation passage, it remains largely intact. However, our simulations show that an overlapping, truncated SFT is absorbed by the passage of an edge dislocation, resulting in dislocation climb and the formation of a pair of less mobile super-jogs on the dislocation. Additional simulations are underway to characterize the matrix of possible dislocation-SFT interactions, including the effect of applied stress and stacking fault energy, and provide rules for dislocation dynamics simulations that can provide insight into the mechanisms responsible for flow localization in irradiated metals.

*This work was performed under the auspices of the U.S. Department of Energy by University of California Lawrence Livermore National Laboratory under contract No. W-7405-Eng-48.*

## REFERENCES

1. L. K. Mansur and E. E. Bloom, *J. of Metals*, **34** (1982) 23.
2. G. E. Lucas, *J. Nuc. Mat.* **206** (1993) 287.
3. B. N. Singh and S. J. Zinkle, *J. Nuc. Mat.*, **206** (1993) 212.
4. H. Trinkaus, B. N. Singh and A. J. E. Foreman, *J. Nuc. Mat.* **251** (1997) 172.
5. M. Victoria, N. Baluc, C. Bailat, Y. Dai, M. I. Lупpo, R. Schaublin and B. N. Singh, *J. Nuc. Mat.* **276** (2000) 114.
6. Y. Dai, M. Victoria, *Mat. Res. Soc. Symp. Proc.*, **439** (1997) 319.
7. N.M. Ghoniem, S.-S. Tong and L.Z. Sun, *Phys. Rev. B*, **139(1)** (2000) 913.
8. T. Diaz de la Rubia and M. W. Guinan, *Phys. Rev. Lett.* **66** (1992) 655.
9. W. J. Phythian, R. E. Stoller, A. J. E. Foreman, A. F. Calder and D. J. Bacon, *J. Nucl. Mat.* **223** (1995) 245.
10. R. S. Averback and T. Diaz de la Rubia, *Solid State Physics*, **51** (1998) 281.
11. Y. N. Osetsky, D. J. Bacon, A. Serra, B. N. Singh, and S. I. Y. Golubov, *J. Nucl. Mat.* **276** (2000) 65.
12. B. D. Wirth, V. Bulatov and T. Diaz de la Rubia, *J. Nuc. Mat.* (2000) in press.
13. M. J. Caturla, N. Soneda, E. A. Alonso, B. D. Wirth and T. Diaz de la Rubia, *J. Nuc. Mat.* **276** (2000) 13.
14. J. Silcox and P. B. Hirsch, *Phil. Mag.*, **4** (1959) 72.
15. Y. N. Osetsky and D. J. Bacon, this conference proceedings.
16. T. Diaz de la Rubia and M. W. Guinan, *J. Nuc. Mat.*, **174** (1990) 151.
17. S. M. Foiles, M. I. Baskes and M. S. Daw, *Phys. Rev. B*, **33** (1986) 7983.
18. M. Ghaly and R. S. Averback, personal communication.
19. D. Rodney and G. Martin, *Phys. Rev. B* **61** (2000) 8714.

**10. DOSIMETRY, DAMAGE PARAMETERS, AND  
ACTIVATION CALCULATIONS**

**NEUTRON DOSIMETRY AND DAMAGE CALCULATIONS FOR THE HFIR-RB-11J,12J IRRADIATIONS** - L. R. Greenwood (Pacific Northwest National Laboratory)\* and C. A. Baldwin (Oak Ridge National Laboratory)

**OBJECTIVE**

To provide dosimetry and damage analysis for fusion materials irradiation experiments.

**SUMMARY**

Neutron fluence measurements and radiation damage calculations are reported for the joint U.S. Japanese experiments RB-11J and RB-12J which were conducted in the removable beryllium (RB) position of the High Flux Isotope Reactor (HFIR) at Oak Ridge National Laboratory (ORNL). These experiments employed a  $\text{Eu}_2\text{O}_3$  thermal shield for the first time to reduce the thermal neutron fluence. The maximum total neutron fluence at midplane was  $1.85 \times 10^{22}$  n/cm<sup>2</sup> ( $9.5 \times 10^{21}$  n/cm<sup>2</sup> above 0.1 MeV), resulting in about 5.5 dpa and 3.6 appm helium in type 316 stainless steel.

**PROGRESS AND STATUS**

The RB-11J and -12J experiments were irradiated in the RB\* position of HFIR during cycles 352 through 361 starting February 7, 1997, and ending July 17, 1998, for a net exposure of 223.92 effective full-power days at 85 MW. The experiment was a collaborative effort of the U.S. Fusion Materials Program at ORNL and Monbusho in Japan. Complete descriptions of the specimen matrices and irradiation assemblies as well as the reactor operating history have been published previously. [1,2]

Neutron dosimetry capsules were inserted at 6 different elevations located at various radial positions in each assembly. The assemblies were rotated after every cycle to minimize any radial flux gradients. The dosimetry capsules consisted of small aluminum tubes measuring about 1.3 mm in diameter and 6.4 mm in length. Each tube contained small monitor wires of Fe, Cu, Ni, Ti, Nb, 0.1% Co-Al alloy, and 80.2% Mn-Cu alloy. Following irradiation, the monitors were removed from the assemblies and analyzed for gamma activities at ORNL.

Upon examination at ORNL, it was found that four of the dosimetry capsules from the 12J experiment were ruptured, as shown in Figure 1. For these capsules, it appears that the copper wires melted through the aluminum capsules. A likely explanation for this behavior is that the copper was not in good thermal contact with the surrounding aluminum capsule, and, therefore, heat was transferred from the copper inefficiently. The resulting elevated temperature of the copper could have been sufficient to melt the aluminum at the point of contact. The copper was then lost in disassembly of the experiment capsule. The formation of a eutectic of aluminum and copper is also likely once melting began. This could reduce the melting point by about 110 °C. However, since the capsule temperature was at 500 °C, the copper only had to be about 50 °C higher than its surroundings to melt through the aluminum capsule, which has a melting point of 660 °C. Fortunately, only the copper monitors were lost in two of the ruptured capsules, and all of the other monitors were recovered. The monitor weights were checked against the fabrication records to ensure no loss of material on the other monitors. In the case of capsule 12J-126, the Co-Al alloy monitor could not be located after disassembly.

---

\* Pacific Northwest National Laboratory (PNNL) is operated for the U.S. Department of Energy by Battelle Memorial Institute under contract DE-AC06-76RLO-1830.

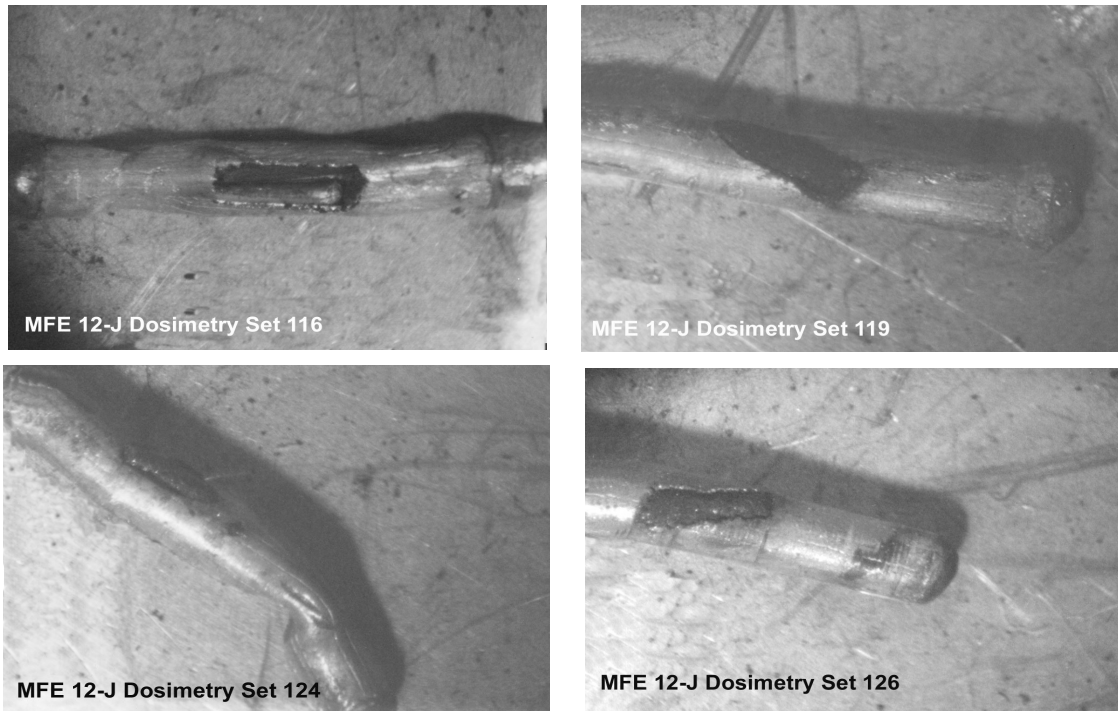


Figure 1. Pictures of ruptured dosimetry monitors from the RB-12J experiment.

The measured gamma activities were subsequently analyzed at Pacific Northwest National Laboratory. The activities were converted to activation rates, as listed in Table 1, by correcting for nuclear burnup, gamma self-absorption, decay during and after irradiation, isotopic abundance, and atomic weight. Burnup corrections were based on an iterative procedure for the thermal/epithermal monitor reactions. The resulting estimates of the thermal/epithermal neutron fluences were then used to calculate burnup corrections for the threshold fast neutron monitor reactions. Burnup corrections were quite small, averaging 1-5% for the thermal/epithermal reactions and < 1.5% for the threshold reaction rates. The activation rates listed in Table 1 are normalized to full reactor power of 85 MW and have a net absolute uncertainty of about 3%.

It should be noted that there was a discrepancy in the records concerning the placement of some of the dosimetry capsules in the 11J subassembly. The positions assigned in Table 1 lead to a consistent dependence of the activation rates with elevation about midplane for both experiments. Consequently, this placement was adopted and the data for both experiments were analyzed together. The activation rates were fit to a polynomial function of form  $f(x) = f(0) [1 + ax + bx^2]$ , where  $x$  is the vertical height from reactor centerline in cm. All of the data are reasonably well fit by the average polynomial with coefficients  $a = -2.744E-3$  and  $b = -1.674E-3$ . The best fit to the data, as given by these coefficients, predicts that the maximum flux position is located about  $-0.8$  cm below midplane. The flux gradient is so shallow that this only produces a flux difference of 0.1% from the midplane position. However, the asymmetry increases to a flux difference of about 12% between the top and bottom of each assembly.

Midplane activation rates were used in the STAY'SL [3] computer code to adjust the neutron flux spectrum. STAY'SL performs a generalized least-squares adjustment of all measured and

Table 1. Activation Rates (atom/atom-s) - HFIR-RB-11J,12J

Position /Monitor	Ht,cm	$^{54}\text{Fe}(n,p)^{54}\text{Mn}$ (E-11)	$^{46}\text{Ti}(n,p)^{46}\text{Sc}$ (E-12)	$^{55}\text{Mn}(n,2n)^{54}\text{Mn}$ (E-14)	$^{63}\text{Cu}(n,\alpha)^{60}\text{Co}$ (E-14)	$^{59}\text{Co}(n,\gamma)^{60}\text{Co}$ (E-9)	$^{93}\text{Nb}(n,\gamma)^{94}\text{Nb}$ (E-10)
11J-128	-13.4	0.998	1.36	3.07	6.42	1.45	2.44
11J-76	-6.6	1.27	1.72	3.82	8.15	1.82	3.11
11J-92	0	1.30	1.66	3.90	8.51	1.95	3.33
11J-94	0	1.33	1.81	4.02	8.57	1.95	3.31
11J-115	6.6	1.23	1.58	3.68	7.89	1.94	3.10
11J-96	13.4	0.844	1.07	2.59	5.59	1.30	2.11
12J-29	-13.4	0.953	1.36	2.87	6.40	1.45	2.44
12J-126	-6.6	1.27	1.71	3.82	7.76*	**	3.24
12J-119	0	1.34	1.73	3.88	*	1.92	3.44
12J-124	0	1.36	1.83	4.01	*	1.92	3.44
12J-116	6.6	1.26	1.62	3.66	8.00*	1.91	3.23
12J-28	13.4	0.878	1.20	2.69	5.76	1.40	2.20

\*Cu samples could not be recovered for capsules 12J-119 and -124. The Cu monitors were recovered for capsules 12J-116 and -126; however, some sample loss may have occurred.  
\*\*Co-Al sample could not be relocated.

calculated values, including the measured activities, calculated spectra, and neutron cross sections. Neutron cross-sections and their uncertainties were generally taken from the ENDF/B-V evaluation [4]. The resulting neutron fluence values are listed in Table 2.

The calculated neutron flux spectrum was obtained from R. A. Lillie (ORNL, private communication). The  $\text{Eu}_2\text{O}_3$  thermal neutron shield initially provides high suppression of the thermal neutron flux and extends into the epithermal energy range. However, due to the high thermal neutron flux in HFIR, the Eu suffers significant burnup as the irradiation progresses, thereby making the thermal shield less effective as the irradiation progresses. The thermal neutron flux, as calculated by R. A. Lillie, is shown as a function of irradiation time in Figure 2. Due to this unusual increase in the thermal neutron flux as well as the shielding effects on the epithermal neutrons, it is difficult to determine a unique solution to the thermal and epithermal fluxes given the dosimetry measurements. Consequently, the thermal neutron fluence in Table 2 has been assigned a high uncertainty. However, the net contribution of the thermal neutrons represents a fairly small perturbation on the mainly epithermal reaction rates for activation and helium production from Ni, as discussed below. The neutron spectral adjustment performed with STAY'SL, as shown in Figure 3, represents an average neutron spectrum over these irradiations.

Neutron damage calculations were performed using the SPECTER computer code [5] at the midplane position of HFIR. Midplane dpa and helium (appm) values are also listed in Table 2.

Table 2. Midplane Fluence and Damage Values for HFIR-RB-11J,12J

<u>Neutron Fluence, <math>\times 10^{21}</math> n/cm<sup>2</sup></u>		<u>Element</u>	<u>dpa</u>	<u>He, appm</u>
Total	18.5 $\pm$ 7%	C	6.9	7.0
Thermal (<.5 eV)	0.26 $\pm$ 50%	Al	10.9	2.4
0.5 eV - 0.1 MeV	8.76 $\pm$ 13%	V	7.0	0.10
> 0.1 MeV	9.48 $\pm$ 11%	Cr	5.9	0.63
> 1 MeV	3.31 $\pm$ 13%	Fe	5.3	1.0
		Ni Fast	5.90	15.7
		<sup>59</sup> Ni	0.01	5.8
		Total	5.91	21.5
		Cu	7.1	0.86

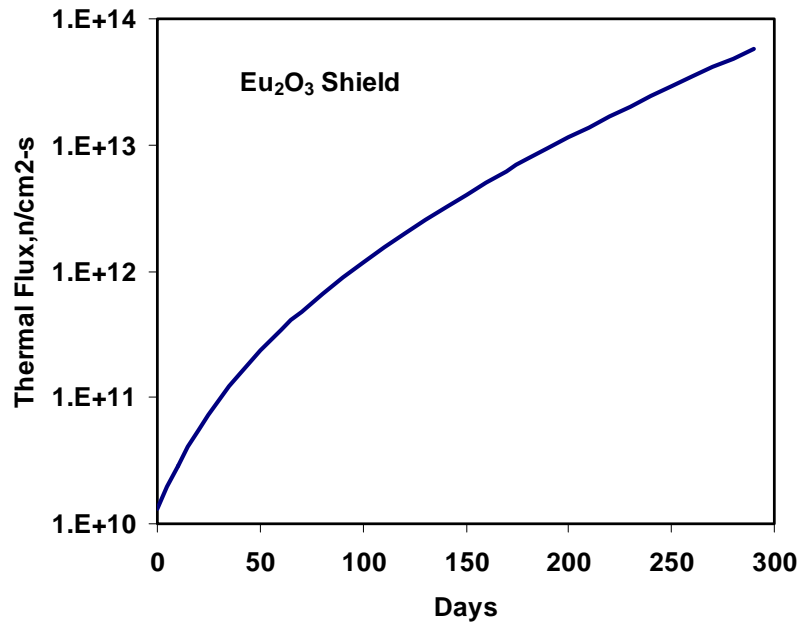


Figure 2. Time-dependent thermal neutron flux in the HFIR-RB showing the burnout of  $\text{Eu}_2\text{O}_3$  shielding, as calculated by R. A. Lillie.

The fluence and damage values at other experimental positions can be calculated by the gradient equation given above. Damage parameters for other elements or compounds have been calculated and are readily available on request.

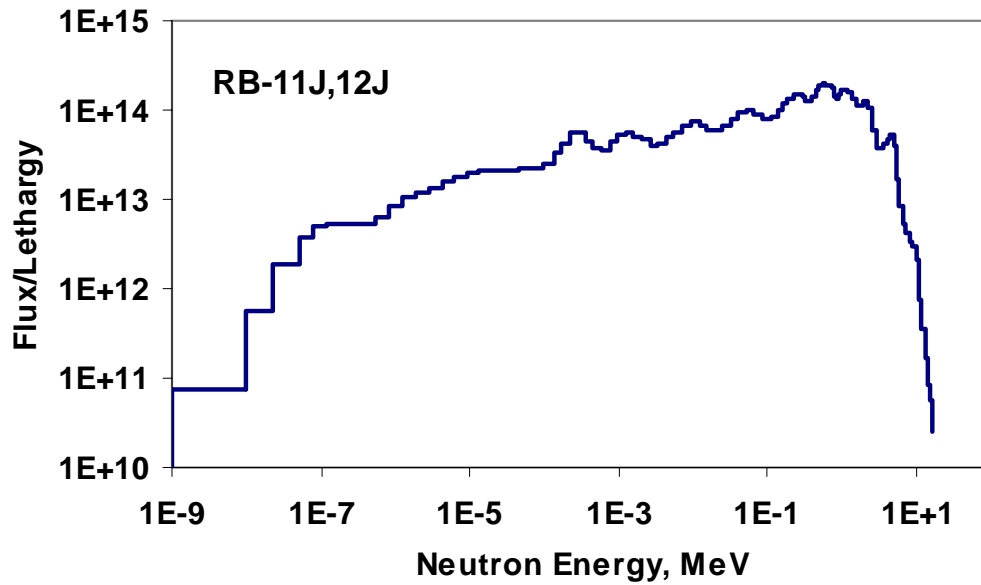


Figure 3. Neutron energy spectrum adjustment for the HFIR-RB-11J/12J experiments using the STAY'SL computer code.

Table 3. DPA and Helium Values for 316 SS in HFIR-RB-11J,12J (includes  $^{59}\text{Ni}$  effect)

Height, cm	He, appm	dpa
-16	2.0	3.4
-14	2.4	3.9
-12	2.7	4.3
-10	3.0	4.7
-8	3.2	5.0
-6	3.4	5.2
-4	3.5	5.4
-2	3.6	5.5
0	3.6	5.5
2	3.5	5.4
4	3.4	5.3
6	3.3	5.1
8	3.0	4.8
10	2.8	4.4
12	2.5	4.0
14	2.1	3.5
16	1.7	2.9

316SS = Fe(0.645), Ni(0.13), Cr(0.18), Mn(0.019), Mo(0.026) wt%

Helium production in nickel and nickel alloys requires a more complicated non-linear calculation [6]. Helium production in stainless steel is thus detailed separately in Table 3.

#### **FUTURE WORK**

Additional experiments that are still in progress or not yet analyzed are detailed in the Fusion Reactor Materials Semiannual Progress Reports.

#### **REFERENCES**

- [1] M. L. Grossbeck, K. E. Lenox, M. A. Janney, D. W. Heatherly, and K. R. Thoms, Fusion Reactor Materials Semiannual Progress Report, DOE/ER-0313/22, pp. 254-283 (1997).
- [2] K. E. Lenox and M. L. Grossbeck, Fusion Reactor Materials Semiannual Progress Report, DOE/ER-0313/25, pp. 307-323 (1998).
- [3] F. G. Perey, Least Squares Dosimetry Unfolding: The Program STAY'SL, ORNL/TM-6062 (1977).
- [4] Evaluated Nuclear Data File, Part B, Version V, National Nuclear Data Center, Brookhaven National Laboratory.
- [5] L. R. Greenwood and R. K. Smither, SPECTER: Neutron Damage Calculations for Materials Irradiations, ANL/FPP-TM-197, January 1985.
- [6] L. R. Greenwood, A New Calculation of Thermal Neutron Damage and Helium Production in Nickel, Journal of Nuclear Materials, Vol. 116, pp. 137-142 (1983).

**11. MATERIALS ENGINEERING AND DESIGN  
REQUIREMENTS**

No contributions.

## **12. IRRADIATION FACILITIES AND TEST MATRICES**

No contributions.